Photoemission experiments in rare earth compounds and magnetic thin films: Study of the electron correlation effects

Krishna Gopal Nath

DOCTOR OF PHILOSOPHY

Department of Structural Molecular Science
School of Mathematical and Physical Science
The Graduate University for Advanced Studies

1998

Table of contents:

List of abbreviations

CI	configuration interaction
CIS	constant initial state
CFS	constant final state
DXM	double crystal monochromator
DCMA	double pass cylindrical mirror analyzer
FMR	ferromagnetic resonance
ESCA	electron spectroscopy for chemical analysis
EDC	electron distribution curve
LEED	low energy electron diffraction
ML	monolayer
MD	magnetic dichroism
MLD	magnetic linear dichroism
MLDAD	magnetic linear dichroism in angular distribution
MCD	magnetic circular dichroism
MCDAD	magnetic circular dichroism in angular distribution
PGM	plane grating monochromator
TY	total yield
UPS	ultraviolet photoemission spectroscopy
UVSOR	Ultraviolet synchrotron orbital radiation
XPS	x-ray photoemission spectroscopy
XAS	x-ray absorption spectroscopy

Abstract

In the present thesis, the results from the study of the core level photoemission for some mixed valent rare earth compounds and artificial thin films of 3*d*-transition metals have been reported. In rare earth and 3*d*-transition metal systems, the outer 4*f* and 3*d* shells are localized and are strongly interacted with the localized core hole during the photoemission process. Because of this interaction, core level photoemission often reflects some obvious final state effects, such as multiplet structures, correlation-induced satellite, charge transfer satellite, lifetime broadening, configuration interaction, valence fluctuation etc. One of the main purposes of the present experiment is to study the spectral features, hence the ultimate final state effects in Tm 5*p*, 4*d*, 4*p*, and 3*d* core levels for mixed valent TmX (X=S, Se and Te). Both the synchrotron radiation and conventional x-ray sources were used for this purpose. By the help of resonant effect and the calculation, a rich information of the electronic structures in the Tm-compounds was obtained in these experiments.

In the transition metal systems, both the core level and the valence *d*-level photoemission are accompanied with well-known satellite structures that are only explained by considering many-body effects. Not only the electronic structure, but also the magnetic properties can be extracted from the photoemission experiments. In the present study, electronic structures and magnetic properties for Ni/Co/Cu(001) system and oxidized Co films were investigated. Magnetic dichroism (MD), a novel technique based on photoemission by proper selecting of orientation of light polarization, directions of magnetization and electron emission, was applied for the magnetism study. For Ni/Co/Cu(001) system, the magnetic state depending on the film thickness was revealed in the core level and valence band photoemission. For Ni-valence band satellite, the resonance effect on the MLD signal was found at Ni3*p*-3*d* excitation regions. In case of oxidized Co film, the modification of electronic structures as a function of both the oxygen coverage and film thickness was studied by Co2*p* and O1*s* core levels photoemission. Magnetic states of the oxidized Co films were also studied by magnetic dichroism experiment.

Chapter 1

General introduction

1.1. Strongly correlated system and photoemission

Photoemission spectroscopy has been extensively utilized to investigate the electronic structures of the strongly correlated 4*f*- and 3*d*-electron systems. Because of the strongly correlated nature, the 4*f*- and 3*d*-electron systems show a variety of physical and magnetic properties. Some fundamental phenomena, such as localized and itinerant nature of unfilled *f*- and *d*-shell, hybridization between the unfilled shell and conduction band are the origins of the variation in the physical and magnetic properties.

Both the outer level (*d* or *f*) and core level are of interest to study in photoemission spectroscopy for strongly correlated systems. The information obtained from the core level and outer level photoemission is different. For example, in case of 4*f* photoemission of the rare earth, the results are used to explain the localized nature and degree of hybridization with the conduction electrons in the solids. The results are thus very important to understand clearly the Kondo effect [1.1], heavy fermion nature [1.2], and valence fluctuation or intermediate valence [1.3] of the rare earth systems.

From the core level photoemission, on the other hand, the nature of interaction between outer shells and the core levels can be revealed. In the rare earth systems, the 4*f*-shells largely maintain their atomic characteristics and they behave as a core level [1.4,1.5]. During the core level photoemission process, the interaction between the core hole and the localized 4*f*-shells is strong [1.6,1.7]. The nature of this interaction is different for several core levels in any atomic system. The different characteristic interactions for different core levels give a variety of spectral shapes in the core levels photoemission. In some cases, the spectral features of the core level photoemission are rather complex. The complex structure in core level photoemission is generally explained by introducing some final state effects, namely multiplet structures, lifetime broadening effect [1.7], configuration interaction (CI) [1.8], preferential Auger decay (Coster-Kronig and super Coster-Kronig) [1.9], and valence fluctuation etc. The valence fluctuation, in other words, the co-existence of different valence states in a single system contributes an extra complexity in the core level spectra. Therefore, core level photoemission is thus very useful to know the details of the electronic structures in rare earth systems.

In the 3*d*-electron systems (both in metal and compounds), the correlation nature of 3*d*-shells and the strong interaction between the 3*d*-shells and the core holes are also essential to describe the core level spectral features. The formation of satellite structures in both the

valence band and core level photoemission spectra in some of the transition metal (TM) and their compounds is explained by using the effects of *d-d* correlation. One of the well-known satellites is the Ni 6eV-satellite [1.10-1.12] in both Ni-valence and core level photoemission spectra. The interaction between the core hole and the *d*-shell is also strong in the transition metal cases and the muliplet structures are also present in the photoemission spectra.

1.2.Core level photoemission in rare earth compounds

In the present study, several core level photoemission spectra are measured for the rare earth systems, Tm monochalcogenides, TmX (X=S, Se and Te). TmX compounds with NaCl structure are known as typical mixed valent compounds [1.10-1.17]. These three compounds show remarkably different physical properties. All of these three compounds are magnetically ordered at low temperature with T_N at 5.18, 1.85-2.8, 0.21K for TmS, TmSe and TmTe, respectively [1.10]. In these compounds, the coexistence of trivalent (Tm^{3+}, $4f^{12}$) and divalent (Tm^{2+}, $4f^{13}$) ions with different strength shows the property of mixed valence. It was found in some photoemission experiments, susceptibility and lattice constant measurements that TmS is mostly trivalent with metallic character, TmSe is typical intermediate valent with metallic character and TmTe is mostly divalent with semiconducting property [1.13-1.17].

In chapter 4, the nature of interaction between the Tm4*f*-electrons with the Tm5*p*, 4*d*, 4*p*, and 3*d* core holes during the photoemission process is investigated.

So far, most of the photoemission experiments for TmX compounds and metallic Tm was mainly confined to the Tm4*f* photoemission study [1.15,1.16,1.18-1.25]. In some of the previous reports, resonance behaviors in Tm4*f* photoemission around Tm4*d*-4*f* absorption edges (hv=150-200eV) [1.19,1.20,1.22,1.25] or around Tm3*d*-4*f* absorption edges (hv=1450-1520eV) [1.21,1.26] were studied. The 4*f*-multiplet structures corresponding to Tm^{2+} and Tm^{3+} ions and their individual resonance effect were successfully distinguished in those resonant photoemission experiments. Whereas a few core level photoemission results for Tm-systems are available indeed. The results of Tm5*p* photoemission in TmSe [1.15], TmS [1.19], TmTe [1.18] and metallic Tm [1.22], Tm4*d* photoemission in metallic Tm [1.27,1.28] and trivalent $TmAl_2$ [1.24], Tm3*d* photoemission in metallic Tm [1.29] have been reported so far.

Because of the same principal quantum number of 4*d* and 4*f* levels, the electrostatic interaction between them is considered to be very large. The photoemission spectrum of 4*d* level thus may affected by the 4*d* core hole-4*f* electron interaction very much. In the preliminary 4*d* photoemission experiment for metallic Tm system [1.27], the existence of multiplet structures and their lifetime broadening effect were not discussed. Recently a detailed study of 4*d* photoemission spectra including multiplet structures and corresponding lifetime broadening effect for some heavy rare earth elements was reported theoretically by Ogasawara *et al.* [1.28]. The comparison with experimental results was also given in Ref. 1.28. The lifetime broadening effect, which is explained in details in Ref. 1.28 for discussing the 4*d* spectral feature, is related to the 4*d*-4*f*4*f* super-Coster-Kronig (sCK) decay process [1.9]. In Ref. 1.28, the results are limited to the 4*d*-spectrum of Tm^{3+}ion. No studies related to the divalent or mixed valent Tm have been reported. In the TmX systems, the Tm4*d* photoemission spectra should show the mixed-valent properties as well as the Tm4*f* spectra. But the spectral features are more complex than those of 4*f* levels. In the Tm4*f* photoemission spectra, the binding energy positions of components for Tm^{3+} and Tm^{2+} are different. Therefore, the components for Tm^{3+} and Tm^{2+} can be easily distinguished. In the 4*d* photoemission, on the other hand, the Tm^{3+} and Tm^{2+} components are not distinguished because they are overlapped each other. The resonant photoemission around Tm3*d*-4*f* absorption edges is therefore very useful to study both components separately in 4*d* photoemission spectra. In a preliminary experiment for trivalent $TmAl_2$ [1.24], the resonant effect in Tm4*d* was described at the 3*d*-4*f* resonance. However, the existence of multiplet structures and their lifetime broadening effect were not discussed in Ref. 1.24.

In the present experiment, the Tm4*d* resonant photoemission spectra were measured at Tm 3*d*-4*f* absorption edges (hν=1450-1550eV). The information of the muliplet structures for each component (Tm^{3+} or Tm^{2+}), their resonant behavior, and the corresponding lifetime broadening effect is expected from the photoemission results. In practice, the resonant photoemission study around these photon energy ranges for heavy rare earth elements is rather difficult to perform. The main obstacles are to get high photon flux and higher energy resolution at the photon energy range hν=1.2-2.0KeV. After installing YB_{66} crystal monochromator at the UVSOR beamline and by using high performance analyzer, the present experiment became possible.

In case of Tm4*p*, the interaction between 4*p* core hole and 4*f* electrons is also strong because of same principle quantum number. However, the lifetime broadening effect is now related to

the 4*p*-4*d*4*d* super-Coster-Kronig type decay process. According to the suggestion by McGuire [1.9] and prediction by Fuggle and Alvarado [1.30], and Ohno and G. Wendin [1.31], the complex Tm4*p* spectra can be explained by the configuration interaction in the final state. No result was reported previously for Tm4*p* photoemission in TmX compounds. In the present study, the 4*p* photoelectron spectra in three Tm-compounds were measured by using conventional x-ray source (Mg*K*α, hν=1253.6eV). Configuration interaction phenomenon fairly explains the 4*p* spectral features.

The shallower core level Tm5*p* in the same compounds may show different photoemission characteristics. The interaction between 5*p* hole and 4*f* shell is rather weak. As a result, even with smaller spin-orbit splitting, the 5*p* spectrum shows nearly separated spin-orbit peaks. But muliplet peaks are also present here. The Tm5*p* photoemission results were previously reported for TmS [1.15], TmSe [1.19], TmTe [1.18] and Tm metal [1.20]. In these experiments, a complete understanding about the multiplet structures and their resonance effect at 4*d*-4*f* (hν=150-200) absorption edge are absent. In order to get a clear picture about the coupling of shallower 5*p* core level with the 4*f*-shell, it is very important to show the muliplet terms by comparing with calculation. Here, the experiment was performed to have clear information of the evidence of valence fluctuation in the 5*p* XPS spectra and also the resonant effect at 4*d*-4*f* absorption edges of different multiplet structures.

In case of Tm3*d* core level photoemission, it is not possible to excite the 3*d* electrons (binding energy ranges of 1.45-1.53keV) with the commonly used x-ray sources (hν<1.5keV). The soft x-ray synchrotron radiation beamline is considered to be a good source to measure photoemission of the deeper 3*d* level. The unpublished data by H. Arai [1.29] is considered to be the first attempt to measure the Tm3*d* level photoemission in metallic Tm sample by using synchrotron radiation. In Ref. 1.29, the existence of muliplet structures was not discussed. In the final part of chapter 4, the Tm3*d* photoemission spectra will be described.

According to the above introductory paragraphs for Tm4*d*, 4*p*, 5*p*, and 3*d* core levels, it can be said that the common interest of the present core level photoemission is to study the effect of core hole-4*f* interaction and the subsequent changes of the spectral feature. Even in the same atomic system, the nature of the core hole-4*f* interaction is dependent on the several parameters. These parameters are owing to the similarity and dissimilarity of the principle quantum number of the core level and the 4*f* shells, the relative values of the exchange interaction and the spin-orbit splitting, strength of the Auger and Auger-like decays, exciting

conditions, degree of mixed-valence, etc. The results from the core level photoemission are expecting to be varied with a rich information of the electronic structure of the mixed valent TmX compounds.

In the present thesis, every photoemission results will be compared with the calculated results in order to obtain the better understanding of the photoexcitation and the decay process of the strongly correlated systems. The calculated results were provided by one of the collaborators Dr. H. Ogasawara in Prof. Kotani group, ISSP, University of Tokyo.

1.3. Thin film magnetism of the 3*d*-transition material

The photoemission experiments for both the core level and valence band in the magnetic 3*d*-transition materials are also very interesting because of the strong influence of the many-body effect via electron correlation in photoemission spectra. Therefore, the knowledge of the correlation in these strongly correlated systems is very important for understanding the spectroscopy result. The formation of the satellite structure in the photoemission for Ni or Co is the direct consequence of the electron-correlation. For example, narrow *d*-band with strong *d*-*d* interaction is held responsible for the formation of satellite structure: known as correlation-induced structure. The nature of the *d*-*d* interaction is also different depending on the dimension of the sample, such as for bulk sample, thin film with very various thickness etc. The single-particle approximation is completely failed to explain the formation of satellite. Apart from metal, the transition metal compounds, for example NiO or CoO also show correlation-induced satellite in core level photoemission and also in valence band photoemission. Though, the mechanism of satellite formation is similar to Ni or Co, the satellite in transition metal oxides is known to be charge-transfer satellite.

In general, electronic interaction in strongly correlated systems governs many phenomena in the solid-state physics. For example, ferromagnetism or antiferromagnetism in the strongly correlated system is the direct evidence of the spin-dependent electron correlation. For any magnetic system, the magnetic state can be studied by applying magnetic dichroism (MD) technique [1.32]. In order to explain the magnetic dichroism signal in photoemission, the knowledge of the electron correlation is thus very important.

It is now well known and firmly established that the ultrathin film systems in nanometer range of 3*d*-materials often show very interesting and striking magnetic properties different from the bulk [1.3,1.34]. Because of rich variety of unusual magnetic properties, the thin film magnetism is considered to be very interesting and challenging field in the recent years. By varying the preparation conditions, i.e., different substrates (non-magnetic, magnetic or semiconductor), substrate temperatures or film thickness, one can modify the electronic structures as well as the magnetic properties of the film. One well-known phenomenon is the transition of easy magnetization axis from in plane to perpendicular direction. This transition depends on the film thickness. For example, Ni film on Cu(001) substrate shows this kind of transition. Up to 7ML (monolayer), Ni film shows in-plane magnetization and above 7 ML, Ni film starts to show a transition towards perpendicular direction [1.34]. As the film morphology is the origin of transition of magnetization, the nature of substrate plays an important role here.

In chapter 5, two different magnetic thin film systems: Ni/Co bi-layer system (here both the Ni and Co films are on Cu(001)) and oxidized Co film are investigated. For Ni/Co/Cu(001) system, in order to observe the effect of the magnetic Co substrate, magnetic linear dichroism signal in element specific photoemission was measured. In the relevant chapter, the dichroism effect of the both main peak (valence band) and the 6eV-satellite peak around Ni3*p*-3*d* absorption edge will be discussed. One of the main purposes of the dichroism study for Ni/Co system is to observe the resonant effect on dichroism signal for Ni 6eV-satellite at Ni3*p* threshold. Though, magnetic dichroism study has been performed in bulk Ni(110) for Ni-valence band satellite at Ni3*p* threshold [1.35], no study was reported previously for thin film system. Other purposes are to check the nature of the interface coupling between two ferromagnetic films (Ni and Co) and to find out the magnetic states of Ni films with different thickness on Co.

Adsorption process of simple molecule on transition metal (TM) surfaces, especially for thin film systems is very important and offers a lot of interest to both the surface science and the magnetism communities [1.36]. For this thesis work, the oxidization process of different thickness of Co film was studied. The information of the chemical states from such kinds of system may be very useful for recording and storage media technology. The results of the core levels (O1*s* and Co2*p*) photoemission spectra will be shown and discussed. The study of the oxidization process of Co film through Co2*p* core level photoemission has not been performed before. Some photoemission experiment [1.37,1.38] for studying the oxidization of Co films

have been reported previously, but using Co3*p* or Co-valence band photoemission. The study of Co2*p* core level photoemission has some advantages over Co3*p* or valence band study. In the former case, the chemical shift peaks of CoO and the satellite peaks are separated and well distinguished.

The photoemission results from the TMO also show the strongly correlated nature. As stated before, the satellite feature in the photoemission spectra for CoO are known to be the charge transfer satellite. The explanation of the photoemission spectra for transition metal oxides (TMO) is therefore based on the charge transfer processes [1.39-1.41] between the transition metal (TM) and ligand atom (here O). In this process, the electron from ligand atom O is transferred to the metal site (TM, unoccupied metal state). Therefore, the TM core level (2*p*) photoemission is sensitive to the electronic structures of the strongly correlated TMO and can be applied to detect even a subtle change in their electronic structures followed by oxidization process. The magnetic properties of oxidized Co-film were also studied by magnetic dichroism experiment. For oxidized Co film, all photoemission spectra were carried out by conventional x-ray sources (Mg$K\alpha$, hν=1253.6eV or Al$K\alpha$, hν=1486.6eV).

1.4. Improvement of the experimental set-up

A chamber for sample preparation and epitaxial growth of thin films was developed during this thesis work. The preparation chamber is equipped with LEED optics, sample transfer mechanism, three water-cooled evaporators, thickness monitor, sample transfer system and magnetic coil etc. After the improvements in the preparation chamber, the thin film study was successfully performed by using the commercial photoelectron spectrometer.

Some interesting phenomena, such as temperature induced valence transition in rare earth systems, magnetic phase transition in 4*f*- and 3*d*-electron systems etc. are possible to study in photoemission if the sample temperature can be varied during the photoemission experiment. During this thesis work, there were some interesting plans to study temperature effect on the dichroism signal hence the magnetic state and the adsorption process in thin films at various temperatures. For these reasons, a liquid He cryostat was constructed and attached with the sample manipulator in the main analyzing chamber. The performance of the cryostat is satisfactory as expected. Unfortunately, the cryostat could not be used in these present

experiments because the sample holder with heating and transfer options was not ready on time. However, some test experiments were carried out successfully by using the cryostat. For example, variation of electronic structure of the organic compounds $(DI\text{-}DCNQI)_2M$ (M= Ag and Cu), temperature-induced valence transition in the Eu-compound were studied. Result for Eu-compound will be shown in the appendix section.

References

1.1. J. Kondo, Prog. Theoret. Phys. **32**, 37(1964).

1.2. Z. Fisk, H. R. Ott, T. M. Rice, J. L. Smith, Nature **320**, 124(1986).

1.3. P. F. de Châtel, Physica **102B**, 335 (1980).

1.4. "The Electronic Structures of Rare-Earth Metals and Alloys: the Magnetic Heavy Rare-Earths", by B. Coqblin, Academic Press 1977.

1.5. Handbook on the Physics and Chemistry of Rare Earths, Vol 19, Edited by K. A. Gschneider jr., L. Eyring. G. H. Lander, G. R. Choppin, North Holland (1993).

1.6. A. Kotani, "Inner shell photoelectron process in solids", (Handbook on synchrotron radiation, p. 611, Vol.2, Edited by G. V. Marr 1987).

1.7. D. A. Shirley, many-Electron and Final-State Effects: Beyond the One-Electron Picture, P165, (Photoemission in Solids I, Springer-Verlag, Edited by M. Cardona and L.Ley).

1.8. U. Gellius, J. Electron Spectrosc. Relat. Phenom. **5**, 985 (1974).

1.9. E. J. McGuire, Phys. Rev. **A 9**, 1840 (1974).

1.10. A. Kotani, Y. Toyozawa, J. Phys. Soc. Jpn. **35**, 1073 and 1082 (1973).

1.11. S. Hüfner, G. K. Wertheim,Phys. Lett. **51**, 299 (1975).

1.12. C. Guillot, Y. Ballu, J. Paigné, J. Lecante, K. Jain, P. Thiry, R. Pinchaux, Y. Pétroff, L. M. Falocov, Phys. Rev. Lett. **39**, 1632 (1977).

1.13. E. Bucher, K. Andres, F. J. di Salvo, J. P. Maita, A. C. Gos sard, A, S. Cooper, and G. W. Hull, Jr., Phys. Rev. **B 11**, 500 (1975).

1.14. D. E. Eastman, F. Holtzberg, J. L. Freeouf, M. Erbaduk, AIP Procc. **18**, 1030 (1973).

1.15. G. Kaindl, C. Laubschat, B. Reihl, R. A. Pollak, N. Mårtensson, F. Holtzberg, D. E. Eastman, Phys. Rev. **B 26**, 1713 (1982).

1.16. R. Suryanarayanan, G. Guntherodt, J. L. Freeouf, F. Holtzberg, Phys. Rev. **B 12**, 4215 (1975).

1.17. G. K. Wertheim, W. Eib, E. Kaldis, M. Campagna, Phys. Rev. **B 22**, 6240 (1980).

1.18. M. Campagna, E. Bucher, G. K. Wertheim, D. N. E. Buchanan, L.D. Loninotti, Phys. Rev. Lett. **32**, 885 (1974).

1.19. S. -J. Oh, J. W. Allen, I. Lindau, Phys. Rev. **B 30** 1937 (1984).

1.20. Y. Ufuktepe, S. Kimura, T. Kinoshita, K. G. Nath, H. Kumigashira, T. Takahashi, T. Matsumura, T. Suzuki, H. Ogasawara, A. Kotani, J. Phys. Soc. Jpn., **67**, 2018 (1998).

1.21. C. Laubschat, E. Weschke, G. Kalkowski, G. Kaindl, Physica Scripta, **41**, 124 (1990).

1.22. C. K. Nicklin, C. Binns, S. Mozley, C. Norris, E. Alleno, M-G. Barthes-Labrousse, G. van der Laan, Phys. Rev. B **52**, 4815 (1995).

1.23. G. Kaindl, W. D. Brewer, G. Kalkowski, F. Holtzberg, Phys. Rev. Lett. **51**, 2056 (1983).

1.24. C. Laubschat, W. Grentz, and G. Kaindl, Phys. Rev. B **37**, 8082 (1988).

1.25. L. I. Johansson, J. W. Allen, I. Lindau, Phys. Lett. **86A**, 442 (1981).

1.26. T. Kinoshita, Y. Ufuktepe, K. G. Nath, S. Kimura, H. Kumigashira, T. Takahashi, T. Matsumura, T. Suzuki, H. Ogasawara, A. Kotani, J. Electron Spectrosc. Relat. Phenom. **88-91**, 377 (1998).

1.27. W. C. Lang, B. D. Padalia, L. M. Watson, D. J. Fabian, P. R. Norris, Faraday Discuss. Chem. Soc. **60**, 37 (1975).

1.28. H. Ogasawara, A. Kotani, B. T. Thole, Phys. Rev. **B50**, 12332(1994).

1.29. H. Arai, Ph.D. thesis (unpublished), Tohoku University (1987).

1.30. J. C. Fuggle, S. F. Avarado, Phys. Rev. **A 22**, 1615 (1980).

1.31. M. Ohno , G. Wendin, Phys. Rev. **A 31**,2318 (1985).

1.32. C. M. Schneider, J. Mag. Mag. and Mat. **175**, 160 (1997).

1.33. M. T. Johnson, P. J. H. Bloemen, F. J. A den Broeder, J. J. de Vries, Rep. Prog. Phys. **59**, 1409 (1996).

1.34. B. Schulz, K. Baberschke, Phys. Rev. B **50**, 13467(1994).

1.35. S. Ueda, S. Imada, Y. Saitoh, T. Muro, M. Kasashima, A. Kimura, A. Kakizaki, S. Suga, J. Electron Spectrosc. Relat. Phenom. **88-89**, 191 (1998).

1.36. P. D. Johnson, Rep. Prog. Phys. **60**, 1217 (1997).

1.37. L. Gonzalez, R. Miranda, M. Salmerón, J. A. Vergés, F. Ynduráin, Phys. Rev. B **24**, 3245 (1981).

1.38. W. Clemens, E. Vescovo, T. Kachel, C. Carbone, W. Eberhardt, Phys. Rev. B **46**, 4198 (1992).

1.39. J. Zaanen, G. A. Sawatzky, J. W. Allen, Phys. Rev. Lett. **55,** 418 (1985).

1.40. Z. X. Shen, J. W. Allen, P. A. P. Lindberg, D. S. Dessau, B. O.Wells, A. Borg, W. Wills, J. S. Kang, S. –J. Oh, I. Lindau, W. E. Spicer, Phys. Rev. B **42**, 1817 (1990).

1.41. K. Okada, A. Kotani, J. Phys. Soc. Jpn. **61**, 449 (1992).

Chapter 2

General aspects of photoemission and related phenomena

2.1. Photoemission spectroscopy: General description

PhotoEmission Spectroscopy (PES) is one of the simplest and direct methods to study the electronic structures of the solid surfaces, interfaces, molecules, and atoms. PES is based on the photoelectric effect, i.e., the emission of electrons from one of those systems after irradiation the system by photon with sufficient energy. Figure 2.1 shows a typical diagram

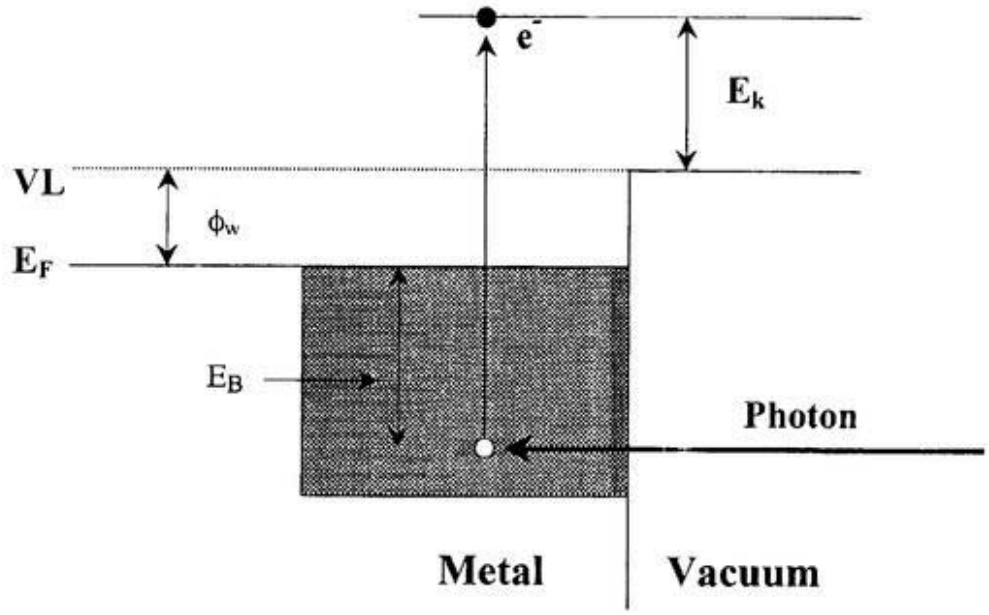

Figure 2.1. Illustration of the photoemission process in a simple metal. Photon with energy hv is annihilated and an electron absorbs the photon energy. VL represents the vacuum level and E_F does the Fermi level. The difference between VL and E_F is the work function of the system. E_k is the kinetic energy of the photoelectron measured from VL, the 'zero kinetic energy' level. E_B is the binding energy measured from E_F.

of the photoemission process for a simple metal. A photon with energy hv impinges into the metal. The electron inside of the metal absorbs the energy of photon. The electron, as a result, is excited to a region above the vacuum level (VL). The electron is then called photoelectron when it leaves from the solid through the vacuum level with kinetic energy E_K. The energy

difference between the VL and Fermi level E_F is called as the work function, ϕ_w. The work function has a characteristic value for individual material. In the spectroscopic point of view, ϕ_w is the threshold energy to produce a photoelectron. Thus, according to the famous Einstein's equation of the photoelectric effect, the maximum kinetic energy of a photoelectron from E_F can be written as follows:

$$E_{K,max}=h\nu-\phi_w . \tag{2.1}$$

Inside of the solid, electrons stay in several energy levels known as valence or core levels. The energy of any particular electron in the energy level is called as the binding energy of that electron. So, the Eq. (2.1) can be modified to express the practical photoemission process in the following way:

$$E_K=h\nu-\phi_W-E_B, \tag{2.2}$$

where E_B is the binding energy of the electron.

The intensity of the photoelectron depending on the energy is the photoemission spectrum, in other words, the energy distribution curve (EDC) [2.1,2.2]. In the photoemission spectroscopy, the electrons are collected and analyzed by the electron analyzer. The EDC is expressed by the following way:

$$N(E_K)dE_K=dC(E_K), \tag{2.3}$$

where $N(E_K)$ is the number of collected photoelectrons per unit time as a function of energy, $dC(E_K)$ represents the number of photoelectrons per unit time with energy interval dE_K centered at E_K.

2.2. Theory of photoemission

In solids, the photoemission process is a complicated process indeed. It is therefore convenient to explain the PES process with a simple model. The most commonly used model for the interpretation of the PES process in solids is the so-called three-step model [2.3]. This model breaks up the complicated PES process into three steps. Each step in this model is considered to be the distinct and individual process. These processes are as follow:

Step 1. Optical excitation of the electron in the solid.

Step 2. Transport of the electron to the surface.

Step 3. Escape of the electron into vacuum.

In the photoemission spectrum, each of these steps has particular contribution, in other words, each step can be related to the specific feature in the spectrum. In Fig. 2.2, the basis of the three-step model is shown. As shown in figure, the "step 1" yields the primary peak, if photoelectrons do not suffer any inelastic loss arising from the "step 2" and "step 3". The photoemission peak therefore represents the maximum kinetic energy from the PES process.

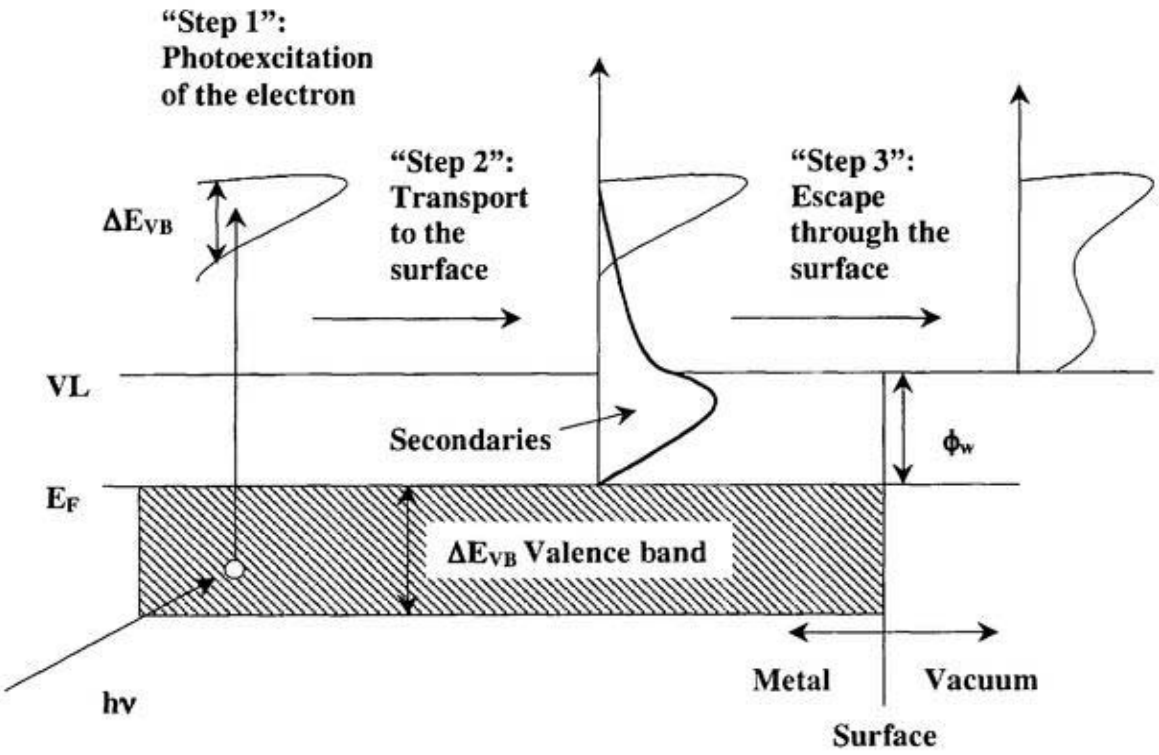

Figure 2.2. PES as a three-step process: 1) photoexcitation of the electron; 2) travel to the surface accompanying with secondaries; 3) penetration through the surface and escape into the vacuum.

In the "step 2", the transportation of electron is occurred towards surface via bulk. During the transportation, the primary electrons may lose some energy through excitation in the bulk and the excitation yields bulk plasmon peak in the spectrum. In the third step where electrons penetrate the surface and escape into the vacuum, the spectrum is affected by the refraction at the surface and the surface plasmon loss. In principle, the whole process of photoexcitation,

transport to and escape through the surface can be treated as one step where the PES is described as transition of an electron from an initial state (bound) to a free electron final state in continuum. In the following, the photoemission process (one electron approximation), structure of the photocurrent, obtained information from PES will be discussed.

2.2.I. One-electron approximation

The photoelectron produced in the PES process can be described as the product of the transition of an electron from an initial state $|\psi_i>$ to a final state $|\psi_f>$ in the continuum in the presence of a photon field with vector potential **A**. The transition probability w between two eigen functions of the Hamiltonian H' can be derived from the Fermi's Golden Rule,

$$w = \frac{2\pi}{\hbar}\left|\langle\psi_f|H'|\psi_i\rangle\right|^2 \delta\left(\mathrm{E}_f - E_i - \hbar w\right) \tag{2.4}$$

where H' denotes the Hamiltonian for the interaction between an electron and a vector potential of the electromagnetic radiation of the field **A**. If higher-order contributions are neglected (dipole approximation), then H' is defined by

$$H' = \frac{e}{2mc}\mathbf{A}.\mathbf{p} \tag{2.5}$$

Here **A** is assumed to be constant and fixed in space. Therefore

$$w \propto \frac{2\pi}{\hbar}\left|\langle\psi_f|\mathbf{p}|\psi_i\rangle\right|^2 \delta\left(\mathrm{E}_f - E_i - \hbar w\right) \tag{2.6}$$

In order to discuss the transition matrix element $<\psi_i|\mathbf{p}|\psi_f>$, the simplest approximation is the one-electron view of initial state and final state wave function. In the N-electron system, after the emission of one electron, the initial state is written as the product of the orbital ϕ_k (k, the running subscript to express the remaining electrons in the orbital ϕ) and the wave function of remaining (N-1) electrons

$$\psi_i(N) = C\phi_{i,k}\psi_{i,R}^k(N-1)\ . \tag{2.7}$$

(R is used to express the remaining electrons in the system)

In the same way the final state wave function can be written for photoelectron $\phi_{f,Ekin}$ and the remaining N-1 electrons as

$$\psi_f(N) = C\phi_{f,Ekin}\psi^k_{f,R}(N-1)\ . \tag{2.8}$$

So, the transition matrix element can be written as the following way

$$\langle \psi_f | \mathbf{p} | \psi_i \rangle = \underbrace{\langle \phi_{f,Ekin} | \mathbf{p} | \phi_{i,k} \rangle}_{\text{one-electron matrix element}} \underbrace{\langle \psi^k_{f,R}(N-1) | \psi^k_{i,R}(N-1) \rangle}_{\text{(N-1)-electron overlap integrals}}\ . \tag{2.9}$$

According to the 'frozen orbital approximation', the remaining orbitals are considered to be the passive orbitals. This means the terms with (N-1) overlap integrals in the initial- and final-state wave functions are invariant. So, from Eqn. 2.9

$$\psi^k_{f,R}(N-1) = \psi^k_{i,R}(N-1)\ . \tag{2.10}$$

Finally, the transition matrix is approximated to a one-electron matrix element. Under this assumption, the photoelectron from the ϕ_k orbital shows the energy (binding energy) related to the negative of Hartee-Fock orbital energy. Thus

$$E_{B,k} \approx -\varepsilon_k. \tag{2.11}$$

which is often called as Koopmans' binding energy.

2.2.II. Many-electron effect

In fact, the system with k orbital and N-1 electrons will react to the sudden change of the total energy in the system following an electron emission. The whole system will try to readjust the remaining charges so as to minimize its energy. The minimization of the energy is known as relaxation process. Because of the relaxation, the final state is considered to be a state with (N-1) electron and 's' excited states (s, the running index to express number of states). So, the Eq. (2.9) can be written by summing over all possible excited states

$$\langle \psi_f | \mathbf{p} | \psi_i \rangle = \langle \phi_{f,Ekin} | \mathbf{p} | \phi_{i,k} \rangle \sum_s C_s, \tag{2.12}$$

with

$$C_s = \langle \psi^k_{f,s}(N-1) | \psi^k_{i,R}(N-1) \rangle. \tag{2.13}$$

Here $|C_s|^2$ is the probability that the sudden emission of one electron from the orbital ϕ_k of N electron ground state leaves the system in the excited state 's' of (N-1) electron system.
There are two conditions that can be derived from (2.13).

Condition. 1. For weakly correlated systems,

$$\psi^k_{f,s}(N-1) \approx \psi^k_{i,R}(N-1) \tag{2.14}$$

This means that $|Cs|^2 \approx 1$ for s = k (in orbital ϕ, the excited state s and remaining state k are same) and $|Cs|^2 \approx 0$ for s ≠ k, i.e., PES shows only the so-called main line peak.

Condition. 2. For strongly correlated systems
For s = k, Eq. (2.12) gives main line emission as condition 1. But there are many non-zero terms due to the strong correlation and these gives additional so-called satellite peaks.

The photoemission spectrum consisting of main lines and satellite lines from a N-electron system with E_0(N) ground state energy is thus written by

$$I \propto \sum_{f,i,k} \left| \langle \phi_{f,EKin} | \mathbf{p} | \phi_{i,k} \rangle \right|^2 \sum_s |C_s|^2 \delta(E_{f,Kin} + E_s(N-1) - E_0(N) - \hbar\omega). \tag{2.15}$$

The expression (2.15) consists of the "lines" created by photoionization of electron from the various orbitals. The expression (2.15) is more convenient to use for atoms and molecules rather than the solids [2.4].

2.2.III. Spectral function and self-energy:

For solids, the expression (2.15) needs some modifications by changing the δ-function (line spectrum without relaxation) into Lorentzian function (broadened spectrum due to the relaxation). The rewritten form of (2.15) is thus:

$$I \propto \sum_{f,i,k} \left| \langle \phi_{f,Ekin} | \mathbf{p} | \phi_{i,k} \rangle \right|^2 A(k,E), \tag{2.16}$$

where $A(k,E)$ is the so-called spectral function [2.5]. The spectral function is related to the final state Green's function as expressed by

$$A(k,E) = \pi^{-1} Im\{G(k,E)\} \tag{2.17}$$

For a non-interacting system, the spectral function is expressed as a δ-function as the expression (2.15). But for an interacting system, for example, where the core hole strongly interacts with surrounding charges and the core-hole peak is shifted and broadened due to relaxation and decay process, the spectral function takes complex form. As a result, the Green's function in the final state in (2.17) is changed and the perturbation must be included in the final state Hamiltonian. The key quantity for describing the dynamics of the interaction is the self-energy of the core hole, $\Sigma(k,E)=\mathrm{Re}\{\Sigma(k,E)\}+i\mathrm{Im}\{\Sigma(k,E)\}$, as it yields

$$G(k,E) = \frac{1}{E - E_k^0 - \sum(k,E)} \tag{2.18}$$

and

$$A(k,E) = \frac{1}{\pi} \frac{\mathrm{Im}\{\sum(k,E)\}}{[E - E_k^0 - \mathrm{Re}\{\sum(k,E)\}]^2 + [\mathrm{Im}\{\sum(k,E)\}]^2} \tag{2.19}$$

Thus, for the strongly correlated system, such as rare earth systems, it is necessary to calculate the self-energy for explaining the photoemission spectra. In the self-energy, the real part describes the relaxation shift and the imaginary part does the broadening.

2.3. Resonant photoemission

In the resonant photoemission technique, a series of photoemission spectra in a particular binding energy range is taken at different photon energy [2.6]. In this process, at particular photon energy, the photoemission cross-section shows a sharp resonant enhancement. The particular photon energy, where the resonance enhancement is occurred, is usually found around the threshold energy of any core level. Two different processes jointly describe the mechanism of the resonant photoemission.

In Fig. 2.3, the description of the resonant photoemission for a rare earth system is given by schematic diagram. For simplicity, the number of 4*f* electron is considered to be one.

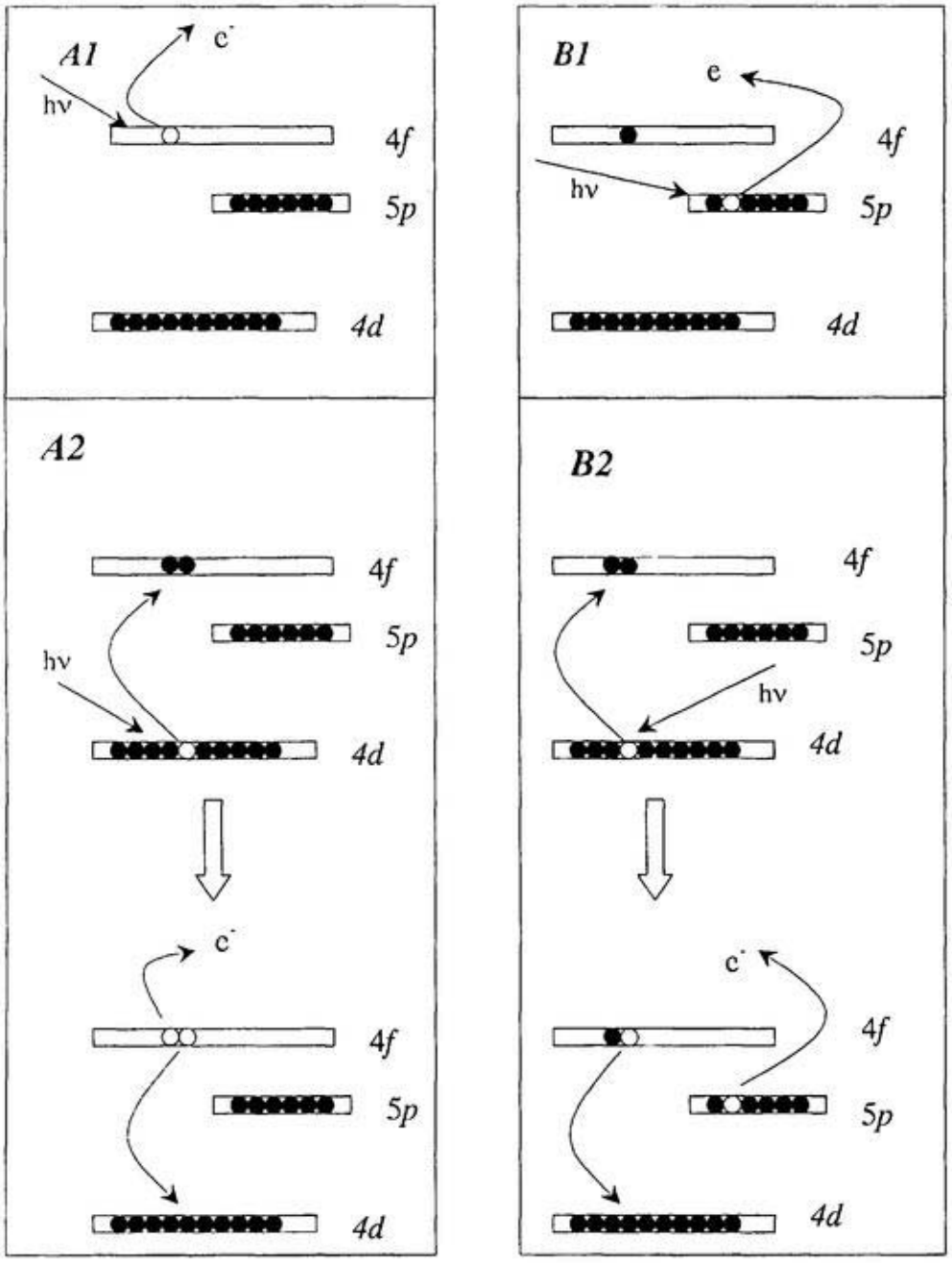

A1: 4*f* photoemission
A2(1): 4*d*-4*f* photoabsorption
A2(2):4*d*-4*f*4*f* super-Coster-Kronig decay

B1: 5*p* photoemission
B2(1): 4*d*-4*f* photoabsorption
B2(2):4*d*-5*p*4*f* Coster-Kronig decay

Figure 2.3. Schematic diagram of the resonant process in 4*f* and 5*p* photoemission.

In process A1, one electron from *f* level is excited into the continuum as a photoelectron after photoionization by the photon with energy equal to 4*d* threshold. The process A2 consists of two steps. At first, one 4*d* electron is excited into the 4*f* level. Secondly, one 4*f* electron may decay to the 4*d* core hole and another 4*f* electron is ejected into the continuum as a photoelectron. This kind of decay is called as super Coster-Kronig (sCK) decay. In process A2, the two steps can not be separated and as a result, two steps are considered to be a single process. The interference between the processes A1 and A2 implies a resonance on the 4*f* photoemission. The interference between the processes B1 (direct 5*p* photoemission) and B2 also show the resonance effect on the 5*p* photoemission. In this case, during the decay (Coster-Kronig) process, one 5*p* electron is ejected into the continuum.

The resonant photoemission is understood according to the theory given by U. Fano [2.7] with the help of a series of characteristic Fano lineshapes. The features of the Fano lineshapes can be obtained by the following way.

According to Fig. 2.3, in the process A2, the first step (4*d* → 4*f* photoabsorption, with N-electron in the 4*f* shell) gives a discrete configuration of $4d^9 4f^{N+1}(|\phi\rangle)$ and the second step (4*d*4*f*4*f* sCK decay) gives a continuum state $4d^{10}4f^{N-1}(e^-)$ ($|\psi_E\rangle$) followed by the autoionization. Here e^- is the photoelectron. In the process A2, the two steps, namely, the 4*d* → 4*f* photoabsorption and the 4*d*-4*f*4*f* sCK decay can not be separated and are considered to be occurred as one-step. The continuum state $4d^{10}4f^{N-1}(e^-)$ ($|\psi_E\rangle$) due to the autoionization is identical to the process A1 in Fig.2.3. The intensity of the 4*f* photoemission ($N(E)$) is given by the square of the absolute value of the amplitudes of the processes A1 and A2 as follow:

$$N(E) = \frac{(2\pi)^2}{h} \left|\left\langle \psi_E \middle| T \middle| \Phi_g \right\rangle\right|^2 \frac{(\varepsilon + q)^2}{1+\varepsilon^2}. \tag{2.20}$$

Here, ($|\Phi_g\rangle$) is the ground state, ($|\psi_E\rangle$) is the final state $4d^{10}4f^{N-1}(e^-)$ with the energy E, T is the dipole transition, ε is a reduced photon energy, $\varepsilon=(h\nu-h\nu_0)/\Gamma$ as $h\nu_0$ is the center of the resonance and Γ is the width of resonance.

In Eq. 2.20, the parameter q is the so-called asymmetry parameter, and is defined by

$$q = \frac{\left\langle \Phi \middle| T \middle| \Phi_g \right\rangle}{\pi V_E^* \left\langle \psi_E \middle| T \middle| \Phi_g \right\rangle}, \tag{2.21}$$

where

$$\Phi = \phi + P\int dE' \frac{V_{E'}\psi_{E'}}{E - E'} \tag{2.22}$$

is the discrete state (intermediate state) modified by the admixture of the continuum state. Therefore, q is the ratio between the photoabsorption plus sCK decay (the modified discrete state the process A2 in Fig. 2.3) and the direct photoemission (unperturbed continuum state). According to the Eq. (2.20), the intensity *N(E)* is therefore dependent on the value of q. Figure 2.4 shows the N(E) in Eq. (2.20) as a function of ε (photon energy) for various values of q. These curves are the Fano lineshapes. It is clear from the figure that photoemission intensity is changed with the incident photon energy. This indicates that the photoabsorption is coherent with the photoemission. As q increases, i.e., the contribution of modified discrete state (quantitatively the contribution of the photoabsorption and sCK decay), the degree of enhancement in photoemission increases.

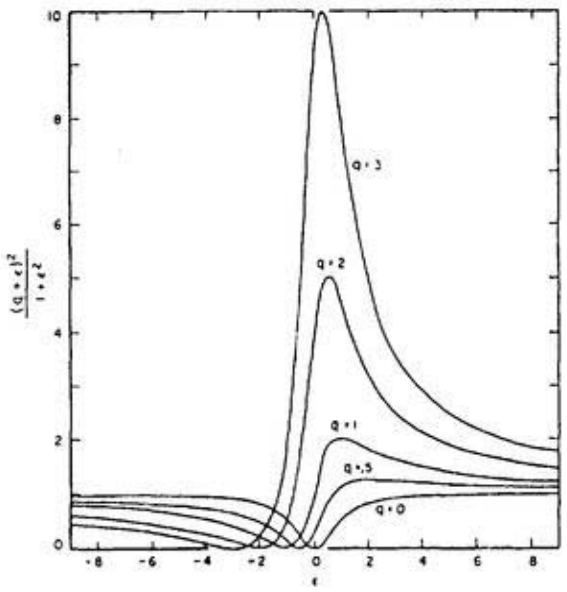

Figure 2.4. Theoretical Fano lineshapes [2.7] for different q values in Eq. (2.19).

Gulliot *et al.* [2.8] gave a more general review of Fano theory. They explained how the resonance behavior of the satellite peak in Ni3*d* bands accords to the Fano line shape at the Ni

$3p$-$3d$ resonance. Other resonance phenomena such as $5d$-$5f$ and $3d$-$4f$ are found for rare earth systems and Actinides systems.

In the resonant photoemission experiment, besides the EDC mode, there are other two modes of measurement for studying the resonance effect more clearly. These are the constant final state (CFS) and the constant initial state (CIS) spectroscopies. In the CFS method, the kinetic energy window of the electron analyzer is fixed at low value in order to record the electrons as a function of photon energy. Because of the collection of low kinetic energy electrons, these electrons are inelastically scattered in the deep area from the surface. The CFS is thus bulk-sensitive and the CFS signal is proportional to the photoabsorption coefficient in the bulk. The CFS can be also carried out by detecting the Auger signal from any adsorbed system. In such cases, the CFS can be considered to be surface sensitive. On the other hand, in CIS, the intensity of the photoelectrons for fixed binding energy is recorded as a function of photon energy. The CIS spectrum is thus useful to identify the individual resonance behavior of any muliplet state in the EDC.

The resonant photoemission spectroscopy using the synchrotron radiation is considered to be a very powerful technique to study the electronic structures of strongly correlated compounds [2.9, and references therein] such as transition metal, rare earth, and actinide systems.

2.4. Final state effects in photoemission spectra

As it is discussed in the section 2.2.II, the photoemission process causes some changes in the system in an atomic scale. The EDC, which should show the exact feature of the ground state, is disturbed because of these changes. As a result, the spectral shape of the EDC is changed into a complex form. The interpretation of the complex is not easy for all cases. The nature of this complex spectrum is the ultimate result of some obvious final state effects [2.10] namely coupling between core hole and unfilled shell, relaxation, electron-electron correlation or inelastic process. In order to study these final state effects, it is important to clarify some other effects arising from the non-monochromated radiation, energy loss, charging or instrumental resolution. Some essential factors related to the spectral feature in the final state will be discussed below.

2.4.I. Multiplet structure in core level spectrum

The interaction between the core hole and the unfilled valence shell leads a number of different final states with different intensities and position in photoemission spectrum. In the following, a simple muliplet structure originating from the exchange splitting will be discussed for three-electron system, lithium (Li) atom.

The ground state configuration of Li is $1s^2 2s^1$. Photoemission of the $1s^2$ shell can give two sets of final states.

$$Li(1s^2 2s^1; {}^2S) + \hbar\omega \rightarrow Li^+ [1s(\downarrow)\, 2s(\uparrow); {}^1S] + e^- \quad (e^-: \text{photoelectron})$$

$$\text{or} \qquad Li^+ [1s(\uparrow)\, 2s(\uparrow); {}^3S] + e^-$$

Because of the coulomb interaction between the singlet and triplet state, they show different energy position in the 1*s* photoemission spectrum.

For rare earth elements, both the valence band and core level have localized and atomic like character. A large number of multiplet structures are present due to the exchange interaction between core hole and valence shell. In order to study the multiplet structures, high-resolution photoemission spectroscopy should be performed. It is difficult to distinguish the multiplet peaks without taking the help of the calculation because of the lifetime broadening effect even performing the high-resolution study. In the experiment, the final state spectrum is considered to be a convoluted (by Lorentzian and Gaussian) spectrum of all muliplet structures. A clear understanding of the multiplet splitting is especially important to study their electronic structures.

2.4.II. Lifetime broadening effect

In photoemission, due to the non-radiative Auger decay and radiative decay, a core hole has finite lifetime, τ. The photoemission peak of the core hole thus shows a lifetime broadening effect associated with all the decay processes [2.11]. The lifetime broadening can be expressed by the following Lorentzian function of the spectral line shape,

$$I(E) = I(E_0)\frac{\Gamma^2}{(E-E_0)^2+\Gamma^2}, \tag{2.23}$$

where *I(E)* is the intensity at energy *E*, *Eo* is the center of the Lorenztian peak, 2Γ is the core-hole lifetime broadening or natural line width which is given by $\tau\Gamma=\hbar$ (from the uncertainty principle). Lifetime broadening effect gives the information of the total Auger transition, radiative decay and photoemission probabilities. In order to get a clear idea about the lifetime

broadening effect of any core level spectrum in experiment, we have to clarify carefully the following several factors that overlap with the true natural line width:

1. Many-electron excitation in the valence band
2. Gaussian broadening due to the phonon and instrumental resolution
3. Strength and position of muliplet peaks
4. Doniach-Sunjic lineshapes (due to the scattering of conduction electrons in metal after core electron ionization).

2.4.III. Configuration interaction (CI)

On the basis of atomic and molecular physics, any stationary state may be described by a mixed or superposition of different electronic configurations. In the photoionization process for any core level, the interaction among different configurations has a significant role to influence the spectral features. As it is shown for resonant photoemission process, the interaction of two configurations controls the photoemission signal. The effect of CI was also found in some other systems. For example, the spectra features of Xe4*p* [2.5] were explained by introducing the CI effect between $4p^5 4d^{10}$ and $4p^6 4d^8 \varepsilon f$ configurations.

2.5. Magnetism study: magnetic dichroism in photoemission

The photoemission process itself has the magnetic information of the material. The photoelectron spectrum is described by a function with many parameters. These parameters are owing to be the photoemission geometry (relative orientation of light electric-vector and photoelectron wave-vector), polarization of impinging light (linear, circular, elliptical, or unpolarized), the spin of the photoelectron, and, in case of any magnetic sample, the direction of magnetization. Photoemission experiments for any magnetic sample are therefore very sensitive to the magnetic order or to the magnetic moments of the surface atoms. One way to get the information of magnetic structure of the surface, hence the surface atoms, is by measuring the spin of the photoelectrons from the valence band or the core levels. The way of measurement is known as spin-resolved photoemission method [2.12,2.13]. In the spin-resolved photoemission method, both the exchange splitting and the spin-orbit splitting are the origins of the spin-polarization. Spin-polarization due to the spin-orbit interaction is also

possible to obtain from the non-magnetic (no exchange splitting) material as suggested by Fano [2.14].

Besides the spin-resolved photoemission, there is another technique of photoemission, namely, magnetic dichroism (MD) [2.15-2.21]. The MD is also a powerful method to study the magnetic properties of the system. The MD measurement has some advantages over the spin-resolved photoemission method where the latter one needs much effort to separate the majority and minority spin electrons. In the MD measurement in photoemission, the fundamental observation is that a single photoemission peak from the core level or the valence band may be resolved into two energetically separated lines, if excited by circularly polarized light or by linearly polarized light under some specific experimental geometry. Magnetic dichroism is explained by one-electron picture [2.20-2.22]. In the atomic description, the hole state with a given angular momentum j in the photoemission process is split into several components with a given projection m_j due to the spin-orbit splitting in the presence of valence spin magnetic moment [2.21]. These components or sublevels are nondegenerate when the excited atom carries a magnetic moment, but rather distributed over an energy range that is similar to the anomalous Zeeman effect of an atom in the presence of external magnetic field.

In the atomic model of magnetic dichroism in photoemission, the angular distribution of photoelectrons ejected from the polarized atom is written as [2.22]:

$$I_j(k,n) = \alpha\omega p \sum_{\lambda\lambda'} \sum_{m_j m_j'} \sum_{\mu} \left\langle \Psi^-_{p\mu} \middle| d_\lambda \middle| \Psi_{nljm_j} \right\rangle \left\langle jm_j \middle| \rho_a \middle| jm_j' \right\rangle \left\langle \lambda \middle| \rho^r \middle| \lambda_j' \right\rangle \left\langle \Psi_{nljm_j} \middle| d^*_{\lambda'} \middle| \Psi^-_{p\mu} \right\rangle \qquad (2.24)$$

In Eq. (2.24), the initial state is described by the quantum numbers $nljm_j$, where n is the principle quantum number, l is the orbital angular momentum, $j=l\pm1$ and m_j are the total angular momentum and its projection, ω is the photon energy and α is the fine-structure constant. In Eq. (2.24), it is considered that no spin-orbit interaction is present in the continuous spectrum.

The first and last terms in Eq. (2.24) are the dipole transition matrix elements in the following form:

$$\left\langle \Psi^-_{p\mu} \middle| d_\lambda \middle| \Psi_{nljm_j} \right\rangle = \frac{2\pi}{\sqrt{p}} \sum_{l_1 m_1} \sum_{m} [j]^{1/2} (i)^{l_1} \exp(i\delta_{l_1})\, Y_{l_1 m_1}(\hat{\mathbf{k}}) (-1)^{1/2 - l - m_j + l_1 - m_1}$$

$$\times \begin{pmatrix} l & 1/2 & j \\ m & \mu & -m_j \end{pmatrix} \begin{pmatrix} l_1 & 1 & l \\ -m_1 & \lambda & m \end{pmatrix} \left\langle \varepsilon l_1 \middle\| d \middle\| nlj \right\rangle, \qquad (2.25)$$

where $\Psi^-_{p\mu}$ is the final state electron wave function which contains in the asymptotic region the superposition of a plane wave propagating in the direction of the electron momentum $\boldsymbol{p}$ and a converging spherical wave, $\boldsymbol{k}=\boldsymbol{p}/|\mathrm{p}|$, μ is the projection of the spin on the laboratory Z-axis, δ_{l_1} is the partial wave shift and $<\varepsilon l\|d\|nlj>$ is the reduced dipole matrix element.

The third term is the photon density matrix. The second term is called as the atomic density matrix. If an ensemble of atoms with total angular momentum j and its projection m_j is polarized in some direction **n** (direction of the magnetic moment), and that is described by an incoherent superposition of the jm_j sublevels, then the second term can be written

$$\left\langle jm_j\left|\rho_a\right|jm_j'\right\rangle = \sum_N \sqrt{4\pi}\ (-1)^{j-m_j}\begin{pmatrix} j & j & N \\ m_j & -m_j' & -M_N \end{pmatrix} Y^*_{NM_N}(\hat{\mathbf{n}})\rho^{\mathbf{n}}_a(j)_{N0}\,, \qquad (2.26)$$

where

$$\rho^{\mathbf{n}}_a(j)_{N0} = \rho^{\mathbf{n}}_{N0} = \sum_{m_1}(-1)^{j-m_1}[N]\begin{pmatrix} j & j & N \\ m_1 & -m_1' & 0 \end{pmatrix}\left\langle jm_1\left|\rho^{\mathbf{n}}_a\right|jm_1\right\rangle \qquad (2.27)$$

The term ρ^n_{N0} is known as the state multipoles. In the atomic model, the polarization state of the core hole produced by photoionization is characterized by the state multipoles [2.20].

Finally, Eq. (2.24) can be written as the following way [2.22]:

$$I_j(\mathbf{k},\mathbf{n}) = \sigma_{nlj}(\omega)\sqrt{3[j]}\sum_{kLN} C^j_{kLN}\sum_{xM}\begin{pmatrix} k & L & N \\ x & M & -M_N \end{pmatrix}\rho^{\gamma}_{kx}\rho^{\mathbf{n}}_{N0}\,Y^*_{LM}(\hat{\mathbf{k}})\,Y^*_{NM_N}(\hat{\mathbf{n}}) \qquad (2.28)$$

This comes from the interference term of the transition matrix elements. Here $\sigma_{nlj}(\omega)$ is the partial photoionization cross section and C^j_{kLN} is a dimensionless parameter which is proportional to the product of two dipole matrix elements and a sin function of the corresponding phase shift difference. The parameter C_{kLN} is considered to be similar to the angular asymmetry parameter β for describing the photoionization cross-sections for atomic orbital with spatial (random and fixed) orientation [2.23].

It is then possible to use the Eq. (2.28) for different experimental geometry depending on the directions of electron ejection (**k**), sample magnetization (**n**) and photon beam (**q**). The different experimental geometry are known as MLDAD (magnetic linear dichroism in angular distribution), MLD (magnetic linear dichroism), MCDAD (magnetic circular dichroism in

angular distribution), MUDAD (magnetic dichroism in angular distribution by unpolarized light).

By using the Eq. (2.28) and the Fig.2.5, those forms of magnetic dichroism can be explained. For simplicity, the discussion is given only for p shell with different values of state multipoles (Eq.2.27) that determine the polarization of hole.

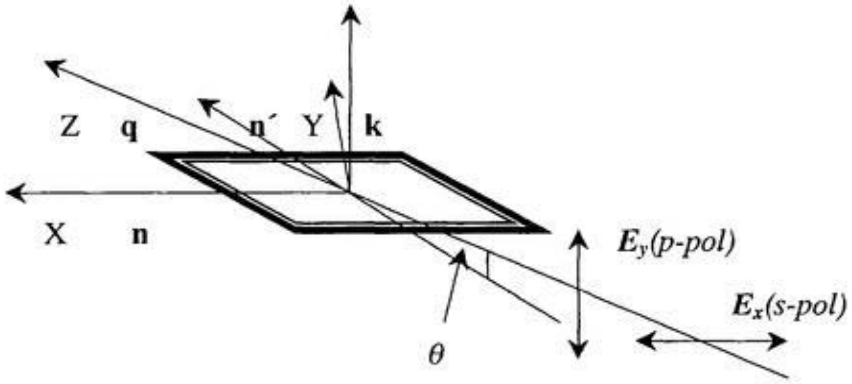

Figure. 2.5. Definition of the geometry of the MD experiments and of the coordinate system. θ is the angle of the light incidence. The directions of **n** and **n´** are orthogonal in the surface plane.

1. MLDAD

By using linearly polarized light (s- and p-polarized) as shown in Fig. 2.5, the following expression can be obtained from the Eq.(2.28).

$$I_j^{MLDAD}(\mathbf{k},\mathbf{n}) = I_j(\mathbf{k},\mathbf{n}) - I_j(\mathbf{k},-\mathbf{n})$$
$$= \frac{\sigma_{nlj}(\omega)}{2\pi}\cdot\frac{3i}{2}C^{j}_{221}(2j+1)^{1/2}\rho^{n}_{10}$$
$$\times\left\{(\mathbf{k}\cdot\mathbf{q})(\mathbf{q}\cdot[\mathbf{k}\times\mathbf{n}])\pm[(\mathbf{k}\cdot\mathbf{q})(k_x n_y + k_y n_x) - 2(\mathbf{n}\cdot\mathbf{q})k_x k_y]\right\} \qquad (2.29)$$

Here upper and lower signs refer to the s- and p-polarized light. For s-polarized light, the Eq. (2.29) gives zero intensity. For p-polarized light and $\mathbf{n}\perp\mathbf{q}$, we get

$$I_j^{MLDAD}(\mathbf{k},\mathbf{n}) = \frac{\sigma_{nlj}(\omega)}{2\pi}\cdot 3i\ C^{j}_{221}(2j+1)^{1/2}\rho^{n}_{10}\sin\theta\cos\theta$$
$$= \frac{\sigma_{nlj}(\omega)}{2\pi}\cdot\frac{3i}{2}C^{j}_{221}(2j+1)^{1/2}\rho^{n}_{10}\ \sin 2\theta \qquad (2.30)$$

The geometry for p-polarized light with $\mathbf{n}\perp\mathbf{q}$ is therefore standard [2.17] for MLDAD measurement. The relative sign and the magnitude of MLDAD in Eq. (2.30) for different magnetic sublevels are defined by the sign and magnitude of the state multipoles in Eq. (2.27).

2. MUDAD

Unpolarized light can be described as an incoherent superposition of s- and p-polarized light. The Eq. (2.30) can be re-written for unpolarized light as follow:

$$I_j^{MUDAD}(\mathbf{k},\mathbf{n}) = \frac{\sigma_{nlj}(\omega)}{2\pi}\cdot\frac{3i}{2}C^j_{221}(2j+1)^{1/2}\rho^n_{10}\ \frac{1}{2}\sin 2\theta \qquad (2.31)$$

Therefore, for using of unpolarized light, the effect of dichroism is 1/2 of that of MLDAD, but the geometry is same.

3. MLD

In case of using the s-polarized light with magnetization along **n** and **n´** directions in Fig. 2.5, then we get,

$$\begin{aligned} I_j^{MLD} &\equiv \left[I_j(\mathbf{k},\mathbf{n}) - I_j(\mathbf{k},\mathbf{n}')\right]_{k\perp n} \\ &= -\frac{\sigma_{nlj}(\omega)}{4\pi}\cdot(2j+1)^{1/2}\rho^n_{20} \\ &\quad\times\left[\frac{3}{\sqrt{2}}C^j_{202} + 3\sqrt{5/7}\ C^j_{222} + \frac{3}{2\sqrt{7}}C^j_{242}\right] \end{aligned} \qquad (2.32)$$

The Eq. (2.32) does not contain any angle dependent term. The dipole photoeffect is defined by the light polarization vector ($\mathbf{E}_x$ in Fig.2.5), but not the vector **q**. The variation of the value in Eq. (2.32) is then completely defined by the state multipole ρ^n_{20}, because all values in the equation is constant.

4. MCDAD

In case of circularly polarized light, the Eq. (2.28) can be written as follows

$$I_j^{MCDAD}(\mathbf{k},\mathbf{n}) = \frac{\sigma_{nlj}(\omega)}{2\pi}(2j+1)^{1/2}\rho_{10}^{n}$$
$$\times\left\{\mp\sqrt{3/2}C_{101}^{j}(\mathbf{n}\cdot\mathbf{q})\mp\sqrt{3}C_{121}^{j}\left[\frac{3}{2}(\mathbf{k}\cdot\mathbf{q})(\mathbf{k}\cdot\mathbf{n})-\frac{1}{2}(\mathbf{n}\cdot\mathbf{q})\right]\right\}$$
$$+\frac{\sigma_{nlj}(\omega)}{2\pi}\frac{3}{2}iC_{221}^{j}(2j+1)^{1/2}\rho_{10}^{n}\times\{(\mathbf{k}\cdot\mathbf{q})[\mathbf{q}\cdot(\mathbf{k}\times\mathbf{n})]\} \qquad (2.33)$$

where upper and lower signs refer to the left and right circularly polarized light. For a particular geometry ($\mathbf{q}\|\mathbf{n}'$), we get,

$$I_j^{MCDAD} = \mp\frac{\sigma_{nlj}(\omega)}{2\pi}\cdot(2j+1)^{1/2}\rho_{10}^{n}$$
$$\times\left[\sqrt{3/2}C_{101}^{j}+\frac{\sqrt{3}}{2}C_{121}^{j}\right]\cos\theta \qquad (2.34)$$

From Eq. (2.34), it is therefore clear that MCDAD, like MLDAD, is defined also by the state multipoles. The information from MCDAD and MLDAD is thus same. In case of MCD, the geometry for ($\mathbf{q}\perp\mathbf{n}$) is usually known as "forbidden geometry". However, according to the Eq. (2.34) and to the result by Schneider *et al.* [2.24] MCDAD is also present in the "forbidden geometry".

In case of the valence band photoemission, the atomic model [2.20,2.22] can not be applied directly for the numerical estimation because of much complexity in the valence band due to the band dispersion. However, it is possible to draw some qualitative consideration from the atomic result. For valence band, it is necessary to consider a series of spherical harmonic [2.25] instead of a single spinor spherical harmonic to calculate the state multipoles and the dipole matrix elements. However, the expressions for different MD methods can be used after the angle correction.

Figure 2.6 shows an example how the spectral features are changed upon changing the light polarization direction (helicity) of circularly polarized light in MCDAD method for a 3*d* element according to Baumgarten *et al.* [2.26]. Figure 2.6 will explain how the combined influence of spin-orbit and exchange interactions contributes the origin of MD. For simplicity, circular dichroism in photoemission is shown that is also comparable with linear dichroism in principle. At the top of the figure, the 2*p* level is split into two $2p_{3/2}$ and $2p_{1/2}$ states. The $2p_{3/2}$

state has four electrons with m_j=-3/2, -1/2, +1/2 and +3/2. On the other hand, the $2p_{1/2}$ state has two electrons with m_j=+1/2, and -1/2. Initially the system has to be considered as a paramagnetic state; i.e. $2p$ level only shows the spin-orbit splitting. Exciting these electrons by completely positive (I^+) and negative (I^-) circularly polarized light, the photoelectrons into the free-electron states (j=1/2, m_j=±1/2) are emitted in different way. The situation leads to a preferential emission according to the atomic selection rule, Δm=+1 and Δm=-1. The emitted intensity is exactly the same (i.e., no asymmetry) in the both cases, but they are highly polarized along the photon spin. Soon after introducing the exchange splitting Δ_x term in the same system (now the ferromagnetic system), the states will further split into minority and

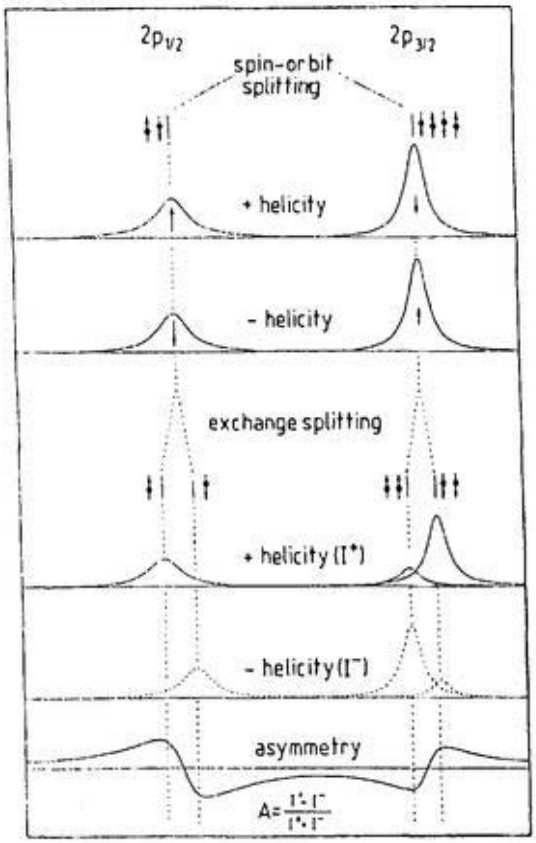

Figure 2.6. Schematic explanation of the origin of magnetic dichroism in any magnetic system by using circularly polarized light. In the $2p$ level, two kinds of splitting are shown. One is from the spin-orbit splitting and another is from the exchange splitting of the ferromagnetic material. The combined effect of spin-orbit and exchange interaction by coupling with the photon polarization shows the dichroism effect.

majority states. Again, exciting these electrons by positive (I^+) and negative (I^-) circularly polarized light, according to the selection rule, the preferential emission will be occurred depending on the minority and majority spin states.

Finally, asymmetry, $A = \left[\left(I^{I^+}_{\text{int.}} - I^{I^-}_{\text{int.}} \right) \Big/ \left(I^{I^+}_{\text{int.}} + I^{I^-}_{\text{int.}} \right) \right]$ of the two spectra shows the 'plus-minus' structure for $2p_{3/2}$ and 'minus-plus' structure for $2p_{1/2}$ level. This asymmetry shape is the evidence of magnetic states in the sample. Instead of changing the helicity of light, one can get the same result by switching the magnetization in reverse direction.

2.6. Surface sensitivity of photoelectrons

Due to the inelastic scattering process of photoelectrons as discussed latter, the escape depth of the inelastic photoelectrons is limited to near-surface region. This means the photoelectron spectroscopy is very surface sensitive [2.27]. Fig. 2.7 shows the "universal curve" [2.28] for the variation of the attenuation length of inelastic photoelectron as a function of photoelectron kinetic energy. The universal curve does not depend on the penetrating depth of the incident photon. In the photoelectron process, the electron may loss its energy in different ways [2.27] such as lattice vibration or phonons, collective excitation of electron-electron interaction or plasmons, single and double-particle excitations. The net effect of all these inelastic effects varies depending on the kinetic energy of the photoelectron. At very lower energies, the electron is unable to create any excitations, in other words, the inelastic loss is very small. So, the attenuation length is higher in lower energy side. On the other hand, for higher energies, the relative cross-section of energy loss is very small and the attenuation length is again long. In Fig. 2.7, the minimum value is at 50eV kinetic energy. The measurement of electron escape depth is done by the overlayer method [2.29]. Intensity of the photoelectrons emitted to the normal direction from a thin metal slab (thin film) can be written by the following exponential function of t, the thickness of the film:

$$I = I_0 \, e^{-t/\lambda} , \qquad (2.35)$$

where the parameter λ is the inelastic mean free path. The determination of λ can be done by the next expression for almost all materials.

$$\lambda^{-1} \cong \sqrt{3}\frac{a_0 R}{E_{kin}}(r_s)^{3/2} \ln\left[\left(\frac{4}{9\pi}\right)^{2/3}\frac{E_{kin}}{R}r_s^2\right], \tag{2.36}$$

where a_o is the Bohr radius, R=13.6eV and r_s is the mean electron-electron distance which is roughly equal for all materials. Thus, expression (2.36) indicates that almost all materials show similar kinetic energy dependence of electron mean free path. This is the reason why the curve in Fig. 2.7 is called as the "universal curve".

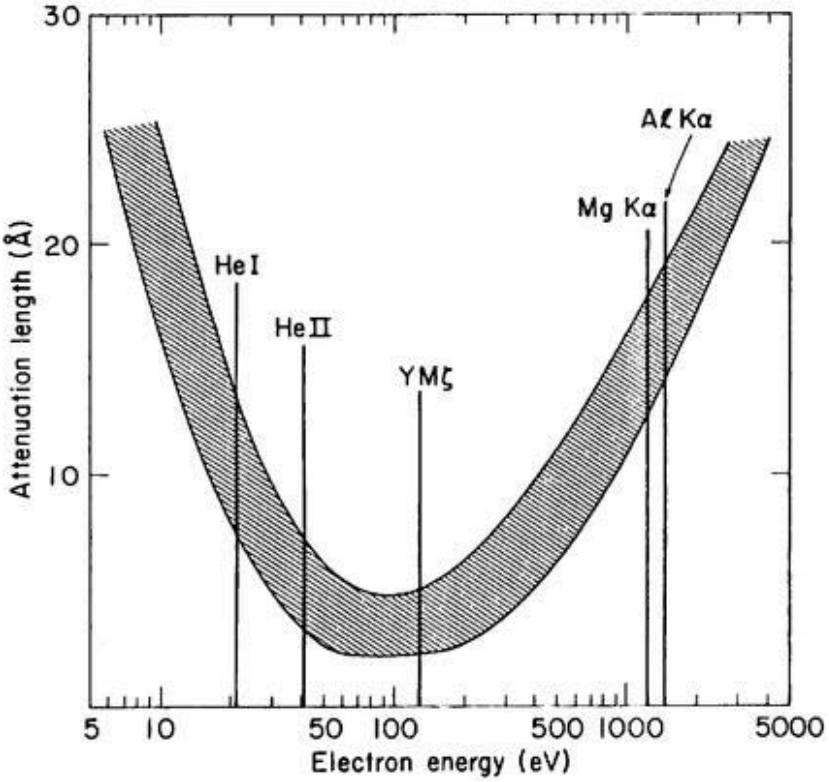

Figure 2.7. The universal curve for photoelectron attenuation depth as a function of kinetic energy [after Ref. 2.29].

References

2.1. G. Margaritondo; "Introduction to Synchrotron Radiation", Oxford University Press 1988, Ch.4.

2.2. Photoemission in Solids I" Edited by M. Cardona and L. Ley, Springer-Verlag (1978).

2.3. W. E. Spicer, Phys. Rev. 112, 114 (1968).

2.4. Stefan Hüfner, "Photoelectron Spectroscopy" Springer (1995).

2.5. G. Wendin, M. Ohno, Phys. Scrip. 14, 148 (1976).

2.6. "Giant Resonances in Atoms, Molecules, and Solids", edited by J. P. Connerade, M. Esteva and R. C. Karnatak, Plenum Press, New York (1985).

2.7. U. Fano, Phys. Rev. 124, 1866(1961).

2.8. C. Guillot, Y. Ballu, J. Paigné, J. Lecante, K. Jain, P. Thiry, R. Pinchaux, Y. Pétroff, L. M. Falocov, Phys. Rev. Lett. 39, 1632 (1977).

2.9. J. W. Allen, " Resonant Photoemission of Solids with Strongly Correlated Electrons" Ch.6, in "Synchrotron Radiation Research: Advances in Surface and Interface Science, Vol. 1, Techniques, Edited by Z. Bachrach, Plenum Press, New York (1992).

2.10. D. A. Shirley: "Many Electron and Final-State Effects: Beyond the One-Electron Picture" in "Photoemission in Solids I" Edited by M. Cardona and L. Ley; Springer Verlag (1978), P.165.

2.11. J. C. Fuggle, S. F. Alvarado, Phys. Rev. A 22, 1615 (1980).

2.12. C. Carbone, E. Kisker, Solid State Comun., 65, 1107 (1988).

2.13. B. T. Jonker, K. –H. Walker, E. Kisker, G. A. Prinz, C. Carbone, Phys. Rev. Lett. 57, 142 (1986).

2.14. U. Fano, Phys. Rev. 178, 131 (1969).

2.15. C. M. Schneider, J. Mag. Mag. and Mat. 175, 160 (1997).

2.16. R. Feder, J. Henk, p. 85 in Spin-Orbit-Influenced Spectroscopies of Magnetic Solids, edited by H. Ebert and G. Schütz, Springer (Berlin, 1995).

2.17. H. B. Rose, T. Kinoshita, C. Roth, F.U. Hillebrecht, p. 105 in Spin-Orbit-Influenced Spectroscopies of Magnetic Solids, edited by H. Ebert and G. Schütz, Springer (Berlin, 1995).

2.18. F.U. Hillebrecht, C. Roth, H. B. Rose, E. Kisker, Phys. Rev. Lett. 70, 3479 (1993).

2.19. D. Venus, Phys. Rev. B 49, 8821(1994).

2.20. B. T. Thole, G. van der Laan, Phys. Rev. Lett. 67, 3306 (1991), Phys. Rev. B 49, 9613 (1994).

2.21. N. A. Cherepkov, Phys. Rev. B 50, 13813 (1994).

2.22. N. A. Cherepkov, V.V. Kuznetsov, J. Phys. B 22, L405 (1989).

2.23. S. M. Goldberg, C. S. Fadley, S. Kono, J. Electron. Spectros. Relat. Phenom. **21**, 285 (1981).

2.24. C. M. Schneider, D. Venus, J. Kirschner, Phys. Rev. B **45**, 5041 (1992).

2.25. J. W. Gadzuk, Phys. Rev. B **10**, 5030(1974).

2.26. L. Baumgarten, C. M. Schneider, H. Petersen, F. Schäfers, J. Kirschner, Phys. Rev. Lett. 65, 492 (1990).

2.27. M. Prutton, "Introduction to Surface Physics" Oxford Science Publications (1993), ch.2, p.22.

2.28. D. A. Shirely, Ch.4, p.193, in "Photoemission in Solids I", Edited by M. Cardona, L. Ley, Springer-Velag (1978).

2.29. M. P. Seah, Surf. Interface Anal. 1, 86 (1979).

Chapter 3

Experimental methods and instrumentation

Related publications:

1. **Title: "Photoelectron spectromicroscopy experiments at the UVSOR facility"**
   Authors: T. Kinoshita, Krishna G. Nath, Y. Haruyama, M. Watanabe, S. Yagi, S. Kimura, A. Fanelsa.
   Journal: J. Electron Spectrosc. Relat. Phenom., **92**, 165-169 (1998).

2. **Title: "Performance of the YB_{66} soft X-ray monochromator crystal at the wiggler beamline of the UVSOR facility"**
   Authors: T. Kinoshita, Y. Takata, T. Matsukawa, H. Aritani, S. Matsuo, T. Yamamoto, T. Takahashi, H. Yoshida, T. Yoshida, Krishna G. Nath, Y. Ufuktepe, S. Kimura and Y. Kitajima.
   Journal: J. Synchrotron Rad., **5**, 726-728 (1998).

3.1. Synchrotron radiation and the UVSOR ring

Synchrotron radiation is a highly intense, stable, collimated, continuos, polarized, and pulsed electromagnetic radiation emitted by charged particles (electrons or positrons) moving at relativistic velocity along a curve trajectory with a large radius of curvature. Synchrotron radiation covers a wide range of electromagnetic spectrum from infrared region through visible, ultraviolet, soft x-ray to hard x-ray region. Figure 3.1 shows a phenomenological description of emitted radiation (dipole pattern) from (a) subrelativistic and (b) relativistic electron in a specified orbit [2.1].

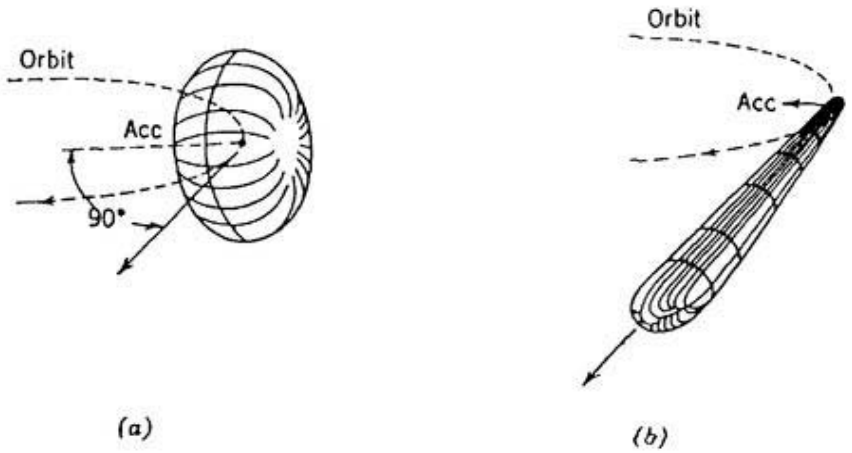

Figure 3.1. Conceptual representation of the radiation pattern from a circulating charged particle for two cases: (a) subrelativistic and (b) relativistic [2.1].

There are three types of magnetic elements placed in the circulating path of the charged particle to generate synchrotron radiation: bending magnet, wiggler, and undulator. At the UVSOR (ultraviolet synchrotron orbital radiation) facility, a 750MeV-storage ring provides the relativistic electrons circulating in an orbit of 53.2m circumference. Figure 3.2 shows the output (on-axis photon intensity as a function of photon energy) of those three sources in UVSOR ring. The characteristic differences among the various sources are clear from the figure.

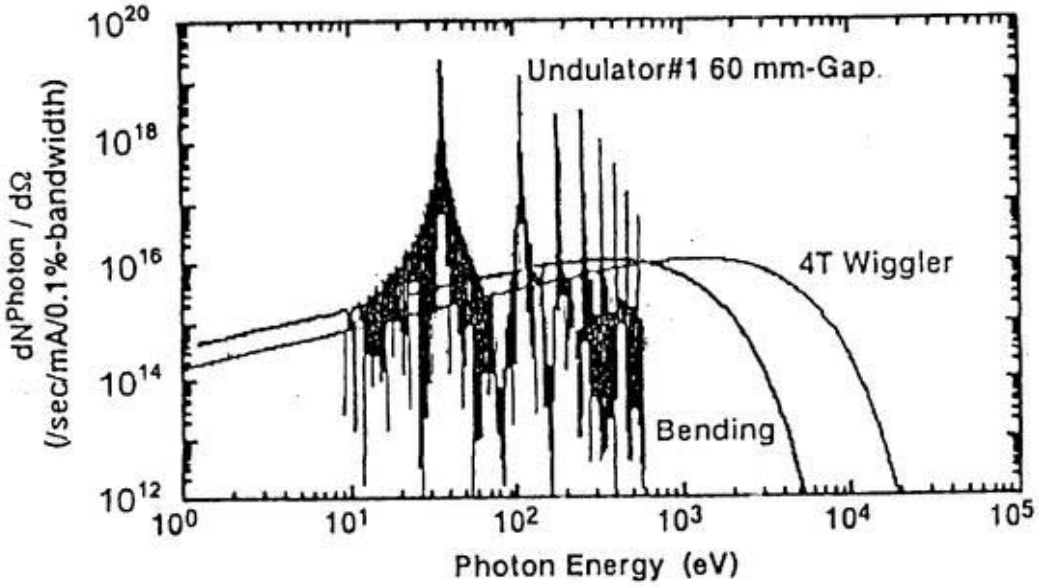

Figure 3.2. On-axis photon intensity as a function of photon energy with 750 MeV electrons in UVSOR ring.

3.2. Photon sources and spectrometers

3.2.I. For Tm5*p* photoemission measurement

The Tm5*p* resonant photoemission experiments around the Tm4*d*-4*f* excitation region were carried out at the beamline BL2B1 in the UVSOR facility. In the following, the descriptions of the beamline, monochromator and the electron spectrometer will be given.

3.2.Ia. Beamline BL2B1

Bending magnet beamline BL2B1 [2.2] is a soft x-ray beamline at the UVSOR facility. This beamline covers the energy range from 50eV to 1000eV. A 2-meter grazing incidence 'Grasshopper' type monochromator (Mark XV, Maker Manufacturing Co.) is installed in this beamline. The schematic drawing of the arrangement of mirrors, slits and grating is shown in Fig.3.3. The operation of the Grasshopper monochromator is based on the coordinated motion of the focusing mirror M_1, entrance-slit mirror S_1, and the grating. The position of the exit slit S_2 is kept fixed during the operation. The Grasshopper monochromator provides excellent and constant resolution over the whole photon energy range. Figure 3.4 shows the photoelectron yield spectra measured by the use of gold (Au) mesh for the beamline BL2B1. The energy resolution of the photon is about 0.4eV at hv=300eV.

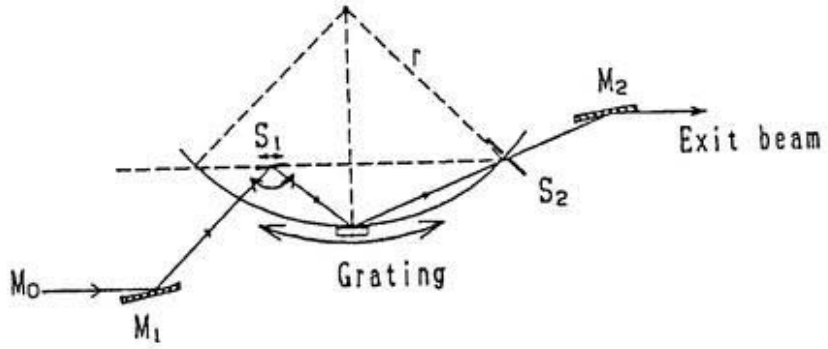

Figure 3.3. The schematic drawing of the Grasshopper monochromator in the BL2B1.

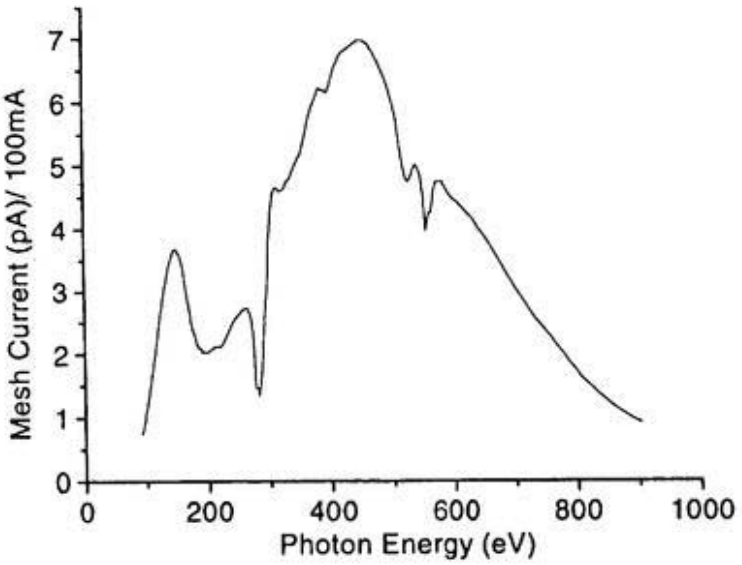

Figure 3.4. The photoelectron yield spectrum of the Au mesh measured at the beamline BL2B1.

3.2.Ib. Spectroscopy system at BL2B1

In the beamline BL2B1, the spectroscopy system consists of an analyzer chamber and a preparation chamber. The pressure of the analyzer chamber is less than $2x10^{-10}$ torr. The

analyzer chamber is equipped with a double pass cylindrical mirror analyzer (DCMA)[2.3] for detecting the photoelectrons. The DCMA is installed at the focusing point of the monochromated light. The DCMA is one of the widely used electron analyzers for synchrotron radiation experiment. The photoelectron spectroscopy in EDC (electron distribution curve) mode including CIS (constant initial state), CFS (constant final state) can be measured using the DCMA. Figure 3.5 shows the schematic diagram of the cross-sectional view and the operating condition of the DCMA.

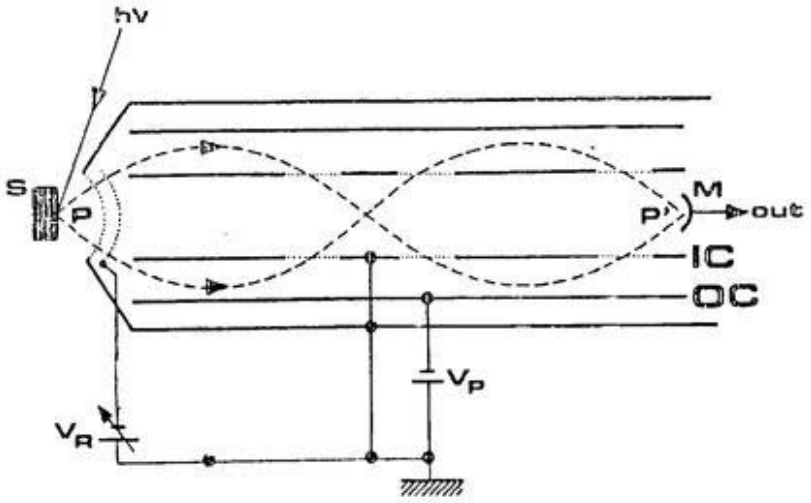

Figure 3.5. The schematic cross-sectional view of the DCMA.

Photoelectrons from point P are focused at the point P′, where the detector is located. The electrons are focused at an angle 42.3º by virtue of the applied voltage Vp between the inner cylinder (IC) and the outer cylinder (OC). The resolution of the photoelectron is less than 0.3eV at hv=150eV.

3.2.II. For Tm4*d* and Tm3*d* photoemission measurements

The Tm4*d* resonant photoemission around the Tm 3*d*-4*f* absorption edges and Tm3*d* photoemission measurements were performed at the beamline BL7A in the UVSOR facility.

The brief description of the beamline, monochromator and the spectroscopy system will be given in the following.

3.2.IIa. Beamline BL7A and YB_{66} and InSb monochromator

The Tm4*d* resonant photoemission around Tm3*d* excitation threshold (hν =1.45-1.52keV) was performed at the beamline BL7A [2.4] at the UVSOR facility. Both the bending magnet and superconducting wiggler (with 4T magnetic field) radiation are available in this beamline. Because of the low photon flux of the bending magnet radiation at these photon energy ranges (hν =1.45-1.52keV) [2.5], performing the photoemission experiments is relatively difficult. The wiggler radiation at BL7A [2.6] with relatively higher photon flux in x-ray region is more suitable for photoemission experiments if the proper monochromator crystal with higher energy resolution is selected. The photon energy range mentioned above is just situated in the area between those covered by crystal monochromator and the grazing-incidence grating monochromator. The YB_{66} crystal is one of the best choices for this purpose which covers the energy range from 1.1 to 2keV with several advantages such as higher energy resolution, no absorption structures originating from the elements of the crystal, high resistivity to the radiation damage *etc.* [2.7]. Recently, the YB_{66} monochromator became available in the BL7A to perform soft x-ray spectroscopic studies in the photon energy range of 1.2-2 KeV [2.8].

The operation of any crystal monochromator for x-ray region is based on the Bragg's law,

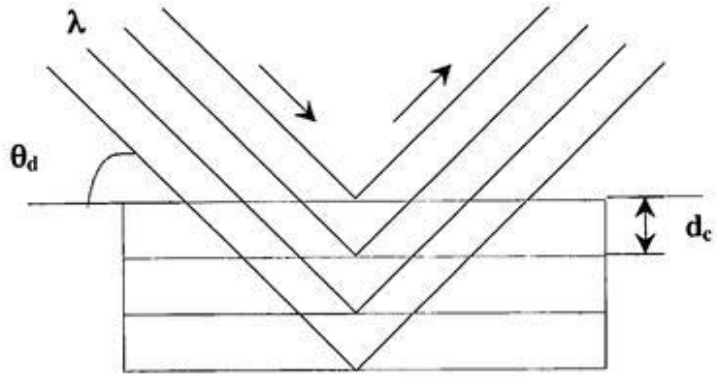

Figure 3.6. Description of the Bragg's law ($2d_c \sin\theta_d = \lambda$) with the interplanar distance (d_c), diffraction angle θ_d and the photon wave length λ.

$$2d_c \sin\theta_d = \lambda, \quad (3.1)$$

which defines the diffraction of the electromagnetic radiation by a crystal. In Eq. (3.1), $2d_c\sin\theta_d$ is the path difference between two successive rays with wavelength λ that impinge on the crystal surface at an angle θ_d. The resolution of the monochromator is derived roughly from the following relation.

$$\Delta h\nu/h\nu = \Delta\lambda/\lambda = \Delta\theta_d \cot\theta_d \quad (3.2)$$

Figure 3.7 shows the schematic view of the arrangement of the double crystal monochromator (DXM) in BL7A. Two crystals with same surface are used to improve the performance with respect to single-Bragg-reflection instrument. As shown in the figure, the beamline set-up is changed from the 0° line for getting wiggler radiation to 2° line for bending-magnet radiation.

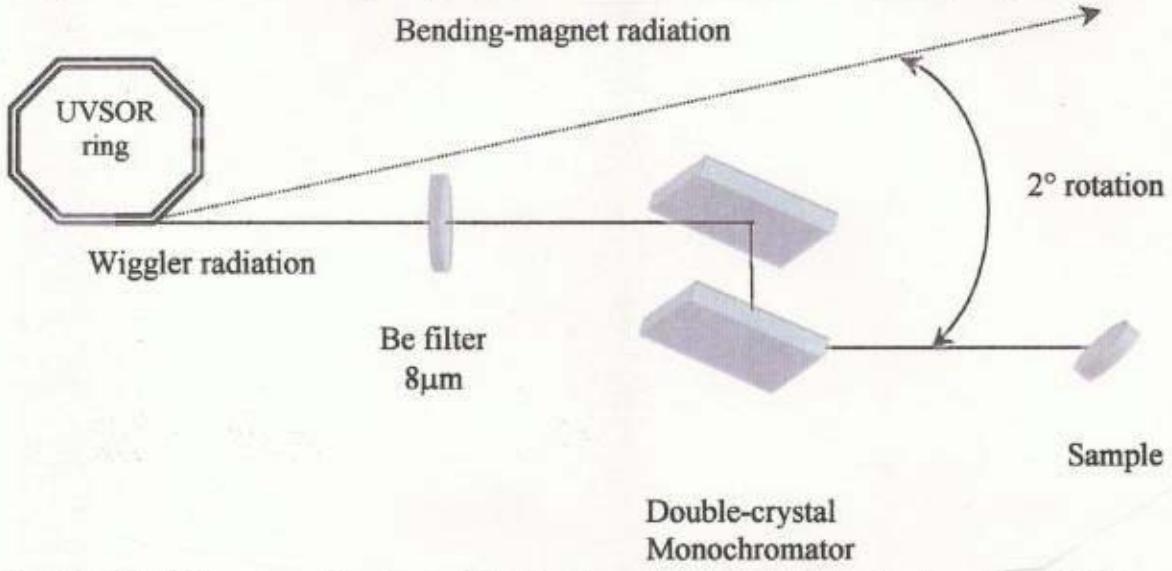

Figure 3.7. The schematic view of the double-crystal monochromator beamline BL7A

Figure 3.8 shows the throughput of the double crystal for both the bending magnet and wiggler radiation for BL7A. The upper three curves for InSb(111), Ge(111) and YB_{66}(400) monochromator crystals represent the wiggler radiation. The lower two curves for Beryl and YB_{66}(400) crystals represent the bending magnet radiation. The figure shows clearly that the wiggler radiation with YB_{66}(400) monochromator crystals is the best choice for the Tm4*d* resonant photoemission experiment around the Tm3*d*-4*f* absorption edges (hν =1.45-1.52keV). In case of wiggler radiation with YB_{66}(400) [2.8], the maximum photon flux of about 10^8

photons $s^{-1}(100mA)^{-1}$ and the energy resolution of about 0.7eV at hv=1.2-2keV were achieved. The lowering of photon flux at lower photon energy is due to the cut-off of Be-filter.

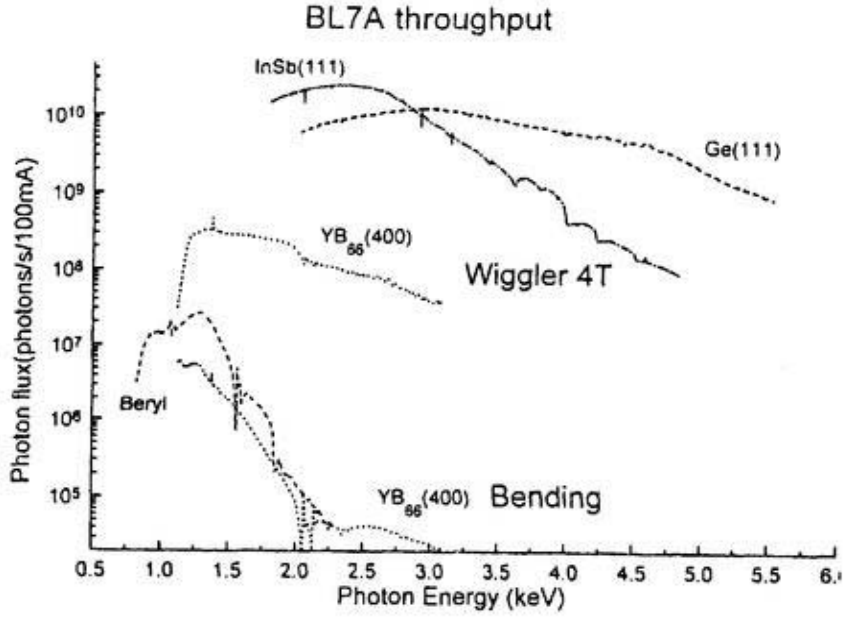

Figure 3.8. The throughput of different double-crystal monochromator used in beamline BL7A. Radiation from the wiggler and bending-magnet section is used.

For Tm3*d* photoemission experiment, the beamline BL7A was also used. In this case, the monochromator crystal was the InSb(111) which covers the energy range of 1.74-4.85keV. The throughput of this crystal is shown in Fig.3.8. The photon flux of about $2x10^{10}$ photons $s^{-1}(100mA)^{-1}$ was obtained at hv=1775.5eV.

3.2.IIb. Spectroscopy system (VG ESCALAB 220i-XL)

The modified ESCASCOPE (FISONS Instrument) spectrometer, named ESCALAB220i-XL, was recently installed at the UVSOR facility to perform the photoemission spectroscopy and spectromicroscopy experiments [2.9]. Photos 3.1 (a) and (b) show the VGESCALAB220i-XL spectroscopy system. During the Tm4*d* resonant photoemission and Tm3*d* photoemission measurements, the system was attached to the end port of the double- crystal monochromator beamline BL7A. In order to get the photon beam from the monochromator at an oblique incident angle, the whole system installed on a rotary stand was rotated about 7.5°. The system consists of a high performance hemispherical analyzer, a conventional x-ray tube with Al$K\alpha$

and Mg$K\alpha$ lines for photoexcitation, a vacuum ultraviolet source, a sputtering gun, magnetic coil, diamond filler and so on. The base pressure of the analyzing chamber is less than 2×10^{-10}torr. An additional chamber (details is described in the section 3.3.I) for sample preparation and epitaxial growth of thin films is also attached to the analyzing chamber.

The electron analyzing process in this system is done by the high performance 180° hemispherical analyzer with mean radius of 150mm that is shown in Fig. 3.9.

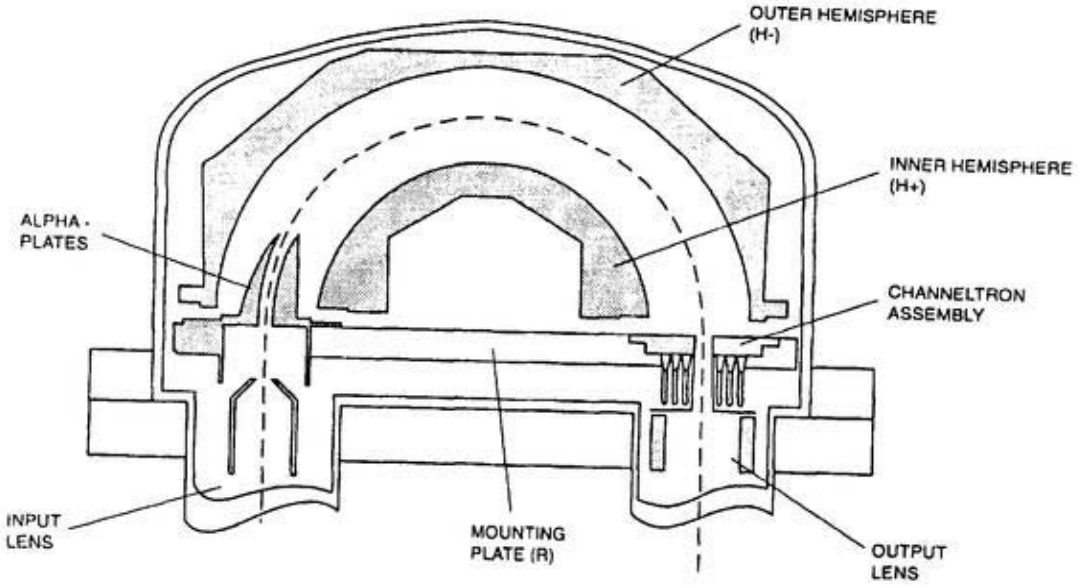

Figure 3.9. The hemispherical analyzer in VGESCALAB220i-XL system.

The analyzer filters the photoelectrons of different kinetic energy coming from the sample via input lens with the help of the outer and inner hemispheres. The required voltages are applied to the hemispheres according to the following relations:

$$V_{Hout} = [(R_1/R_2)-1]E_p + V_r \quad (3.3)$$

$$V_{Hin} = [(R_2/R1)-1]E_p + V_r \quad (3.4)$$

Here, V_{Hout} and V_{Hin} are the applied voltages in outer and inner hemispheres, R_2 and R_1 are the radius of the outer and inner hemispheres, E_p is the analyzer pass energy and Vr is the retarding voltage at the entrance slit of the analyzer.

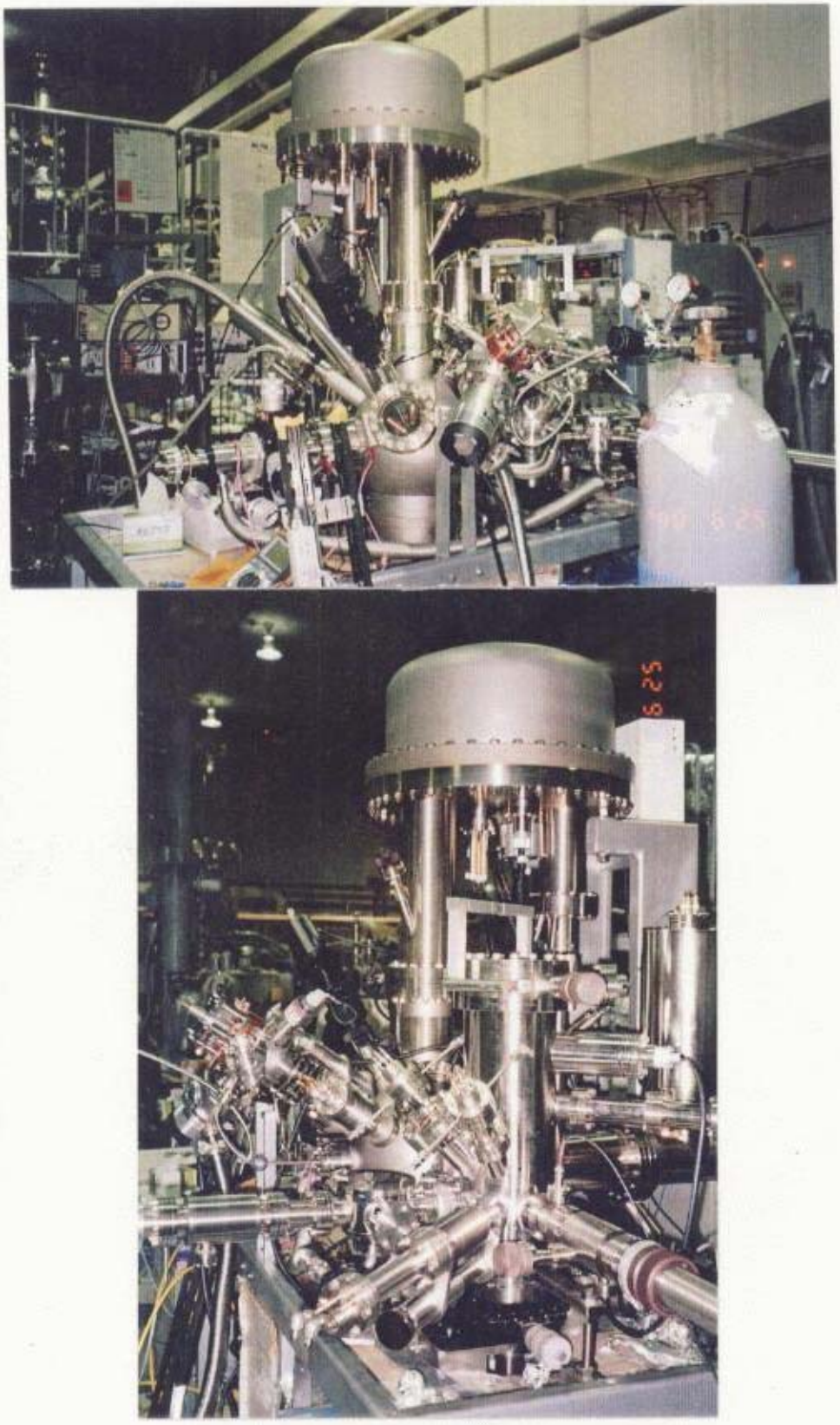

Photo 3.1. VGESCALAB220i-XL spectromicroscopy system. (Up) View from manipulator end. (Bottom) View from preparation chamber end.

The photoelectron system can be operated in two modes, one is photoemission image mode and another is photoelectron spectroscopy mode. In the spectroscopy mode, the array of six channeltrons (shown in Fig. 3.9) is used for detection of photoelectron. In the imaging mode, the photoelectron directly reaches to the imaging detector. It is expected from the commercial argument that the spatial resolution of 2μm for the imaging mode and 20μm for the spectroscopy mode can be achieved. The imaging is used to element-specific imaging of the sample surface, magnetic domain imaging [2.9. The spectroscopy mode is used for studying very small sample [2.9], getting precise information from inhomogeneous surfaces and so on. Figure 3.10 shows schematically how these two modes work.

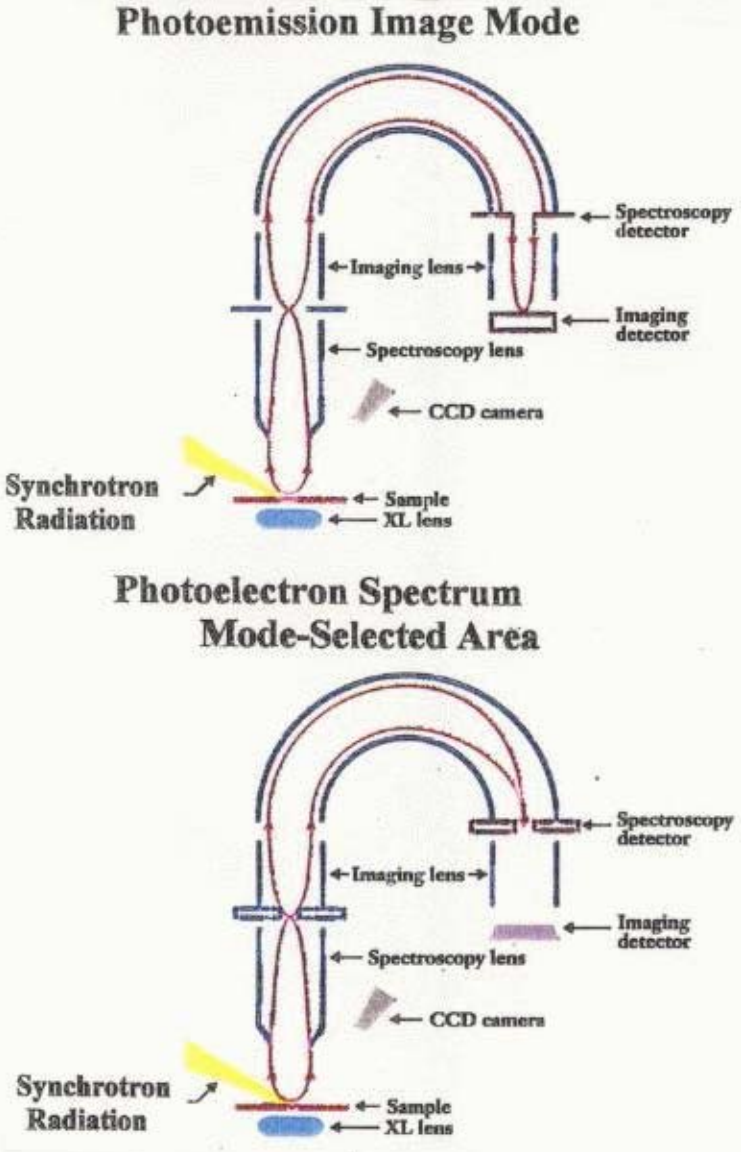

Figure 3.10. Photoemission image mode (top) and photoelectron spectrum mode (bottom).

One of the advantages of this spectroscopy system is that the system has several options for selection the measurement area by means of two apertures in the input lens system. The smallest detection area is ϕ 20μm and the largest area is 3mm x 2mm. By using the high performance hemispherical analyzer and the large detection mode, the photoemission experiment was possible even with lower photon flux. In Fig. 3.11, the lens assembly is shown. By changing the width of the two apertures, i.e., the acceptance angle aperture and the field of view aperture, the path of the photoelectron is controlled according to the selected detection area.

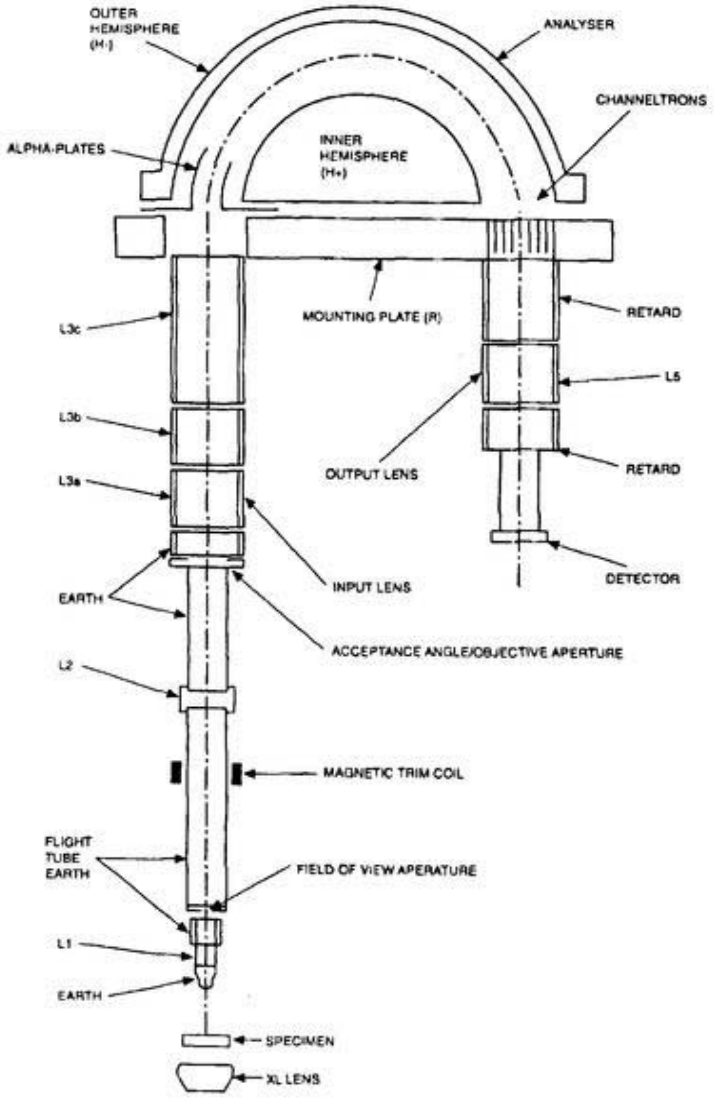

Figure 3.11. Lens system of VGESCALAB spectrometer system.

3.2.III. For Ni/Co system

The following beamline and the set-up are used for magnetic dichroism study for Ni/Co system.

3.2.IIIa. Beamline BL5B

In order to study the thin film magnetism by means of magnetic linear dichroism (MLD) in photoemission, the VGESCALAB 220i-XL system was connected to the beamline BL5B [2.10] at the UVSOR facility. The available photon energy range of this beam line is 10-1000eV. The BL5B consists of a plane grating monochromator (PGM). For getting light of different wavelength, three gratings and six mirrors are installed in the beam line. The optical design of the PGM is illustrated in Fig. 3.12. Synchrotron radiation coming from the bending magnet is made parallel by two premirrors M_0 and M_1. This beam is then diffracted by one of the three gratings (G_1–G_3). The diffracted beam is focused on the slit S_2 by one of the several mirrors (M_{20}-M_{26}). Finally, light form the slit S_2 is focused on the point Q towards the experimental chambers by the toroidal mirror M_3.

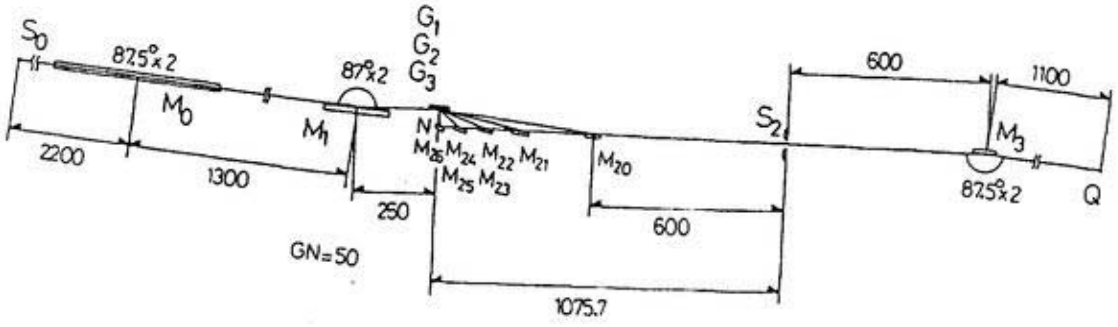

Figure 3.12. Optical design of the PGM monochromator in the beamline BL5B.

Figure 3.13 shows the throughput spectra of beamline BL5B detected by a gold mesh. In the figure, GM indicates the combination of grating (G) and mirror (M). In the present thin film

measurements, the photon energies were selected from the combinations 24 and 23. The photon energy resolution is less than 0.2eV at hν=50-150eV.

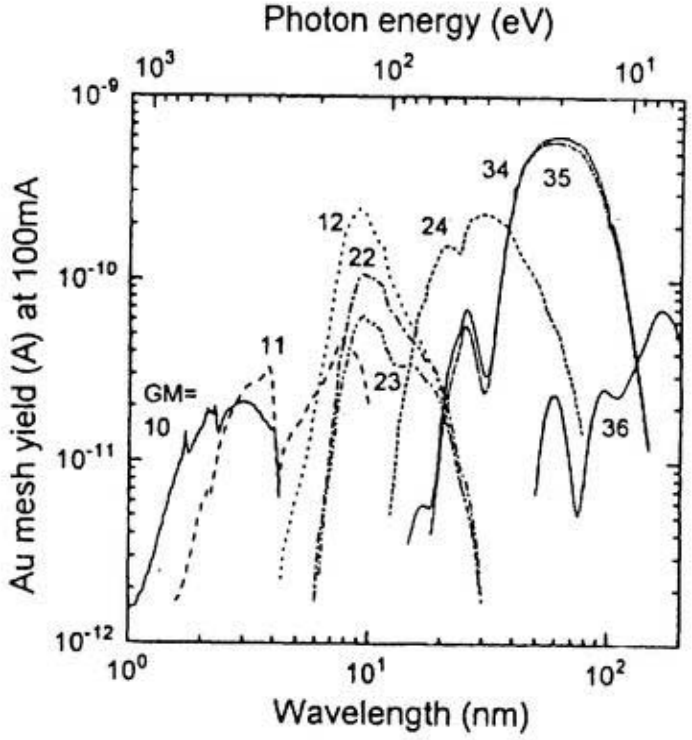

Figure. 3.13. The throughput spectra for different grating-mirror (GM) combinations of the beamline BL5B detected by the gold mesh (84% transmission).

Figure 3.14 shows the schematic diagram of the arrangement of optical components and

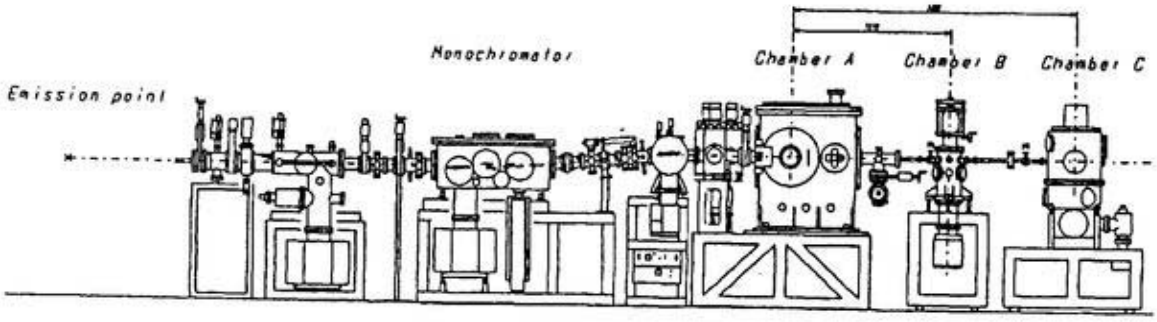

Figure 3.14. Schematic diagram of the beamline BL5B.

different chambers in the BL5B. The beamline BL5B is also used to calibrate the optical components. The chamber A is used to calibrate of optical component and chamber B is used for optical measurement of solids. During the MLD experiment, the chamber C was replaced by the ESCALAB220i-XL system. With a rotation angle 7.5°, the whole chamber was connected via a bellow to the chamber B in the beamline.

3.3. Improvements of the system

3.3.I. Preparation chamber

A chamber for sample preparation and growth of epitaxial thin films has been developed and attached to the VGESCALAB220i-XL system. Three water-cooled evaporators, a quartz thickness monitor, LEED (low energy electron diffraction) optics, a video camera for taking LEED pattern are installed in the preparation chamber. In Fig. 3.15, different components of the preparation are shown by schematic diagram.

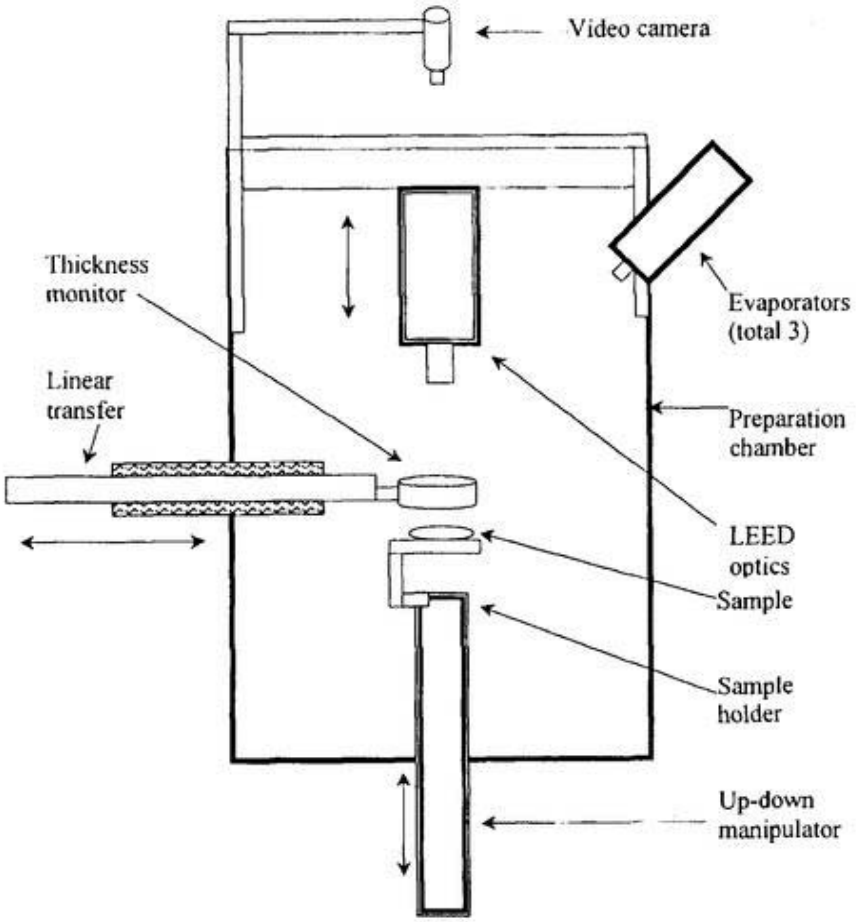

Figure 3.15. Schematic view of the preparation chamber.

3.3.II. Laboratory made evaporators

For the thin film experiments, several water-cooled evaporators were constructed and attached to the preparation chamber. The evaporator works according to the electron bombardment technique. Figure 3.16 shows the schematic drawing of several electrical feedthroughs, such as tungsten filament (thickness, ϕ=0.2mm), evaporating material (rod-shaped, ϕ=2mm) of the evaporator. Tungsten filament is used to generate the hot electrons.

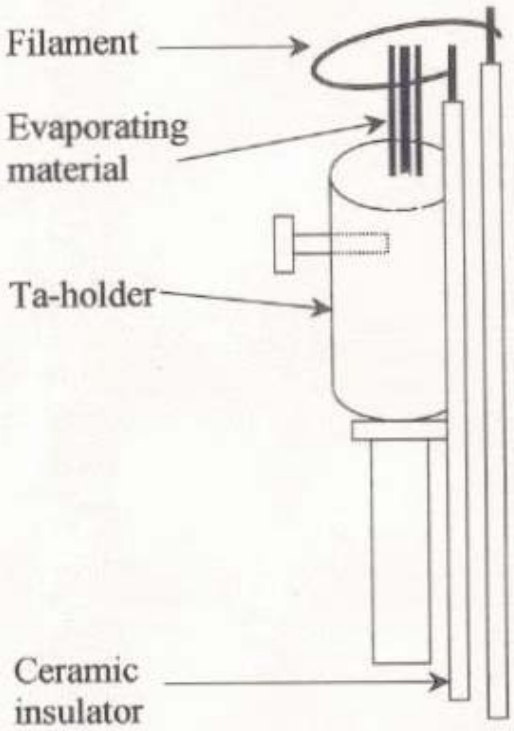

Figure 3.16. Schematic drawing of the electrical feedthroughs of the evaporator. This figure is comparable with the photo 3.2.

Photo 3.2. Picture of the electrical feedthroughs of the evaporator.

These hot electrons are then attracted by the high positive voltage applied to the evaporating material (Ni or Co). After striking the evaporating material, the electrons continuously produce the metal-vapor from the surface of the evaporating material when the surface temperature goes up. The evaporating rods are attached mechanically by using Mo-screw with a Ta-holder and are carefully kept in the center position of the filament. In order to prevent the emission from the holder, the high melting point material (Ta) is used. The picture of the evaporator is shown in photo 3.3. The whole components of the electrical feedthroughs are inserted inside of the water jacket, which is shown in photo 3.6. A collimator is used on the top of the water jacket to control the metal beam for making thin film only on the sample surface, but not elsewhere inside the preparation chamber.

In the present experiments, the conditions for metal (Ni or Co) evaporations are the following.

Filament current = 3.8-4.0 amp (A).

Filament voltage =5volts.

High voltage = $1.5x10^3$volts.

Emission current = 13-18 mA.

Typical evaporation rate = 0.5-1 Å/min

Distance between evaporation source and the sample = 120mm

Photo 3.3. Picture of the evaporator with water-jacket and collimator. This part along with the electrical feedthroughs is inserted into the preparation chamber.

3.3.III. Liquid He cryostat

In order to study temperature dependence of photoemission spectra, a liquid He cryostat has been constructed and attached to the manipulator in the VGESCALAB system. The cryostat can be used for liquid nitrogen also. The cryostat itself is a long stainless steel (SUS) pipe with inner diameter 12mm and thickness 0.5mm. In order to avoid heat loss, a Cu-made radiation shield is attached to the 'front part' of the cryostat. In Fig. 3.17, the drawings of the cryostat (inside and outside assemblies) and the radiation shield are shown. Unfortunately, during the

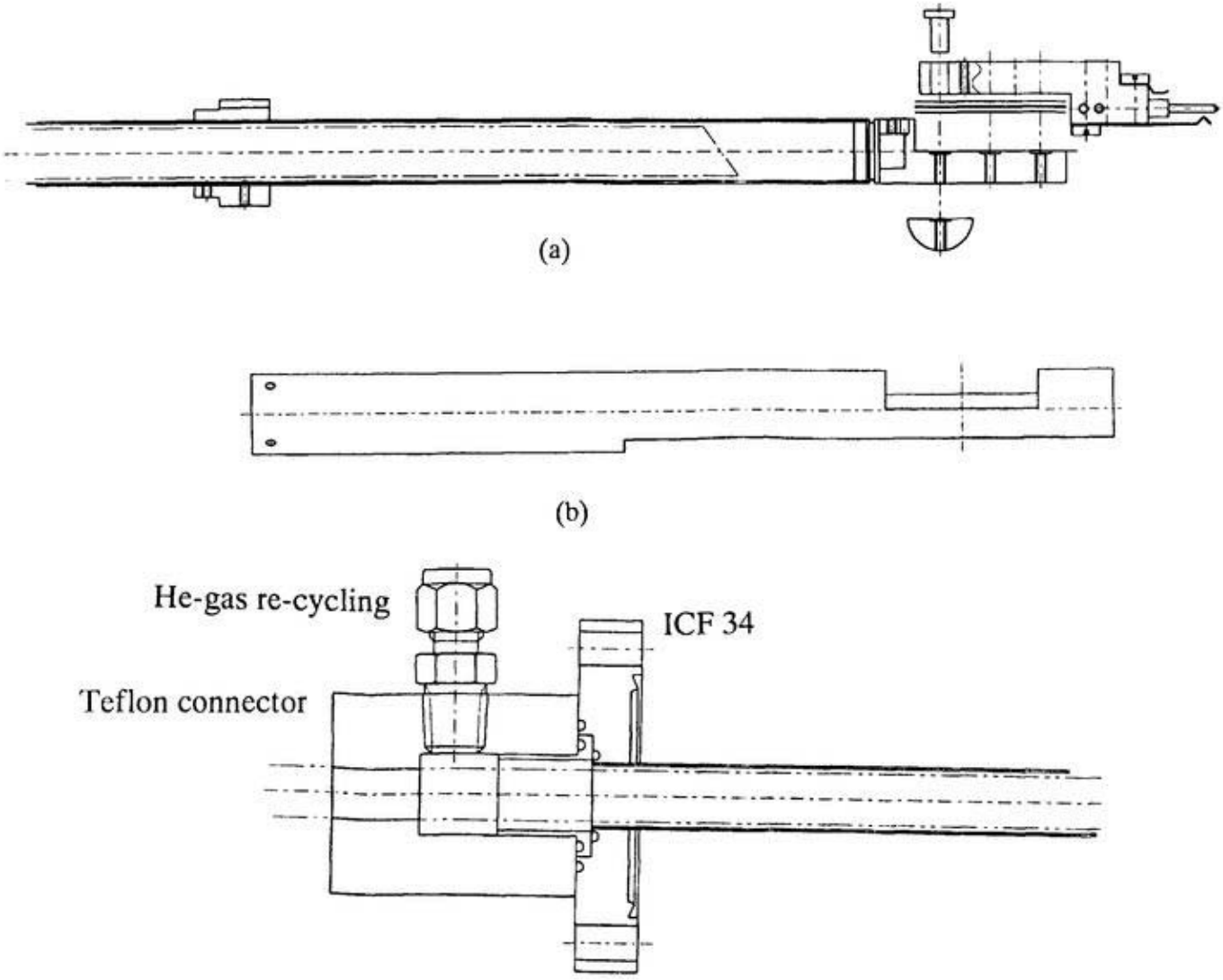

Figure 3.17. Drawings of the cryostat. (a) 'Front part', inside the ultrahigh vacuum (UHV). (b) Cu-made radiation shield. (c) Outside assembly with Teflon connector for recycling the He-gas.

test measurement [2.12], the radiation shield was unable to use because of the position of magnetic lens that was just below the sample holder.

Figure 3.18 shows different parts around the 'cold-end' of the cryostat. A Cu-connector is attached with the 'cold-end' of the cryostat (stainless steel pipe). This connector works as a heat exchanger to another Cu-holder. This Cu-holder is used to build up the sample transfer mechanism. The sample transfer system in the cryostat is made in a similar way that the system can be used with the commercial transfer rod (installed in the preparation chamber) also. A thin sapphire sheet is used between the Cu-connector and the Cu-holder for electrical and thermal (at high temperature) isolation. Sapphire is a good heat conductor at very low temperature. But, the heat conductivity declines with increasing temperature. That's why, sapphire is very useful for this purpose where heating and cooling is carried out in a single system. The chromel-alumel type thermocouple is used to monitor the temperature. Two pairs of thermocouple are used in the both sides of the sapphire to observe the temperature difference. Usually temperature was found to be same in both sides. All parts of sample transfer mechanism are made of Cu to achieve maximum heat flow to the sample.

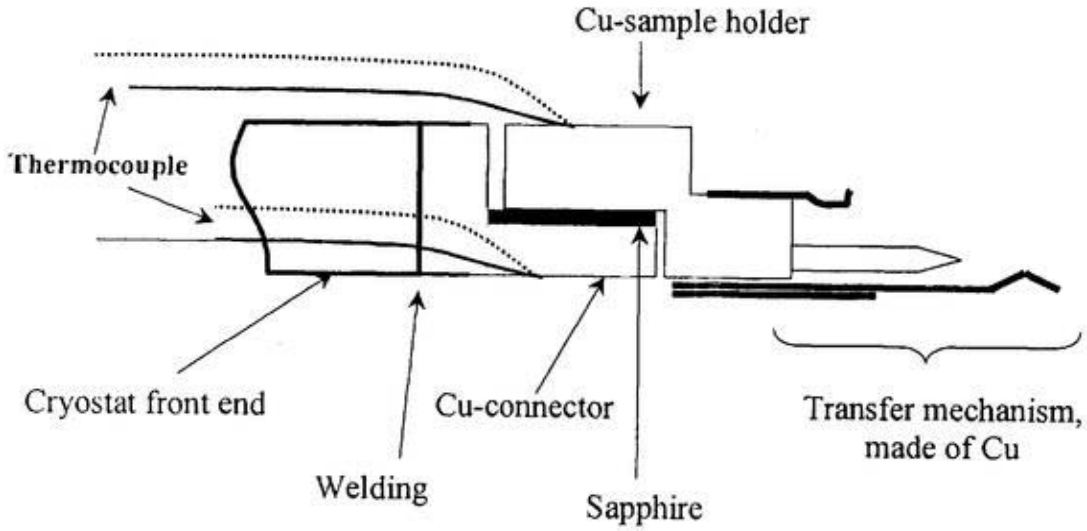

Figure 3.18. Schematic view of 'cold-end' of the cryostat and the sample transfer mechanism.

In order to use the cryostat for thin film experiment, a special kind of sample holder of high melting point metal, such as Mo, is needed that should have both heating and transfer options.

Unfortunately, the Mo-sample holder including both the heating and transfer options was not completed during the thin film measurement. As a result, no measurement of thin film magnetism as a function of temperature was performed. Instead, some measurements were performed successfully by using the cryostat where the sample does not need to heat. The results from those temperature dependent photoemission for Eu-compound is given in the appendix B. The sample was the temperature-induced valence transition material $EuNi_2(Si_{0.25}Ge_{0.75})_2$. During this experiment, the minimum temperature about 33K for liquid He and about 83K for liquid nitrogen was achieved. As it was expected, the temperature might be go down more if the radiation shield is used after some modification.

In Fig. 3.19, the circulation system of liquid He for the cryostat is shown by schematic diagram. Commercial He-transfer tube is used for this purpose. Because of the internal pressure of the He-reservoir, liquid He flows continuously inside the cryostat through the transfer tube. The gaseous He comes back from the 'cold-end' of the cryostat. In inset, the expanded view of the 'cold-end' is shown. The He-gas is then exhausted through the connector via a recycle line equipped with pump and flow meter.

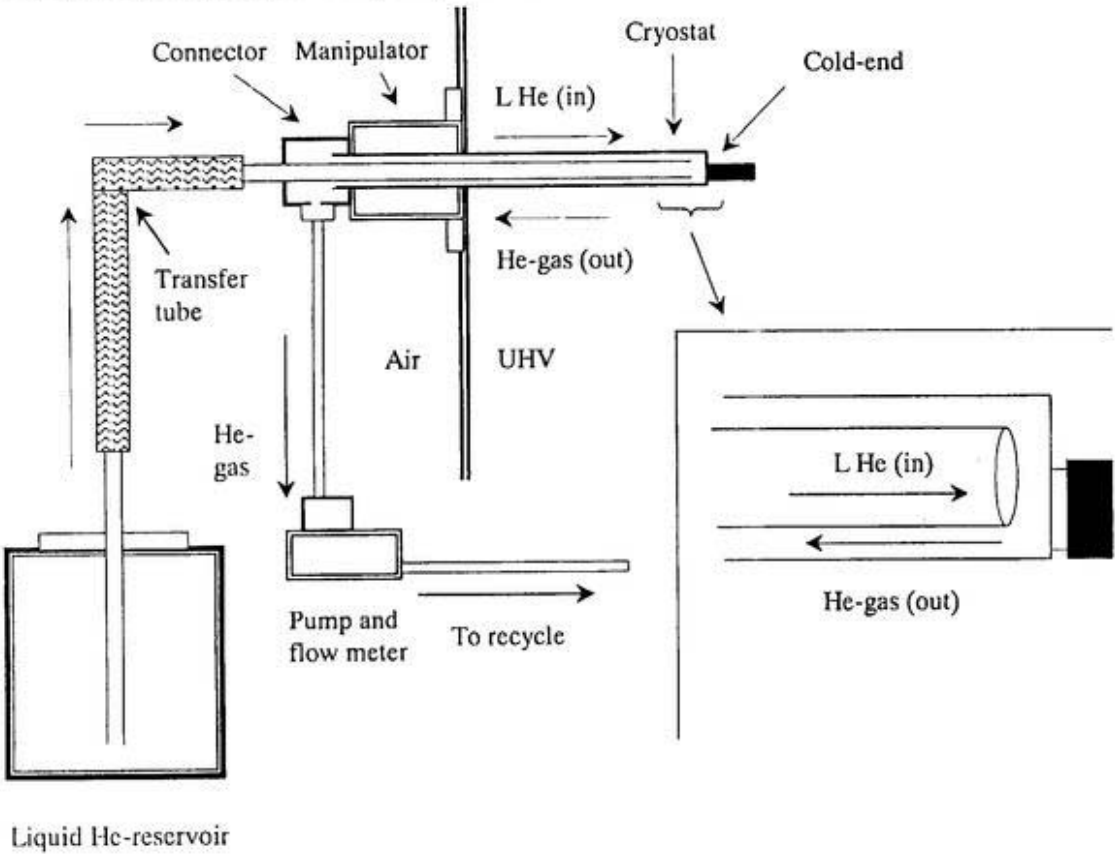

Figure 3.19. Schematic diagram of the circulation system for liquid He and He-gas.

3.4. Sample preparation and growth

3.4.I. TmX

Tm monochalcogenides samples were provided by one of the collaborators Dr. T. Matsumura, Tohoku University.

3.4.Ia. Sample growth

All TmX (X=S, Se and Te) single crystal samples were grown by standard Bridgman method [2.13] with a tungsten crucible and a high frequency induction furnace. High purity Tm (99.9%, source: Ames Lab. USA) and S, Se and Te (99.999%) metal are used for growing the sample. As the valence of the TmX compounds varies with the chemical composition [2.14-2.16], the respective composition ratio of Tm and chalocogenides were carefully selected as starting materials. Initially, the Debye-Scherrer method and magnetic susceptibility measurement were used to characterize all samples. Effective Bohr magneton (μ_B) estimated from the susceptibility measurement were 7.006, 6.328, and 4.609 for TmS, TmSe, and TmTe, respectively at the temperature range of 100 K to 300 K. The mean valences estimated from the susceptibility measurement were 2.799, 2.530 and 2.017 for TmS, TmSe and TmTe, respectively. As a comparative analysis of mean valence derived from the susceptibility measurement, valence band UPS and XPS, 4*d*-4*f* and 3*d*-4*f* absorption spectra will be given in the chapter 4.

3.4.Ib. Sample preparation in UHV

Since the samples are very sensitive to the contamination even in the ultrahigh vacuum (UHV) environment, a lot of cares were taken during the sample preparation. Though, the cleaving method (taking out some layers from the surface) is the best to get fresh surface for such kind of NaCl structural sample, it was not possible to get cleaved surface during the experiment. Instead, the scraping by diamond filler in UHV or Ar ion sputtering was used to obtain the clean surface. Except for the Tm4*d* resonance photoemission experiment, scraping method was used every time. Sputtering with Ar ion of 2keV energy was applied to clean the surface. Unfortunately, the sputtering could not clean the surface of TmTe. The surface of TmTe is porous-like. As a result, some unaffected oxide region was left even after the

sputtering. All the cleaning procedures are carried out at room temperature. The cleanness of the sample was checked by monitoring the O1*s* peak intensity. The O1*s* intensity was kept below the noise level during the experiment by performing the cleaning procedure frequently.

3.4.II. Magnetic thin film

Thin film systems were prepared *in situ* by means of newly developed preparation chamber for VG ESCALAB system.

3.4.IIa. Cu(001) substrate preparation

All kinds of thin film reported in this thesis were deposited on clean Cu(001) substrate. A higher degree of attention was taken to clean the Cu(001) sample. After the several cleaning procedures, the clean surface was finally achieved. In the following, the steps of cleaning are given that have done before inserting the sample into the UHV chamber:

I. **Mechanical polishing:** Mechanical polishing was done by successive use of (a) sandpaper with 180, 240, 400 and 600 grit, (b) Nylon cloth with polishing liquid including Al_2O_3 (of 5μm and 1μm) and finally (c) micropolish cloth with polishing liquid including Al_2O_3 (of 0.1μm and 0.05μm).

II. **Electrochemical polishing:** Before inserting into the vacuum chamber, the sample was cleaned by electrochemical polishing [2.17] to remove the mechanically damaged layers due to process I. The electrochemical polishing gives a mirror surface.

After inserting into the UHV chamber, several processes were performed to get clean sample. Initially, degassing was carried out to remove simple gases from the sample. But it was found that mild sputtering (Ar ion energy 0.5eV for 30 minutes) was very useful before degassing the sample. After degassing procedure, sputtering with 1.2keV Ar ion was carried out. This high-energy Ar ion cause some disorder on the surface. Another mild sputtering was therefore done before heating the sample. The annealing temperature was about 800K. These cycles were repeated until sharp (1x1) LEED pattern was observed. Sometimes, the Cu(001) shows the clear (1x1) LEED pattern even in the presence of some oxygen on the surface [2.18]. In such a case, the best way to check the cleanness of the sample is the monitoring of the O1*s* XPS peak that should be kept below the noise level. At the same time, the presence of other possible surface contamination such as C, S was also checked by C1*s* and S2*s* photoemission spectra.

3.4.IIb. Thin film growth

In the preparation chamber, the quartz thickness monitor is equipped with a linear motion. After the calibration of the deposition rate (nÅ/min, n takes any value) by the thickness monitor, the monitor was pulled back and the sample was placed at the same position of the thickness monitor. No angle correction was necessary for getting the exact thickness on sample. High purity (4N) Ni and Co rods were used for the evaporation. After bake out the preparation chamber, a long-time and extensive degassing procedure was performed to remove all unwanted components present in the evaporating materials and also inside of the tungsten filament. The pressure of the preparation chamber was about $8x10^{-10}$ –$2x10^{-9}$ torr during the film deposition on Cu(001) surface. The deposition rate was kept around 0.5Å/min to 1 Å /min that was checked before and after the film growth on the sample.

3.4.IIc. Magnetization

Before taking the photoemission for dichroism study, all kinds of magnetic films are magnetized by a magnetic coil located nearby the sample. The magnetic coil of with inner diameter 8mm is made of a Cu-wire of 2mm thickness. The length of the coil is 20mm and the number of turn was 10. The magnetic field was applied via a pulse current by a condenser (33μF). After charging with 800volts, the condenser is then discharged in the magnetic coil. The inductance and the magnetic field along the center axis of the coil are 0.31 henry and 163 gauss, respectively.

References

2.1. "Vacuum ultraviolet spectroscopy I", Edited by J. A. Samson, D. L. Ederer, Academic press(1998).

2.2. "UVSOR Activity Report 1997", April 1998, p. 10.

2.3. P. A. Palmberg, J. Elctron, Spectrosc. Relat, Phenom. **5**, 691 (1974).

2.4. T. Murata, T. Matsukawa, S. Naoé, T. Horigome, O. Matsudo, M. Watanabe, Rev. Sci. Instrum., **63**, 1309 (1992).

2.5. "UVSOR Activity Report 1997", April 1998, p. 21.

2.6. E. Nakamura, H. Hama, H. Yamazaki, T. Kinoshita, O. Matsudo, H. Yonehara, T. Kasuga, G. Isoyama, M. watanabe, J. Elctron, Spectrosc. Relat, Phenom. **80**, 421 (1996).

2.7. J. Wong, G. Shimkaveg, W. Goldstein, M. Eckart, T. Tanaka, Z. U. Rek, H. Tompkins, Nucl. Instrum. Methods A, **291** 243 (1990).

2.8. T. Kinoshita, Y. Takata, T. Matsukawa, H. Aritani, S. Matsuo, T. Yamamoto, T. Takahashi, H. Yoshida, T. Yoshida, Krishna G. Nath, Y. Ufuktepe, S. Kimura, Y. Kitajima; J. of Synchrotron Rad., **5** (1998) 726-728.

2.9. T. Kinoshita, Krishna G. Nath, Y. Haruyama, M. Watanabe, S. Yagi, S. Kimura and A. Fanelsa" J. Electron Spectrosc. Relat. Phenom., **92**, 165 (1998).

2.10. M. Sakurai, S. Morita, J. Fujita, H. Yonezu, K. Fukui, K. Sakai, E. Nakamura, M. Watanabe, E. Ishiguro, K. Yamashita, Rev. Sci. Instrum., **60**, 2089 (1989).

2.11. See appendix A.

2.12. See appendix B.

2.13. "Preparation and basic properties of the rare earth", B. J. Beaudry, K.A. Gschneidner, Jr., in "Hand book on the rare earths", Edited by K.A. Gschneidner, Jr, L. R. Eyring, North-Holland Publishing Co. Amsterdam (1978).

2.14. E. Bucher, K. Andres, F. J. di Salvo, J. P. Maita, A. C. Gossard, A, S. Cooper, and G. W. Hull, Jr., Phys. Rev. B **11,** 500 (1975).

2.15. B. Batlogg, H. R. Ott, E. Kaldis, W. Thöni, P. Watcher, Phys. Rev. B **19**, 247 (1979).

2.16. K. Andres, W. M. Walsh, Jr. S. Darack, L. W. Rupp, Jr. and L. D. Longinotti, Solid State Commun. **27**, 825 (1978).

2.17. See appendix C.

2.18. F. M. Leibsle, Surface Science, **337**, 51(1990).

Chapter 4

Core level photoemission study of TmX

Related publications:

1. **Title:** **"4*d* core-level resonant photoemission spectroscopy of thulium monochalcogenides around the Tm 3*d* threshold"**
   Authors: Krishna G. Nath, Y. Ufuktepe, S. Kimura, T. Kinoshita, H. Kumigashira, T. Takahashi, T. Matsumura, T. Suzuki, H. Ogasawara, A. Kotani.
   Journal: J. Electron Spectrosc. Relat. Phenom., 88-89, 369-375 (1998).

2. **Title:** **"Resonant photoemission studies of thulium monochalcogenides around the Tm 3*d* threshold"**
   Authors: T. Kinoshita, Y. Ufuktepe, Krishna G. Nath, S. Kimura, H. Kumigashira, T. Takahashi, T. Matsumura, T. Suzuki, H. Ogasawara, A. Kotani.
   Journal: J. Electron Spectrosc. Relat. Phenom., 88-89, 377-384 (1998).

3. **Title:** **"Resonant photoemission studies of thulium monochalcogenides around the Tm 4*d* threshold"**
   Authors: Y. Ufuktepe, S. Kimura, T. Kinoshita, Krishna G. Nath, H. Kumigashira, T. Takahashi, T. Matsumura, T. Suzuki, H. Ogasawara and A. Kotani.
   Journal: J. Phys. Soc. Jpn., 67, 2018-2026 (1998).

4. **Title:** ***"4d-4f* and 3*d*-4*f* resonant photoemission of TmX (X= S, Se and Te)"**
   Authors: S. Kimura, Y. Ufuktepe, Krishna G. Nath, T. Kinoshita, H. Kumigashira, T. Takahashi, T. Matsumura, T. Suzuki, H. Ogasawara, A. Kotani.
   Journal: J. Mag. Mag. Mat., 177-181, 349-350 (1998).

4.1. General properties of TmX

Thulium monochalcogenides TmX (X = S, Se, Te), a unique series with NaCl structure, show interesting and diverse electrical, optical and magnetic properties [4.1]. In TmX, the two magnetic configurations are the $4f^{12}$ (in Tm^{3+}ion, J=6) and $4f^{13}$ (in Tm^{2+}ion, J=7/2). The $4f$ shells are overlapped with the extended conduction band [$5d^16s^2$]. The normal electronic configurations of two valent component in TmX are Tm^{3+} [$4f^{12}(5d6s)^3$] and Tm^{2+} [$4f^{13}(5d6s)^2$]. The well known but the simplest argument for this series has been drawn from the lattice constant measurement and subsequent valence estimation [4.1]. From that measurement, it is suggested that the TmS is the mostly trivalent, TmSe is typical intermediate valent, and TmTe is the mostly divalent. Figure 4.1 shows the change of lattice constants for different rare earth monochalcogenides (LX) [4.1]. The values of Tm compounds are indicated by dotted line. Among the Tm compounds, TmTe, TmSe, and TmS have the highest, intermediate, and lowest values, respectively. The instability of the valences in TmX is also changed corresponding to the lattice constant of individual compound.

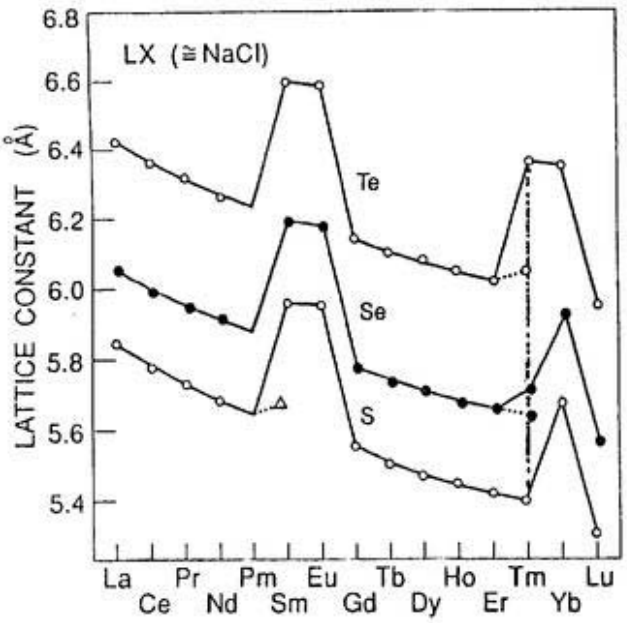

Figure 4.1. Lattice constant of rare earth monochalcogenides, LX. In three curves, the values for TmX are shown by dotted line (vertical). For TmSe and TmTe, the extra two values represent the change of valence due to the stoichiometry, pressure or oxidization variation. Data are taken from Ref.4.1.

The previous calorimetric study showed that the ground state of TmS is metallic [4.2]. The antiferromagnetic Néel temperature (T_N) of TmS was found to be 5.18K from the following experiments, such as specific heat measurement [4.1,4.2], susceptibility measurement [4.2], and neutron-diffraction experiment [4.3]. From the resistivity measurement [4.1,4.4], it was found that TmS shows high-temperature Kondo-like behavior. The metallic characteristics of TmS are also verified by photoemission experiment [4.5].

TmSe also shows magnetic ordering at T_N =1.8K [4.1]. A detailed study of specific heat, conductivity, susceptibility has been done to understand the intermediate valent property of TmSe [4.1,4.6,4.7].

Same as TmS and TmSe, TmTe also shows magnetic orderings below the T_N ~1K [4.1]. Magnetic, valence, and some other physical properties of TmTe have been studied in details [4.1,4.8]. In those studies, TmTe was characterized as a semiconductor with band gap of 0.35eV where Tm-valence in TmTe was found to be mostly divalent.

4.2. Electronic structures and density of states for TmX

The density of state and the nature of mixed valence in the TmX can be explained easily by considering of lattice constant. The schematic explanation of the electronic structures and the density of states [4.9] are shown in Fig. 4.2. The dotted line represents the Fermi level. Due to the crystal field splitting, the *5d* conduction band is divided into two sublevels t_{2g} and e_g. The centers of gravity of t_{2g} and e_g are also indicated by dashed lines. As shown in Fig. 4.1, the lattice constant is large for TmTe because of the large anion Te. As a result, the crystal field splitting is smaller for TmTe (in Fig. 4.2). The value of this splitting is 10Dq=1.1eV [4.10]. The ground state of Tm is $4f^{13}\ ^2F_{7/2}$. If one electron is removed from the $4f^{13}$ state by the following reason, the localized $4f^{12}$ state is formed at about 6.5eV below the $4f^{13}$ state. This $4f^{12}$ state can be observed in TmS and also in TmSe. In TmTe, the localized $4f^{13}$ state is separated from the bottom of the $5dt_{2g}$ by the energy gap ΔE. No state is present around the Fermi level in normal pressure and temperature. This indicates the existence of semiconducting property in TmTe [4.10]. The electron does not remove from the $4f^{13}$ states, which means the divalent nature of TmTe.

In the middle of Fig. 4.2, the electronic structure is given for TmSe. Due to the reduction of the lattice constant of TmSe, the crystal field splitting is enhanced. As a result, the sublevel t_{2g} in the conduction band is now overlapped the $4f^{13}$ state. In this situation, parts of the *4f*

electrons spill into the conduction band creating a $4f^{12}5d$ state. Due to the hybridization, $4f^{13}$-$4f^{12}5d$ state becomes a narrow $4f$ band.

In case of TmS, the lattice constant takes the lowest value among the TmX compounds as shown in Fig. 4.1. The corresponding crystal field splitting is thus enhanced. As a result, a $4f^{13}$ electron is converted completely into $5d$ electron. Thus, the $4f^{13}$ level is now empty. According to the BIS (bremsstarhlung isochromat spectroscopy) measurement [4.11], the empty $4f^{13}$ level stays above the Fermi level. But the occupied $4f^{12}$ level is about 6.5eV below the Fermi level.

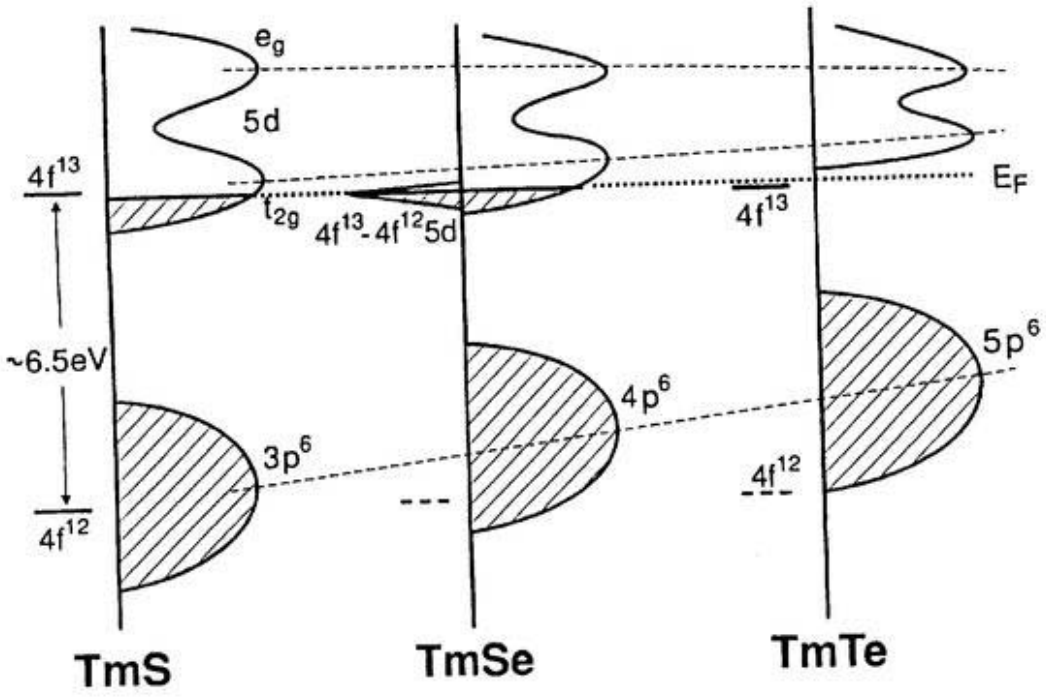

Figure 4.2. Schematic explanation of the electronic structures and the density of states in TmS, TmSe and TmTe [4.9]. Dotted line represents the position of the Fermi level, E_F. Two dashed lines are drawn to show the trend of change of the crystal field splitting in TmX.

4.3. Photoemission result (off-resonant): Tm4*f* valence band

The off-resonant photoemission spectra of the Tm4*f* valence band were measured for clean TmX systems using both the synchrotron radiation (hν=140eV) and x-ray source (Mg*K*α, hν=1253.6eV). Total energy resolution was less than 0.5eV at hν=140eV and 0.7eV at hν=1253.6eV. The spectrum taken at hν=140eV is considered to be rather surface sensitive according to the photoelectron universal curve (shown in chapter 2). Spectrum for unclean

(oxidized) sample was also measured to observe the effect of contamination (mainly oxygen) on the spectral features.

4.3.I. TmTe, mostly divalent

The Tm4*f* photoemission spectrum of TmTe is shown in Fig. 4.3. In Fig. 4.3(a), the spectrum of oxidized sample is included for reference. In Figs. 4.3 (b) and (c), the clean sample spectra

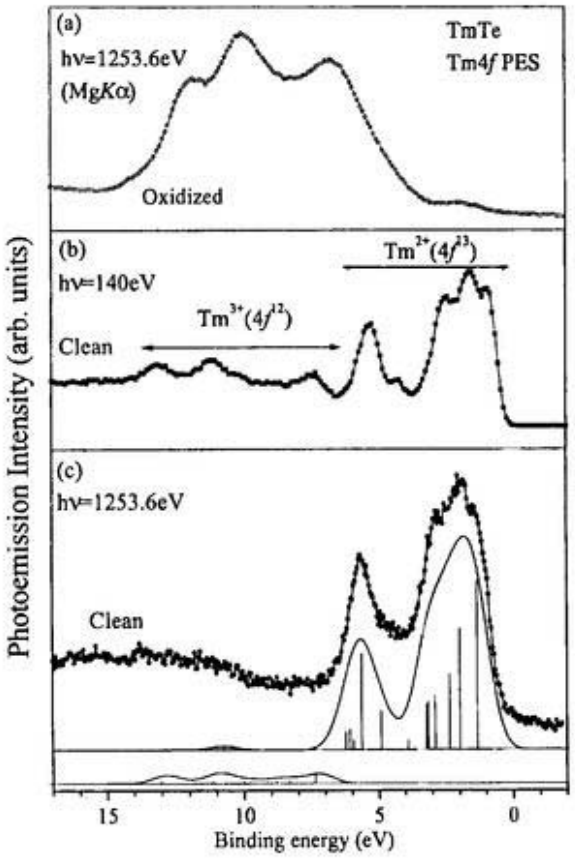

Figure 4.3. Valence band (Tm4*f*) photoemission spectra for TmTe, the mostly divalent compound. (a) Spectrum (open circle) for oxidized sample using Mg*K*α radiation (hν=1253.6eV). (b) Spectrum (solid square) for clean sample taken at hν=140eV. (c) For clean sample (solid circle) using Mg*K*α radiation. The solid lines represent the calculation. The muliplet structures are shown by the vertical lines.

are shown taken at hν=140eV and hν=1253.6eV, respectively. The spectral features of both spectra in (b) and (c) for clean sample are nearly same. But several peaks are more

distinguished in the spectrum in (b) because of higher resolution. The spectra for clean sample show dominant signal in the lower binding energy side close to the Fermi level ('0' binding energy indicates the Fermi level). The energy gap between the Fermi level and lowest energy state in the *4f* level was found to be about 0.43eV. The value is nearly same as reported in the previous results [4.5,4.10]. The existence of the energy gap is the evidence of the semiconducting property in TmTe. By comparing with the calculated spectra and the previous photoemission [4.5,4.10,] and resonant photoemission results [4.12], it is clear that the signal at 0.43-5.6eV represents the divalent properties of TmTe. On the other hand, the weak emission around 6-15eV represents the trivalent characteristics. The trivalent peaks are shifted to the higher binding energy than those are in TmS and TmSe (results for TmS and TmSe are given below). The features of Tm^{3+} are more clearly observed in (b) than in (c). The probable reason of these differences will be discussed later in the Sec. 4.8. In the calculated spectra, several final state multiplets are shown, which are indicated by vertical lines. It is known from the calculation that the emission for Tm^{2+} contains 69 different final states that originate from the $4f^{13}(^2F_{7/2}) \rightarrow 4f^{12}(^3H_6)$ dipole transition. The emission for Tm^{3+} consists of 211 different final state components. In order to follow the instrumental resolution in the experimental curve, a Gaussian width of 0.6eV (FWHM) is used to convolute the calculated spectra. The absolute binding energy positions for both divalent and trivalent components can not be determined from the present calculation. The peak positions in the experimental spectrum are thus considered as references to fit the calculated spectra. In Fig. 4.3 (a), the spectrum for oxidized (unclean) sample is also shown. Usually, the oxidized sample shows mostly trivalent nature; probably Tm_2O_3 is formed.

4.3.II. TmS, mostly trivalent

Tm*4f* photoemission spectra for clean and oxidized TmS are shown in Fig. 4.4. The calculated spectra (solid lines) with multiplet structures are also compared here. In each spectrum, the $4f^{12}$ (Tm^{3+}) emission is strong because of the mostly trivalent characteristic of TmS. By comparing the results with the previous one [4.5] and the present calculation, and resonant photoemission, it is found that the weak signal near the Fermi level (binding energy from 0 to 5.6eV) is originating from the Tm^{2+} in TmS. The presence of the density of states

around the Fermi level indicates metallic nature of TmS. As suggested before [4.5], 4*f*-5*d* hybridization may be present around the Fermi level.

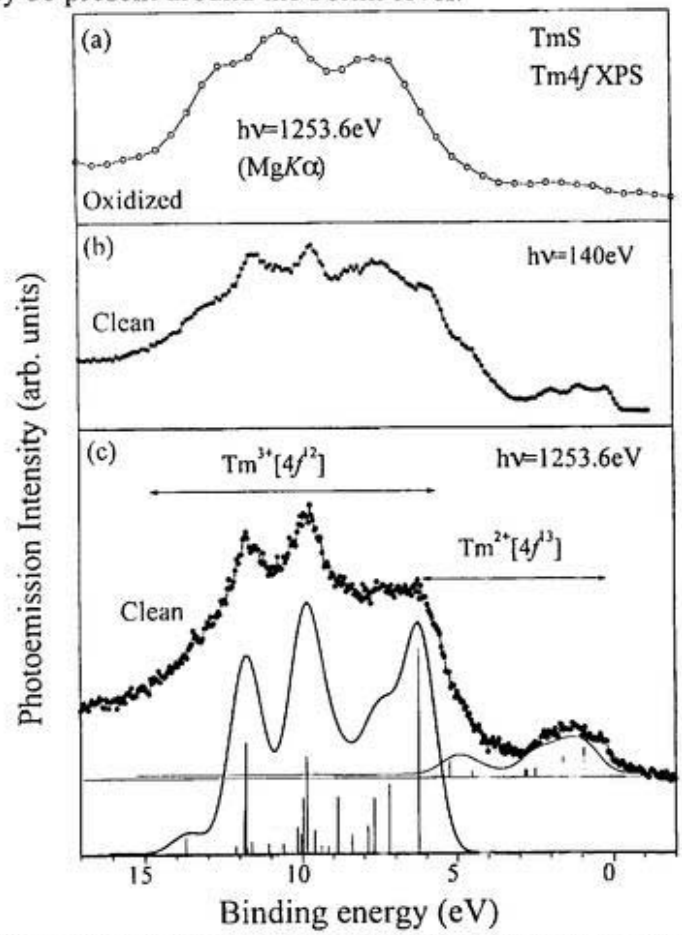

Figure 4.4. Valence band photoemission spectra for TmS, the mostly trivalent compound. (a) Spectrum for oxidized sample measured by using Mg*K*α (hν=1253.6eV). (b) Spectrum for clean sample at hν=140eV. (c) Spectrum for clean sample at hν=1253.6eV (Mg*K*α).

4.3.III. TmSe, typical intermediate valent

The valence band photoemission results for typical intermediate valent TmSe are shown in Fig. 4.5. The spectrum for oxidized sample in (a) shows almost trivalent nature because of the formation of Tm_2O_3. The calculated spectrum is shown together with experimental results. The photoemission signal at 0-5.6eV binding energy region is from the divalent part. The emission around the Fermi level indicates the metallic nature of TmSe. As shown in the figure, the valence band photoemission spectra for clean TmSe shows both the divalent and trivalent components with nearly equal strength. The peak intensity of the divalent part in (b) is

relatively stronger than that in (c). This means the estimated mean valences from these two spectra might be different to each other. The reason will be discussed later in detail in Sec.4.8.

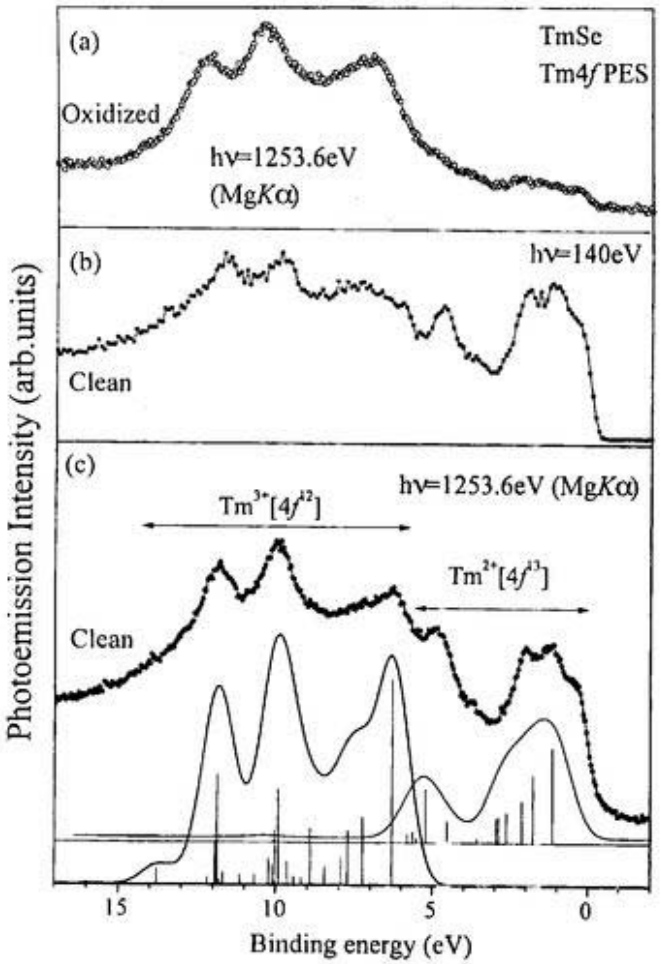

Figure 4.5. Tm4*f* photoemission results for TmSe, the typical intermediate valent compound. (a) Spectrum for oxidized sample taken at hν=1253.6eV (Mg*K*α). (b) Spectrum for clean sample taken at hν=140eV. (c) Spectrum for clean sample taken at hν=1253.6eV (Mg*K*α).

4.4. Tm5*p* core level photoemission and the resonant effect

In order to study the effect of electrostatic interaction between the shallower 5*p* core level with the localized 4*f* states, the Tm5*p* XPS and the resonant photoemission spectra around Tm4*d* (hν=150-200eV) threshold have been measured. The interaction between the 5*p* hole and the 4*f* shell is rather weak. As a result, even with smaller spin orbit splitting, the 5*p* spectrum shows separated spin-orbit peaks.

The photoemission results of Tm5*p* have been reported previously by several authors for TmTe [4.13], TmS [4.5], TmSe [4.14], and Tm metal [4.15]. In these results, the spectral

features of 5*p* photoemission were discussed. The spin-orbit doublet peaks in 5*p* photoemission spectra are further split into two different peaks and show the chemical shift depending on the Tm valences. In Ref.4.13, the chemical shift was found to be 3.5±0.1eV in TmTe for the two sets of spin-orbit doublet peaks corresponding to Tm^{3+} and Tm^{2+}. The result was interpreted as a consequence of the spontaneous interconfiguration fluctuations in Tm compound. G. Kaindl and co workers [4.5] have also reported the same features in 5*p* photoemission for TmS. They observed the valence induced splitting (chemical shift) is 2.6±0.2eV for $5p_{3/2}$ and 3.1±0.4eV for $5p_{1/2}$. Actually, in Ref. 4.5, the origin of the divalent components was considered to be the surface components. In case of TmSe [4.14], chemical shift was found to be ~2.7eV for $5p_{3/2}$ and ~4.1eV for $5p_{1/2}$. These values in Ref. 4.14 are not similar with the previous results [4.5,4.12]. In addition, the resonant behavior of 5*p* levels at 4*d*-4*f* resonance was also studied in Ref.4.14.

The existence of the multiplet structures in the spectra was not discussed in those results. In order to get a clear picture about the coupling of 5*p* level with the 4*f* shell, it is very important to study the muliplet structures by comparing with calculation.

Recently Nicklin *et al.* [4.15] reported the resonant behavior of $5p_{3/2}$ and $5p_{1/2}$ individual multiplets at 4*d*-4*f* resonance for Tm metal (Tm^{3+}) and compared with the calculation. The spin-orbit splitting was found to be about 7eV for Tm^{3+}. No divalent peak was observed in their result. Though they mentioned the several peaks around the $5p_{3/2}$ and $5p_{1/2}$ levels, their results only represent the trivalent characteristics. Therefore, there is a lack of information about the binding energy shift of 5*p* peaks due to the valence and the nature of multiplet coupling with $4f^{12}$ and $4f^{13}$ in the mixed valent system.

In the present study, the 5*p* XPS were measured by using Mg*K*α radiation and the resonant photoemission spectra were measured at Tm 4*d*-4*f* absorption edges (hv=150-200eV). The contributions of divalent and trivalent Tm ions in the photoemission spectra will be discussed separately. Because of the presence of multiplet structures and broadened feature in all core level spectra for TmX, it is rather difficult to define a particular state as a spin-orbit peak. It is, therefore, reasonable to define by "$5p_{3/2}$" peak region instead of $5p_{3/2}$ peak.

4.4.I. Spectral features of Tm5*p*

4.4.Ia. Tm5*p* XPS in TmSe

Figure 4.6 shows the Tm5*p* XPS spectra in TmSe excited by Mg*K*α (hν=1253.6eV)

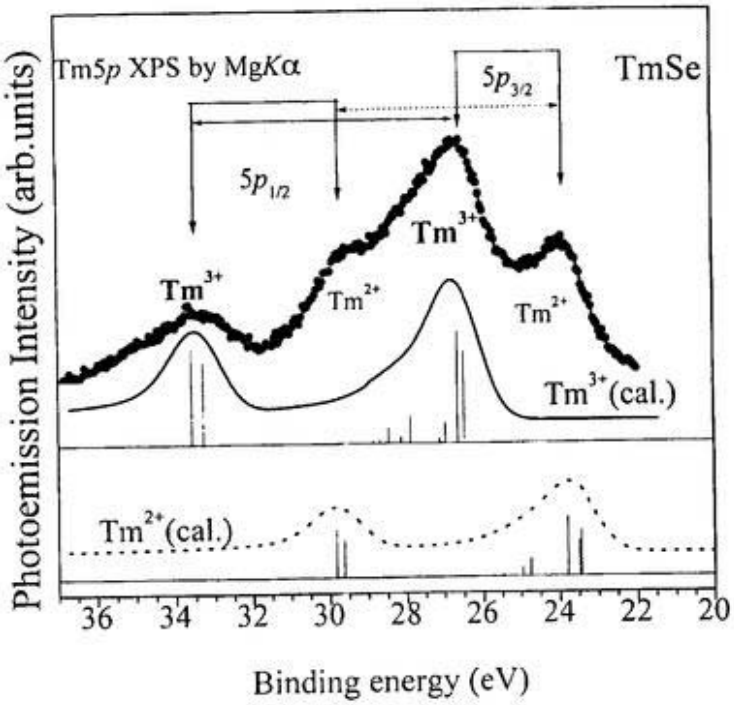

Figure. 4.6. Experimental (solid circle) photoemission spectrum for Tm5*p* core level of TmSe. The spectrum shows the mixed valent properties where the ratio Tm^{3+}: Tm^{2+} = 1:0.51 was obtained from the peak intensity of $5p_{3/2}$ states after background subtraction. Vertical arrows show the chemical shift and horizontal arrows (solid for Tm^{3+} and dot for Tm^{2+}) show the values of spin-orbit splitting depending on the Tm valences. Two calculated spectra, for Tm^{3+} and Tm^{2+}, are also shown herewith with a same ratio as the experimental one. The vertical line represents the multiplet structures.

radiation. In order to clarify the mixed valent property of TmSe, two calculated spectra (solid line for Tm^{3+} and dotted line for Tm^{2+}) are also shown herewith. The both calculated spectra were convoluted with 0.7eV Gaussian to mimic the experimental resolution. Instead of fixed Lorentzian, the spectra are also convoluted with Doniach-Sunjic line shape for explaining the metallic behavior of TmSe. The experimental spectrum for the intermediate valent TmSe is considered to be the superposition of the divalent and trivalent components. Because of the presence of both $4f^{12}$ (Tm^{3+}) and $4f^{13}$ (Tm^{2+}) components, the Tm5*p* XPS shows two sets of spin-orbit doublet corresponding to two valences. Generally for any strongly interacting rare

earth system, the binding energy position of different states in the core level photoemission depends on the $4f$-electron occupation number i.e., the different screening channel [4.16]. For example, in the $3d$ photoemission spectra for several rare earth compounds, the peak corresponding to the "hole-$4f^n$" ("hole-$4f^{n+1}$") configuration is in the higher (lower) binding energy [4.16].

Due to the electrostatic interaction between the $5p$ hole-$4f$ electrons, $5p$ photoemission spectra should show the multiplet peaks together with the spin-orbit doublet peaks. Though the calculation for both the Tm^{2+} and Tm^{3+} components in Fig. 4.6 show several line spectra that corresponds the multiplets, the spectra convoluted with 0.7eV(HWHM) Gaussian do not show any multiplet peaks except the spin-orbit doublet peaks. Experimental spectrum also shows the same features. Because of the poor resolution of the XPS spectra, the muliplet peaks are not resolved clearly. Instead, the evidence of the presence of the muliplet peaks in the $5p$ resonant spectra (discussed later) is comparatively clear because of the resonant effect and better resolution.

In the previous result [4.14], the values of the apparent $5p$ spin-orbit splitting were found to be 5.9eV for divalent component and 7.3eV for trivalent component. The difference between these two values is 1.4eV. This difference originates from the variation of exchange interaction between $5p$ core hole and the $4f^{12}$ (S=1) and $4f^{13}$ (S=1/2) configurations [4.14].

In Fig. 4.6, the peaks at binding energies of 23.9 and 29.8eV represent divalent properties in "$5p_{3/2}$" and "$5p_{1/2}$" peak regions, respectively. On the other hand, the peaks at 26.6 and 33.5eV show the trivalent characteristics in "$5p_{3/2}$" and "$5p_{1/2}$". The apparent spin-orbit splitting for trivalent component is 6.9eV and for divalent part is 6.0eV. The difference between these two values of spin-orbit splitting is 0.9eV. This value is smaller than the previous result [4.14]. The chemical shifts are 2.7eV for "$5p_{3/2}$" and 3.7eV for "$5p_{1/2}$". These values are also different from the previous results [4.5, 4.14]. In Ref. 5, the Tm$5p$ spectrum in TmS taken at hv=50eV shows a strong background at the higher binding energy side. Because of this strong background, there might have some errors to estimate the values of the spit-orbit splitting. On the other hand, in Ref. 4.14 by S.J. -Oh and co-workers, the divalent components in their TmSe sample were comparatively strong. As a result, the trivalent components in $5p$ photoemission were relatively week. The trivalent peaks were also affected by the strong background. The estimation of the values of spin-orbit splitting therefore may include some errors. In the present experiment, the comparison with the calculation further confirms the position of the $5p_{3/2}$ and

$5p_{1/2}$ peaks. As a result, the present estimated values are more acceptable than those from the previous results [4.5,4.14].

4.4.Ib. Tm5*p* XPS in TmS and TmTe

The figures 4.7(a) and (b) show photoemission results for the mostly trivalent TmS and the

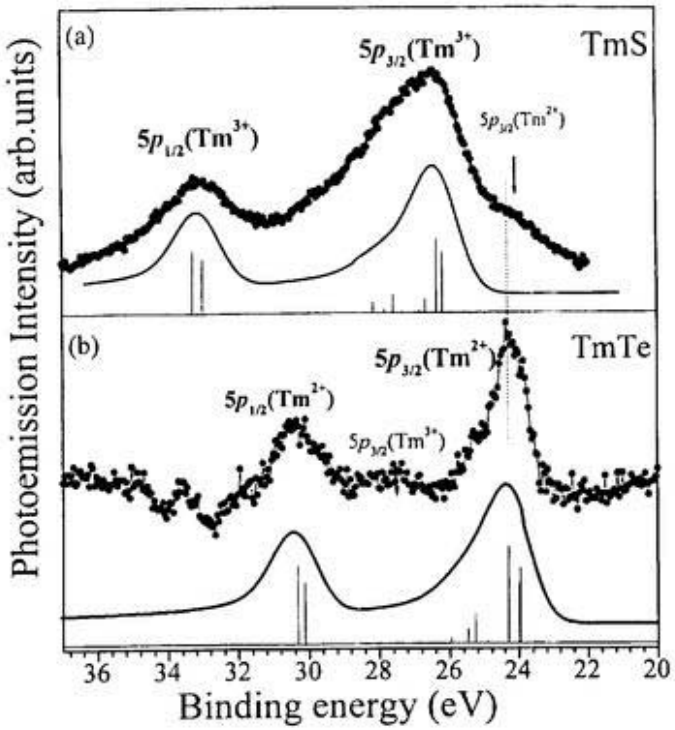

Figure 4.7. Tm5*p* XPS spectra for TmS (a) and TmTe (b). The spectra are compared with the calculated Tm^{3+} and Tm^{2+}, respectively. These spectra were also measured by using Mg*K*α radiation. Though both TmS and TmTe show the mostly trivalent and divalent properties, small amount of divalent in TmS and trivalent in TmTe are present. Because of semiconducting property, the divalent peak in TmTe is little bit shifted towards higher binding energy than that of TmS one.

mostly divalent TmTe, respectively. The calculated spectra (solid lines) are also shown for both TmS and TmTe. The estimated mean valence from the susceptibility measurement of TmS is 2.799 [4.12]. This means that TmS can be treated as mostly trivalent one, but with a fraction of divalent. By comparing with the result for intermediate valent TmSe in Fig. 4.6 and mostly divalent TmTe in Fig. 4.7(b), the emission of trivalent component in TmS is confirmed.

It is already shown in valence band photoemission result that weak divalent signal is also present in the Tm4*f* XPS spectra for TmS in Fig. 4.4. Similar to 4*f* XPS, 5*p* XPS also shows some divalent structures in Fig. 4.7(a). The weak shoulder around 24eV is belonging to $5p_{3/2}$ of divalent part. The value of spin-orbit splitting was found to be 6.9eV. The both experimental and calculated (convoluted with spectra Doniach-Sunjic line shape and 0.7eV Gaussian) show the asymmetrical shape at the higher binding energy of the spin-orbit peak region.

In (b), the spectrum for TmTe is not from the raw data. In the spectrum from raw data, the higher binding energy parts of 5*p* level (around 29-34eV) are overlapped with satellite peaks originating from the Te4*d* levels. The spectrum was measured by using Mg$K\alpha$ (hν=1253.6eV) line. This line at hν=1253.6eV, the superimposed state of $K\alpha_{1,2}$ lines, is commonly used as the source. Besides $K\alpha_{1,2}$ lines, there are also two satellite lines, namely $K\alpha_3$ and $K\alpha_4$ with relative intensities of 9% and 5%, and photon energies of 1262.1 and 1263.7eV, respectively [4.17]. In the present experiment, the x-ray line is not monochromated. Therefore, Te4*d* levels show the satellite peaks at lower binding energy side because of that secondary radiation for Mg$K\alpha$. After subtraction the satellite peaks, the true contribution of divalent components is derived as is shown in Fig.4.7(b). In case of TmTe in Fig. 4.7(b), the experimental spectrum shows the mostly divalent characteristics. Though the mean valence from the susceptibility measurement is 2.017, there are some trivalent components around 27.5eV. The position of the trivalent peak in TmTe is in 1eV higher binding energy than that of TmS. This may be occurred due to the surface core level shift. The discussion about the peak shift will be given in sec.4.8. The spreading of line spectra in calculation is narrower than that of TmS because of the weaker 5*p*-4*f* coupling for divalent part. The spin-orbit peaks are therefore narrower than those of trivalent TmS. The value of spin-orbit splitting is 6.0eV, which is almost same as for divalent part in TmSe.

The difference between the lineshapes of metallic TmS and semiconducting TmTe is also very clear. In TmS, the spin-orbit peak has an asymmetry at the higher binding energy range of the peak. The spectrum for TmS can be described as a Doniach-Sunjic line shape by excluding the multiplet structures. The origin of this asymmetry is due to the scattering of the conduction electrons after the core level photoionization. In case of semiconductor, the asymmetry is absent in the core level spectrum. Therefore, the spectrum for TmTe shows almost symmetrical feature around the spin-orbit peak. This also proves that TmTe is a semiconductor and TmS and TmSe are metal.

4.4.II. Resonance at 4*d*-4*f* absorption edges

At 4*d*-4*f* photoabsorption, a 4*d* electron is excited into an empty 4*f* level. The 4*d*-4*f* photoabsorption spectra are relatively simple for Tm because the intermediate state has only 0 or 1 holes for Tm^{2+} and Tm^{3+}, respectively. The 4*d*-4*f* photoabsorption spectrum is expanded over a broad energy range in excess of 20eV due to the excited state multiplet structures [4.18]. From the selection rule in the LS (Russel-Saunders) coupling scheme, dipole allowed transitions are $^3H_6$, $^3H_5$ and $^3G_6$ with different photon energy positions. The absorption process can be written as follows [4.14,4.18-19]:

$$\left.\begin{aligned} 4d^{10}5s^25p^64f^{12}\ (^3H_6) + h\nu &\rightarrow 4d^95s^25p^64f^{13}\ (^3H_6) \\ &\rightarrow 4d^95s^25p^64f^{13}\ (^3H_5) \\ &\rightarrow 4d^95s^25p^64f^{13}\ (^3G_5) \end{aligned}\right| \quad \text{for } 4f^{12} \text{ configuration}$$

and

$$4d^{10}5s^25p^64f^{13}\ (^2F_{7/2}) + h\nu \rightarrow 4d^95s^25p^64f^{14}\ (^2D_{5/2}) \quad \text{for } 4f^{13} \text{ configuration.}$$

In Fig. 4.8, the 4*d*-4*f* absorption spectra [also can be expressed by total yield (TY) spectrum] are shown for TmS, TmTe and TmSe, respectively. The calculated spectra for Tm^{3+} and Tm^{2+}

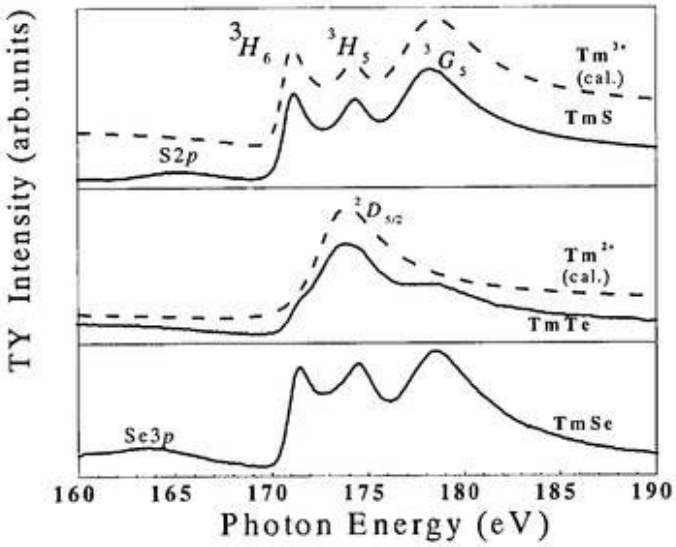

Figure 4.8. Experimental total yield (TY) spectra (solid line) for 4*d*-4*f* photoabsorption in TmS (top), TmTe (middle) and TmSe (bottom), respectively. Dashed lines with TmS and TmTe represent the calculation for Tm^{3+} and Tm^{2+}. The peaks Se2*p* and Se3*p* from anions are overlapped with the pre-threshold region in TmS and TmSe spectra. The transition to the final states $^3H_6$, $^3H_5$ and $^3G_5$ for trivalent and $^2D_{5/2}$ for divalent ion are labeled, respectively.

(dashed line) are also shown in the same figure. For TmS, the spectrum consists of three peaks, $^3H_6$, $^3H_5$ and $^3G_5$ and these are the on-resonant conditions of photoemission for trivalent component. The corresponding photon energies are about 171, 174 and 178eV. Actually there is another intermediate state $^1H_5$, but the weakest one and is at about 12eV above the $^3G_5$ level. On the other hand, in case of TmTe, only single transition to $^2D_{5/2}$ is possible. Therefore, the Tm4*d*-4*f* absorption spectrum shows single prominent peak at 173eV. The shoulders at photon energy of ~171eV and ~178eV and the buried signal at 174eV indicate the presence of small amount of Tm^{3+} in TmTe. The absorption spectrum for TmSe is shown in the bottom of the figure, which includes both Tm^{3+} and Tm^{2+} components.

The final states of absorption are considered as the intermediate states of the resonant photoemission, which may decay in several ways. The decay after 4*d*-4*f* absorption is known as super-Coster-Kronig (involving 4*f* photoemission) or Coster-Kronig (involving core levels photoemission other than 4*f*) decay. At 4*d*-4*f* resonance, the decay channels related to the 4*f*, 5*p* and 5*s* levels are described as 4*d*-4*f*4*f*, 4*d*-5*p*4*f* and 4*d*-5*s*4*f*. The all processes involved in resonance are described below (also described in Sec. 2.3):

Initial state		Intermediate state		Final state	
$4d^{10}5s^25p^64f^n$ + hν	→	$4d^94f^{n+1}$	→	$4d^{10}5s^25p^64f^{n-1}$ + e^-	..... (A1)
				$4d^{10}5s^15p^64f^n$ + e^-	..... (B1)
				$4d^{10}5s^25p^54f^n$ + e^-	.....(C1)

The three final states are 4*f*, 5*s* and 5*p* photoemission, respectively. At the same time, there is also direct photoemission at same photon energy as described below:

Initial state		Final state	
$4d^{10}5s^25p^64f^n$ + hν	→	$4d^{10}5s^25p^64f^{n-1}$ + e^-	..... . (A2)
		$4d^{10}5s^15p^64f^n$ + e^-	..... (B2)
		$4d^{10}5s^25p^54f^n$ + e^-	.....(C2)

So, the process (A1) and (A2) have same initial state and final state. Interference between them shows an enhancement in 4*f* photoemission. The ultimate effect is that an intensity modulation of 4*f* photoemission is occurred around the 4*d*-4*f* absorption edges. Same

arguments are applicable for 5*s* and 5*p* core levels. For example, the resonant effect of 5*p* level occurs due to the interference of the 5*p* emission of process (C1) and another direct 5*p* emission of process (C2). It will be shown from the resonant photoemission results for Tm4*f* and Tm5*p* that the 4*d*-5*p*4*f* Coster-Kronig decay is a weak comparatively to the 4*d*-4*f*4*f* super-Coster-Kronig decay.

4.4.III. Resonant effect of Tm5*p* for Tm^{3+} ion

4.4.IIIa. Result in EDC

Though TmS is the best choice to study the resonance effect for Tm^{3+}, the 5*p* photoemission taken at several on resonant conditions are overlapped with the *LMM* Auger decay from sulfur (S). As a result, true resonant effect of Tm5*p* can not be separated in TmS. Instead, the trivalent components in TmSe have been selected for this purpose.

Figures 4.9(a-d) show the Tm5*p* resonant photoemission spectra in TmSe. Figure 4.9(e) represents the 4*d*-4*f* TY spectrum for TmSe, which includes the both Tm^{3+} and Tm^{2+} components [4.13,4.16,4.18]. The off-resonant photoemission spectrum taken at hv=169eV(1) is shown in the Fig. 4.9(d). In the off-resonant photoemission spectrum, the signal from both Tm^{3+} and Tm^{2+} components are appeared. Calculated spectra are also shown for both valence components (solid line for Tm^{3+} and dotted line for Tm^{2+}). Existence of two valence components indicates the mixed valent property of TmSe at the off-resonant condition. In the TY spectrum, the single divalent resonance peak ($^2D_{5/2}$) and the middle trivalent resonance peak ($^3H_5$) are overlapped around the positions 2(hv=173eV) and 3(hv=174eV) as discussed before.

In Fig. 4.9(c), the photoemission spectrum taken at 2(hv=173eV) shows the resonance effects for both the divalent and trivalent Tm5*p* states. But the divalent part is relatively stronger than trivalent one because peak at hv=173eV actually represent the divalent condition. In Fig. 4.9(c), the experimental spectra shows some unusual structures coming from the poor signal to noise (S/N) ratio that suppress the true multiplet structures. In case of on-resonant condition 3(hv=174eV), both valent components show almost equal resonance enhancement in Fig. 4.9(b). In Fig. 4.9(a) for on-resonant condition 4 (hv=178eV), the trivalent parts are dominant. This means at hv=178eV, the resonance enhancement is mainly occurred for trivalent part.

Because of the poor S/N ratio in Figs. 4.9(a-d), some unusual structures have been appeared, which are mixed with the true multiplet peaks. Even at this situation, the evidence of the presence of the multiplet structures is also apparent if the results from calculation and XPS results in Figs. 4.6 and 4.7 are compared. In case of resonant photoemission, the origins of the different peak shapes are therefore due to (a) poor S/N ration and (b) variation of resonant effect for different multiplet peaks for a particular exciting condition.

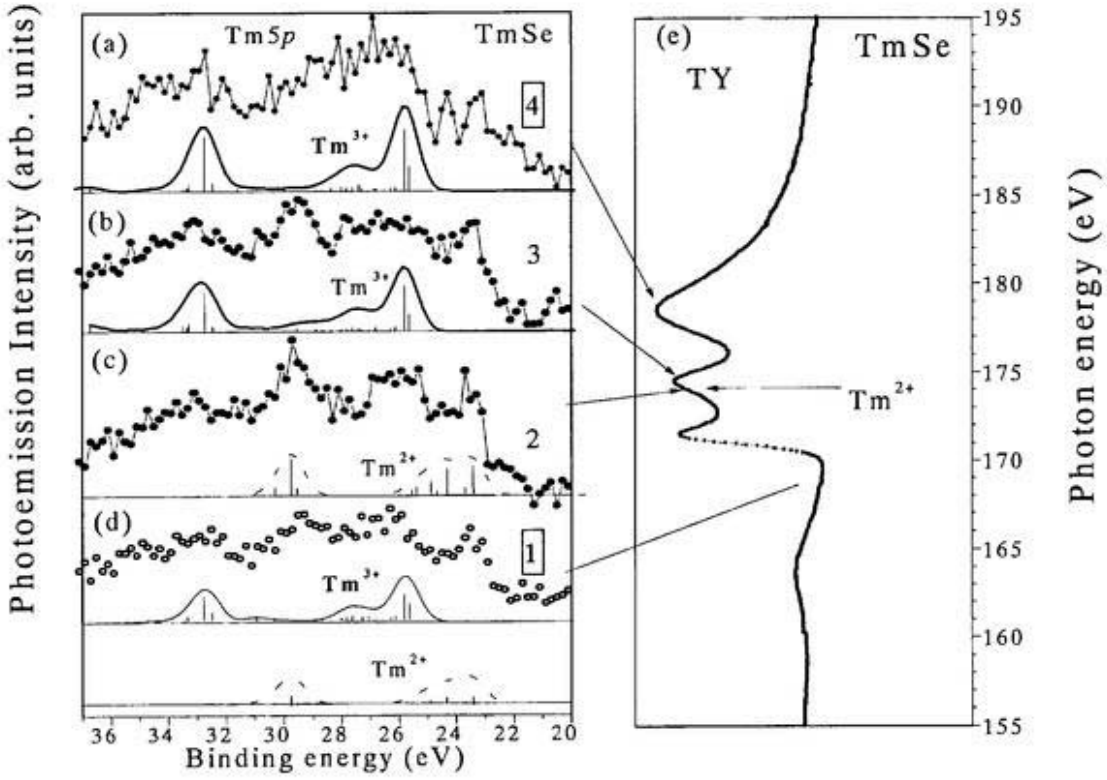

Figure 4.9. (a-d) Experimental and calculated Tm5*p* resonant photoemission spectra of TmSe at on-resonant [hv=173(2), 174(3) and 178eV(4)] and off- [hv=169eV(1)] resonant conditions, respectively. The photon energies are selected from the total yield (TY) spectrum in Fig. 4.9(e). Solid lines represent the calculation for the trivalent component and dashed ones do for the divalent one.

4.4.IIIb. Result in CIS

Figure 4.10 shows the result of constant initial state (CIS) measurement of the 5*p* peaks in TmSe. The CIS measurement was carried out to study directly the resonant behavior of trivalent parts in 5*p* photoemission spectra. The CIS spectrum for binding energy 25.3eV represents the resonance behavior of "$5p_{3/2}$" (Tm^{3+}) peak region. In the lower part, the CIS for 33.4eV binding energy shows the resonant behavior of "$5p_{1/2}$" (Tm^{3+}). The CIS for 4*f* level (BE 11.9eV) at the 4*d*-4*f* resonance and 4*d*-4*f* TY spectrum are also shown for the reference. All CIS spectra for 5*p* and 4*f* show three peaks that are similar to the experimental 4*d*-4*f* TY spectrum. The CIS spectra for BE25.3eV are normalized by multiplying with factor 1.5. This means that the resonance enhancement of 33.4eV is relatively higher than that of 25.3eV. This is explained in the following way. In the CIS spectra, the relative intensity of any particular resonance peak is not same for two binding energies (BE33.4 and 25.3eV). This means that

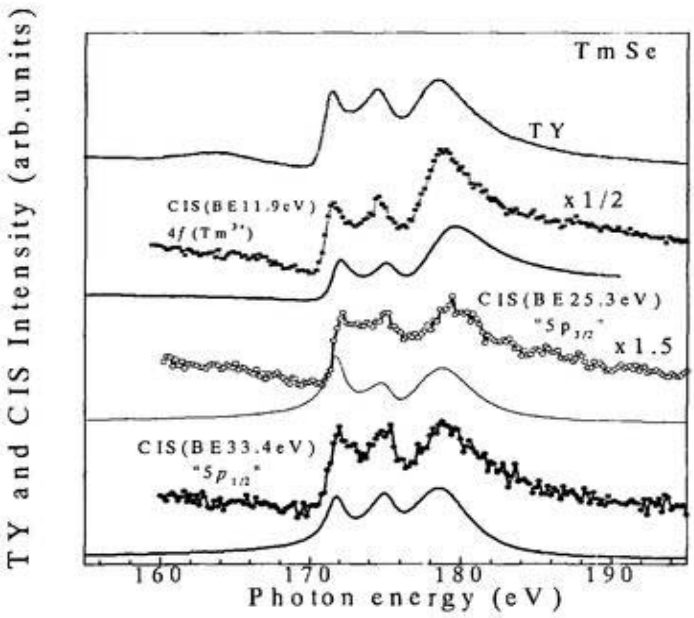

Figure 4.10. CIS spectra for binding energy 25.3eV ("$5p_{3/2}$", open circle) and for 33.4eV ("$5p_{1/2}$", solid circle) in TmSe. Calculated CIS spectra (solid line) are also shown herewith. In order to make comparison, the 4*d*-4*f* TY spectrum and the CIS for Tm4*f* (solid square) in TmSe at 4*d*-4*f* resonance are also shown.

the different spin-orbit peaks do not resonate in the same way at any particular resonant condition. The origin of this difference is the variation of relative strength of the partial decay channels at 4*d*-4*f* resonance. For example, in case of the binding energy 33.4eV, the first two

peaks at hv=171 and 174eV have nearly equal strength both in experimental and calculated spectra. But in the CIS for 25.3eV, the middle resonance peak (174eV) is less intense than the first one (171eV). The peak around 178eV-photon energy is relatively prominent for both cases. In case of 4*f* (BE 11.9eV in Fig. 4.11) CIS result, the $^3G_5$ peak at hv=178eV is extensively strong as compared with other two peaks. Thus, the CIS result shows that the resonance effect of multiplet peaks in both the 5*p* and 4*f* photoemission is dependent on the preferential decay channel. The same phenomenon was also reported previously for $TmAl_2$ and $EuPd_3$ compounds at 3*d*-4*f* resonance [4.19]. The CIS spectra from the calculation are also given here for comparison. Although the overall agreement with calculation seems to be good for two 5*p* binding energy cases, there is some disagreement especially for $5p_{3/2}$ (BE25.3eV) case. At 25.3eV binding energy in the photoemission spectra, the tail of the divalent $5p_{3/2}$ peak at higher binding energy is overlapped with trivalent part. As a result, the experimental CIS for 25.3eV is not exactly similar to the calculated one. But for 33.4eV binding energy, no divalent part is present and the agreement with the calculation is better.

4.4.IIIc. Strength of 5*p* resonance at 4*d*-4*f* absorption edges

In the following, a quantitative discussion will be given for comparing the strength of 4*d*-5*p*4*f* (Coster-Kronig) decay channel with that of the 4*d*-4*f*4*f* (super-Coster-Kronig) decay channel at 4*d*-4*f* resonance. The trivalent components in TmSe are chosen for this purpose. The selected binding energies are 11.9eV for 4*f* and 26.6eV for 5*p* from Fig. 4.11. In these two binding energy positions, almost no divalent components are mixed with trivalent one. In Fig.4.11, two spectra are shown; one is for on-resonant condition (at hv=178eV) and another is for off-resonant condition (at hv=169eV).

It was found that resonance enhancement is 2.2 times for 5*p*(26.6eV) and 4.4 times for 4*f* (11.9eV). These values of resonant enhancement are obtained from the spectra for on- and off resonant in Fig.4.11 where the selections of the linear backgrounds are shown by dotted and solid lines. This values of resonance enhancement indicates that 4*d*-5*p*4*f* decay channel is also active but not so strong as 4*d*-4*f*4*f* decay channel. The intrinsic photoionization cross-section of 4*f* is nearly 16 times higher that that of Tm5*p* around hv=178eV. In Fig. 4.12, the atomic subshell photoionization cross-sections of Tm4*f*, 5*p* and 4*d* are shown according to Ref. 21. In spite of such low cross section, the Tm5*p* spectra can be observed at the 4*d*-4*f* resonant

condition. The present photoemission result of 5*p* reveals two essential utilities of resonant photoemission. One is to enhance weak signal where the intrinsic cross section is very low. Another is to separate the valence component in the core level photoemission for mixed-valent compound where two sets of photoemission signal are present for two valences.

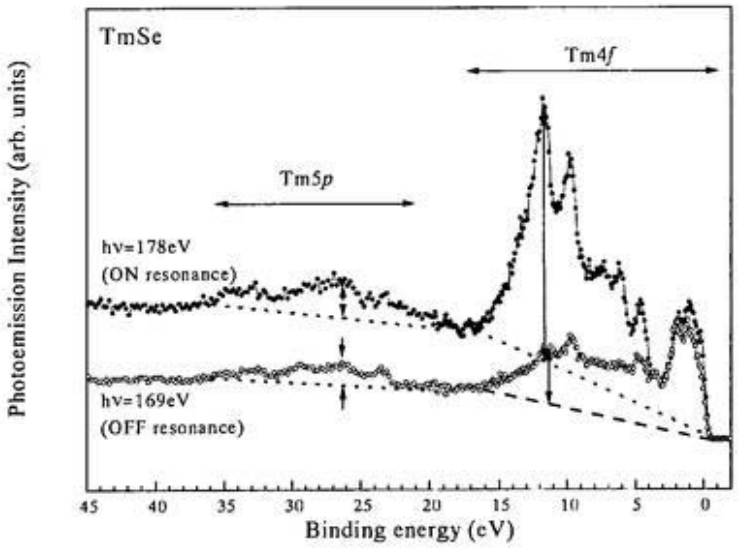

Figure 4.11. Tm4*f* and Tm5*p* resonant photoemission spectra in TmSe at 4*d*-4*f* resonance are shown altogether. The states of highest resonant enhancement shown by arrow are used to discuss the relative strength of each decay channel associated with 4*f* or 5*p* level.

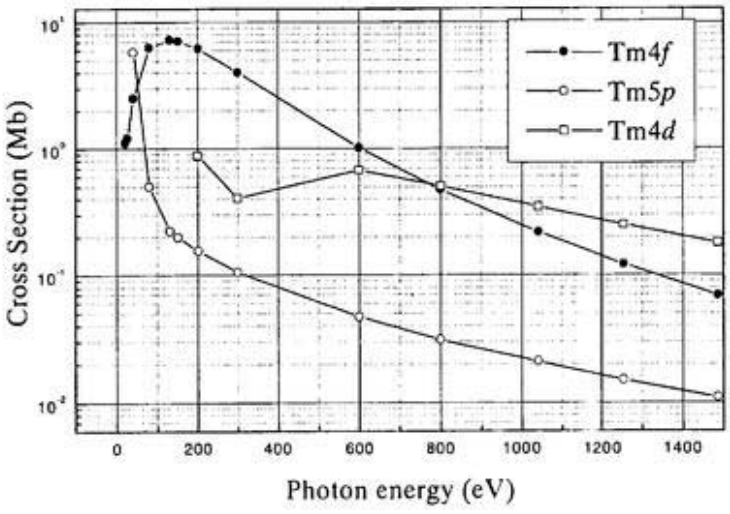

Figure 4.12. Atomic subshell photoionization cross-sections of Tm4*f*, 5*p* and 4*d* [4.21].

4.4.IV. Resonant effect of Tm5*p* for Tm^{2+} ion

4.4.IVa. Result in EDC

The resonant behavior of divalent Tm will be shown here. Figures 4.13 (a) and (b) show the on- and off- resonant 5*p* photoemission spectra, respectively in TmTe, the mostly divalent

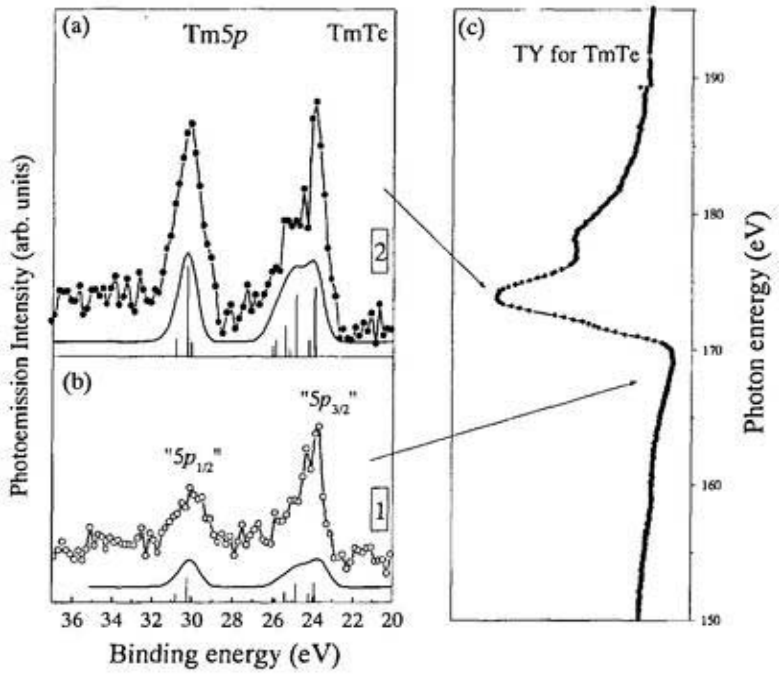

Figure 4.13. Tm5*p* resonant photoemission spectra for TmTe, the mostly divalent compound. (a) The on-resonant photoemission taken at hν=173eV(2). (b) The off-resonant photoemission at hν=169eV(1). (c) 4*d*-4*f* TY spectrum for TmTe. Solid lines represent the calculation for Tm^{2+}.

compound. The excitation energies are selected from the total yield (TY) spectra in Fig. 4.13(c). The solid line represents the calculation for Tm^{2+}. The on-resonant photoemission spectrum (solid circle) was taken at~173eV. The off-resonant spectrum was taken at hν=169eV. From the comparison of the on-resonant spectrum with the off-resonant one, it is clear that the divalent Tm5*p* levels are enhanced due to the resonance effect. It is also noticed that the resonance effect is larger for higher binding energy states, i.e. around 30.5eV ("$5p_{1/2}$"

peak region) than that of lower energy state around 24eV ("$5p_{3/2}$" peak region). The multiplet terms are also present in these spectra. Because of the higher resolution, the multiplet peaks in both the off- and on-resonant photoemission spectra are clearly observed.

4.4.IVb. Result in CIS

The resonance effect of Tm^{2+} was also observed in the CIS results. The experimental and calculated CIS spectra of Tm5*p* are shown in Fig. 4.14. The 4*d*-4*f* TY and Tm4*f* (BE5.2eV)

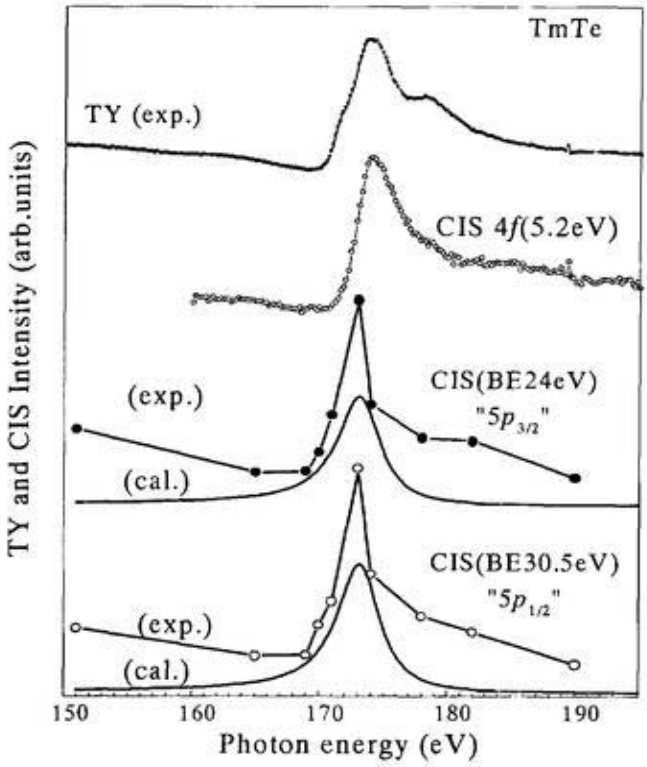

Figure 4.14. CIS spectra for the divalent Tm "$5p_{3/2}$" (BE 245eV) and Tm "$5p_{1/2}$" (BE30.5eV) in TmTe. The corresponding calculated (solid line) spectra for Tm^{2+} are also shown. The 4*d*-4*f* TY and Tm4*f* (BE5.2eV) CIS spectra are also given for comparison.

CIS spectra are also shown in the top of Fig. 4.14. The shapes of the experimental (solid circle for BE 24eV and open circle for BE 30.5eV) and the calculated 5*p* CIS spectra are almost similar to the TY spectrum and the 4*f* CIS for BE 5.2eV. The CIS results are the evidence of

the divalent characteristics of selected binding energy positions in Tm5*p* photoemission. The peak intensity of $^2D_{5/2}$ in CIS spectrum for 30.5eV binding energy peak is stronger than that of 24eV binding energy position. It is clear from this CIS result that the decay channel related to $5p_{1/2}$ levels is more intense than that of $5p_{3/2}$ as it is also shown in the EDC results in Fig. 4.13. As a result, the statistical branching ratio ($5p_{3/2}$: $5p_{1/2}$ = 2:1) of 5*p* level is changed at on resonance as seen in Fig. 4.13. This is due to the difference of Auger decay probability of the intermediate state.

4.5. Tm4*d* core level photoemission

The electrostatic interaction of 4*d* core hole with the unfilled 4*f* shell is very strong because of the same principle quantum number. As a result, the photoemission from Tm4*d* level shows large effect of the correlation, such as the existence of a large number of multiplet structures, the effects of the relaxation and decay of core holes. [4.22,4.23]. In some preliminary experiments, the 4*d* core level photoemission in rare earth metals, such as La, Ce, Sm, Eu, Gd, Tb, Dy, Er, Tm, Yb and Lu [4.24,4.25], mixed-valent compound SmB_6 [4.26] have been reported. The systems such as La (with $4f^0$) or Yb and Lu (with $4f^{14}$) usually show simple structures exhibiting distinguished spin-orbit peaks. In these simple cases, the interpretation of the experimental result is very straightforward. For other cases where the spectrum is more complex due to the extended multiplet structures, interpretation of the experimental result needs to include some final state effects. For example, one of the important effects is the lifetime broadening of the core hole.

The lifetime broadening effect is interpreted as the collapsing nature of the core holes to the ground state during the photoionization process. Here, comparison with the calculation is essential to get the clear understanding of the final state effects. Recently H. Ogasawara and co-workers [4.27] have studied theoretically the lifetime broadening effect of the multiplet structure in 4*d* XPS spectra for heavy rare earth systems and compared with experimental results. They showed that lifetime broadening effect of the multiplet structure in 4*d* spectra strongly depends on the binding energy. The explanation of lifetime broadening phenomenon was given in Ref. 4.27 on the basis of the consideration of strong 4*d*-4*f*4*f* ($N_{4,5}$-$N_{6,7}$-$N_{6,7}$) super-Coster Kronig decay [4.22,4.23] process. None of the previous results, the mixed valent properties in Tm4*d* for TmX was studied. In the following section, before discussing the

resonant effect of the 4*d* core level, spectral features of Tm4*d* photoemission (off-resonant) measured by using Mg*K*α radiation condition will be shown.

4.5.I. Spectral feature of Tm4*d* XPS and lifetime broadening

Figure 4.15 shows the off-resonant Tm4*d* photoemission spectra for TmS, TmTe and TmSe, respectively. In these spectra, the backgrounds are subtracted by Shirley's method [4.28]. The

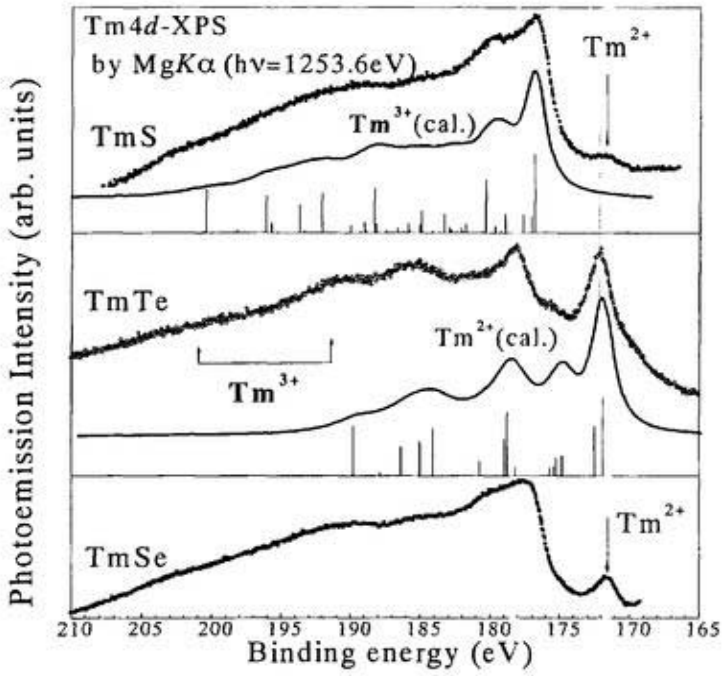

Figure 4.15. Tm4*d* XPS (off-resonant) spectra excited by Mg*K*α radiation. Spectra for the mostly trivalent TmS (top), for the mostly divalent (middle) and the typical intermediate valent TmSe (below) are shown. In all spectra, the backgrounds are subtracted. Calculated spectra for Tm^{3+} and Tm^{2+} are also shown. The divalent components in TmS, and TmSe and trivalent ones in TmTe are also indicated.

solid lines with the TmS and TmTe spectra represent the calculation for Tm^{3+} and Tm^{2+}, respectively. The vertical lines indicate the multiplet peaks. It is obvious that all three spectra

must show the mixed valent character as same as Tm5*p* photoemission. Therefore, some divalent emission in TmS and some trivalent emission in TmTe are expected to be observed. Exactly this is seen in the top of Fig. 4.15 for TmS where the small divalent part is indicated by arrow at the lower binding energy side. The origin of this peak is confirmed by comparing with the middle spectrum for the mostly divalent TmTe. In TmS, the calculated spectrum given here represents only for Tm^{3+}. In fact, the divalent component is not only present at the lower binding energy side, but also at the higher binding energy sides. Around the higher binding energy side, the component from both valence components are overlapped with a certain ratio. This is clearer in case of typical intermediate valent compound TmSe in the bottom of the figure.

In TmS, the multiplet peaks belong to Tm^{3+} are spread over 25eV. Around binding energy of 178.0eV, the spectrum shows maximum intensity. This structure shows a sharp peak with asymmetry in the higher binding energy side. Except for this peak, the spectral features become broadened and no sharp structure is present in the higher binding energy region. The calculated spectrum also shows the same features as the experimental one. The calculated spectra are convoluted with 0.6eV Gaussian to mimic the instrumental broadening and term dependent Lorentzian (Γ_f) to include lifetime broadening effect. According to Ref. 4.27, fixed Lorentzian can not reproduce the experimental spectrum. This means that the effect of the lifetime broadening and its dependency on the binding energy of the different Tm4*d* states must be considered in calculation. To reproduce the experimental spectrum in calculation, it is therefore necessary to introduce the term dependent Lorentzian (Γ_f) i.e., a linear function of binding energy. This is expressed as follow:

$$\text{Term dependent Lorentzian } (\Gamma_f) = 0.1(E_B\text{-}E_0)\text{eV},$$

where E_0 is the lowest binding energy in the Tm4*d* spectrum.

The above relation indicates that the lifetime broadening of several states in the multiplet structure varies with their binding energy. Strong coupling between the core hole and localized 4*f* shell rejects the constant lifetime concept. Therefore, the lifetime of core hole depends on the strength of the super-Coster-Kronig (s-CK) transition rate involving 4*f* electrons [4.22].

The lifetime broadening effect according to the selective Auger transition can be easily understood by spin-selection rule and electron correlation effect [4.22,4.27]. Figure 4.16 shows the schematic diagram of spin-selection for decay process according to Ref. 4.27. Two different schemes are explained where one is for the system with less than half filled 4*f* electrons and the other one is for more than half filled case. In the case of less than half filled, the 4*d*-4*f*4*f* sCK decay is allowed for the spin anti-parallel state at higher binding energy side. On the other hand, the 4*d*-4*f*4*f* s-CK decay is forbidden in the lower binding energy side for spin-parallel state. As a result, the 4*d* spectrum, for example in Eu, shows sharp peak (broadened) at lower (higher) binding energy side. In the more than half filled case, the decay process (4*d*-4*f*4*f* s-CK) becomes possible for the lower binding energy states also. Thus, the lower binding energy states also show broadened structure. In general, this spin-selection rule can not explain the broadening effect completely for all rare earth elements.

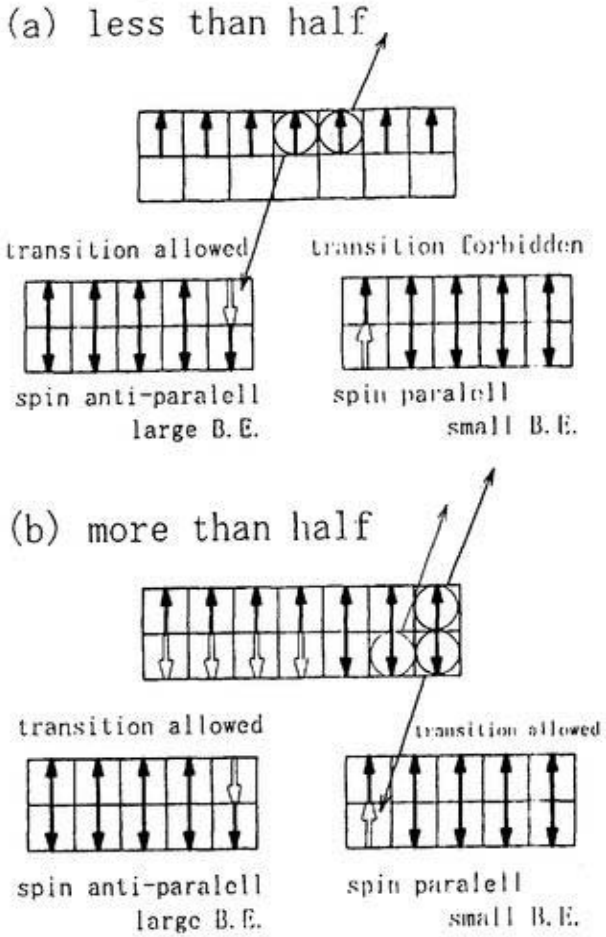

Figure 4.16. Schematic representation of spin selection rule for super-Coster-Kronig decay process according to Ref.4.27. (a) For less than half filled case. (b) For more than half filled case.

As shown in Fig. 4.15 for TmTe, the case with 13 $4f$ electron should be explained by the scheme for more than half filled system. That means lower binding energy states must show extended and broadened feature. However, the spectrum for $4d$ photoemission spectrum for TmTe in Fig. 4.15 shows a sharp peak in the lower binding energy side.

The broadening due to the lifetime of core hole, on the other hand, may explain fairly the spectral features in the $4d$ XPS. The lifetime broadening effect is simply explained through the electron correlation effect. The lower binding energy states are described with spin-parallel electrons (or holes) separated by the Pauli-exclusion principle. The states with spin-antiparallel electrons stay at higher binding energy side and these electrons are strongly interacted. This higher order interaction causes more broadened feature in the higher binding energy side. This interaction is denoted as the "configuration interaction" (CI). The general tendency of $4d$ spectrum is to be more broadened at higher binding energy than the lower one, so that the lower binding energy peaks are sharp with long core hole lifetime as shown for the spectrum in Fig. 4.15. However, the linearity between the spectral broadening and the binding energy does not hold exactly in the whole binding energy region. This is considered to be the reason why some of the multiplet peaks in the calculation do not show similar feature as the experimental ones.

In the middle of Fig. 4.15, the spectrum mainly represents the divalent characteristics because TmTe is the mostly divalent compound. Because of the weaker $4d$-$4f$ exchange interaction of divalent Tm than that of trivalent Tm, the multiplet structures are spread about 19eV (172-190.5eV), smaller than that of TmS. The lower binding energy peak (Tm^{2+}) in spectrum for TmTe is 0.5eV higher (at BE172eV) than that (BE171.5eV) in spectrum for TmS. This difference in binding energy, which originates from the semiconducting properties in TmTe, is indicated by dotted line. The TmTe spectrum also shows lifetime broadening effect depending on the binding energy. The spectrum for TmTe may have some trivalent components buried at the higher binding energy position. The marked area under the experimental curve indicates the possible position of the weak trivalent signal.

In the bottom of Fig. 4.15, the spectrum for TmSe shows the intermediate valent characteristics. By comparing with the calculated Tm^{3+} and Tm^{2+} spectra, it can be said that the photoemission signals from both components are overlapped around 178-190.5eV. As a result, the spectral feature around that specific region in TmSe is neither like TmS nor TmTe. The peak at 171.5eV is originating from the divalent part that is confirmed by comparing with the

TmTe spectrum. The situation for mixed valent TmSe is different from the light rare earth compound SmB_6 [4.26]. It was found in Ref. 4.26 that the contribution from Sm^{3+} (4*d*) is nearly separated from Sm^{2+} (4*d*) with small degree of overlapping. As a result, the contributions from both components in case of SmB_6 were easily distinguished. But in TmSe, to separate different valent components is not so easy as SmB_6 [4.26]. In this respect, resonant photoemission is considered to be very powerful method in order to separate the valence components as discussed for Tm5*p* photoemission.

In the following, the 4*d* resonant photoemission around 3*d*-4*f* absorption edges will be shown. It is very curious to know the final state effect through lifetime broadening in core level photoemission depending on the excitation conditions. In order to investigate these complex features of the core level photoemission spectra in more detail, the resonant photoemission technique may be useful.

4.5.II. Resonance at 3*d*-4*f* absorption edges

Unlike resonant photoemission at 4*d*-4*f* absorption edges, the photoemission experiments at 3*d*-4*f* absorption edges have not been widely studied. Few references are available for latter case. For example, resonant effect in 4*f* photoemission at Tb3*d* and Ce3*d* absorption edges was reported by J. W. Allen *et al.* [4.29]. That was the first such kind of experiment. Laubschat and co-workers [4.20] also reported same experiment for several rare earth compounds. In Ref.4.20, though they have explained the resonance effect in the Tm4*d* photoemission by EDC and CIS results for trivalent compound $TmAl_2$, they did not discuss details of the 4*d* photoemission and the existence of 4*d* multiplet structures including their resonance behaviors. There are also some results discussing the 4*d*-core level resonant effect for Eu [4.30,4.31]. For example in Ref.4.30, U. Becker *et al.* discussed the resonance effect of Eu 4*d* core level at the excitation energies of the 3*d*-4*f* absorption edge. The 4*d* multiplet structures in the final state were not observed in their results. In order to discuss the resonant behavior of the 4*d* core level photoemission, consideration of the final state multiplet structure in any heavy rare earth system is necessary. Furthermore, in the case of Tm-compounds, the contribution of divalent and trivalent components should be described individually in resonant photoemission.

In the case of 3*d*-4*f* absorption, every possible decay channel to 3*d*-core hole causes the excitation of $3d_{5/2}$ (only at $3d_{3/2}$ edge), 4*f*, 4*d*, 4*s*, 4*p*, 5s, 5*p* or some satellite electrons to continuum state (photoemission) [4.17,4.19]. The resonant effect of the core level can be

described by the same way as the 4*d*-4*f* resonance. Here, the decay of 3*d* core hole is Coster-Kronig type and is occurred after the 3*d*-4*f* absorption around hv=1450-1520eV. The main processes are written in the following way (here, other decay channels except for 4*f* and 4*d* are intentionally omitted):

Initial state	Intermediate state	Final state	
$3d^{10}4d^{10}4f^{n} + hv \rightarrow$	$3d^{9}4d^{10}4f^{n+1} \rightarrow$	$3d^{10}4d^{10}4f^{n-1} + e^{-}$	..... (A1)
		$3d^{10}4d^{9}4f^{n} + e^{-}$	.....(B1)

And, the direct photoemission is

$3d^{10}4d^{10}4f^{n} + hv \rightarrow$	$3d^{10}4d^{10}4f^{n-1} + e^{-}$	..... (A2)
	$3d^{10}4d^{9}4f^{n} + e^{-}$	....(B2)

So, the process (A1) and (A2) show resonance enhancement in 4*f* photoemission when the interference is occurred between them. Similarly, process (B1) and (B2) are responsible for the resonance effect in 4*d* photoemission.

In Fig. 4.17, the TY spectra for TmS (a) and TmSe (b) are shown. The solid lines are the calculated spectra for Tm^{3+} and Tm^{2+}. In order to measure the Tm4*d* resonant photoemission spectra, the different photon energies are selected from the TY spectrum. The TY (for TmS) spectrum shows four peaks at photon energies 1460.5, 1462.5, 1465 and 1508eV, which are identified with the transition to the final states $^{3}H_{6}$, $^{3}G_{5}$, $^{1}H_{5}$ and $^{3}H_{5}$, respectively. The calculated spectrum in the figure also shows the same structure as experimental one. The photon energies mentioned above correspond to the on-resonant conditions for trivalent Tm. The position at hv=1456eV is considered as the off-resonant (pre-threshold) one.

In fact, TmTe should be the best choice to study the resonant effect of divalent component. Unfortunately, the clean TmTe surface could not be achieved during this experiment. Instead, the TmSe can be used for this purpose because TmSe also shows divalent characteristics. In Fig 4.17(b), the TY spectrum of TmSe represents the intermediate valent properties. The resonant condition of divalent part from this TY spectrum will be used to study the divalent Tm4*d* photoemission. The dominant features of the TY spectra in TmSe are similar to that of TmS in Fig. 4.17(a), i.e., trivalent peaks at the photon energy of 1460.5, 1462.5, 1465 and 1508eV. In addition, there exits obviously a shoulder at the photon energy of 1459.6eV that belongs to the divalent component as shown in the calculated curve with single peak. This peak describes the transition to the final state $^{2}D_{5/2}$. The presence of divalent shoulder is very clear

in the inset where both TmS (solid circle) and TmSe (open circle) spectra are shown. It is clear from this expanded view that only TmSe spectrum indicates the shoulder. This is the condition for the on-resonant photoemission spectrum of divalent 4*d* photoemission. The peak position and the structure of the both trivalent and divalent TY spectra are comparable with the previous experimental results for $TmAl_2$ [4.20,4.33] and calculated result for Tm^{3+} [4.32].

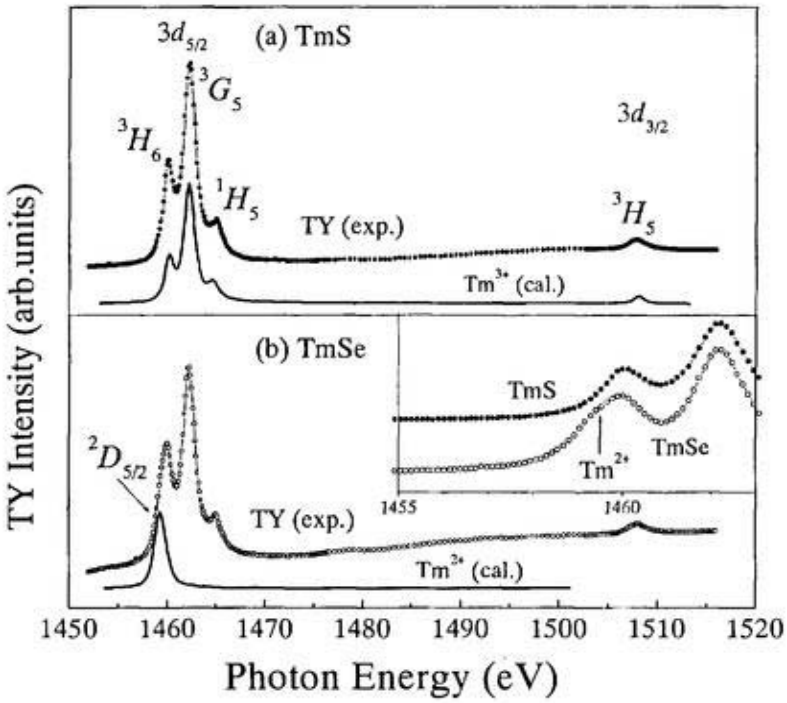

Figure 4.17. 3*d*-4*f* TY spectra for TmS (a) and TmSe (b) with calculation (solid lines). The final states of the transitions are $^3H_6$, $^3G_5$, $^1H_5$ and $^3H_5$ with photon energy position 1460.5, 1462.5, 1465 and 1508eV, respectively are labeled. In (b), the spectrum for TmSe also shows the same structure as TmS, but there is an extra shoulder at 1459.6eV for transition to $^2D_{5/2}$ state. The existence of this shoulder is clearly observed in inset where the comparison is shown very closely.

4.5.III. Resonant effect of Tm4*d* for Tm^{3+} ion

4.5.IIIa. Result in EDC

As mentioned earlier, TmS is known to be almost trivalent compound. In order to study the 4*d* core level photoemission spectra for trivalent ion, the results of TmS will be shown in this section. Figures 4.18(a-d) show the on- and off- resonant 4*d* core level photoemission results for TmS along with the XPS spectrum (a) excited by Mg*K*a radiation. The spectra show almost trivalent nature, but with small amount of the divalent component (buried). The backgrounds are subtracted by Shirley's method for all photoemission spectra. The excitation energies indicated by alphabet (A-D) are selected from the TY spectrum shown in Fig.4.17 (e). Three of

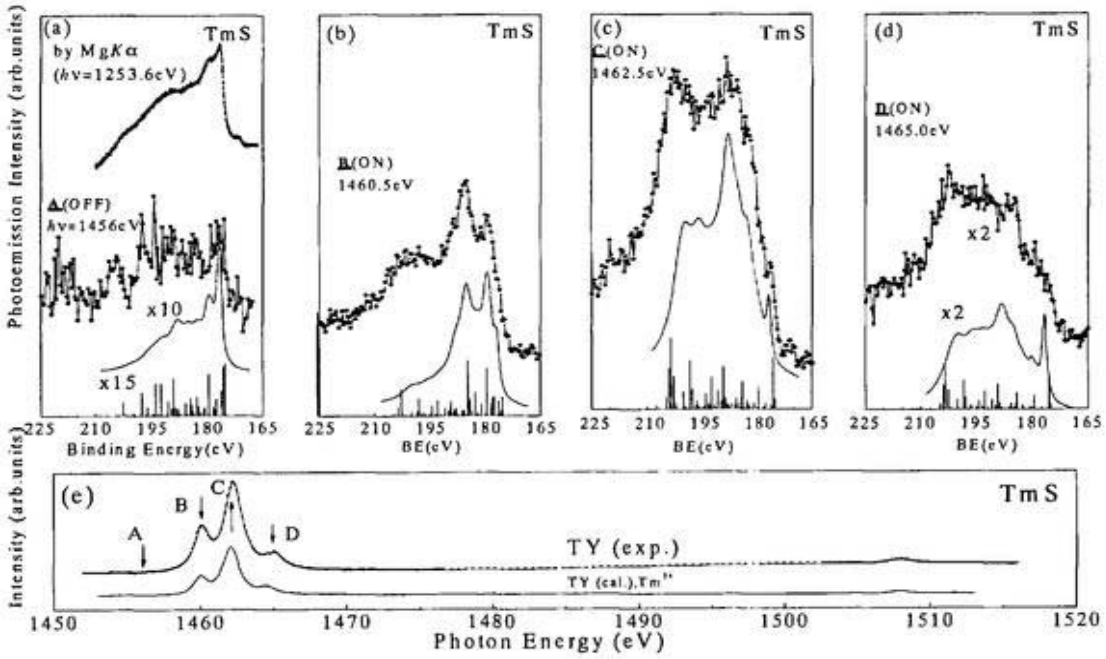

Figure 4.18. (a)-(d) Tm4*d* photoemision spectra of TmS. (a) The off-resonant spectrum along with the XPS spectrum excited by Mg*K*α radiation. (b)-(d) The on-resonant spectra. All solid curves represent the calculated for each resonance condition of the trivalent Tm ion. (e) In TY spectrum, the on- and off-resonant conditions are labeled by A and B-D, respectively.

these excitation energies (B-D) represent the on-resonant conditions of trivalent Tm ion, namely correspond to $^3H_6$, $^3G_5$, and $^1H_5$ intermediate states. It is noticed that the 4*d* spectra are enhanced very much (about 10 times of off-resonant one) under the 3*d*-4*f* resonant condition. The resonance effect of Tm4*d* spectra in Figs. 4.18(b-d) is explained by considering the

interference between the direct 4*d* photoemission and the 4*d* excitation to continuum state as already described in Sec. 4.5.II. The similar phenomenon (but different number of 4*f* electrons) has been reported for Eu [4.30]. Instead of single 4*d* peak in Ref.4.30, Tm4*d* photoemission in the present experiment shows several multiplet peaks in both off- and on-resonant spectra. The every possible final state in the 4*d* multiplet for Tm^{3+} ion was shown by line spectra. The measured 4*d* spectrum was considered as the convoluted form of these line spectra by lifetime broadening and the experimental resolution. The off-resonant spectrum excited by Mg*K*α radiation, which is already explained in the section (4.5.I) in Fig.4.15, is also shown for comparing with off resonant spectrum at hν=1456eV.

In order to describe the resonance effect of the 4*d* multiplet peaks, the preferential decay channels of individual excited state have to be considered. Some of the final states are considered to take part strongly in decay excitation process and show relatively stronger resonant enhancement. For example in Fig. 4.18 (b), the spectrum at hν=1460.5eV shows two dominant peaks with binding energies of ~180.5eV and ~185.5eV. Calculation also shows almost the same feature. At the second and third resonance conditions (at hν=1462.5 and 1465eV, respectively), the 4*d* higher binding energy parts are more enhanced than lower binding energy parts. This distinction of resonant effect in 4*d* multiplet peaks depends on the strength of relevant Auger decay of individual excited state.

At the same time, the shape of both on- and off-resonant spectra is affected by the lifetime of 4*d* core hole. The explanation for lifetime broadening given for off-resonant Tm4*d* XPS in section 4.5.I is also applicable for resonant photoemission spectra. The accordance between the experiment and the calculation seems fairly good. But some differences between the observed results and calculations still exist for on-resonant condition. For example, in Figs. 4.18(b) and (c), the peak at the binding energy of ~200eV in the calculated spectra is not so intense as it is in experimental ones. In case of resonant photoemission, it can be assumed that the sCK transition rates may be dependent on the resonance-induced 4*d* states. Therefore, the linearity between the spectral broadening and the binding energy does not hold exactly for all 4*d* states. The above argument may be the probable explanation why some peaks in calculation are not exactly observed in the experimental curve.

4.5.IIIb. Result in CIS

The concept of the preferential decay channel at 3*d*-4*f* resonance can be explained clearly by the CIS result. The CIS spectra for several Tm4*d* binding energy states are shown together with the results of CIS for 4*f* and 3*d*-4*f* TY spectrum in Fig. 4.19. The features of CIS for both the 4*d* and 4*f* levels are nearly similar to the TY spectrum. Though the CIS spectra do not include many data points, but it is enough to make some discussion. For 4*f* (BE=12.5eV) CIS, the peak at hν=1462.5eV ($^3G_5$) is the most prominent. The peak at hν=1460.5eV ($^3H_6$) is not so strong. The intensity ratio of peak at hν=1462.5eV ($^3G_5$) to peak at hν=1460.5eV ($^3H_6$) is determined

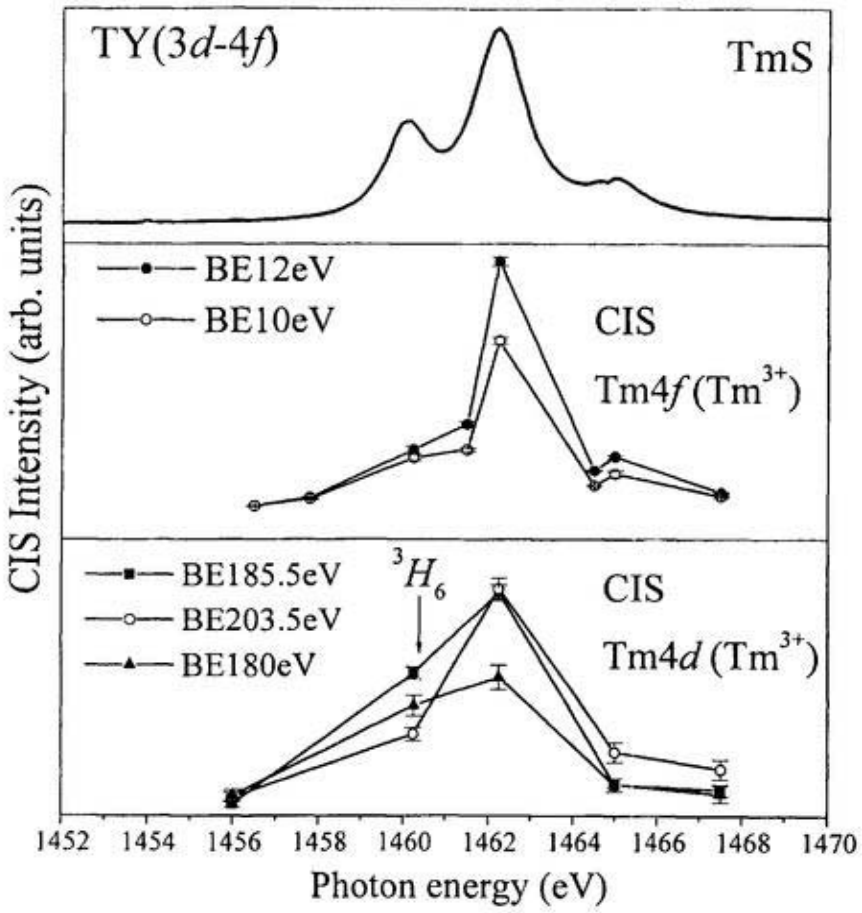

Figure 4.19. Tm 4*d* CIS spectra for TmS at 3*d*-4*f* resonance. In order to make comparison, Tm4*f* CIS (middle) and 3*d*-4*f* TY (top) are also shown. Each CIS spectrum is obtained by plotting the normalized intensity of the selected binding energy position in the photoemission spectra in Fig. 4.18.

to be 4.17±0.19. Now, turning to 4*d* CIS, the peak at hν=1462.5eV ($^3G_5$) is still prominent. But the $^3H_6$ final state peak is comparatively stronger than that of 4*f* CIS. In 4*d* CIS (bottom), the spectra are shown for three binding energy positions, 180, 185.5 and 203.5eV, respectively. All of three spectra show the trivalent characteristics that are confirmed by the CIS results. In 4*d* case, the peak ratio at hν=1462.5eV ($^3G_5$) to hν=1460.5eV ($^3H_6$) is 1.31±0.04 (for BE180eV), 1.57±0.01 (for BE185.5eV) and 1.31±0.04 (for BE203.5eV). These values are smaller than that of 4*f* CIS. This means that the peak at hν=1460.5eV ($^3H_6$) is relatively strong for 4*d* and the 3*d*-4*f* excitation states at hν=1460.5eV decays preferentially to 4*d* photoemission channel as reported for $TmAl_2$ [4.20]. The evidence of preferential decay channel was also found in the calculation of TY spectrum. In the calculation of TY, 4*d* decay channel should be considered together with that of 4*f*. Otherwise, the shape of the TY can not be reproduced.

4.5.IV. Resonant effect of Tm4*d* for Tm^{2+} ion

4.5.IV.a. Result in EDC

In order to study the resonant effect for divalent components (Tm^2) separately, photoemission spectra were taken for TmSe, the typical intermediate valent compound. Figures 4.20 (a) and (b) show the 4*d* resonant XPS results for TmSe around the 3*d*-excitation region. In Fig. (c), the TY spectrum of TmSe is shown. Position "1" is the off-resonant condition and position "2" is the on-resonant condition. The position "2", overlapping with the trivalent resonant condition $^3H_6$ actually represents divalent characteristics as already shown in Fig. 4.17 and discussed in the Sec. 4.5.II. The 4*d* photoemission spectra taken at this photon energy is shown in Fig.4.20 (b). Since the resonance trivalent peak ($^3H_6$ at hν=1460.5eV) is very close to divalent one, it is rather difficult to separate the divalent parts from trivalent ones completely. From the comparison with the calculated spectrum, it can be said that the spectrum in Fig.20 (b) shows almost divalent nature with small amount of the trivalent one. The spectral shape of the buried trivalent part in this condition may be similar to that in Fig.4.18 (b).

It is concluded that the intensity of 4*d* core level originating from the divalent Tm ion is also enhanced due to the resonance effect. It is urged from the comparison of the experimental results with the calculation that the lifetime broadening depending on the multiplet structure is

also affected by the resonant condition as same as in the case of trivalent 4*d* spectra. Since the off-resonant spectrum in Fig.20 (a) shows the mixed-valent nature, the divalent components are not separated in the result. That's why, the calculated results for both divalent and trivalent parts are shown for reference.

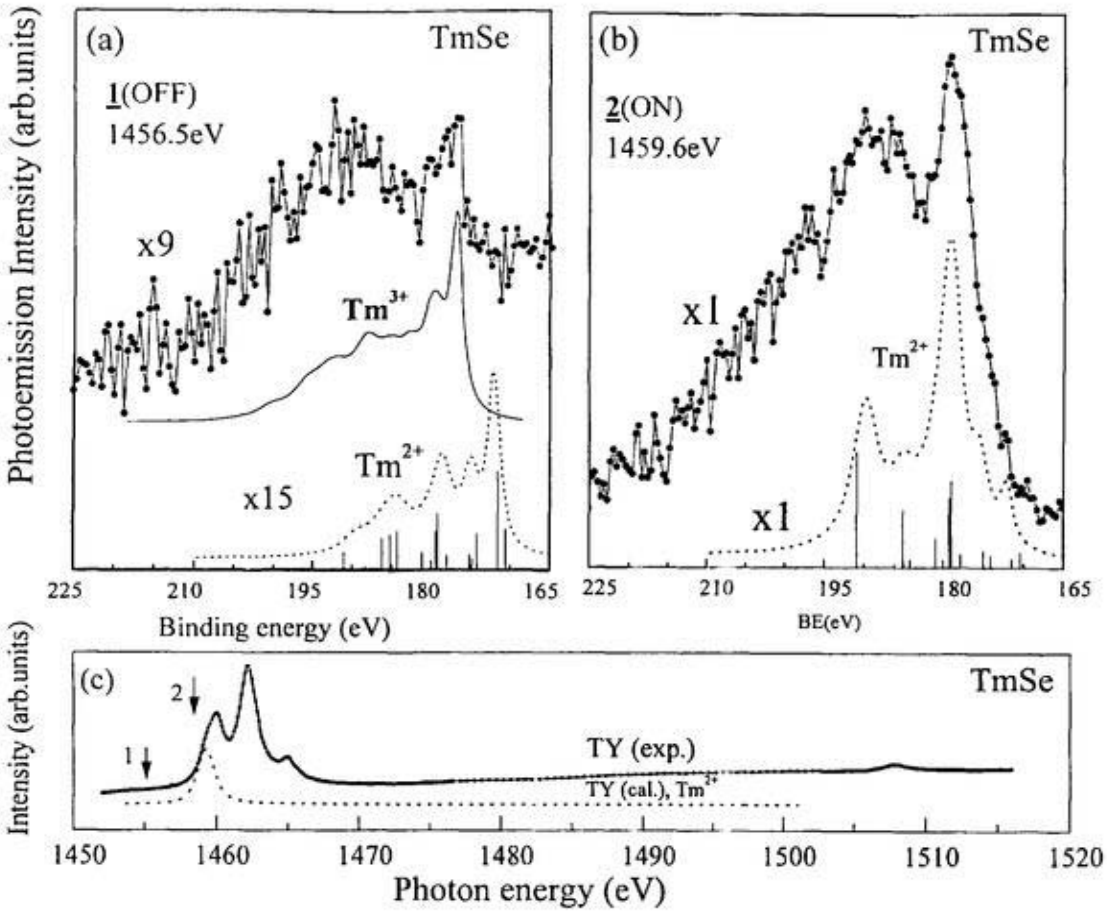

Figure 4.20. (a) and (b) Tm 4*d* core level photoemission spectra for off- and on- resonant conditions, respectively. The 3*d*-4*f* absorption spectra, from which the excitation conditions are selected, is shown in (c). The doted curves represent the calculation for Tm^{2+} ion in each excitation condition. Because TmSe is mixed valence, the calculated spectrum of Tm^{3+} ion (solid line) is shown in the off-resonant spectrum.

4.5.IVb. Result in CIS

The CIS spectra were also taken for divalent Tm4*d*. The results are shown in Fig. 4.21 together with CIS results of divalent Tm4*f*. The selected binding energy is 179eV in 4*d* XPS.

In fact, the binding energy position 179eV does not represent pure divalent state. Some trivalent component is mixed around this binding energy position that was already discussed in Sec. 4.5.I and in Fig. 4.15 for off-resonant 4*d* XPS. The existence of the mixed valent state at this or around this binding energy becomes clearer in the CIS spectrum. The CIS spectra for BE179eV is considered to be superimposed of two valence components, the strong divalent and weak trivalent. In this 4*d* case, as it is already shown, the decay of $^3H_6$ state is a preferential one to 4*d* (Tm^{3+}) level. Because of the relatively intense $^3H_6$ peak, the CIS for 4*d* shows a broad maximum around hv=1460eV. Two resonance peaks are therefore present here. One is $^2D_{5/2}$ belonging to divalent part and another is $^3H_6$ for trivalent part. This is not the case for the CIS of BE 1.5eV, only single peak belonging to the divalent component is observed.

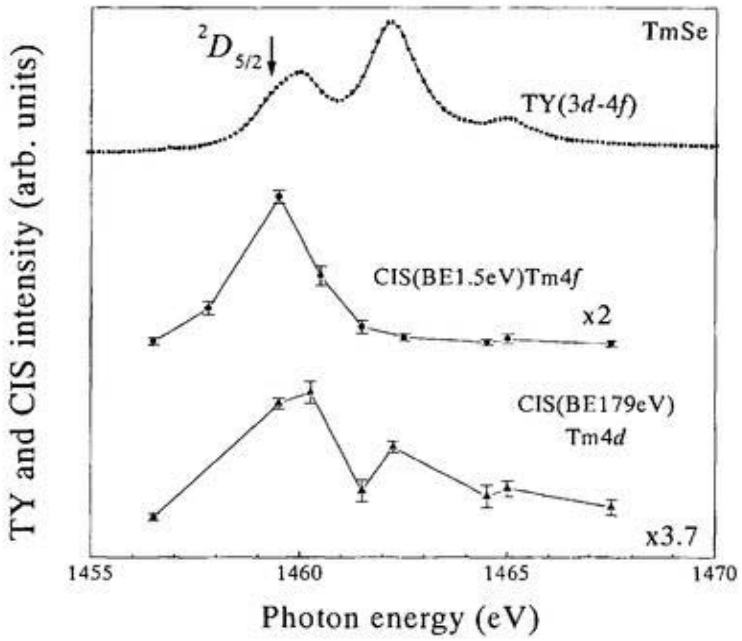

Figure 4.21. CIS results for Tm4*d* (BE179eV) along with CIS for 4*f* (BE1.5) and 3*d*-4*f* TY spectrum. The position of the excitation condition $^2D_{5/2}$ of Tm^{2+} peak in the TY spectrum is marked by arrow.

4.6. Tm4*p* core level photoemission

In the present section, the results of Tm4*p* photoemission measured by using Mg*K*α radiation are discussed. Because of the same principal number of 4*p* and valence 4*f*, the electrostatic interaction between them is also strong as 4*d*-4*f* interaction. In case of 4*d* XPS as described in the previous section, the large exchange interaction rather than the spin-orbit coupling dominates the overall multiplet feature. As a result, the 4*d* photoemission spectra usually do not show the separated $4d_{5/2}$ and $4d_{3/2}$ peaks. On the other hand, in case Tm5*p* photoemission, the spin-orbit peaks are nearly distinguished even with a smaller value of spin-orbit splitting. In 4*p* XPS, besides the 4*p*-4*f* exchange interaction, the effect of CI (configuration interaction) in the final states involving the nearest sub-shell (here 4*d*) also modifies the 4*p* spectral shape. As a result, the physical identity of atomic $4p_{3/2}$ and $4p_{1/2}$ levels is changed into complex structures. Though the values of spin-orbit splitting of 4*p* level are larger than those of 4*d* level, the strength of CI in the final state is dominant to change the feature of 4*p* photoemission spectrum.

4.6.I Tm4*p* XPS results

4.6.Ia. TmS, mostly trivalent

The experimental and calculated spectra of Tm4*p* photoemission for TmS are shown in Figs. 4.22(a-e). Fig. 4.22(a) shows two spectra, one is for oxidized sample and another is for clean sample measured by using Mg*K*α radiation (hv=1253.6eV). The backgrounds of the experimental spectra are subtracted by Shirley's method. Although TmS is mostly trivalent compound, a small amount of divalent component is overlapped with the trivalent features. The position of the divalent peaks at lower binding energy is marked by arrow. Details about overlapping will be discussed latter in the spectra for TmSe, namely the intermediate valent compound. One of the divalent components of "$4p_{3/2}$" peak region is located at the binding energy of ~327eV which is clearly observed in Fig.4.25 (a) for the mostly divalent compound TmTe (discussed latter). The valence band photoemission spectra studied by G. Kaindl *et al.* [4.5] shows that the emission of $4f^{13}$ (Tm^{2+}) originates mainly from the top most surface layer. Even in the bulk sensitive experiment by T. Kinoshita *et al.* [4.34], the valence band photoemission shows some divalent components. The present experiment is also considered to be rather bulk sensitive, but it was not possible to separate the surface and bulk contributions.

The divalent parts are mixed with trivalent components especially in the higher binding energy sides. In the experimental spectrum, the satellite originating from excitation by the secondary

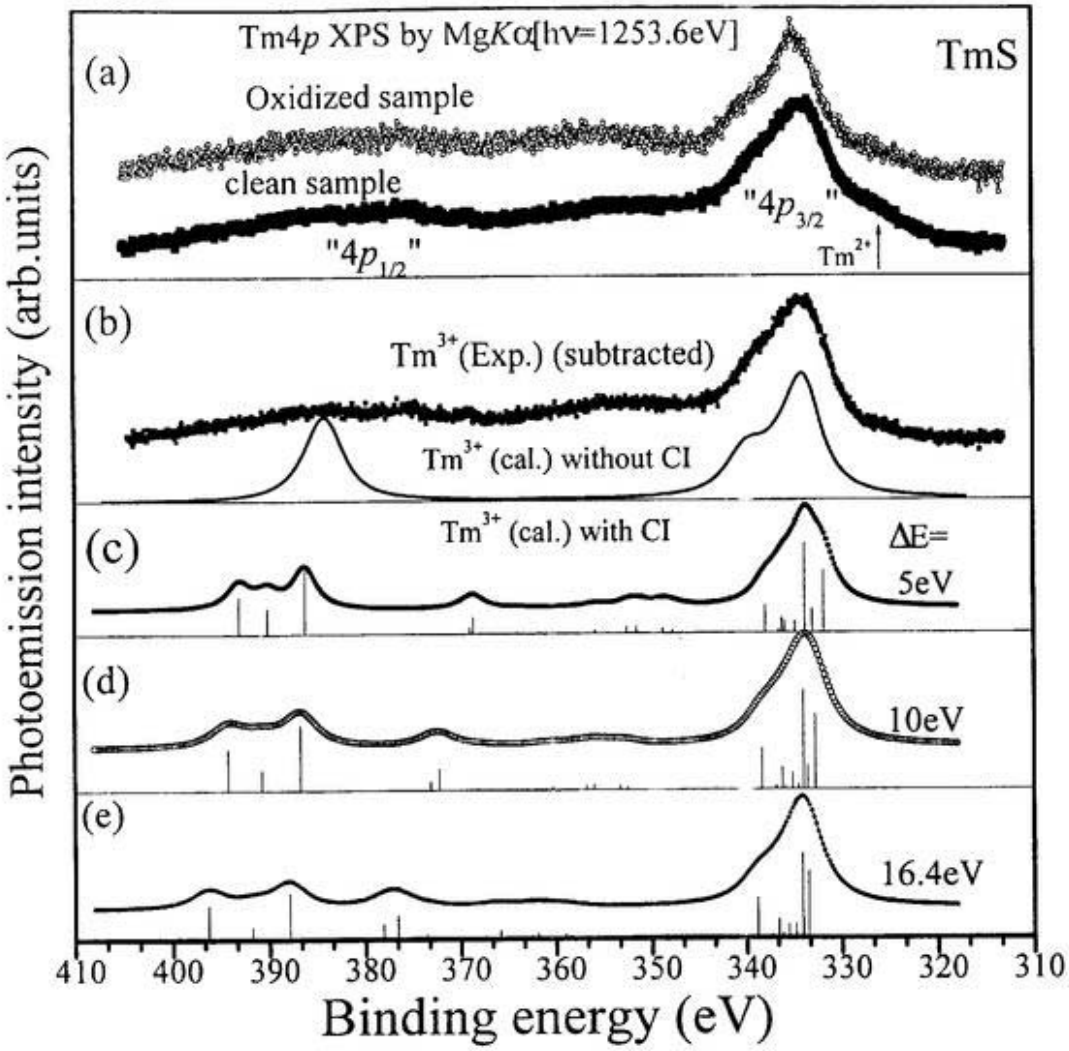

Figure 4.22. Experimental and calculated photoemission spectra for Tm4*p* core level of TmS. (a) Spectra for oxidized sample (open circle) and for clean sample (solid circle). The both spectra are measured by using Mg*K*α radiation (hν=1253.6eV). (b) Spectrum (open square) for nearly pure trivalent components obtained by subtracting the divalent and satellite (due to Mg*K*α secondary lines) parts (discussed in text). Solid curve represents the calculation for Tm^{3+} ion without considering the CI effect. (c-e) Calculated spectra with CI. Vertical bars are line spectra. For the best fitting with experiment, different values of the energy separations between two configurations ($4p^5 4d^{10} 4f^{12}$ and $4p^6 4d^8 4f^{13}$) are considered. The values are 5eV in (b), 10eV in (c) and 16.4eV in (d). In the calculation, the spectra are convoluted with 2.0eV Lorentzian (HWHM) and 0.6eV Gaussian (HWHM).

line (hv=1262.1eV) of Mg$K\alpha$ is also present at 9.5eV lower than the main "$4p_{3/2}$" peak region. In order to get the signal for the pure trivalent component, the divalent parts and the satellite part are subtracted from the raw data (solid circle in Fig. 2.22(a)). For subtraction of divalent part, the mean valence of TmS is assumed to be 2.88, which is estimated from Tm4*f* XPS (discussion of mean valence is given later in Sec. 4.8) for this sample. In order to get divalent part, the experimental spectrum for TmTe is considered here. The mean valence of TmTe is estimated to be 2.05 from Tm4*f* XPS data where the contribution of trivalent is rather weak (only 5%). The spectrum (open square) in (b) therefore represents almost trivalent nature in Tm4*p*.

It is noticed in Fig. 4.22 (b) that the Tm4*p* spectrum spreads over 70eV and shows a number of peaks that are present over the whole binding energy range. In the Tm atom, which is considered to be a trivalent ionic state, the energy separation between two spin-orbit 4*p* peaks ($4p_{3/2}$ and $4p_{1/2}$) is approximately 50eV. In the same figure, the calculated spectrum without considering the effect of CI is also shown. The difference between the experimental spectrum and the calculated one (without CI) is apparent. The spectrum (in Fig. 4.22(b), without CI) represents that kind of atomic characteristic of trivalent Tm ion where the spin-orbit peaks are well distinguished. In case of experimental one, the spectrum does not show the same atomic characteristics as calculated one (without CI). In the experimental one, the peak at the binding energy of ~334eV is comparatively sharp and prominent but with shoulder. At the higher binding energy ranges, i.e."$4p_{1/2}$" peak region, the experimental spectrum does not show any sharp structure. The shape in this area can be considered as "structure less" though some weak multiplet peaks are still appeared. The "$4p_{1/2}$" peak region seems to be totally smeared out over a large energy range. The features of the experimental spectrum are described by considering the configuration interaction

In Figs. 4.22 (c), (d) and (e), the calculated 4*p* XPS spectra including CI between these two configurations, $4p^5 4d^{10} 4f^{12}$ and $4p^6 4d^8 4f^{13}$, are shown. The calculated spectra in Figs 4.22(c-e) are convoluted by 2.0eV Lorentzian and 0.6eV Gaussian width. The vertical lines in the calculated spectra represent the position and the relative strength of the 4*p*-multiplet peaks. The energy separation (ΔE) between the two configurations is approximately 16.4eV that was calculated from original HF calculation for atomic case. However, this value can not directly used in the solid state case. That's why the spectrum in Fig.4.22 (e) does not reflects entirely the experimental one. There may exist another intermediate value of energy separation that can

adjust more accurately with the experiment. But it is rather difficult to find the exact value. For the best fitting with experimental result, the energy separations are also taken to be 5eV and 10eV. In the calculation, the exact binding energies for $4p$ levels are not calculated. The experimental binding energy positions are used as references to compare with the calculated one. It is clearly shown that the calculated spectra with CI fairly reflect the experimental one. This strongly supports the ultimate effect of CI in the $4p$ XPS spectrum. Besides the smeared spectrum in the higher binding energy side, there are several multiplet peaks in the whole range of $4p$ spectrum. The comparison with calculation shows good agreement, but not exactly reproducible. Especially at the higher binding energy side, the calculated spectra show some clear multiplet peaks, but not in the experimental spectrum. The reason of this difference is not clear.

The lifetime broadening effect including the CI is explained as the following. In the case of Tm^{3+}, the two configurations of $4p^5 4d^{10} 4f^{12}$ and $4p^6 4d^8 4f^{13}$ are considered in calculation to reproduce the experimental spectra. There is a strong coupling between these two configurations through Coulomb interaction. The intermediate state of this interaction is described by the following way. A $4d$ electron undergoes into a transition to a $4p$-hole ($4p$-hole propagation to $4d$ hole) and another $4d$ electron is recoiled to certain excited state, in this case to the $4f$ bound state. So, a $4\underline{d}^2$ (underline means hole) state is formed. In the previous section, the lifetime broadening effect in Tm$4d$ photoemission spectra was described by introducing the $4d$-$4f4f$ sCK decay process. Generally, two-$4d$-hole state has shorter lifetime than that of the one $4d$- or one $4p$-hole state. Here, we have to consider the binding energy position of any multiplet peak in $4p$ spectrum whether it is below or above the $4\underline{d}^2$ threshold energy. The $4\underline{p} \rightarrow 4\underline{d}$ transition lacks sufficient energy to conserve in the intermediate state. In other words, the $4p$ levels are below the threshold energy. As can be seen from the figure, "$4p_{3/2}$" peak region are pushed to the lower binding energy when CI is switched on, while "$4p_{1/2}$" peak region are spread over wide energy region, because the $4d^8 4f^{13}$ configuration overlaps in this region. This is because the $4p^5 4f^{12}$ states are split into roughly two parts: $4\underline{p}_{1/2}$ and $4\underline{p}_{3/2}$, while the $4d^8$ states are not but spread a several 10eV. The average position of $4p^5$ configuration is lower than $4d^8$. Therefore, "$4p_{1/2}$" peak region is overlapped with $4d^8$ states. By the HF calculation, it was found that both of the "$4p_{3/2}$" and "$4p_{3/2}$" regions are below the threshold for Tm^{3+} and Tm^{2+}+ ions.

4.6.Ib. TmTe, mostly divalent:

In order to study the divalent characteristic, Tm4*p* photoemission spectra are measured for TmTe. In Fig. 4.23(a), the Tm4*p* XPS measured by using Mg*K*α radiation is shown. The spectra from the oxidized and the clean samples are shown altogether. In the oxidized sample, the trivalent components are dominant because there may be present a large amount of Tm_2O_3. By comparing the spectra of the oxidized sample and the spectrum for TmS in Fig. 4.22(b), the

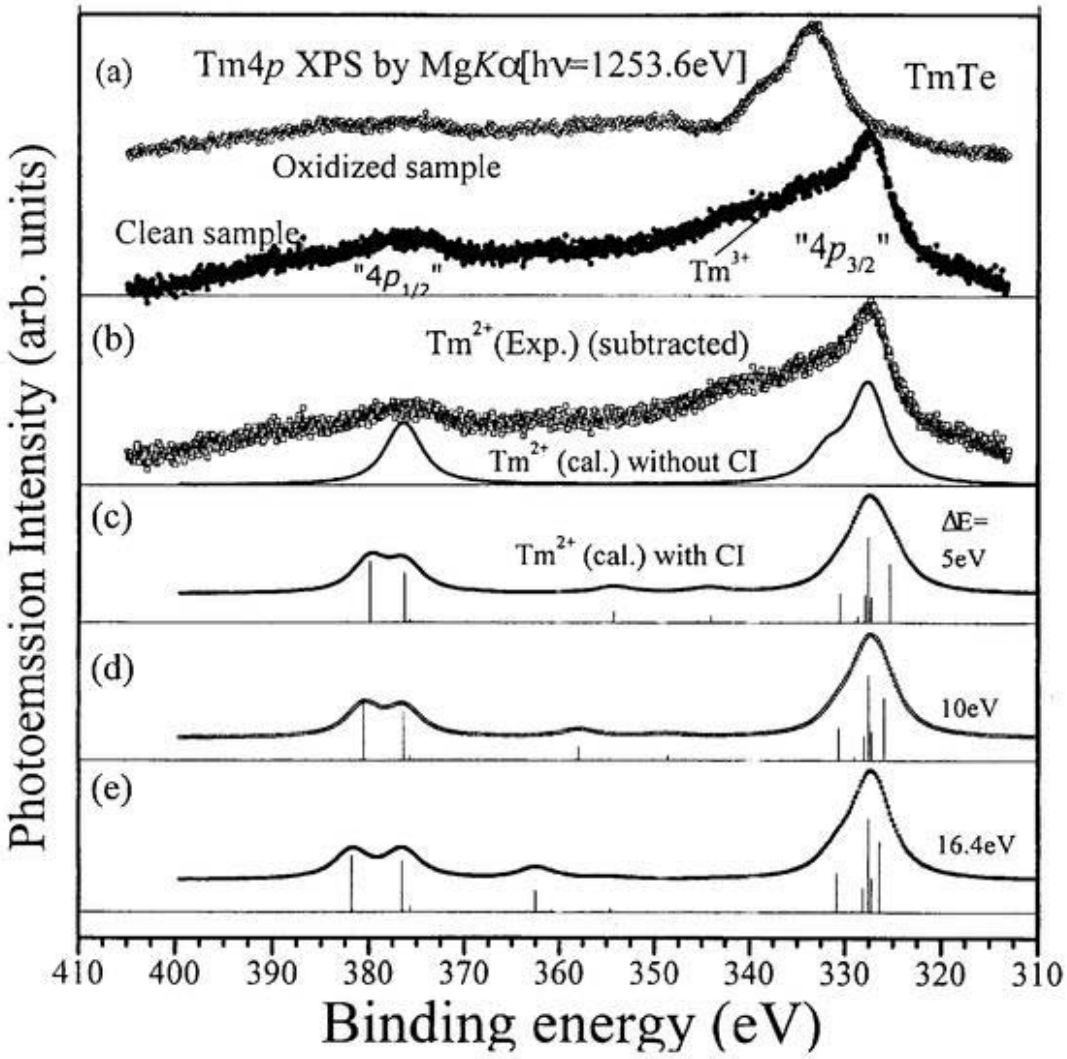

Figure 4.23. Same as TmS in Fig.4.22 but for TmTe, the mostly divalent compound.

measured spectrum for TmTe is considered to be mostly divalent, but with a small amount of trivalent component (indicated by arrows). This trivalent structure is not, of course, originating

from the oxygen induced trivalent component, but from the trivalent part from TmTe itself. The dominant peak at the binding energy of ~327.5eV represents the divalent component that is ~6.5eV lower than the trivalent peak for TmS in Fig. 4.22(a). It is noticed that the binding energy of the divalent peak around "$4p_{3/2}$" region for TmTe is in 0.5eV higher than that of divalent peak in TmS in Fig. 4.22(a) and TmSe in Fig. 4.24(a) because of the semiconducting property of TmTe.

As described for TmS, the Tm4*p* spectrum for TmTe is interpreted by considering the CI effect. The two configurations are different as the number of 4*f* electron is changed for divalent Tm. The two configurations are now $4p^5 4d^{10} 4f^{13}$ and $4p^6 4d^8 4f^{14}$. In the intermediate state of the CI, the 4*f* shell becomes fully filled which has the same configuration of Yb metal.

In Fig. 2.23 (b), the spectrum (open square) for pure divalent component in TmTe is shown after subtracting the experimental trivalent component from the spectrum in Fig. 2.22 (b). In order to subtract the trivalent component, the mean valence was assumed to be 2.05 for TmTe. The calculated spectrum (solid line) without CI is also shown in the same figure. Similar to TmS case, this calculated spectrum without CI does not represent the experimental curve. Therefore, three calculated spectra are shown in Figs. 4.23(c-e) for different values of energy separation 5, 10 and 16.4eV along with the line spectra. From the comparison with the calculation, it is therefore necessary to consider the CI effect in calculation to reproduce the spectrum. In case of TmTe, the "$4p_{1/2}$" region was found to be relatively sharper than that of TmS.

4.6.Ic. TmSe, typical intermediate:

The 4*p* XPS results for intermediate-valent compound TmSe are also discussed. Figure 4.24(a) shows the 4*p* XPS result for TmSe of the both oxidized sample and clean sample. The shoulder at binding energy of ~327eV represents the divalent component. In the spectrum for oxidized sample, almost no divalent component is present. The clean sample spectrum is considered to be a superposition of the trivalent and divalent parts with ratio Tm^{3+}: Tm^{2+} = 1:0.51. This ratio was estimated from the peak intensity (height) of the divalent (binding energy ~327eV) and trivalent (binding energy ~334eV) of "$4p_{3/2}$" region. The valence of Tm in TmSe was found to be 2.68, which was calculated from this ratio. The comparison of this

value with others values derived from the valence band photoemission, 4*d*-4*f* and 3*d*-4*f* XAS, and susceptibility measurement will be given in Sec.4.8.

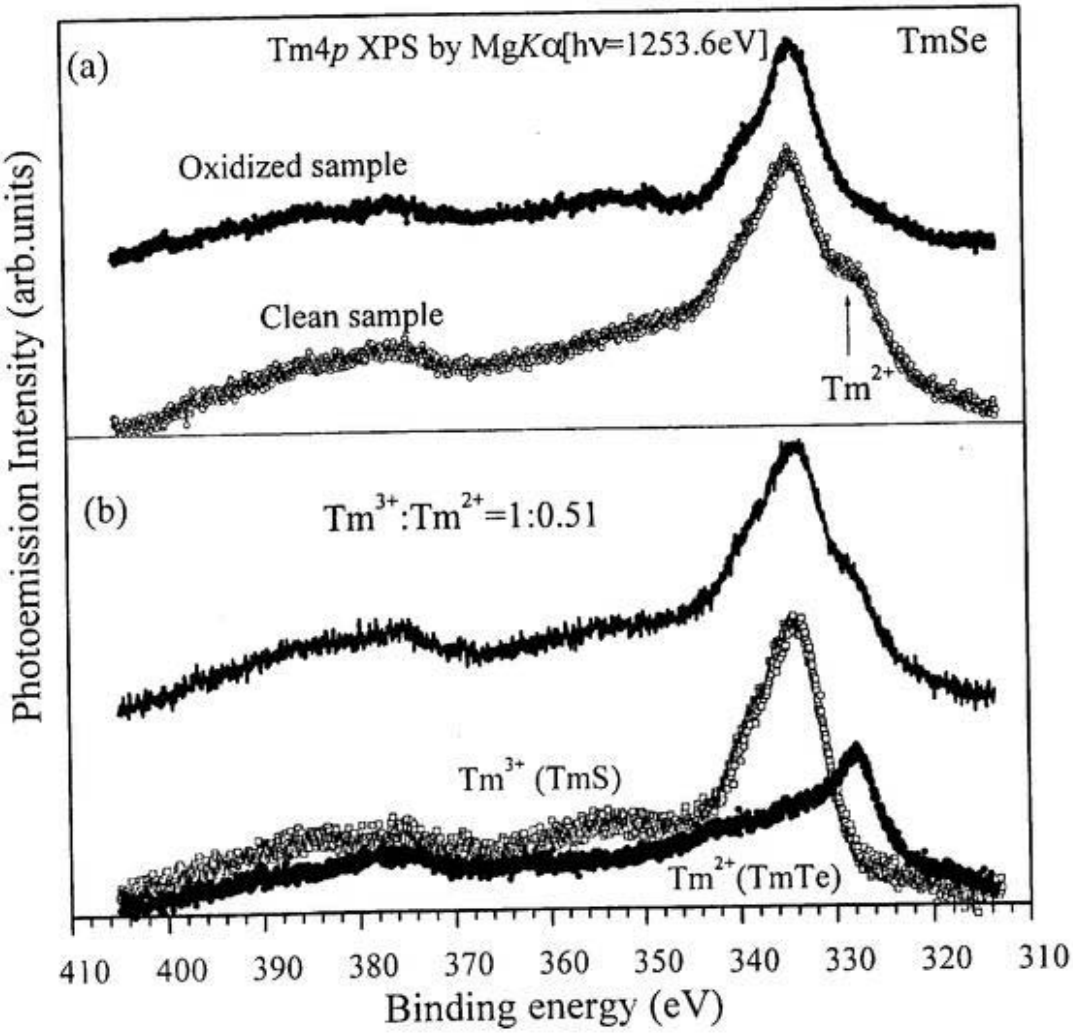

Figure 4.24. Experimental photoemission spectra for Tm4*p* core level of TmSe, the typical intermediate valent compound. In (a), the oxidized sample shows only the trivalent characteristics as TmS in Fig. 4.22(b). The spectrum (open circle) for clean sample is considered to be the superposition of the divalent and trivalent parts. The ratio, Tm^{3+}: Tm^{2+} is estimated to be1: 0.51. (b) Two spectra for TmS (solid square) and TmTe (open square) are also shown to make the intermediate valent property of TmSe clearer.

In order to make the superposition effect clearer, three different spectra are also shown in (b). In the lower panel of Fig. 4.24(b), the spectrum with open square represents Tm^{3+} (from TmS,

shown in Fig. 4.22(b)) and the spectrum with solid circle represents Tm^{2+} (from TmTe, shown in Fig. 4.23(b)). In the same figure, the spectrum (solid line) in the upper panel is the sum of those two spectra (for Tm^{3+} and Tm^{2+}) with Tm^{3+}: Tm^{2+}= 1:0.51. The spectrum derived from the experimental $Tm^{3+}$and Tm^{2+} contributions shows nearly same feature as the spectrum for TmSe given in Fig. 4.24(a). The result indicates that the core level photoemission is also important to observe the mixed-valent property. Because the difference between the lowest energy states of Tm^{2+} and Tm^{3+} is about 7eV in 4*p* XPS, the peaks at lower binding energy belonging to both components can be distinguished clearly. But in the higher binding energy region, the different muliplet peaks are overlapped and can not be distinguished so easily.

4.7. Tm3*d* core level photoemission:

Finally, the feature of Tm3*d* photoemission spectra will be described by comparing with calculation. The photoemission of the deeper 3*d* shell in the heavy rare earth elements is not usually accessible where the photon energy source is conventional Al*K*α (hν=1486.6eV) radiation. The soft x-ray synchrotron radiation beamline is thus a suitable source to measure deeper 3*d* level. The comparison with calculation will also be given.

The Tm3*d* XPS results for TmS are shown in Fig.4.25. The spectrum (solid circle) mainly

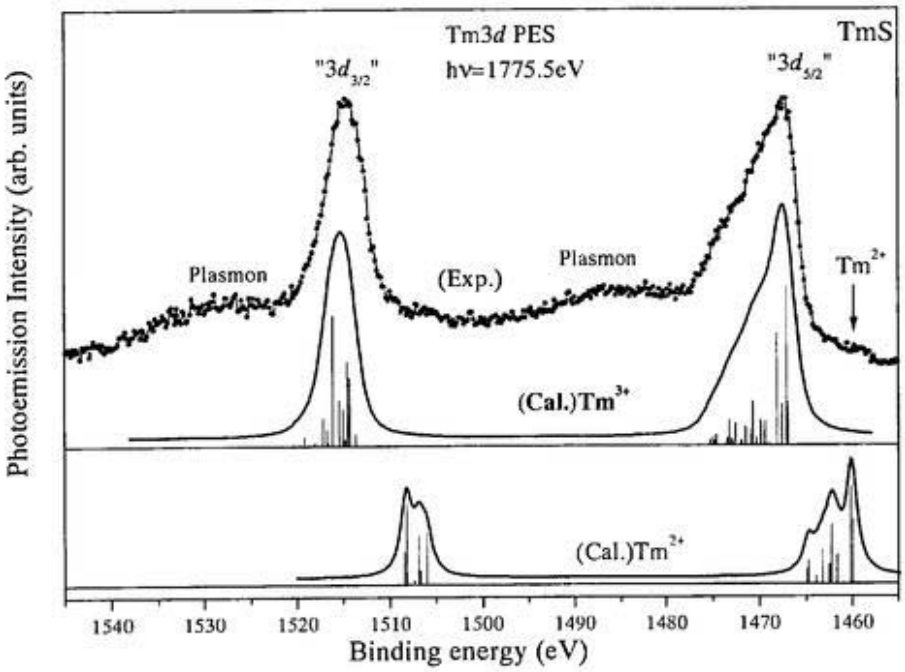

Figure 4.25. Tm3*d* photoemission result for TmS (solid circle). Solid lines show the calculation for Tm^{3+} and Tm^{2+} ions. The excitation energy was hν=1775.5eV. The experimental spectrum shows the mostly trivalent nature. The small amount of Tm^{2+} component is present as shown by arrow in the lower binding energy side. The calculated spectrum is convoluted with 0.7eV Lorentzian (HWHM) and 0.8eV Gaussian (HWHM).

shows the trivalent characteristics whereas a small amount of divalent component is also present in this spectrum, which is shown by arrow at lower binding energy side. Unfortunately,

it was not possible to measure the Tm3*d* XPS for clean TmTe and TmSe for studying the divalent characteristics. However, the binding energy position of divalent "Tm3$d_{5/2}$" peak region was successfully figured out from the spectrum for TmSe, though the sample was not completely oxygen-free. Background subtraction of the experimental curve was done by Shirley's method. The excitation photon energy was 1775.5eV. The calculation is also shown in the same figure for comparison, where the spectrum is convoluted with 0.7eV Lorentzian and 0.8eV Gaussian.

The energy separation of the two dominant peaks is about 48eV. The states around "3$d_{5/2}$" and "3$d_{3/2}$" peak regions are significantly broadened. As compared with the calculation, the origin of this broadening is the presence of the multiplet structures. This shows that the correlation between 3*d* core hole and the 4*f* shell is quite strong. However, the situation seems to be different from those of 4*d* and 4*p*. The Tm3*d* photoemission spectra are not affected so much by lifetime broadening effect. The reason is that contribution from the decay channel involving unfilled 4*f* shell, which bear the term dependent broadening, are relatively small. The calculation for Tm^{2+} is shown in the lower part. It is also noticed that multiplet peaks affect the divalent one. The spectral feature for TmS is nearly same as the previous result for metallic Tm [4.35].

4.8. Discussion of the mean valence

From the various photoemission spectra, the mean valences of three compounds are derived [4.36]. The mean valences are estimated from the intensity ratio of the divalent and trivalent part in each material. The evaluation method is described as follows. After subtracting the background for the experimental curve, the components of the divalent and the trivalent parts are separated and integrated respectively. Then the mean valence is calculated according to the following formula:

$$v = 2 + \frac{13\left(I^{3+}\right)}{12\left(I^{2+}\right) + 13\left(I^{3+}\right)},$$

where I^{3+} and I^{2+} are the integrated intensities of the Tm^{3+} and Tm^{2+} components, respectively. But the integrated intensity was not considered for core level photoemission where the multiplet peaks corresponding to Tm^{3+} and Tm^{2+} components are overlapped. In such cases, the peak intensity (height) was considered to get I^{3+} and I^{2+}. The results are tabulated in the

following table. In the table, the kinetic energy and the escape depth are shown to indicate the surface or bulk sensitivity of the specific measurement.

Table 4.1

Mean valences of TmS, TmSe and TmTe evaluated from the 4*d*-4*f* absorption (4*d*-4*f* XAS), 3*d*-4*f* absorption (3*d*-4*f* XAS), 4*f* UPS (ultraviolet photoemission spectroscopy, at hv=140eV), 4*f* XPS (at hv=1253.6eV), 4*p* and 5*p* XPS (at hv=1253.6eV) and magnetic susceptibility (χ) measurement.

Compounds	4*d* XAS	3*d* XAS	4*f* UPS	4*f* XPS	4*p* XPS	5*p* XPS	χ
TmS	2.91	2.81	2.93	2.88	-	2.80	2.799
TmSe	2.79	2.63	2.68	2.69	2.68	2.68	2.530
TmTe	2.15	-	2.35	2.05	-	-	2.017
Kinetic energy E_k (eV)	6	6	130	1250	900	1225	
Escape depth ~λ(Å)	<25	<25	5-7	14-18	9-12	14-18	

(-): Not estimated

The contributions of bulk and surface component in the tabulated values are not separated in the present experiment. Instead, it can be said that except for 4*f* UPS (at hv=140eV), all measurements are rather bulk sensitive. So the values obtained from 4*f* UPS are biased to surface one and values from other sources are biased to bulk one. Results for TmS show that several bulk sensitive experiments (except for 4*d* XAS) have lower value than that of surface sensitive one (4*f* UPS). This indicates that surface is more trivalent than the bulk one. In other word, the degree of mixed valence is higher in bulk than the surface. In Ref. 4.5, it was reported that the divalent part in TmS is located at the top most surface layer. This means the valence from the surface sensitive experiment should show lower value than those of bulk sensitive one. According to the present result, it can be said that the surface of TmS is not divalent indeed. In Ref. 4.5, the presence of divalent surface was verified by exposing oxygen on the surface. The amount of divalent was then reduced as the oxygen reacted with divalent

Tm by forming Tm_2O_2S (according to Ref.4.5) in the surface top most layer [4.5]. But, they did not indicate the thickness of the oxide layer. There are some possibilities to grow several oxide layers because the Tm compounds are very reactive to oxygen. It is therefore difficult to conclude that the surface layer is only divalent.

Now for TmSe, the obtained results from all experiments (except 4*d* XAS) are nearly the same. This indicates that the sample is homogeneously intermediate valent. But the degree of the mixed valence may be slightly different for the bulk and surface because of the larger value of valence for 4*d* XAS. But, the surface in TmSe is not only divalent as predicted in Ref. 4.5. In case of TmTe, only four values are evaluted. During the experiment, 3*d* XAS for TmTe was not able to measure. On the other hand, the exact intensity of trivalent component in core level for TmTe and TmS can not be extracted due to the overlapping nature. Among the four values, all the bulk sensitive experiments show lower values of valence whereas the surface sensitive one shows higher value. This suggests that the trivalent component is coming from the surface of TmTe. At the same time, the trivalent peak positions in 4*f* UPS, 4*f* XPS and 5*p* XPS are shifted to higher binding energy (described in sec. 4.3.I and 4.4.Ib) than those of TmSe and TmS. This shift is about 1eV. For 4*f* UPS, this is not only due to the semiconducting nature (energy gap 0.43eV) of TmTe but also the surface shift of the trivalent component. Same kind of binding energy shift of trivalent components to higher value was found in Tm (0001) and Yb(111) [4.37].

4.9. Conclusion

In this chapter, the results of photoemission spectra were discussed in different core levels for mixed valent Tm-monochalcogenides. One of the common purposes of the present core level photoemission was to study the effect of the core hole-4*f* exchange interaction on the spectral shape. Besides this exchange interaction, the configuration interaction involving the 4*f* shells and the subsequent spectral broadening due to the core hole decay, valence fluctuation and its effect on the spectra shape were also discussed. Four different core levels, namely, the shallow core level Tm5*p*, the deep core levels 4*d* and 4*p*, and the deeper core levels 3*d* were studied. Because of the same principal quantum number of 4*d*, 4*p* and 4*f* electrons, the interaction among them is relatively strong. The spectral shapes for 4*d* and 4*p* levels were changed very much due to the electron-interaction. In case of other core levels, 5*p* and 3*d*, the

interaction with 4*f* shells was not strong enough to change the spectral features so much. Though different strengths of hole-4*f* interaction were found, the evidence of the presence of the multiplet structures was observed in all core level photoemission spectra. In general, higher resolution photoemission is needed to observe many multiplet peaks. In the present experiment, the multiplet peaks in some core level spectra (5*p*) were not distinguished because of the energy resolution. But the broadened spectra feature in those cases strongly indicates the presence of multiplet structures.

Because of the mixed-valence, the different valent components are overlapped with each other with in a specific energy range for 4*d* core levels spectra and also in 5*p* with a small amount of overlapping. In order to study the different valence components, the resonant photoemission technique was applied. The valence components were thus successfully distinguished and separated by using resonance effect.

At first, the photoemission results for the shallow core level 5*p* have been shown. The results of 5*p* level are quite interesting because spectrum shows the mixed valent nature of the Tm monochalcogenides. The "$5p_{3/2}$" and "$5p_{1/2}$" peak regions contains several multiplet peaks, which are shown by line spectra in the calculation. It is also estimated the energy separation of the spin-orbit splitting by considering the intense multiplet peaks around "$5p_{3/2}$" and "$5p_{1/2}$". The values, estimated here, are more reasonable than those reported previously. The resonant photoemission of 5*p* levels around the 4*d*-4*f* excitation regions was also carried out. The resonant enhancement was found for the both divalent and trivalent components. The resonant behavior of the individual state is different depending on the excitation energy. This was shown by the experimental and calculated CIS measurement. Though 5*p* spectrum shows broad structure, but it is not so complex as 4*d* or 4*p* level.

In the Tm4*d* photoemission, the spectra for all three compounds show the complex structures. The spectral shapes were explained by considering the multiplet structures and the corresponding lifetime broadening effect. The resonant photoemission of 4*d* core level for TmS and TmSe were also carried out around the 3*d*-4*f* excitation regions. It was found that the final state multiplets of 4*d*-core level belonging to both the trivalent and divalent components strongly resonate at the 3*d*-4*f* absorption edges. The resonant behavior of 4*d*-multiplet peaks is described as the involvement of the preferential decay channel of individual excited state after the 3*d*-4*f* resonant absorption. The spectral features of 4*d* multiplet in the final state vary according to the excitation conditions and the different Tm-valences. At the same time, the

lifetime broadening phenomenon is also introduced to describe this variation of spectral shape. Both the off- and on-resonant photoemission spectra show the lifetime broadening effect depending on the multiplet structures. It was specified that the lifetime broadening of the different 4*d* states strongly alters with the binding energy by the help of resonant effect. Calculations, in which such decay processes are considered, contain the same arguments as the present experiments.

The photoemission results of another deep core level 4*p* for all three Tm-compounds have been also discussed in detail. Because of the strong correlation between the 4*p* hole and the 4*f*-shell, several multiplet peaks are appeared in the 4*p* XPS. The lifetime broadening effect in the 4*p* XPS was also discussed by introducing configuration interaction. It was shown that the broadening effect is not constant over the whole 4*p* binding energy range. The "$4p_{1/2}$" region was found to be more smeared out than the "$4p_{3/2}$". Although, it can not exclude the possibility that the "$4p_{1/2}$" regions are above the ionization threshold as the case of Xe [4.38], we have assumed both of the "$4p_{1/2}$" and "$4p_{1/2}$" regions are below the threshold according to the HF calculation. In this situation, the disappearance of the"$4p_{1/2}$" peak is due to the spread of muliplet peaks and to the large decay ratio of two 4*d* hole states which overlaps and strongly mixes with the"$4p_{1/2}$" peak. The calculated spectra, where CI effect is included, also show nearly same kind of spectral features as the experimental one.

In the Tm3*d* photoemission, a good number of multiplet peaks originating from the 3*d*-4*f* coupling were found. The "$3d_{5/2}$" and "$3d_{3/2}$" peak regions are locally broadened and are separated by spin-orbit splitting. The experimental spectrum accords well with the calculation.

Finally, estimated valences in each material were given for several electron spectroscopic measurements. The probable origin of the deviation of mean valences in different measurement was also discussed by considering the surface and bulk sensitivity of each measurement. The result shows the surface of TmS is not exactly the divalent as predicted earlier. On the other hand, result indicates that surface of TmTe has trivalent characteristics and TmSe is homogeneously intermediate valent.

References

4.1. E. Bucher, K. Andres, F. J. di Salvo, J. P. Maita, A. C. Gossard, A, S. Cooper, and G. W. Hull, Jr., Phys. Rev. B **11,** 500 (1975).

4.2. A. Berton, J. Chaussy, J. Flouquet, J. Odin, J. Peyrard, J. Holtzberg, Phys. Rev. B **31,** 4313 (1985).

4.3. J. Peyrard, J. Flouquet, P. Haen, F. Lapierre, J. Chaussy, J. Holtzberg, C. Vettier, J. Magn. Magn. Mater. **31-34,** 433 (1983).

4.4. F. Lapierre, P. Haen, B. Coqblin, M. Ribault, F. Holtzberg, Physica B, **108,** 1351 (1981).

4.5. G. Kaindl, C. Laubschat, B. Reihl, R. A. Pollak, N. Mårtensson, F. Holtzberg and D. E. Eastman; Phys. Rev. B **26**, 1713 (1982).

4.6. A. Berton, J. Chaussy, B. Cornut, J. Flouquet, J. Odin, J. Peyrard, J. Holtzberg, Phys. Rev. B **23**, 3504 (1981).

4.7. J. Flouquet, P. Haen, F. Lapierre, Y. Lassailly, C. Vettier, J. Appl. Phys. **57**, 1 (1985).

4.8. H. R. Ott, F. Hulliger, Z. Phys. B-Condensed Matter **49**, 323 (1983).

4.9. "Intermediate Valency and Heavy Fermions", by P. Wachter, in "Handbook on the Physics and Chemistry of Rare Earths", Edited by K. A. Gschneidner Jr., L. Eyring, G. H. Lander, G. R. Choppin, Vol. 19, Chap. 132, North Holland Pub. Amsterdam (1993).

4.10. R. Suryanarayana, G. Güntherodt, J. L. Frrouf, F. Holtberg, Phys. Rev. B **12**, 4215 (1975).

4.11. BIS results (by Y. Baer et. al.) is compiled at p. 70 in Ref. 9.

4.12. Y. Ufuktepe, S. Kimura, T. Kinoshita, K. G. Nath, H. Kumigashira, T. Takahashi, T. Matsumura, T. Suzuki, H. Ogasawara, A. Kotani, J. Phys. Society of Japan, **67**, 2018 (1998).

4.13. M. Campagna, E. Bucher, G. K. Wertheim, D. N. E. Buchanan, L.D. Loninotti, Phys. Rev. Lett. **32**, 885 (1974).

4.14. S. -J. Oh, J. W. Allen, I. Lindau, Phys. Rev. B **30**, 1937 (1984).

4.15. C. K. Nicklin, C. Binns, S. Mozley, C. Norris, E. Alleno, M-G. Barthes-Labrousse, G.Van der Laan: Phys. Rev. B **52**, 4815 (1995).

4.16. F. U. Hillebrecht, J. C. Fuggle, Phys. Rev. B 25, 3550 (1982).

4.17. M. Cardona, L. Ley, Photemission in solids I, Springer-Verlag (Berlin 1978), p.52.

4.18. Gaint Resonances in Atoms, Molecules and Solids, Edited. J. P. Connetade, J. M. Esteva, and R.C. Kartanak (Plenumm Press, New York 1987).

4.19. J. Sugar, Phys. Rev. B **5**, 1785 (1972).

4.20. C. Laubschat, E. Weschke, G. Kawalaski, and G. Kaindl, Phys. Scrip. **41**, 124 (1990).

4.21. Atomic subshell photoionization cross sections and asymmetry parameters: by J. J. Yeh and I. Lindau, in " Atomic Data and Nuclear Data Tables" 32, 1 (1985).

4.22. E. G. McGuire, Phys. Rev. A **9**,1840 (1974).

4.23. M. Ohono and G. Wendin, Phys. Rev.A **31**, 2318 (1985).

4.24. S. P. Kowalczyk, N. Edelstein, F. R. Mcfeely, L. Ley, D. A. Shirley, Chem. Phys. Lett. **29**, 491, (1974).

4.25. W. C. Lang, B. D. Padalia, L. M. Watson, D. J. Fabian, P. R. Norris, Faraday Discuss. Chem. Soc. **60**, 37 (1975).

4.26. J. –N. Chazalveil, M. Campagna, G. K. Wertheim, P. H. Schmidt, Solid State Commun. **19**, 725 (1976).

4.27. H. Ogasawara, A. Koatani, B. T. Thole, Phys. Rev. B **50**, 12332(1994).

4.28. D. A. Shirley, Phys. Rev B **5** , 4709 (1972).

4.29. J. W. Allen, S. -J. Oh, I. Lindau, L. I. Johansson, Phys. Rev. B **29**, 5927 (1984).

4.30. U. Becker, H. G. Kerhoff, D. W. Lindle, P.H. Kobrin, T. A. Ferret, P. A. Heimann, C.M. Trusedale and D. A. Shirley, Phys. Rev. A 34, 2858 (1986).

4.31. S. Cramm. U. Grabowski, C. Kunz, J. Schimdt-May, F. Senf and L. Incoccia, J. Electron Spectrosc. Relat. Phenom. **42**, 89(1987).

4.32. B. T. Thole, G. van der Laan, J. C. Fuggle, G. A. Sawatzky, R. C. Karnatak, J. –M. Esteva, Phys. Rev. B **32**, 5107 (1985).

4.33. G. Kaindl, W. D. Brewer, G. Kalkowski, F. Holtzberg, Phys. Rev. Lett. **51**, 2056 (1983).

4.34. T. Kinoshita, Y. Ufuktepe, K. G. Nath, S. Kimura, H. Kumigashira, T. Takahashi, T. Matsumura, T. Suzuki, H. Ogasawara, A. Kotani, J. Electron Spectrosc. Relat. Phenom. **88-91**, 377 (1998).

4.35. H. Arai, Ph.D. thesis (unpublished), Tohoku University (1987).

4.36. S. Kimura, Y. Ufuktepe, K. G. Nath, T. Kinoshita, H. Kumigashira, T. Takahashi, T. Matsumura, T. Suzuki, H. Ogasawara, A. Kotani, J. Mag. Mag. And Mat. **177-181**, 349 (1998).

4.37. M. Bodenbach, A. Höhr, C. Laubschat, G. Kaindl, M. Methfessel, Phys. Rev. B **50**, 14446 (1994).

4.38. U. Gelius, Electron Spectrosc. Relat. Phenom. **5**, 985(1974).

Chapter 5

Study of magnetic thin films (Ni/Co system and oxidized Co-film)

Related publication:

1. **Title:** **"Study of Magnetic Linear Dichroism (MLD) for different thickness of Ni-film grown on ferromagnetic Co(001) in element specific photoemission"**
   Authors: Krishna G. Nath, Y. Haruyama, S. Kimura, Y. Ufuktepe, and T. Kinoshita.
   Journal: J. Electron Spectrosc. Relat. Phenom., (in print).

5.1.a. Magnetic anisotropy in thin film

Ferromagnetic systems, both thin film and bulk, show intrinsic 'easy' and 'hard' directions of magnetization. This magnetic anisotropy is one of the important properties of the magnetic materials. The magnetic anisotropy is strongly connected to the crystalline symmetry and the shape of the samples. The orientational dependent energy of the magnetization is described by the following relation [5.1]:

$$E = -K \cos^2\theta, \tag{5.1}$$

where θ is the angle between the magnetization axis and the surface normal, K is the anisotropy constant that determines the strength of the anisotropy. According to the equation (5.1), for positive K, E takes minimum value when θ=0° or 180°. In this condition, the preferred direction of the magnetization is the perpendicular to the surface (along surface normal). The anisotropy energy K (defined per unit volume) is often called as the effective anisotropy K_{eff}, which includes every possible contribution from different sources in the magnetic system.

In the thin film and multilayer systems, the effective anisotropy K_{eff} is usually obtained from a linear relationship of the volume contributions (Kv, per unit volume) and the surface or interface contribution (Ks, per unit area). The surface or interface anisotropy was initially pointed out by Néel [5.2]. This anisotropy originates from the lowered symmetry at the surface or interface. For a thin film system with thickness t, the effective magnetic anisotropy energy is expressed by the following way [5.3]:

$$K = K_{eff} = K_V + 2K_s/t \tag{5.2}$$

Here K_s (J m^{-2}) is the difference between anisotropy of the surface or interface atoms and that of inner bulk atoms. In order to evaluate the K_{eff}, i.e., to know the easy axis of magnetization of the magnetic system, the values of K_s and K_v must be determined. The both contributions can be determined by plotting $K_{eff}.t$ (mJ/m^2) as a function of t. Figure 5.1 shows an example of such a result for Co/Pd multilayer [5.4]. As shown in the figure, the negative value of K_v favors the in plane magnetization and the positive value of K_s favors the perpendicular magnetization.

The result in Fig. 5.1 supports the usual behavior of the magnetic anisotropy and does follow the Eq. (5.1).

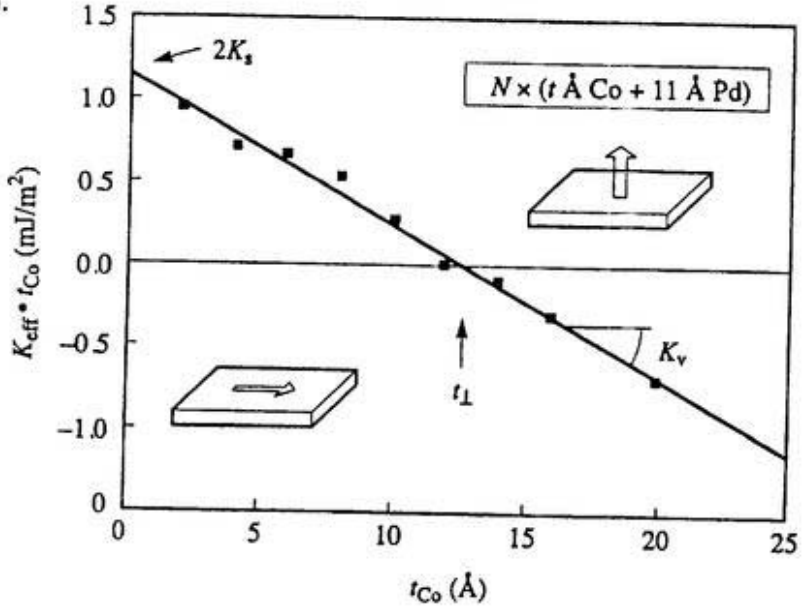

Figure 5.1. Magnetic anisotropy per unit area [$K_{eff}.t$ (mJ/m^2)] as a function of Co thickness t of Co/Pd multilayer system. Data are taken from Ref. 5.4.

The origins of the magnetic anisotropy in the magnetic systems are the magnetic dipolar anisotropy or shape anisotropy and the magnetocrystalline anisotropy. The dipolar anisotropy of the system can be described via an anisotropic demagnetization field [5.1],

$$H_d = -N M \tag{5.3}$$

Here M is the magnetization vector and N is the shape-dependent demagnetizing factor. The demagnetization field originates from the free poles during the magnetization and is proportional to the magnetic free-pole density. For a thin film system, N is zero except along the perpendicular direction [5.4]. The anisotropy energy from the demagnetizing field can be obtained from the magnetostatic energy E_d in the following way:

$$E_d = -\frac{\mu_0}{2V}\int M.H_d dv\,, \tag{5..4}$$

where μ_0 is the permeability of the vacuum. From Eq. (5.4), the following expression can be obtained:

$$E_d = \frac{\mu_0}{2}\mu_0 M_s^2 \cos^2\theta \tag{5.5}$$

Here, E_d is the contribution of the anisotropy energy per unit volume, M_s is the saturation magnetization and θ is angle between magnetization direction and the surface normal. According to the expression (5.5), this contribution favors the in plane magnetization rather than a perpendicular one.

The origin of the magnetocrystalline anisotropy is the spin-orbit interaction. The electron-spins, in a localized system, are coupled to the orbits via the spin-orbit interaction and are influenced by the crystal lattice. In any magnetic system, the energy from the total magnetic moment (spin + orbital) therefore depends on the crystal symmetry. In any low dimensional system, such as thin film system, this crystalline anisotropy yields a surface or interface anisotropy different from the bulk one.

In the thin films or multilayer systems, the magnetocrystalline and shape anisotropies are thus related to the determination of K_v and K_s contributions in Eq. (5.2). As shown in Fig. 5.1, therefore, the balance between the surface or interface and volume contributions determines the easy axis of magnetization. The usual behavior is that any thin film with very few atomic layers should show the perpendicular magnetization because K_s is dominant. For example, Fe thin film below 2.5 atomic layer of on Cu(001) shows perpendicular magnetization [5.5]. Some other systems, such as Fe/Ag(001) [5.6] and Co/Au(111) [5.7] also show the perpendicular magnetization when the thickness is very low. On the other hand, it has been reported that Ni film on Cu(001) at lower thickness shows in plane magnetization [5.8-5.10]. In order to explain this unusual behavior, another origin of the magnetic anisotropy, namely the magnetoelastic anisotropy, is also introduced [5.10].

In addition to the shape and magnetocryalline anisotropy, magnetoelastic anisotropy also contributes to the effective anisotropy (K_{eff}). Magnetoelastic anisotropy originates from the strain in the system. Strain may arise from the thermal expansion, nature of deposition process, and the lattice mismatch between the adjacent layers. Among them, the lattice mismatch is very important for thin film and multilayer systems. Depending on the order of lattice mismatch, the growth condition of any thin film is classified into two categories, (a) coherent growth with lower mismatch and constant strain (means uniform strain that does not depend on the thickness) and (b) incoherent growth with misfit dislocation and thickness-dependent strain. Thus, a critical thickness is obtained sometimes in any thin film system where the two growth modes can be distinguished around that critical thickness. In the coherent growth mode,

the anisotropy from the constant strain contributes to K_v. On the other hand, for the incoherent mode, the anisotropy from the thickness-dependent strain contributes to K_s.

In case of the Ni/Cu(001) system, around 7ML (monolayer, equal to the interlayer distance d = 1.70Å, determined from nearest neighbor distance $a_p \approx 2.51$Å), Ni film shows transition of magnetization from in-plane to perpendicular direction [5.7-5.9]. In Ref. 5.10, it was found experimentally that the value of K_s was negative (-77 μeV/atom) and K_v was positive (30 μeV/atom). The results from Ref.5.10 are shown in Fig.5.2. It was also found that Ni on Cu(001) grows in a coherent mode up to 7ML [5.10]. In the coherent region, the negative K_s is dominant. This negative and dominated K_s together with large demagnetization field keeps the magnetization (M) in the film plane. Above 7ML, K_s is affected by the thickness-dependent strain anisotropy. As a result, the influence of the negative K_s decreases with increasing thickness. In the higher thickness region, the magnetization thus shows perpendicular one because of large positive K_v. For Ni films on Cu, the presence of misfit dislocations and incoherent growth mode above 7ML was verified by the STM (scanning tunneling microscope) measurement [5.11].

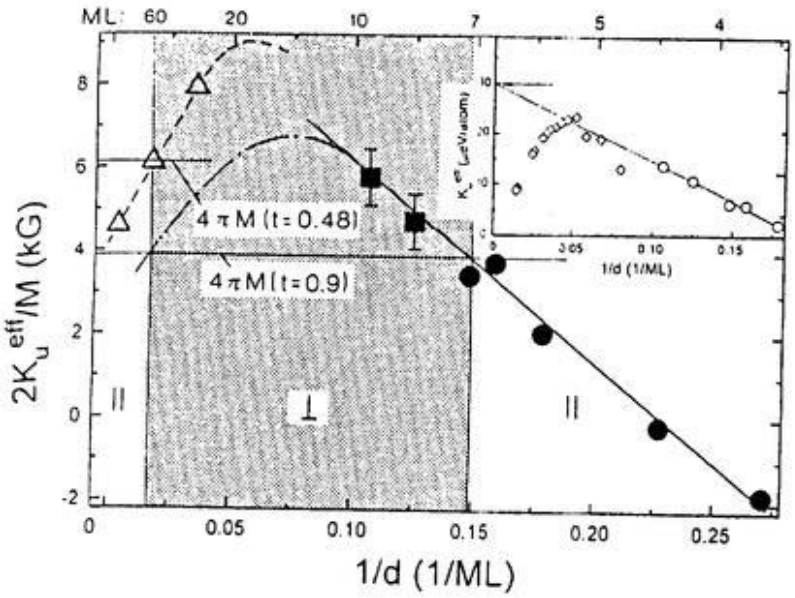

Figure 5.2. FMR (ferromagnetic resonance) result of the effective anisotropy (uniaxial) energy of Ni/Cu(001) as a function of Ni-thickness (in ML). The shaded region represents the perpendicular magnetized state and white areas represent the in plane magnetized state. The result shows the transition of magnetization from in-plane to perpendicular direction around 7ML. Data are taken from Ref. 5.10.

5.2. Ni/Co system

5.2.I. Introduction

The photoemission experiments were carried out for Ni/Co system to study magnetic properties of this thin films system. Magnetic dichroism experiment was carried out for this purpose. The specific purposes of the present dichroism study in photoemission are (a) to study the Ni 3*p*-3*d* resonance effect on the dichroism signal for valence band satellite in case of Ni thin film and (b) to find out the magnetic behaviors of Ni on ferromagnetic Co.

Dichroism experiments in photoemission for valance band satellite were previously reported by Ueda and co-workers for bulk Ni(110) sample [5.12]. They applied MLDAD (magnetic linear dichroism in angular distribution) and MCDAD (magnetic circular dichroism in angular distribution) to get dichroism for valence band satellite at Ni 3*p*-3*d* excitation energy. In Ref. 5.12, MCDAD shows prominent dichroism signal for satellite region, but MLDAD shows very week dichroism signal. No such kind of result has been reported so far for Ni thin film system. It is thus interesting to study the dichroism of the satellite in case of thin film. At the same time, it is also interesting to find out how the results from thin film differ from those of bulk samples.

It is important to mention here why the performing of MLDAD and MCDAD was not possible during this experiment in the UVSOR facility. The circularly polarized light from the helical undulator has not been allotted to the common users so far. The linearly s-polarized light, where the electric vector of the polarized light is on the horizontal plane (plane of the storage ring), is only available source for doing such kind of dichroism experiment. By using the hemispherical analyzer (installed in the 'vertical' direction) of the VG system and s-polarized light, it is rather difficult to perform the MLDAD experiment. The MLD has been chosen therefore to perform the present dichroism experiment because it is possible to follow the MLD geometry (described in chapter 2 and latter in this chapter) by using the s-polarized light and the 'vertical' analyzer. The results are also important to know the capability of the MLD for studying the thin film magnetism.

In order to grow the epitaxial Ni film, Cu(001) substrate is preferable [5.13]. Here, we have to keep in mind that Ni on Cu(001) shows a transition of magnetization from in-plan to perpendicular direction at 7ML. According to the MLD geometry and by using s-polarized light, it is possible to study only the in-plane magnetized Ni film below 7ML in the present experimental set up. In the case of Ni film of less than 7ML on Cu(001), there are some

possibilities to get Cu photoemission signal together with Ni one. Because of the same binding energy position of Ni3*d* and Cu3*d* bands, photoemission signal from Cu3*d* bands may overlap with the signal from Ni3*d* bands. Especially, the Ni 6eV satellite structures are overlapped with the tail of the broad Cu3*d* emission. The situation creates some ambiguities to find out true photoemission and dichroism signals for Ni 6eV-satellite peak as well as main peak. Instead, if different substrate is used, for example Co, then it is possible to overcome the above difficulties. In the photoemission spectra, Co does not show any signal around the Ni 6eV-satellite region.

Finally, it is very curious to study the capability of epitaxial growth of Ni on Co, the magnetic phases of Ni/Co and the interface coupling between Ni and Co. It is also technologically influential to compare the magnetic property of any uncoupled film (ferromagnetic film on non-magnetic substrate, Ni/Cu) with that of the coupled film (ferromagnetic film on magnetic substrate, Ni/Co). The Ni/Co system has not been extensively studied as done for Ni/Cu system. The MUDAD (U, unpolarized) result for Ni2*p* level for 12ML Ni on Co was reported by Schneider et al. [5.14]. In Ref. 5.14, it was found that 12ML Ni on 5ML Co substrate shows in-plane magnetization. This can be considered as a primary result of this system.

5.2.II. Growth status of Co and Ni film

The Co film on Cu(001) substrate is known to exhibit a tetragonally distorted FCC structure, known as FCT (T, tetragonal), having layer spacing of ~1.76Å for 1ML, ~1.77Å for 2ML, ~1.76Å for 3ML and ~1.73Å for 5-10ML along Cu [001] direction [5.15]. According to the preparation condition and the nature of Cu substrate in the present experiment, it was estimated that the lattice constant (vertical) of Co should have the similar value as reported in Ref. 5.15. The LEED pattern of Co-film shows p(1x1) structure. The Ni film evaporated on the FCT Co (001) also shows same LEED pattern same as Co on Cu (001). This means that the surface atomic structure of Ni on Co is same that of Co on Cu(001). In Figs. 5.3 (a-c), three LEED patterns are shown for the clean substrate Cu(001), 10ML Co on Cu(001) and 8ML Ni on Co(10ML)/Cu(001), receptively. In order to estimate the film growth structure of Ni on Co, some assumption was taken. The growth of Co film on Cu(001) is a typical example of epitaxial growth. It was experimentally confirmed that the Co-film growth on Cu shows in a nearly perfect layer by layer mode from 2ML [5.15]. Above 5ML, the electronic structure of

Co film approaches to bulk electronic structure [5.16]. The thickness of the Co film was therefore chosen 10ML to ensure that the electronic structure of Co film can be treated as bulk-like. On the other hand, Ni on Cu shows also tetragonally distorted FCC structure with vertical

(a) (b) (c)

Figure 5.3. LEED pattern for (a) Cu(001) at E_k (primary electron energy)=125eV, (b) Co(10ML)/Cu(001) at E_k=135eV, and (c) Ni(8ML)/Co(10ML)/Cu(001) at E_k=142eV.

layer spacing ≈1.70 Å (for 5-11ML) [5.13]. Because the close lateral lattice match between Co and Cu, Ni/Co(001) should exhibit similar structures to those of Ni/Cu(001). In order to take this kind of assumption, the effect of interface energies and surface free energies of Ni/Co and Ni/Cu are ignored. Evaluating of these effects, that may modify the details of growth mode, is rather complex.

5.2.III. Reference XPS spectra

Core level photoemission is known as the element specific proof to explore the components present in the system under investigation. In the thin film study, the core level photoemission can be used to identify the growth of Co and Ni film on Cu. This is also useful for a quantitative analysis of the thin film. Figure 5.4 shows some representative Cu, Co and Ni2*p* spectra in three systems; (1) Cu(001) just after the UHV cleaning process (solid circle), (2) Co(10ML)/Cu(001) after Co evaporation (open circle) and Ni(8ML)/Co(10ML)/Cu(001) after Ni evaporation (solid square). All spectra shown in Fig. 5.4 were measured by using Al$K\alpha$ radiation (hν = 1486.6eV). Because of the higher kinetic energy (KE=500-750eV) of the

photoelectrons, these core level results are considered to be relatively bulk sensitive. The inelastic mean free path (λ) at this kinetic energy range is about 10-15Å. That's why a weak

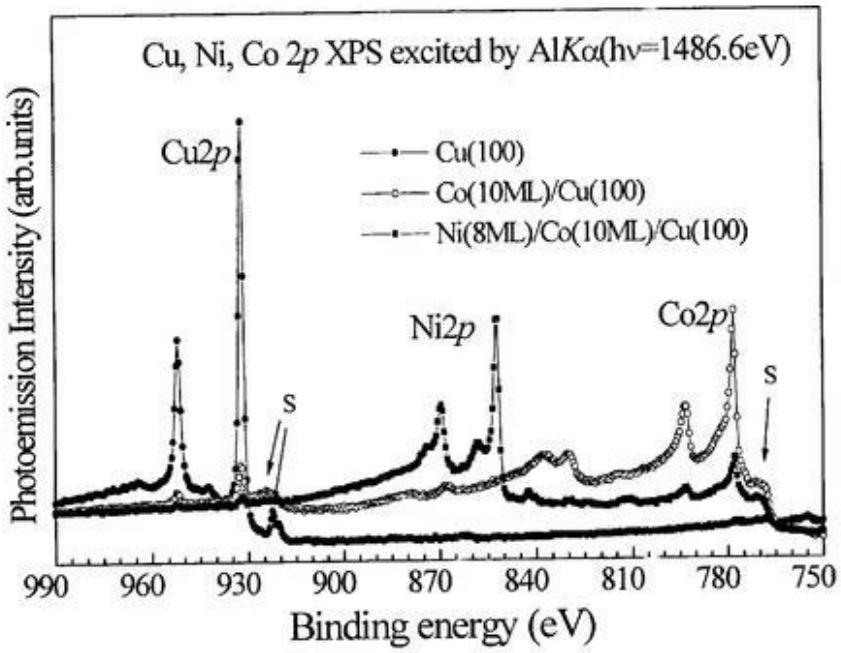

Figure 5.4. The core level photoemission spectra of Cu, Co and Ni2*p* for different system excited by Al*K*α radiation. The detection area was less than 1mm x 1mm.

Cu signal is observed for the Co(10ML)/Cu(001) system. These three spectra were also used to check the cleanness of the Cu surface after removing the previously deposited films (Ni and Co) on the same surface.

In Fig. 5.4, the additional structures at the lower binding energy side (higher kinetic energy) (labeled by "S") are identified as the peaks originating from the satellite emission of the Al*K*α line.

5.2.IV. Ni 6eV-satellite

5.2.IVa. Formation of satellite

In Ni, each core level and valence band photoemission spectra are accompanied with a prominent satellite at about 6eV larger binding energy of the main line. According to Kotani

and Toyozawa [5.17], the satellite in the open *d*-shell ions is caused by different screening channel during the photoionization. Hüfner and Wertheim [5.18] verified the formation of satellite in photoemission experiments. According to Ref. 5.17, two kinds of screening produce two different final states: $c^{-1}\ 3d^{10}\ 4s^1$ and $c^{-1}\ 3d^9\ 4s^2$ where c^{-1} is the core hole. The final state $c^{-1}3d^{10}\ 4s^1$ shows the main peak where an additional charge from the *sp* conduction band can be put in the 3*d* orbitals leading a formation of $3d^{10}$ configuration. On the other hand in the final state $c^{-1}\ 3d^9\ 4s^2$, two-hole bound state is formed where an additional charge from the *sp* conduction band can screen the two-hole state with in the wide 4*s* band. In this case, this final state shows the satellite peak. The two-hole configuration is an excited state and the excitation energy is about 6eV. In the case of valence band photoemission, the two final states are $3d^9\ 4s^1$ (main peak) and $3d^8\ 4s^2$ (satellite peak).

5.2.IVb. Resonance effect on 6eV-satellite

Around the Ni 3*p*-3*d* absorption edges, the intensity of Ni 6eV-satellite in valence band photoemission modulates depending on the incident photon energy. When the photon energy approaches near the 3*d* threshold, then the two-hole bound state is possible to form as a consequence of *CVV* super-Coster-Kronig decay process. This is written in the following way:

$$3p^6 3d^9 + h\nu_{3p} \rightarrow 3p^5 3d^{10} \rightarrow 3p^6 3d^8 + e^- \qquad (5.6)$$

(e^-: the photoelectron from *d*-level)

At the same time, at this photon energy (3*p* threshold) there is also a direct photoemission expressed by

$$3p^6 3d^9 + h\nu_{3p} \rightarrow 3p^6 3d^8 + e^- \qquad (5.7)$$

Actually, process (5.6) and (5.7) show the same final state, which is the two-hole bound state as explained in section (5.2.IVa). The two processes (5.6 and 5.7) overlap each other coherently and the final product is the resonant enhancement in the satellite intensity [5.19].

5.2.V. Schematic geometry for MLD

The geometry of the magnetic linear dichroism (MLD) experiment is shown in Fig. 5.5. The sample surface is determined to be parallel to the XY plane. Cu [100] direction is along Y-axis. The s-polarized light with electric vector (**E**) impinges on the sample surface at α=15° out of XY-plane along Y-axis. Photoelectrons are collected at θ=8° out of the sample Z-axis (see inset). The film was magnetized along X- and Y-axis. It is not confirmed about the easy magnetization direction for Ni/Co(001) system because sufficient information has not been reported about this system. But in the present study, magnetization was carried out successfully along [100] direction and was able to observe the MLD. Two spectra, $I(M_x)$ and $I(M_y)$, were recorded individually after the magnetization of the film along the X and Y-directions in the XY-plane. The dichroism signal is obtained by calculating the asymmetry; i.e. the difference between those two spectra divided by sum of them, $[I(M_x)-I(M_y)] / [I(M_x)+I(M_y)]$.

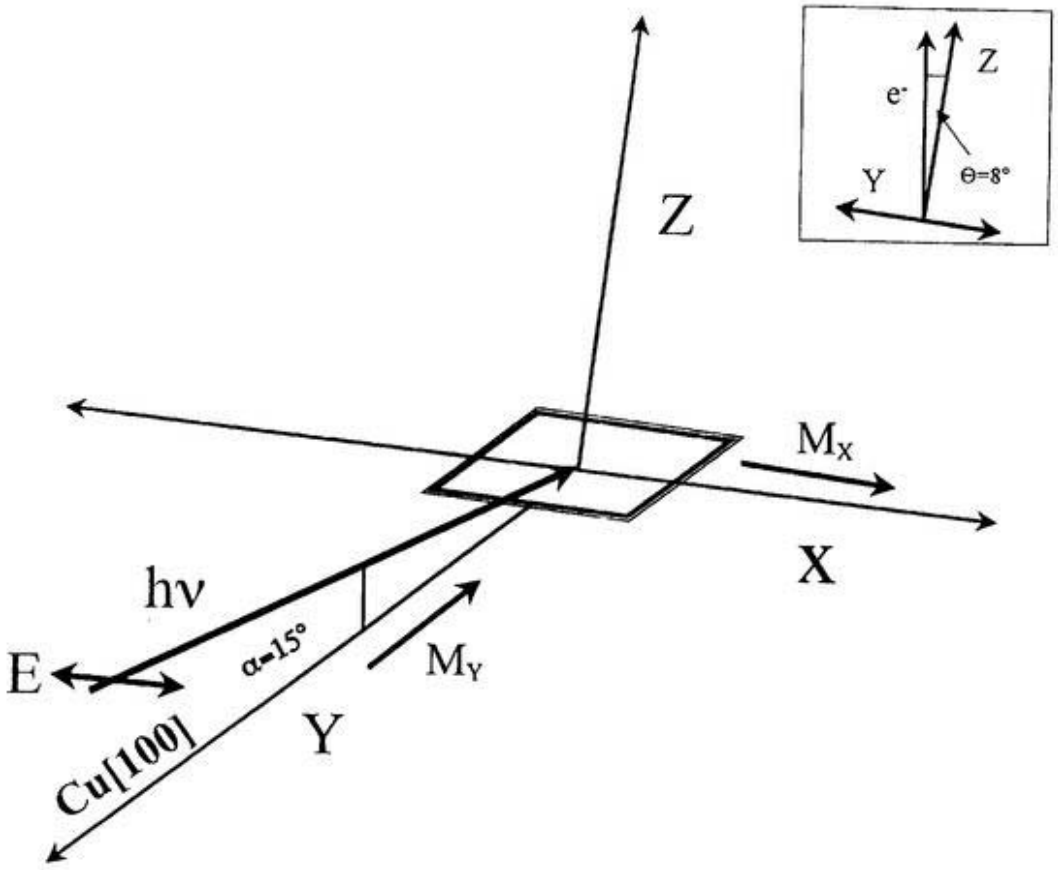

Figure 5.5. Schematic geometry of MLD used in this experiment (description is given in the text).

5.2.VI. Ni3*d* resonant photoemission spectra for different Ni-thickness

Figure 5.6(a) shows several photoemission spectra of valence band region for different thickness (n=ML) of Ni on Co(001)/Cu(001) at 3*p*-3*d* resonant condition (hv=67.2eV). In the binding energy scale, the "zero" level indicates the Fermi level. The total energy resolution at

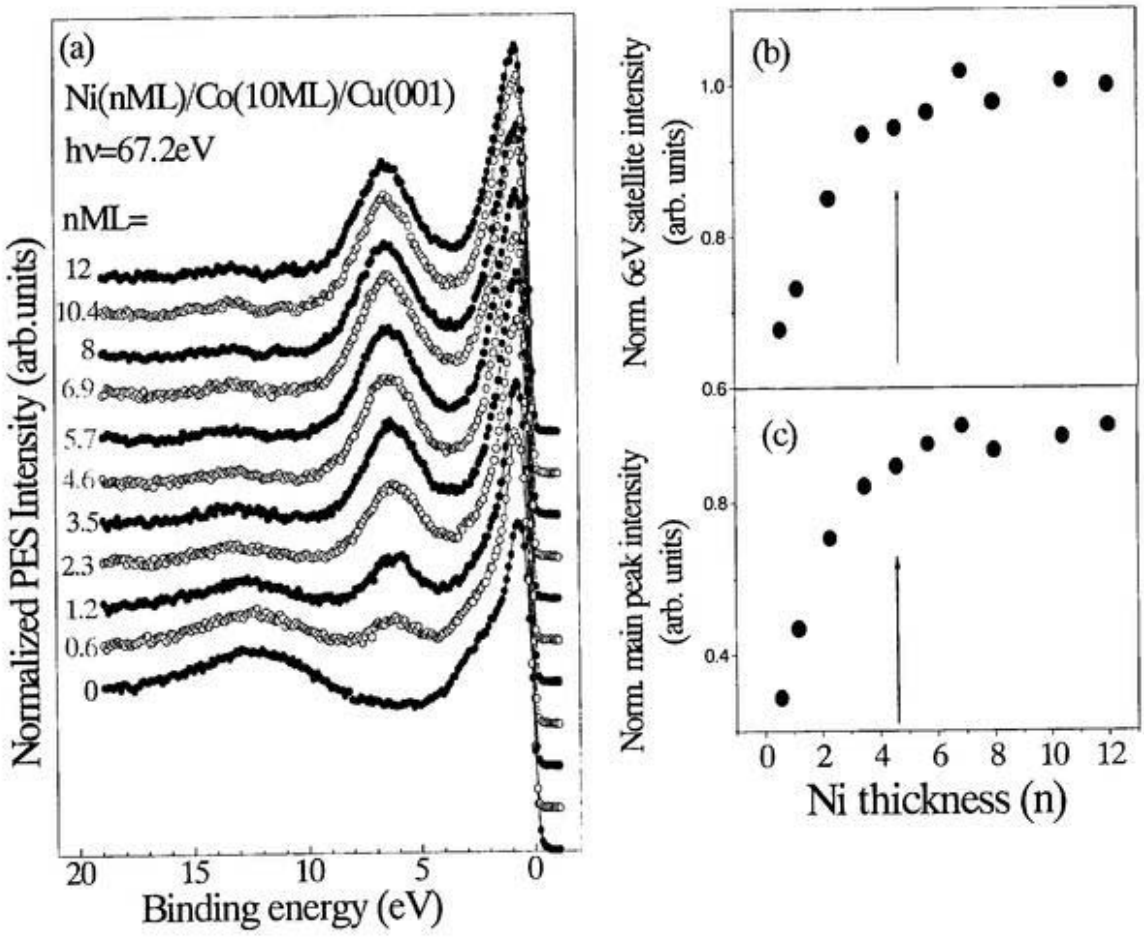

Figure 5.6. (a). Photoelectron spectra of Ni3*d* states for different thickness (n=ML) of Ni grown on Co(10ML)/Cu(001) at Ni3*p*-3*d* on resonant condition. (b) The variation of 6eV-satellite peak intensity as a function of Ni thickness. (c) Variation of intensity for the main peak.

this photon energy is about 0.3eV, which was estimated from the width of the Fermi level in the Ni valence band spectra. The photoemission spectra except for n=0 show the two dominant peaks. One is located near the Fermi level known to be as main band peak with Ni3d^9 configuration. Other peak stays at 6eV below the main peak. This is the "6eV- satellite" peak assigned as Ni3d^8 final state configuration. This satellite peak shows a strong resonant enhancement at the 3p-excitation energy that was explained via super Coster-Kronig (sCK) decay process as already explain in the previous section. From these spectra, it is clear that the 6eV-satellite emission is not overlapped with any signal from Co-site. Thus, the satellite peak can be considered as a pure element specific emission.

In Fig. 5.6(b), the variation of satellite peak intensity of different spectra in Fig. 5.6(a) is shown. The satellite intensity is normalized by the intensity of maximum thickness (n=12). As shown in the figure, the satellite peak intensity in these spectra is increased with increasing the film thickness. But at nearly 4.5ML (8Å), the intensity shows almost saturated value.

In the case of Ni3d^9 main peak, the generalization about the variation of peak intensity usually gets some ambiguities because the Ni-main peak is overlapped with Co3d band emission. In order to get the true signal of Ni, the Co signal for every spectrum in Fig. 5.6(a) was therefore subtracted by using overlayer method (described in Sec.2.6). In Fig. 5.6(c) shows the intensity variation for the main peak after normalization at n=12ML. It is clear from the figure that the main peak also shows same behavior of the variation of peak intensity as that of satellite peak. Besides, the electron mean free path with kinetic energy around 60eV is not more than 8Å. This means that the emission of Ni3d^9 main peak is considered to be nearly free from any Co signal above 4.5ML range.

5.2.VII. MLD results

5.2.VIIa. Ni3d MLD for 8ML Ni

In Figure 5.7 (a), two spectra for Ni(8ML)/Co(10ML)/Cu(001) are shown simultaneously taken at the photon energies of 67.2eV (on resonance). The two spectra represent the intensities for two different magnetized states, one is along to X-axis (full circle) and another is parallel to Y-axis (open circle). The intensity is normalized so as to obtain the same background count rates of the two spectra for the higher binding energy side. The main peak

and the satellite peak are labeled as usual. It is assumed here that no Co-emission is present in the whole energy range of photoemission as explained above. In figures 5.7(b) and (c), the expanded view of satellite region and main peak region, respectively are shown. The asymmetry i.e. the MLD ($[I(M_x)-I(M_y)] / [I(M_x)+I(M_y)]$) obtained from two different spectra signal (solid circle) is given in the same figure. The different muliplet terms in the satellite

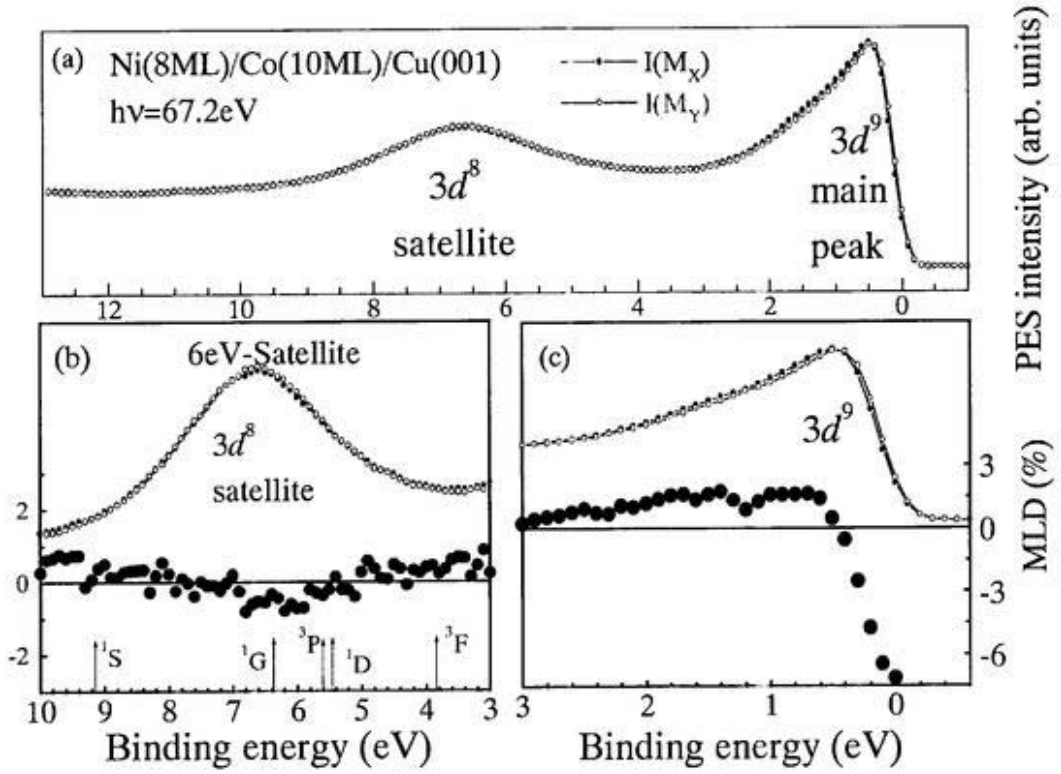

Figure 5.7. (a) Two spectra for two magnetized states (along X- and Y-axis in Fig. 5.6) for 8ML Ni on Co at Ni3*p* threshold (hν=67.2eV). (b) and (c) Expanded view of satellite and main peak region with their corresponding MLD signal (asymmetry). The position (not intensity) of different muliplet structures in the satellite region is also shown according to Ref. 5.20.

region are also shown. The binding energy positions (not the intensity) of these multiplets are indicated according to the Ref.5.20. In the bottom of figures 5.7 (b) and (c), both the satellite peak ($3d^8$) and the main peak ($3d^9$) show asymmetry (i.e., MLD) but in opposite direction to each other. In the previous study for MLDAD and MCDAD measurements for the bulk

Ni(110) sample [5.12], in the MLDAD result, the 6eV-satellite does not show any prominent dichroism signal whereas the main peak shows signal at 3*p* excitation threshold. On the other hand, the MCDAD is rather strong for both the 6eV-satellite and the main peak with opposite sign. The present result is similar to that reported MCDAD result. In the present experiment for 8ML Ni on Co, the presence of magnetic dichroism signal indicates that the Ni film on Co shows in-plane magnetization.

Though the nature of coupling between Ni and Co was not detected for 8ML Ni in the present experiment, it was assumed that the coupling might be ferromagnetic type with in-plane magnetization. This is assumed because the 10ML Co on Cu(001) also shows in-plane magnetization. Recently, the photoelectron emission microscopy (PEEM) experiment also indicates the in-plane magnetization for 8ML Ni on 15ML Co/Cu(001) and ferromagnetic coupling between Ni and Co [5.21], which supports the present results. In order to observe the coupling behavior, core level photoemission is useful, if it is possible to measure the core levels from both Ni and Co simultaneously. The thinner film fulfils this condition. The results from thinner film (n=2.3ML) will be shown later.

In Figures 5.8 (a) and (b), the MLD results for Ni(8ML)/Co(10ML)/Cu(100) taken at the

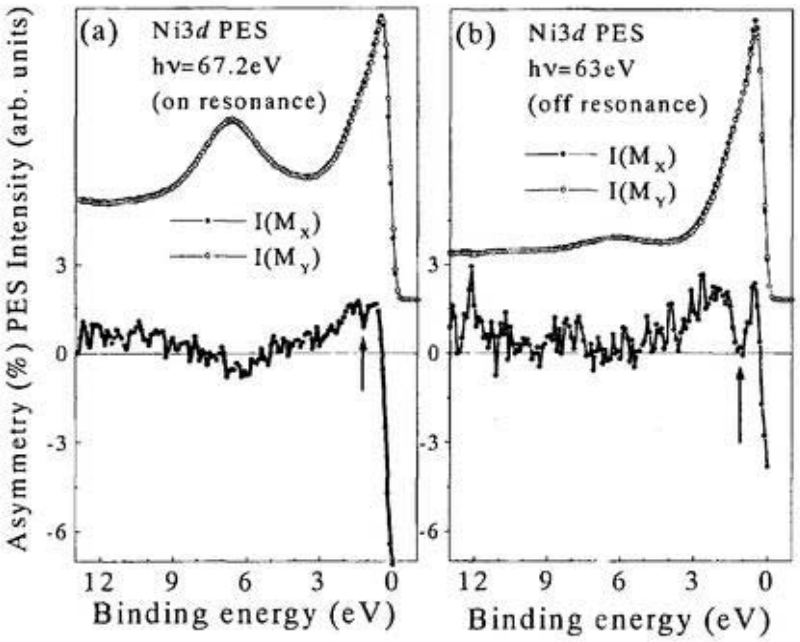

Figure 5.8. MLD results for Ni(8ML)/Co(10ML)/Cu(001) taken at the photon energies of 67.2eV (on-resonant) in (a) and 63eV (off-resonant) in (b).

photon energies of 67.2eV (on-resonant) and 63eV (off-resonant) are shown, respectively. The shape of asymmetry for the main peak is almost same for the on-resonant condition in Fig. 5.8 (a) and off-resonant condition in Fig. 5.8 (b). But the dip structure (downwards, marked by arrow) at the binding energy of ~1.2eV at off-resonant condition is stronger than that of on-resonant condition. Probably this variation may arise from the photon energy dependence from different Ni3*d* states and the corresponding polarization effect on the MD signal. The asymmetry for satellite peak at off-resonance is not so strong as the on-resonance one, although it shows the opposite trend from the main peak. It can be interpreted that the 3*d*-3*p* resonant process mainly guides intensity of the asymmetry for 6eV-satellite. The contribution of dichroism signal from different multiplet peaks (shown in Fig. 5.7) around the satellite region could not be detected in this experiment. A detailed theoretical interpretation needs for clear understanding of dichroism behavior in the satellite region.

5.2.VIIb. Ni3*d* MLD for thicker film

Ni3*d* MLD for 11ML Ni film on the same Co(001) substrate at Ni3*p*–3*d* resonant condition was also studied. The dichroism result is shown in Fig.5.9(a). This thicker film also shows

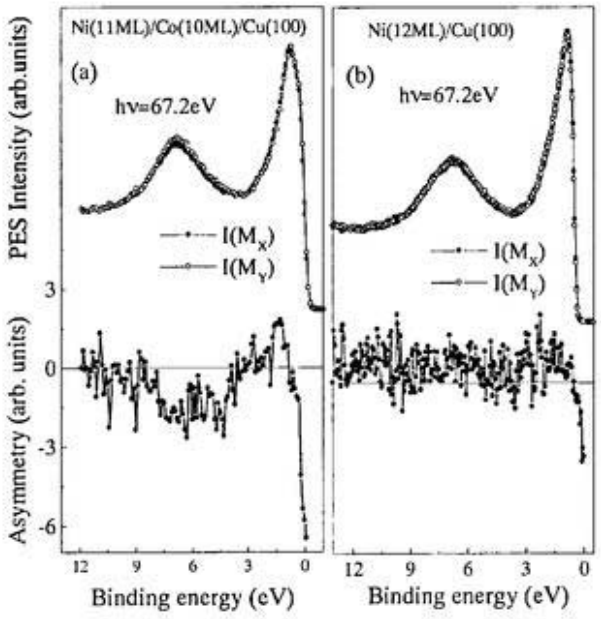

Figure 5.9. (a) MLD for 11ML Ni on Co(10ML). (b) MLD for 12 ML Ni on Cu(001).

dichroism with positive direction for main peak and negative direction for satellite peak. Though the shape of asymmetry around satellite region shows some unwanted noise structures, the negative direction of satellite MLD is apparent. It is concluded therefore that 11ML Ni film on Co(001) is ferromagnetically coupled with the Co substrate and shows in plane magnetization. But in the case of Ni film of 12 ML on Cu (001), no dichroism signal was observed for the both main peak and satellite peak under the same experimental geometry. This indicates that 12 ML Ni film on Cu does not show any in-plane magnetization that agrees with the results reported previously [5.14].

5.2.VIIc. Core level MLD (Ni3*p*, Co3*p*) for thinner film

In the case of thinner film, for example, 2.3 ML (4 Å) Ni on Co (001), the photoemission intensity of Ni3*d* states does not have saturated value. At the same time, the Ni3*d* main peak emission is not free from Co-valence band emission as shown in Fig.5.6 (a). As a result,

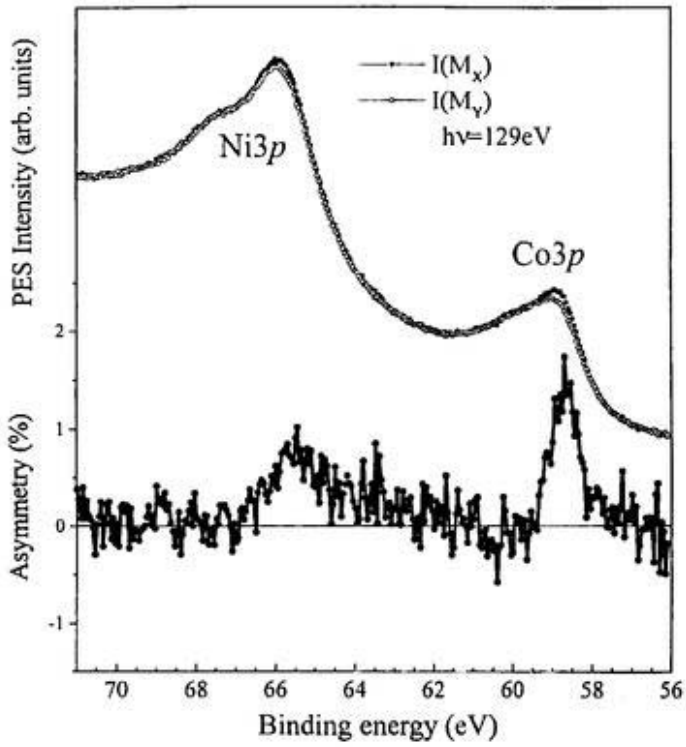

Figure 5.10. In the upper part, Ni3*p* and Co3*p* photoelectron spectra are shown for two magnetized states measured simultaneously at the same experimental geometry. The Ni-film was 2.3ML(4Å) on 10ML Co(001) substrate. The photon energy was 129eV. The lower part shows the asymmetry where the MLD sign for Ni 3*p* and Co3*p* is in the same direction.

some ambiguities are appeared to find out the true MLD signal for Ni of the main peak. It is thus difficult to study the magnetic phase of this lower thickness film by Ni3*d* MLD. The magnetic properties from this kind of multilayer system can be easily studied by the core level spectroscopy, which is considered as an element specific measurement.

In Figure 5.10, the MLD results for Ni3*p* and Co3*p* core levels are shown, which are measured simultaneously for 2.3 ML Ni-film. The experimental geometry was the same as that of Ni3*d* MLD measurement. The excitation photon energy was 129.0eV. The lower panel in this figure shows the dichroism signal (asymmetry) for the both Co and Ni. The features of dichroism signal for the both Co3*p* and Ni3*p* levels consist of a sharp positive peak at lower binding energy and a broad negative structure at the higher binding energy. The shape of Co3*p* asymmetry spectrum is nearly identical to the previous MLDAD results measured for Co-film on Cu(100) [5.22]. In the case of Ni3*p* MLD, present result is nearly similar to the experimental and calculated MCD results for the bulk Ni(110) sample reported by G. van der Laan et al.[5.23]. Besides MCD [5.23], The Ni3*p* result is also comparable with the previous MLDAD result for the same bulk sample [5.24]. The same MLD signs (positive peak at lower binding energy) for these two elements indicate that the Ni-Co interface has ferromagnetic coupling. But from this result, it was not possible to separate the individual contribution of MLD signal from Ni-surface and Ni-Co interface.

5.2.VIII. Conclusion

The magnetic properties of Ni ultrathin film of different thickness grown on ferromagnetic Co-substrate are studied by magnetic linear dichroism in element specific photoemission. It was tried to identify the nature of MLD signal for different Ni3*d* states around the Ni3*p*-3*d* resonance. The measurement shows that the dichroism signal is present for the both Ni main peak and satellite peak at on resonance condition of 8ML Ni on Co. The sign of MLD for main peak is opposite to that of satellite peak. The dichroism signal for satellite region at off-resonant condition is not so strong as that of the main peak. In practice, it is essential to measure the MLD for satellite at several photon energies around Ni 3*p*-3*d* absorption edges to get overall resonance effect on MLD. The present result reports only for two energies without comparing with calculation. However, the results clearly show that the 3*p* resonant effect is present on the MLD of the 6eV-satellite. MLD for 11ML Ni was also studied at on-resonant condition. The result shows the same MLD feature as that of 8ML Ni.

Though the electron-correlation effect is the origin of the resonant effect on satellite MLD, but the actual mechanism is not clear from this experiment. In the spin-polarized photoemission for 6eV-satellite, positive spin-polarization was found for the satellite peaks [5.25]. The spin-polarization at Ni3*p* threshold is discussed directly by the spin-interaction between the 3*p*-electrons and the 3*d*-electrons [5.25]. It was also found the evidence for Fano interference (described in Sec. 2.3, ch.2) in the spin-polarization of 6eV-satellite in the valence band photoemission for Ni(110) bulk sample [5.26]. These results indicate that the spin (of electron)-interaction has a vital role to understand various phenomena related to the satellite peaks. On the other hand, besides the bulk sample or thicker film, very thin Ni film should show different characteristics, such as low intense satellite peaks, stronger main peak etc. as the electronic structure of the thinner film is quit different. In case of film sample, the hybridization with the substrate has also some effect on the electron-interaction for Ni-film. In the present Ni-MLD experiment, it is not clear why satellite region show opposite sign of MLD that that of main peak. The results therefore need the comparison with the calculation.

In the case of 2.3ML Ni, the selection was the 3*p* core level photoemission instead of valence band emission to ensure the element specific emission. It was found from the MLD signal that Ni and Co are ferromagnetically coupled at the interface. All Ni-films studied here show in plane magnetization. Finally, it is worthily verified that the MLD is also useful to study the thin film magnetism in photoemission experiment.

5.3. Oxidized Co-film

5.3.I. Introduction

In the present section, the results of the core level (Co2*p* and O1*s*) photoemission in oxidized sample are described. The photoemission spectra of transition metal oxides (TMO) are understood on the basis of the charge transfer (CT) process [5.27,5.28] between the TM and ligand atom (O) [charge transfer from occupied adsorbate to unoccupied metal]. Transition metal compounds show diverse electrical conductivity and magnetic properties [5.28-5.31]. Although TM compounds have the unfilled 3*d* shell as the metal, some of them (NiF_2, NiO, CuO, etc) show insulating behavior and some (NiS, V_2O_3, etc) show metal-to-nonmetal transition [5.30 and references there in]. In order to solve this contradiction, Mott [5.32] and Hubbard [5.33] suggested the interatomic charge fluctuation model. The model is described as follow:

$$d_A^n d_B^m \rightarrow d_A^{n-1} d_B^{m+1}, \tag{5.7}$$

where A and B are the transition metal sites.

According to Mott and Hubbard, the energy required for the above transfer process should be less than the 3*d* bandwidth. As a result, some transition metal compounds with large *d-d* coulomb correlation energy U (U>*w*, where *w* is the 3*d* bandwidth) show no electrical conduction. These types of compounds are known to be Mott-Hubbard insulators. The Mott-Hubbard model works well for early transition metal compounds, but not for late transition metal compounds. Later, J. Zaanen, G. A. Sawatzky, J. W. Allen [5.28] gave an improved theory about the band gaps and the electronic structures of the TM compounds. The theory by J. Zaanen *et al.* includes two types of charge fluctuations. One is conventional Mott-Hubbard type fluctuation and the second one is charge transfer between the ligand state and the metal *d* level. The second process is written as follow:

$$d^n \rightarrow d^{n+1}\underline{L}\ , \tag{5.8}$$

where $\underline{L}$ denotes the hole in the anion valence band.

The typical Mott-insulators NiO and CoO have been already established to be charge-transfer insulators [5.34,5.35]. Photoemission studies from the valence band and the core levels have

been widely used to study their electronic structures. For example, Co2*p* XPS has been studied experimentally and theoretically to analyze the spectral feature and to understand the electronic structure of CoO clearly [5.29,5.34,5.36]. In the calculation, charge-transfer model was successfully used to reproduce the Co2*p* photoemission spectra [5.31,5.36].

Bulk CoO has the NaCl structure. In CoO, each transition metal cation is surrounded by the octahedron of six oxygen ions as the nearest-neighbors. The calculation of Co2*p* XPS in Ref. 5.34 has been carried out by assuming the CoO_6 structure. It has been reported that the CoO phase can be obtained by exposing O_2 on the fresh Co-surface [5.37-5.42] at certain amount of O_2-expouser. It was found in the previous experiments [5.37,5.39,5.40] that at initial stage of oxidization, oxygen absorbs dissociatively (chemisorbed state). In the next stage of oxidization with higher exposure, the formation of crystalline CoO is started. The presence of CoO phase was verified in those results by studying the Co valence band or Co2*p* XPS.

Most of the Co-oxidization studies have been done for the bulk Co, where bulk Co is stable at room temperature and shows hcp structure. In case of bulk sample, the whole oxidization process is restricted at only the hcp phase if the experiment is performed at room temperature. Instead of bulk sample, CoO phase can be obtained on the Co thin film by exposing oxygen. The crystalline Co is now possible to grow on suitable substrate, such as Cu(001) [5.15,5.39,5.42]. The electronic and magnetic properties of thin film are different from the bulk because of the reduced dimension. The reactivity to the simple molecule such as O_2 of thin film system should be different from the bulk one.

In this section, photoemission result will be applied for studying the nature of oxidization process for different thickness of Co film. The oxidization process will be studied by analyzing the modification of the shape in Co2*p*XPS spectra measured by using Mg*K*α radiation. A few results of oxidization process of the Co ultrathin film was reported previously [5.38,5.39]. But Co2*p* core level photoemission spectroscopy was not studied in those experiments. To study the Co2*p* level has some advantages over the study using Co3*p* or valence band. The advantages are follows:

1. The photoemission signal from Co2*p* can be considered to be element specific. The element specific measurement is very useful in the case of both the thinner film and thicker film. Valence band photoemission, on the other hand, is suffered from the overlapping with the substrate signal.

2. The photoemission spectra in CoO are accompanied with the correlation-induced satellite, known as charge transfer satellite. Because of the large spin-orbit splitting for Co2*p* level, these satellite structures are apparent very much in Co2*p* photoemission than those in Co3*p* or valence band photoemission.
3. As the formation of CoO is occurred during the oxidization process, the chemical shift peak Co2*p* peak and satellite structure in the Co2*p* can be used as a direct indication of the formation of CoO on Co film.

In the thin film system, the electronic structure as well as magnetic structure is changed depending on the thickness of the film. The different stages (chemisorption or formation of CoO) of oxygen reactivity on Co film are thus expected to be different depending on the Co thickness.

It is also interesting to study the oxidization effect to the magnetic properties of the thin film system. Previously, the magnetic state of Co in oxidized film was studied by spin-resolved photoemission in valence band and 3*p* level [5.39]. In Ref. 5.39, no spin-polarization was found for 14ML Co when the film is exposed with 10L O_2 (1L = 10^{-6} torr. sec). The result in Ref. 5.39 is considered to reflect the surface-sensitive information because the kinetic energy of photoelectron is about 40eV that shows the minimum mean free path in the universal curve (shown in chapter 2). Here, the result of MUDAD (magnetic dichroism in angular distribution by unpolarized light) study will be shown for the 5ML Co film after exposing different doses of oxygen on 5ML Co film. The x-ray tube (Mg$K\alpha$) was used for this purpose. The present experiment is consider to be rather bulk sensitive than that in Ref. 5.39 because of the higher kinetic energy of the photoelectrons and the results include information from both the bulk and surface.

5.3.II. Sample growth and oxidization

The Co-film on Cu(001) was prepared in the same way as already discussed in the previous section for Ni/Co system. The same VGESCALAB system was used. The rate of the Co-evaporation was 0.4ML per minute. Oxygen was introduced to inside of the analyzer chamber by a variable leak valve. The unit of exposure is in Langmuir, L (1L=10^{-6} torr. sec.). The ion gauge reading was used to check the rate of exposure. After the required exposure, the sublimation pump was flashed more than one times in order to prevent further oxidization due to the residual oxygen.

5.3.III. Results

5.3.IIIa. Oxidization of 5ML Co

In the following, the results of the oxidization process of 5ML Co film on Cu(001) are discussed. The 5ML Co film was chosen in this experiment because both the magnetic property and the electronic structure of this film are well-studied [5.40,5.41]. Here, the change in the electronic structures of Co film upon exposing oxygen was studied by Co2*p* core level photoemission spectroscopy excited by unpolarized Mg*K*α radiation (hν=1253.6eV). At the same time, O1*s* spectra were taken to study the nature of oxygen absorption for different exposures on Co. All XPS spectra were taken at room temperature and at normal emission.

Figure 5.11 shows the results of the Co2*p* photoemission spectra for different O_2-exposure.

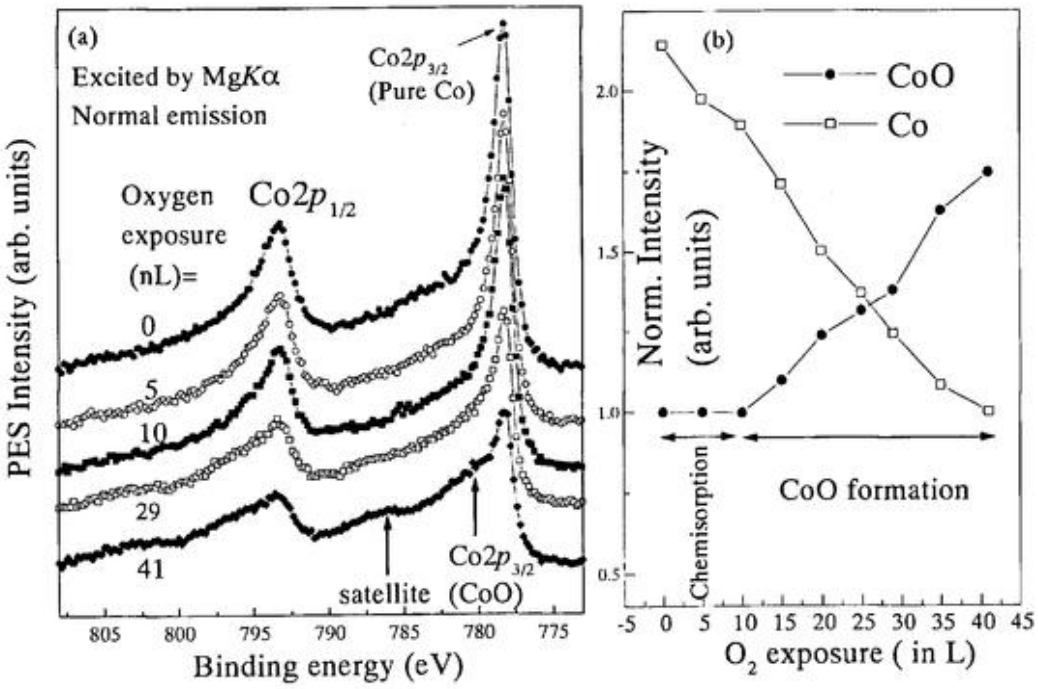

Figure 5.11. (a) Co2p XPS spectra of 5ML Co with different O_2-exposure excited by Mg*K*α radiation. At higher exposure, two peaks, the main peak at 780.2eV and the satellite peak at 786.2eV originating from CoO, are shown by arrow. (b) The variation of intensity of the both Co2p peaks for pure Co (binding energy, BE=778.2eV) and CoO (BE=780.2eV) is shown. Both intensities are normalized by the maximum intensity of Co (at 0L-exposure) and CoO (at 41L-exposure) to get the exact nature of variation (see text).

In Fig. 5.11(a), some representative Co2*p* spectra are shown. At initial stage of oxidization (>10L), the spectral features do not change so drastically. But at higher exposure (<10L), an additional Co2$p_{3/2}$ peak (at binding energy of ~780.2eV) along with charge-transfer satellite (at binding energy of ~786eV) is gradually increasing with increasing O_2-exposure. This peak originates from the CoO phase besides the Co2*p* peak of pure Co film. According to the previous results for CoO [5.34], the position of Co2$p_{3/2}$ peak of CoO phase is confirmed. The peak at binding energy 780.2eV is assigned as final state peak $d^8\underline{L}$ (L stands for ligand hole state) and the higher binding energy satellite is assigned as the final state with a mixture $d^9\underline{L}^2$ and d^7 states [5.31,5.36] on the basis of charge transfer (CT) theory. The energy separation between the main line (BE780.2eV) in CoO and the satellite line is about 6eV as shown in Fig. 5.11. This is consistent with the previous results [5.31,5.35]. This separation of satellite peak from the main one was calculated from the energy difference of the *d*-*d* electron correlation energy (U_{dd}) and the charge transfer energy (Δ) [5.31,5.35].

There are two distinct behaviors of oxidization process for Co film. According to Ref.5.39, the oxidization at initial stage (<7L) is confined in the dissociative adsorption stage, where the oxygen atoms are in chemisorbed phase with the c(2x2) surface symmetry [5.39]. It has been reported [5.39] that at this low-exposure range, some modification of valence states at surface is occurred due to the presence of oxygen. The surface sensitive measurement [5.39] of Co3*d* photoemission at hν=45eV confirmed the change in valence states. In the present experiment, which is considered to be rather bulk sensitive, no such kind of change in Co2*p* peak was found at low-exposure range. In the second stage at higher O_2-exposure, the crystalline CoO is started to form gradually with increasing the oxygen exposure. In the present experiment, the transition was found around 7-10L of oxygen exposure. The exposure region of transition is nearly same as reported previously [5.39] where the transition region was around 5-7L. The result is in accordance with the present one within experimental errors.

In Fig. 5.11 (b), the existence of the two phases is clearly shown in the curves of the normalized Co2$p_{3/2}$ peak intensity for both the pure Co (solid square) and CoO (solid circle). As it is shown in the figure, the intensity for CoO remains constant up to 10L. This means that no additional peaks at 780.2eV binding energy position was observed at this stage. But the peak intensity for the pure Co is decreased with increasing O_2-exposure. This indicates that the dissociative adsorption occurs at the lower exposure region. Above the 10L, the intensity of the Co2*p* peak for CoO is started to increase with O_2-exposure. This means the crystalline CoO

phase is started to form on the film surface with increasing exposure. At a certain stage in the higher exposure range, the oxidization gets the saturation condition (not shown here). After the exposure of 10L, the surface shows the p(1x1) symmetry. The corresponding LEED patterns will be shown later.

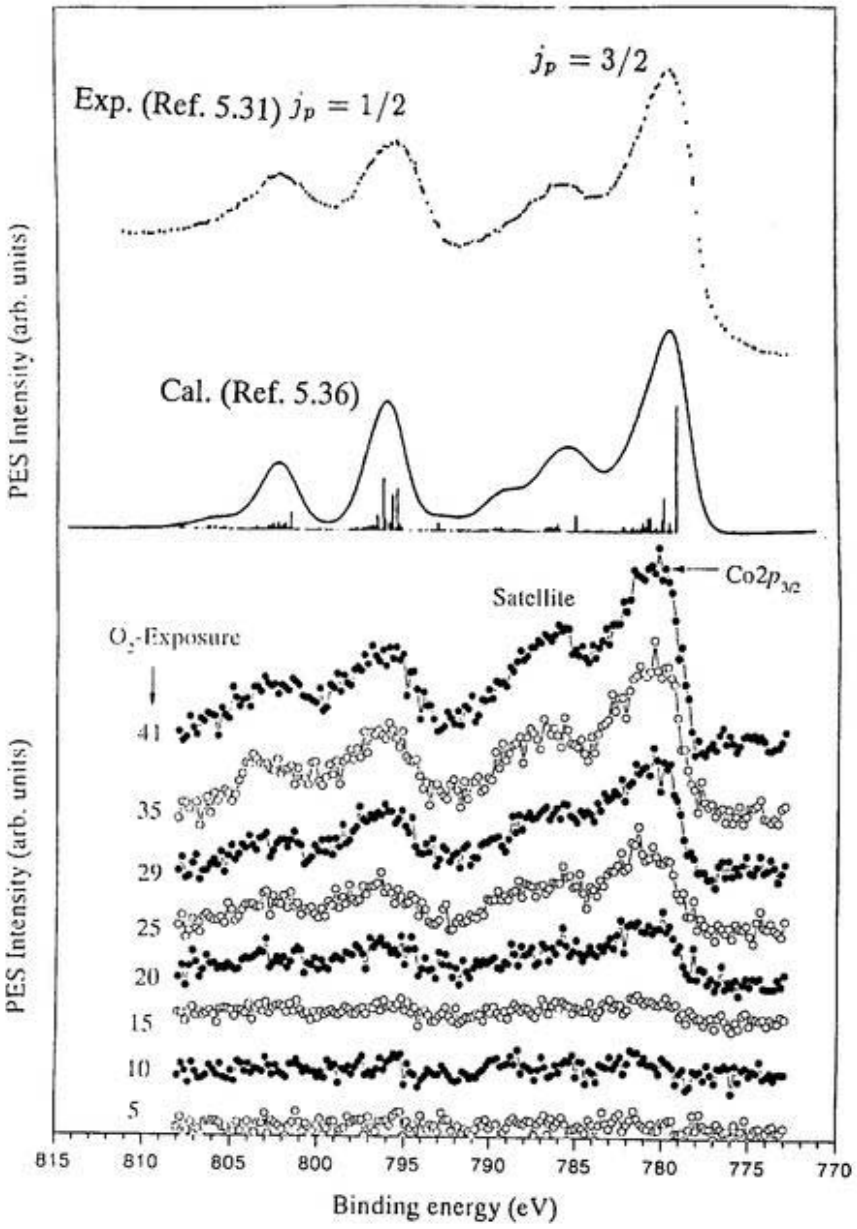

Figure 5.12. Co2*p* spectra for CoO. The spectra are extracted from the raw spectra shown in Fig. 5.11(a) (Top) Previous experimental (Ref.5.31) and calculated (Ref.5.36) results for bulk crystalline CoO. (Bottom) Contribution of CoO in the Co2*p* spectra, which are derived from the spectra in Fig. 5.11(a).

Each spectrum illustrated in Fig. 5.11(a) with O_2-exposure higher than 10L have to be considered as the superposition of two spectra, one is from the pure Co and another is from the CoO. After some normalizing procedures, the contribution of the Co was extracted. The normalization procedure is as follows. Initially, Co2$p_{3/2}$ signal from the pure Co was normalized by the maximum intensity at 0L-exposure. The normalized signals of the pure Co were subtracted from the measured spectra shown in Fig. 5.11(a) to get the signal from CoO phase. The intensity of Co2$p_{3/2}$ from CoO was then normalized by the maximum one (at 41L). The subtracted results are shown in Fig. 5.12 (bottom) together with previous experimental (Ref.5.31) and calculated (Ref.5.36) results (top) for bulk crystalline CoO.

The spectra in Fig. 5.12 show clearly that the intensity of the Co2$p_{3/2,1/2}$ main peak and satellite peak for CoO is increased with increasing oxygen exposure. Because of the high sensitivity of the core level spectrum to the chemical composition of the system, a subtle change of the charge transfer (CT) process can be detected from the CoO spectra in Fig. 5.12. The spectra in Fig.5.12 also show broadened feature for the both main peak and the satellite peak. The broadened feature indicates the existence of multiplet structure as suggested by Okada and Kotani [5.36] in their CT-M (charge transfer multiplet) model.

The transition from dissociative adsorption to CoO formation on the Co film can be identified by the results of O1*s* XPS. It was found that the binding energy of the O1*s* peak is shifted depending on the O_2-exposure [5.35]. The profile of O1*s* spectrum is also useful to find out the limit of saturation of CoO formation.

Figure 5.13 shows some of the O1*s* spectra for different oxygen coverage measured by using Al*K*α radiation (hν=1486.6eV). In Fig. 5.13, the O1*s* binding energy positions are shifted depending on the O_2-exposure. According to the Ref.5.30, the binding energy O1*s* from crystalline (stoichiometric) CoO is about 529.5eV. On the other hand, the binding energy for non-stoichiometric oxygen is considered to be 530.4eV [5.37]. In Fig. 5.13(b), the spectrum for O(25L)/Co(1ML) [the Co2*p* spectral feature for O(25L)/Co(1ML) system will be discussed latter) shows peak at about 529.6eV. From the comparison with the previous result [5.37], this means that the formation of CoO is occurred at this stage. On the other hand, the spectrum for O(103L)/Co(5ML) shows the peak shift towards a bit higher binding energy (529.75eV).

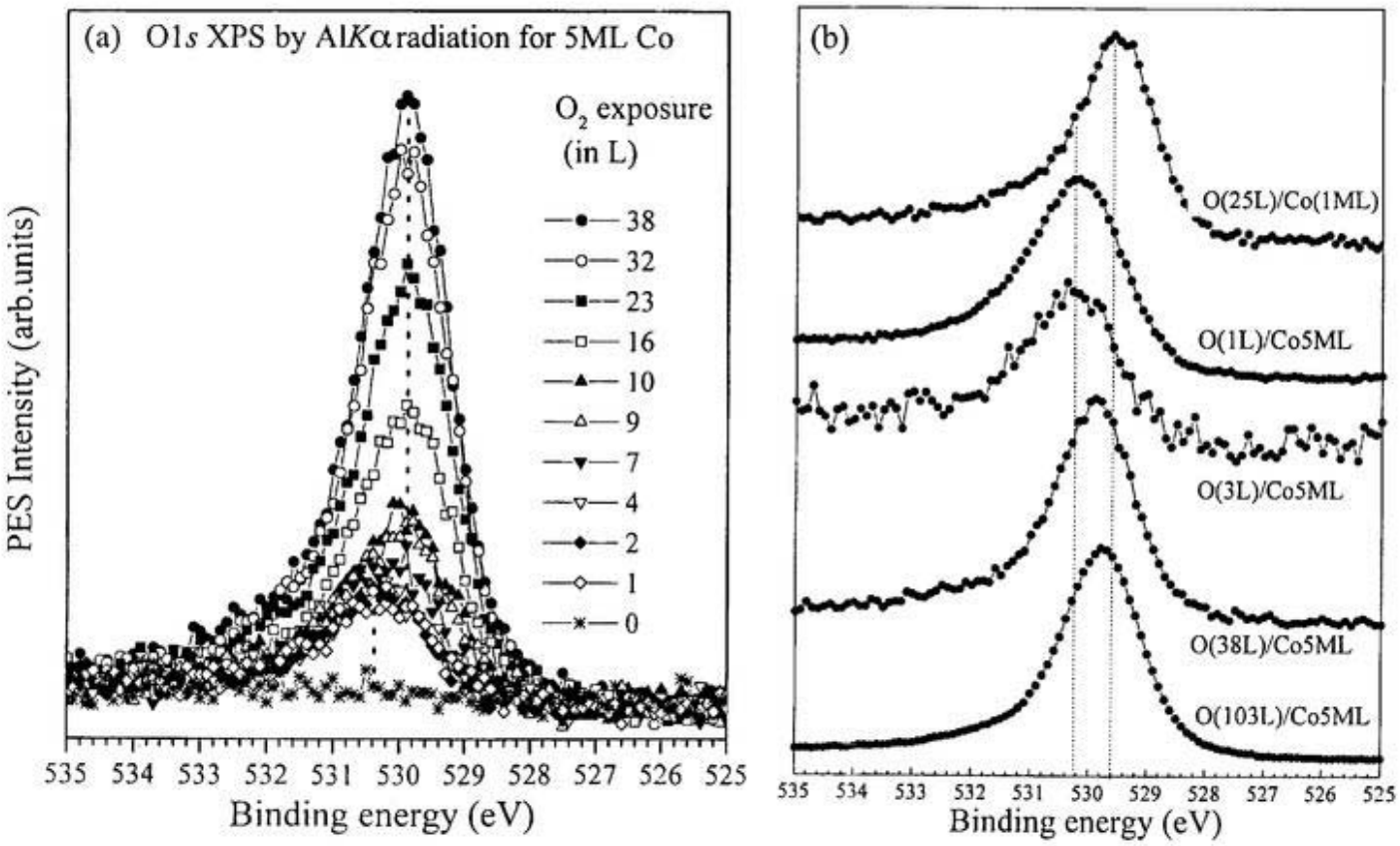

Figure 5.13. (a) O1*s* XPS spectra for different O_2-exposure on 5ML Co measured by using Al*K*α radiation. The spectra for higher exposure show binding energy shift towards lower energy sides. The shift of binding energy of O1*s* peak is clearly observed in the figure as indicated by dotted lines. It is also noticed that initial sticking rate is very high if the spectrum with '0L' exposure (star) compares with spectrum for coverage '1L' (open diamond). (b) Some of the O1*s* XPS spectra for different systems (discussed in the text), which are used to identify the crystalline and non-crystalline phases.

In the following table, the summary of the O1*s* peaks for various systems shown in Fig.5.13(b) and their assignment are given. The results from the previous experiments are also given altogether.

Table 5.1. Summary of O1*s* peaks for different systems

System	Reference	O1*s* peak (binding energy in eV)	Assignment
CoO (bulk)	[5.31]	529.5	Oxygen in crystalline CoO
CoO (after exposing bulk Co)	[5.37]	529.5	Oxygen in crystalline CoO
Co (bulk with low O_2 exposure)	[5.37]	530.4	Oxygen as chemisorbed/ Contamination
Co film (1ML) + 25L O_2-exposure	Present	529.6	Oxygen in crystalline CoO
Co film (5ML) + 1L O_2-exposure	Present	530.3	Oxygen as chemisorbed
Co film (5ML) + 3L O_2-exposure	Present	530.3	Oxygen as chemisorbed
Co film (5ML) + 38L O_2-exposure	Present	529.95	Oxygen in crystalline CoO (partly formed, unsaturated)
Co film (5ML) + 103L O_2-exposure	Present	529.75	Oxygen in crystalline CoO (nearly formed, almost saturated)

As it is shown in the table, O1*s* peak at binding energy 530.4eV and 529.5eV can be considered to be the reference values for oxygen at chemisorbed state and at crystalline CoO, respectively. By analyzing the tabulated value, it is possible to characterize the O1*s* spectra for 5ML Co given in Fig.5.13 (a). For higher O_2-exposure (>10L) in Fig. 5.13(a), the spectra show the peak at binding energy 529.95eV. As this binding energy position is higher than that (529.5eV) of crystalline CoO, it can be estimated that the corresponding CoO phase is only partially formed even for O(38L)/Co(5ML). In the lower exposure range in the same figure, the O1*s* peak position is found to be 530.4eV. This value is similar to that of chemisorbed phase

Considering the lattice constant of the bulk CoO (4.24Å) [5.37], the 41L exposure on 5ML Co film yields three to four atomic layers of CoO. In Ref.5.34, the saturation limit of the formation of Co for bulk Co was estimated to be about six to eight atomic layers of CoO. The present results shows that CoO is partly formed (not saturated) at 41L exposure. In case of 15L, the thickness is 2.0-2.5 Å, which is equal to one atomic layer of CoO. The results in Table 5.2 indicates that one atomic layer (2D) of CoO may be formed initially followed by higher thickness of CoO.

5.3.IIIb. LEED pattern

Figure 5.14 shows several LEED patterns for clean Co surface as well as oxidized Co surfaces with 3.2, 20 and 60L O_2, respectively. As it is discussed in the previous section, the

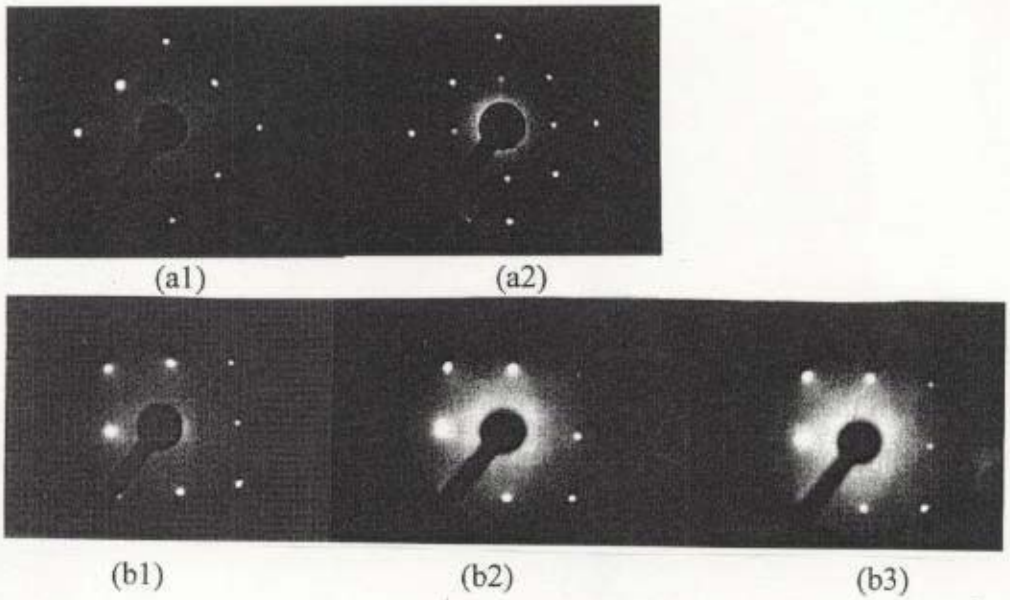

Figure 5.14. LEED patterns for O/Co/Cu(001) systems.

(a1) Co(5ML)/Cu(001) at primary electron energy E_K=121eV.

(a2) O(3.2L)/Co/Cu(001) at E_K=110eV.

(b1) Co(5ML)/Cu(001) at E_K=125eV.

(b2) O(20L)/Co(5ML)/Cu(001) at E_K=123eV.

(b3) O(60L)/Co(5ML)/Cu(001) at E_K=123eV.

given in the table. This means the oxygen with exposure less than 10L adsorb dissociatively on the Co surface, i.e., the oxygen atoms are in a chemisorbed phase on the surface.

The spectra for coverage '7L' and '9L' in Fig. 5.13(a) show some complex structure. They show a broad peak, which can be considered as the superposition of two peaks around 529.9-530.4eV binding energy. This indicates that some O1*s* components from partially formed CoO are also present along with the dissociative phase. This probably comes from the inhomogeneous nature of the Co-surface. From the comparison of relative intensity for spectra with '0L' and '1L' oxygen, it was found that the initial sticking rate was comparatively high.

In the following, the thickness of CoO crystal formed on the 5ML Co film surface is estimated for different O_2-exposure. The expression $I_n=I_o \exp(-d_n/\lambda)$ was used to estimate the thickness. Here, I_n= intensity of $Co2p_{3/2}$ for pure Co at n-exposure, I_o= initial intensity without any oxygen, d_n= thickness of overlayer (CoO), λ = attenuation length of photoelectron (taken from the universal curve for the electron kinetic energy 473eV). It should be noted that the values would be used only for rough estimation because of some ambiguities. The sources of these ambiguities are the difficulties to select the constant background for all the spectra and the estimation of exact photoelectron escape depth in the present experiment. In the above expression of I_n, to determine the λ, two values are considered at kinetic energy 473eV to compensate the effect of width (band) in the universal curve. The values are 9 Å (minimum) and 11 Å (maximum). Two values of thickness are therefore extracted that can be used for estimation of probable error.

Table 5.2. Estimated CoO thickness for various O_2-exposure on 5ML Co film

Oxygen-exposure (in L)	41	35	29	25	20	15	10	5
Overlayer (CoO) thickness (in Å)	6.9-8.3	6.1-7.5	4.9-6	4.0-5	3.2-3.9	2.0-2.5	1.1-1.4	0.7-0.9

structure in chemisorbed surface has c(2x2) symmetry that counterparts to the LEED pattern in Fig. 5.14(a2) for 3.2L coverage. The LEED patterns in (b2) and (b3) for CoO phase on Cu show the p(1x1) symmetry.

5.3.IIIc. Co-thickness dependence oxidization

The oxidization was also carried out in order to study the nature of oxygen reactivity depending on the thickness of the Co film. Figure 5.15 shows the results from this experiment.

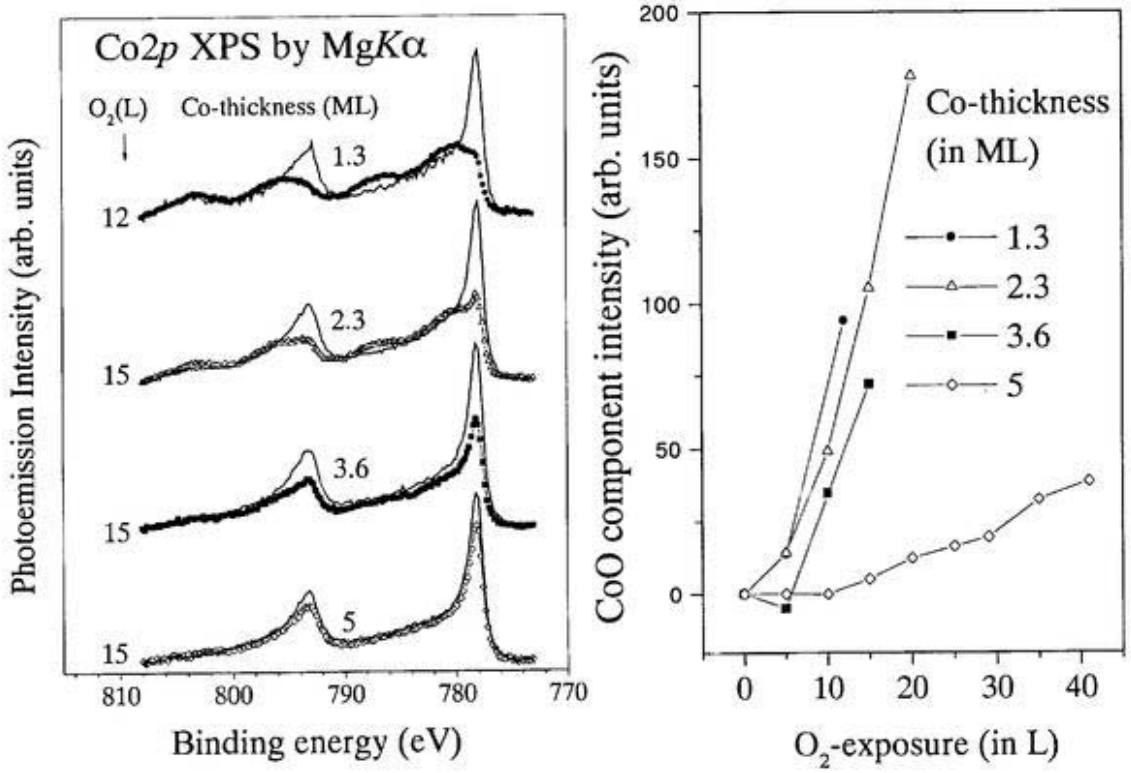

Figure 5.15. (a) Co2*p* XPS spectra for 1.3 (solid circles), 2.3 (up triangles), 3.6 (solid squares) and 5 ML (open squares) Co film with O_2-exposure 12, 15,15 and15L, respectively. With every spectrum for oxidized sample, an additional spectrum of clean Co film (solid line) is given for comparison. (b) Change of normalized intensity of the Co2$p_{3/2}$ peak (BE780.2eV) originating from CoO for the four different thickness of Co film as a function of O_2-exposure.

In Fig.5.15(a), for four different sets of two Co2*p* spectra for Co(1.3ML) and O(12L)/Co(1.3ML), Co(2.3ML) and O(15L)/Co(2.3ML), Co(3.6ML) and O(15L)/Co(3.6ML), Co(5ML) and O(15L)/Co(5ML), respectively are shown. Spectra for clean samples in Fig. 5.15(a) are shown by solid lines. Here, the study was concentrated only to observe the early oxidization process rather than to find out saturation condition.

The result in Fig. 5.15 (a) clearly shows that the oxidization process depends on the film thickness. The 1.3 ML Co-film at 12L-exposure shows strong peaks around 780.2eV binding energy (main) and 786.2eV binding energy (satellite) that originates from the CoO. The intensity of this peak is gradually decreasing with increasing the Co-thickness. For example, even with higher O_2-coverage (here 15L), the spectrum for 2.3ML Co does not show the same intensity of the CoO component that for 1.3ML Co. This oxidization behavior is clearly shown in Fig. 5.15 (b). In this figure, the normalized (by the same way as done for 5ML Co in Fig.5.11) intensity of the CoO component for the Co2$p_{3/2}$ peak is shown. The result is different from the previous result [5.37]. In Ref. 5.38, the behavior of oxidization process for different thickness [n(ML)= 0.4, 0.7, 1.3, 8-10] Co film was reported. In the case of 1.3, 3 and 8-10ML Co in Ref.5.38, it is concluded that the early oxidization does not depend on the Co thickness. In the Fig. 5.15, the results from Ref.5.38 are shown.

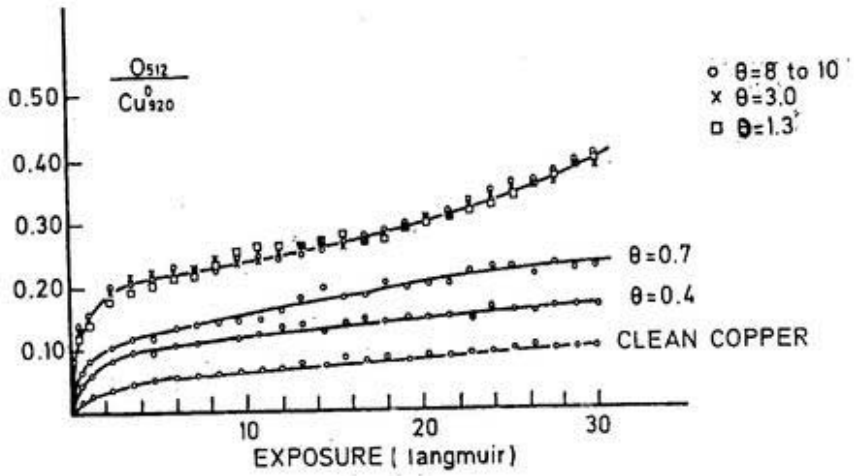

Figure 5.16. Peak-to-peak intensity of the oxygen *KLL* Auger transition versus oxygen exposure for different Co thickness. Data are taken from Ref. 5.38. The result indicates that the oxygen absorption does not depend on the Co thickness (θ, ML) as the curves for θ =1.3,3 and 8-10ML are superimposed.

The probable reasons of this difference of the present result from the previous one are listed below.

1. In the present experiment, the variation of oxidization process was derived from the analyzing of the photoemission intensity for CoO component. As no CoO component is present at the chemisorbed state, the curves in Fig.5.11(b) and Fig.5.15 (b) for CoO component should be considered as a direct indication of different adsorption stages of oxygen. On the other hand in Ref. 5.38, the characterization of oxygen adsorption was done by using fixed value of oxygen *KLL* Auger peak (512eV) and Cu *LMM* Auger peak (920eV). As they did not consider the effect on peak energy shift upon formation of CoO, their result might be modified to some extent. As a result, small amount of chemical change on the surface was probably ignored. In the present experiment, however, it was possible to detect even a subtle change that was already shown in Fig.5.12 for CoO contribution (also in table 5.2) for 5ML Co film.
2. Another possible reason may be the condition of thin film growth in Ref. 5.38. It is now well established that Co on Cu(001) shows p(1x1) symmetry [5.15]. In Ref.5.36, it was reported that Co on Cu(001) shows a c(2x2) symmetry. There were some possibilities to have some oxygen on the Cu substrate prior to the Co deposition. During the deposition, the oxygen was transferred to the Co surface. Therefore, oxidization was done in Ref. 5.38 on the reconstructed c(2x2) surface, not on the p(1x1) fresh Co surface.
3. Final reason is connected to condition of the introducing the oxygen inside the chamber. There might be some variations of estimating the amount of exposure if the oxygen partial pressure is not kept in similar range in different experiment.

On the other hand, the saturation limit of CoO formation in the present experiment depends on the Co thickness. The result is similar to the previous result [5.38]. Figure 5.17 shows the saturated Co2*p* photoemission spectra of CoO for 1ML and 5ML Co films. In Fig. 5.17, though the spectrum (solid circles) for O(103L)/Co(5ML) is overlapped with the contribution of pure Co, it is considered to be a saturated spectrum as no additional intensity changes upon exposing more oxygen. In the middle, the spectrum was derived from the upper spectrum (solid circles) by subtracting the contribution of pure Co. The thickness of CoO for 5ML Co film was found to be 12.4-15.2Å, which was estimated by the same way as it was

done in Sec. 5.6.IIIa. The value for saturated CoO in Ref.5.36 is also similar to this value. In the bottom of Fig.5.17, the spectrum for 1ML Co with 25L oxygen exposure also shows nearly similar feature as that of the middle spectrum and is also considered to be the saturated one. The results from Fig.5.17 show that the saturation condition of CoO formation is Co thickness dependent.

Though the two spectra (middle and bottom) are nearly same to each other, there are some differences around the main peak (BE780.2eV) and the satellite peak (BE786.2eV). For example, both the main peak and the satellite peak for the spectrum (middle) of 5ML Co are relatively sharper than those of 1ML Co film with 25L-O_2. It is assumed that the difference has come from the variation of site symmetry in these two cases. This will be discussed in Sec.5.3.IIId.

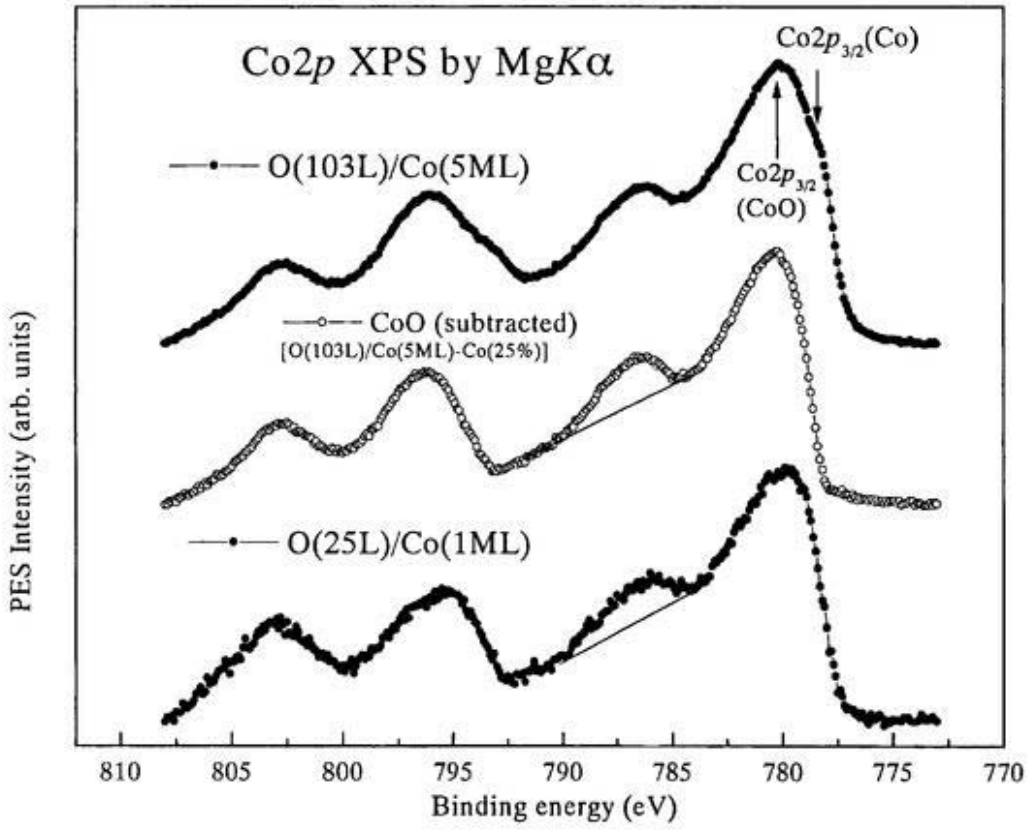

Figure 5.17. Co2*p* photoemission spectra of saturated CoO phases. (Top) Spectrum (solid circles) for O(103L)/Co(5ML)]. In this spectrum, some contribution of pure Co is overlapped. (Middle) Spectrum (open circles) for the contribution of CoO, derived from the upper spectrum by subtracting the contribution of Co. (Bottom) Spectrum (solid circles) for O(25L)/Co(1ML). No signal from pure Co is present in this spectrum.

5.3.IIId. Two-dimensional (2D) CoO phase for 1ML Co

It is rather difficult to estimate the exact thickness of CoO in the 1ML Co film at the saturated condition. Though it has been believed that Co grows on Cu(001) in a perfect layer-by-layer mode [5.14], the nature of first ML growth is not ideal layer-by-layer one. By x-ray photoelectron diffraction experiment [5.42], it was reported that the surface consists of 2ML-high islands for the first monolayer deposition. It was also reported [5.43] by STM experiment that the thickness of the most islands is one monolayer up to 0.3 monolayer. Upon deposition of additional Co, some of the first monolayer islands grow in size, and before becoming the complete first monolayer, growth of the second monolayer becomes significant. In such a case, the first monolayer does not form a complete coverage on the substrate. Instead, the 1ML film consists of ~10% 2ML islands, ~60% 1ML islands and ~30% uncovered Cu surface. The size of the islands also depends on the time of deposition [5.42].

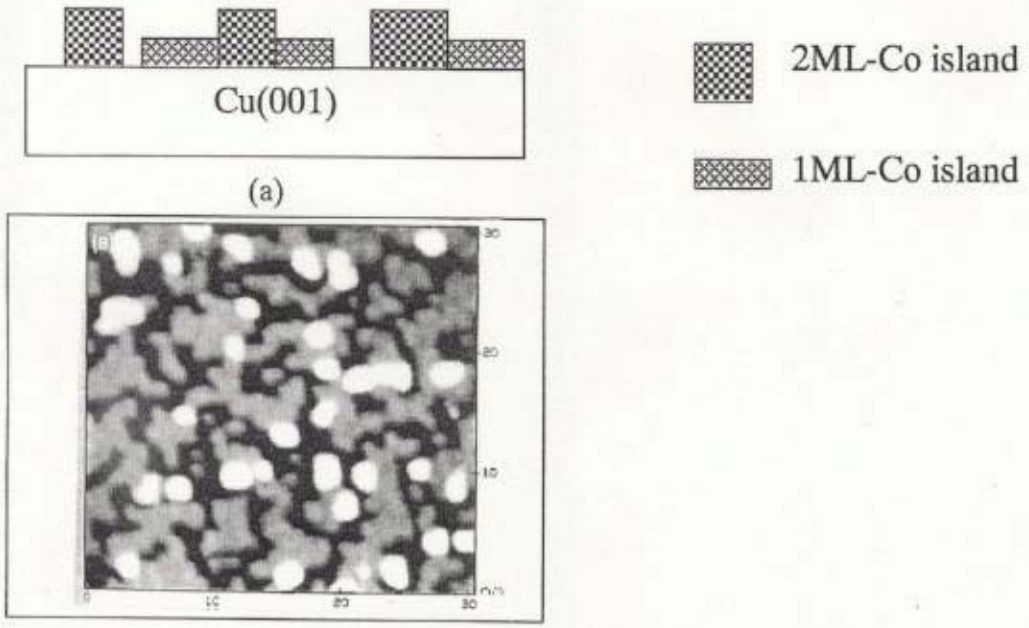

Figure 5.18. (a) The surface structure of 1ML Co film in this experiment, which is assumed by comparing with the previous result. (b) STM image of 1ML Co film [4.43]. The white, grey, and black areas represent the 2ML-high islands, 1ML-high islands, and uncovered Cu surface regions, respectively.

Therefore, the 1ML Co film can be considered to be granular with islands of nanometer diameter, which are separated by uncovered Cu surface regions. The probable structure (schematic with side view) of 1ML Co film is shown in Fig. 5.18. The 1ML film in this experiment is thus considered to be a structure of some 1ML-high and 2ML-high islands with some uncovered area as shown in Fig. 5.18(a). The STM result from Ref. 5.43 is also shown in Fig. 5.18(b) for comparison.

For formation of CoO phase on 1ML Co-film, three separate cases can be considered. They are shown in Fig. 5.19 (a-c) and discussed in the following:

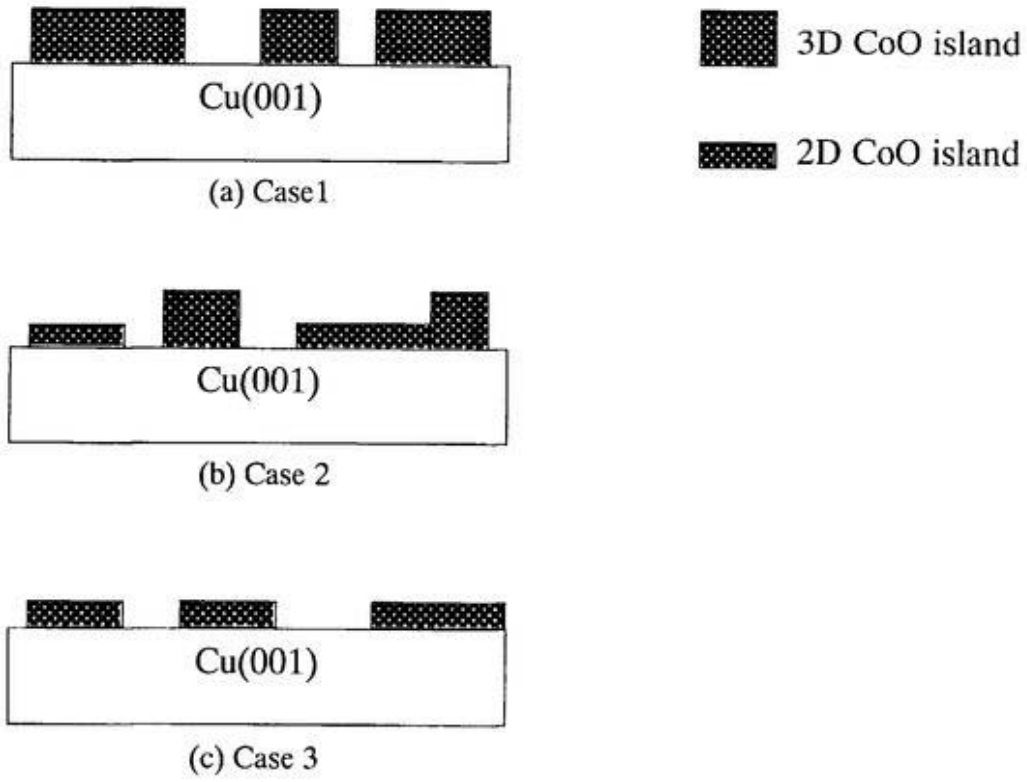

Figure 5.19. Three proposed cases of CoO formation for 1ML Co film.

Case 1: Three-dimensional (3D) CoO islands are formed. Due to the strong Co-O bonding, 1ML Co islands is changed into 3D CoO phase. Therefore, no 2D CoO phase is present on the surface.

Case 2: Both 3D and 2D CoO islands are formed on the surface while keeping the uncovered Cu-surface as usual. The 2D CoO phase is formed in the region of 1ML Co on the surface.

Case 3: Only 2D CoO phase is formed. In this case, it is assumed that oxygen releases its energy for reconstruction of 1ML island on the surface and the saturated 2D CoO phase is formed.

Among the three cases, the 'Case1' may be not the real situation if we analyze the Co2*p* spectra in Fig. 5.17. Both spectra (middle one for 5ML Co and bottom one for 1ML Co) represent the nearly saturated CoO phase. This was already verified in Fig. 5.13 (b) and in the Table 5.1. But the spectral features of these two spectra are not exactly similar. It is expected that another structure of CoO phase different from 5ML Co is present in oxidized 1ML Co film. In Fig. 5.17, the broad and more flat structures in the satellite and also in the main peak indicate that there may exist some mixing of multiplet structures originating from different or multi-phases of CoO. If there is no mixing of multiplet structures, then the CoO phase on 1ML Co is considered to different from 5ML case. Therefore, 'Case2' and/or 'Case3' are more favorable. This means some different structure other than the CoO_6 one (CoO_6 structure represents the bulk or 3D situation) is also present in 1ML Co film after oxidization. In order to reproduce calculation for the Co2*p* spectra in such a system with 2D CoO phase, it is urged here that the planar CoO_4 model may be appropriate.

For the results given in Fig. 5.17, some additional discussion is given here. It is well known that the electronic structure in the thin film of monolayer range (<2ML) is different than that in the thicker film or bulk system [5.16]. The simple interpretation is that the reduced co-ordination number in the system (for example 1ML of Co film) results in narrowing of the *d*-band. This narrowing causes a redistribution of the charges in the upper and lower part of the *d*-band [5.44]. It was predicted by R. Miranda et al. [5.45] that for 2.1 Al (atomic layer) of Co on Cu(001), the overall localized *d*-states might be increased due to the band narrowing. According to Ref. 5.45, the situation of the *d*-band is that the band is accompanied with more *d*-electrons with respect to the *s*-electrons than the bulk and less *d*-holes at the Fermi level. The self-consistent theoretical calculations for unsupported monolayer of Fe, Co and Ni [5.46] and Ni on Cu(001) [5.47] also suggest that the number of *d*-electron in the monolayer is larger than

in the bulk. The effect of the *d-d* interaction in photoemission for a monolayer film is therefore expected to be different.

In the Cu2*p* core level photoemission spectra for CuO (with d^9-electrons) and Cu_2O (with d^{10}-electrons), it was found that the former one show relatively stronger satellite peaks than in the latter one [5.48]. In case of Cu_2O, the feature of the satellite structure is relatively broad. As the charge transfer process is the origin of the satellite peaks in the transition metal compounds, the system with less populated d^9-electrons must have large populated charge transfer from the neighboring oxygen atoms. This will provides strong satellite feature in the photoemission spectra.

Now for the results in Fig. 5.17, it can be said that 1ML Co might have more *d*-electrons that in the 5ML Co (according to Ref. 5.45). Therefore, the spectrum for 1ML Co is accompanied with less-populated charge transfer from the neighboring oxygen atoms. As a result, the spectrum for 1ML Co shows relatively weak satellite peak than that for 5ML Co. Together with this argument, different phases of CoO in 1ML oxidized Co film are also responsible for the broadening of the satellite structure.

5.IV. Magnetism of oxidized Co film

The magnetic properties of the oxidized Co(5ML) film was also studied by using magnetic dichroism experiment. As already discussed in the chapter 2, the magnetic linear dichroism (MLD) in angular distribution (AD) experiment is also possible to perform by using unpolarized light. The result from this experiment will be used to reveal the unaffected magnetic state in the oxidized thin film. In the previous experiment [5.39] where surface sensitive spin-polarized photoemission measurement was carried out to study the magnetic behavior of oxidized film, O(10L)/Co did not show any ferromagnetic property. The present

result will show the existence of ferromagnetic state of oxidized Co film even at higher oxygen exposure.

In Fig.5.20, the geometry of MUDAD experiment is shown. The light is coming at an angle 55° out of normal axis. The sample was rotated about 6° around X-axis along Y-axis. This means that photoelectrons coming out at an angle 6° out of Y-axis are detected as shown in inset. In this condition, the MUDAD signal was found to be maximum (in this experiment and also in previous result with 8° [5.49]) due to the photoelectron diffraction effect. The sample is magnetized along the Cu[110] direction which is the easy magnetization direction of Co-thin film system [5.50]. The electric vector of the unpolarized light is considered as an incoherent superposition of E_1 and (E_2+E_3) components. E_1 is parallel to the [110] parallel to the [110]

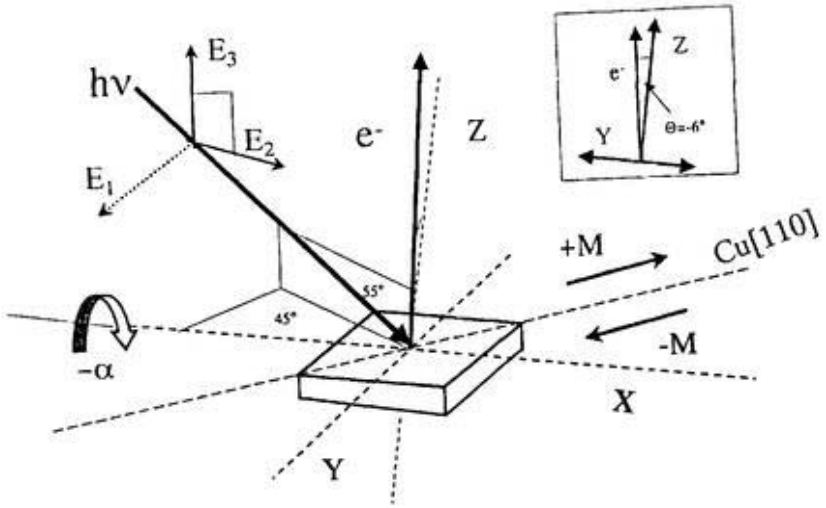

Figure 5.20. The experimental geometry of MUDAD. The detailed description of this geometry is given in the text. The directions of M+ and M- are shown along [110] direction.

direction and it has no contribution to the dichroism signal upon reversing the magnetic field. The resulting electric vector component form E_2 and E_3 will actually contribute to the dichroism signal. But, the maximum signal will be smaller of factor 2 than the usual MLDAD signal. Figures 5.21 (a-d) show the MLDAD result for different systems. In each figure, two photoemission spectra (in upper panel) were taken for two opposite magnetization directions, M+ (solid circle) and M- (open circle). Two spectra show different profile both in the intensity

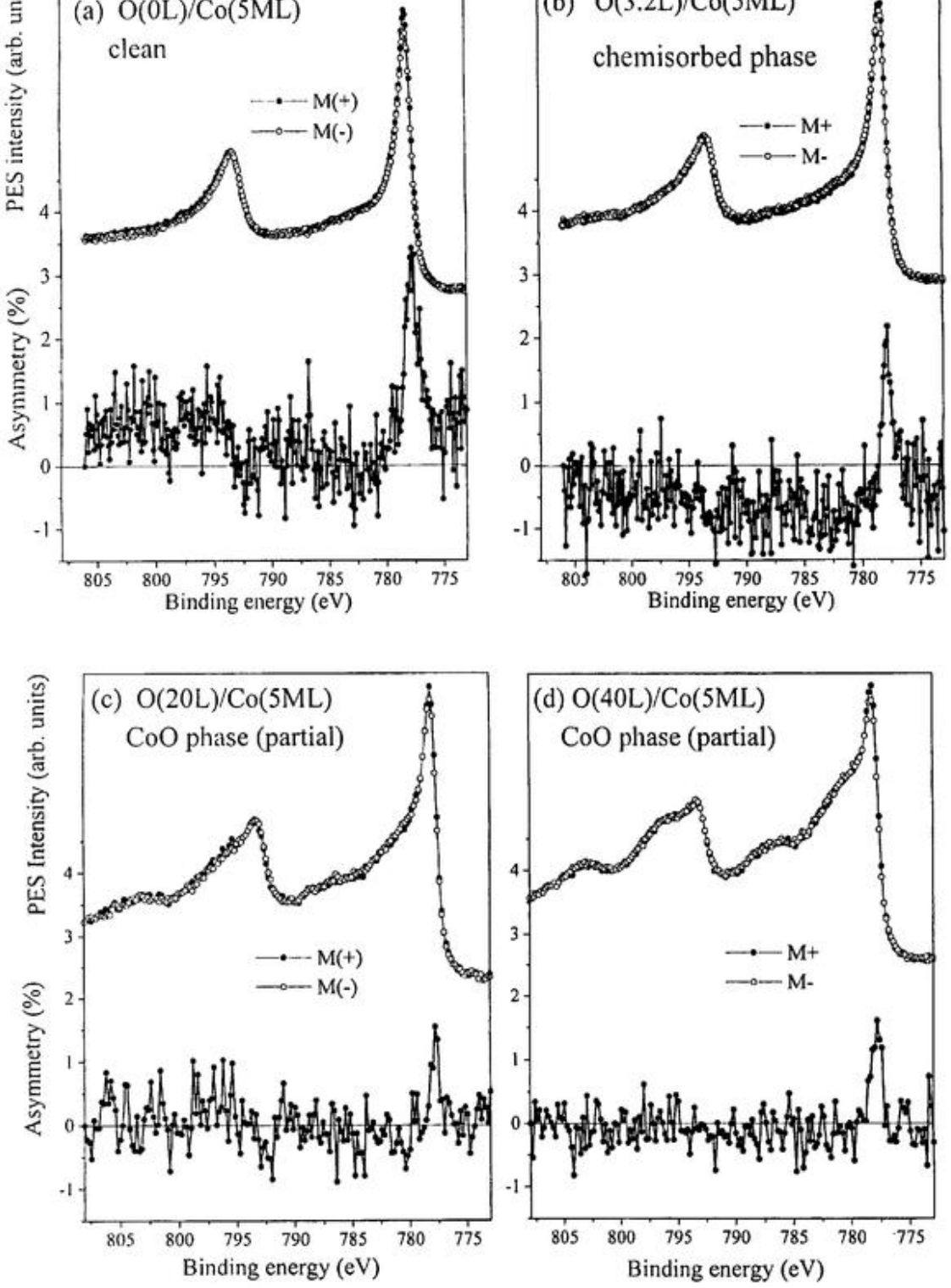

Figure 5.21. MUDAD results in Co2*p* photoemission spectra excited by Mg*K*α line for clean Co 5ML film in (a), O(3.2L)/Co(5ML) in (b), O(20L)/Co(5ML) in (c) and O(40L)/Co(5ML) in (d), respectively are shown. In each figure (upper panel), two spectra were taken for M+ (solid circle) and M- (open circle). The asymmetry is shown in lower panel of each figure.

and the energy position from each other. In the bottom, the dichroism signal is shown that is referred as asymmetry i.e. the difference of the intensity of the two spectra divided by their sum. The asymmetry is then shows a plus-minus shape for Co2$p_{3/2}$ and minus-plus shape for Co2$p_{1/2}$. Fig. 5.20 (a) shows the dichroism results for clean Co film. In order to check the effect of chemisorbed oxygen and the paramagnetic CoO phase on Co-film, MUDAD results for O(3.2L)/Co(001), O(20L)/Co(001), O(40L)/Co(001) systems are shown in Figs. 5.21 (b-d), respectively. As all the photoemission spectra were taken at zero magnetic field, the effect of the magnetic field of the sample is neglected.

In case of both the clean Co and O(3.2L)/Co, the feature of the asymmetry curve remains same but slightly reduces in intensity for O(3.2L)/Co because the magnetic state changes on the surface. Turning to the CoO phase (partial), both the spectra in (c) for 20L and in (d) for 40L also show dichroism signal, but weak. The present result differs from the previous result [5.39], where 14 ML Co film with 10L oxygen did not show any spin-polarization signal for the valence band. The present result can be compared with another spin-polarized photoemission experiment [5.51] for hcp Co film on W(110), which is rather bulk sensitive. In Ref. 5.51, Co film with 40L oxygen also shows spin-polarization in valence band. So, on the basis of the present result and the previous bulk-sensitive result [5.51], the following two possibilities depicted in Fig. 5.21 can be proposed to estimate the origin of the dichroism signal for higher oxygen coverage.

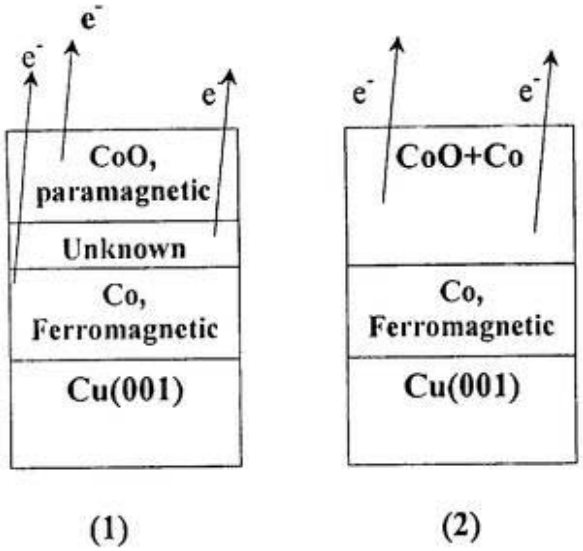

Figure 5.21. The two possibilities are proposed to explain the origin of MUDAD signal in Fig. 5.19 (c) and (d).

In case (1), photoelectrons for pure Co are considered to be originating from the unaffected bulk Co-site and also from the interface of Co and CoO layer. CoO has paramagnetic state at room temperature with T_N=290K. But the nature of interface is unknown. For case (2), photoelectrons may be coming only from the surface where some Co is still unaffected. But after comparing with the previous surface sensitive result [5.39], it can be said that surface is not the origin of the dichroism signal any more. On the other hand, the kinetic energy of photoelectron in this experiment is around 480eV. The electron escape depth is about 9-11Å, which indicates the bulk sensitivity of this experiment rather than the previous one. So, the first assumption is more favorable for the present result. This discussion reveals that, in Ref. 5.39, they actually did not find the any spin-polarization near the surface region. Information from the bulk was not included in their results. This may be the difference with the present experiment.

5.3.V. Conclusion

The above experiment showed the spectral variation of core level photoemission spectra as a function of both the oxygen exposure and Co-thickness on Cu(001). It was found that the Co2*p* core level was very useful to study the oxidization process. As the change of the electron-correlated structure, such as satellite peaks, multiplet structures are very clear, the experiment is considered to be a direct proof for the study of the oxidization. Both the main peak for Co in CoO and the charge transfer satellite showed the pure element specific signal.

It was found that the oxidization stages are different depending on the Co-thickness. Both the early oxidization and the saturation limit depend on the Co-thickness. Thinner films are more reactive and show an early formation of CoO than that of thicker film. It can be predicted that the narrowing of the *d*-band with increasing the density of states around the Fermi level may be the origin of the early formation of CoO in thinner film. The result indicates that there are some possibilities to grow the 2D CoO in the 1ML Co film together with 3D CoO phase. On the basis of the present result, it is urged that planar type CoO_4 structure may be appropriate to reproduce the Co2*p* photoemission spectra for 2D CoO phase. In order to get the clear picture of the local structures of oxidized 1ML Co film, it is therefore necessary to perform some different measurements, such as STM (scanning tunneling microscope), photoelectron spectromicroscopy with higher lateral resolution.

References

5.1. W. J. M. de Jonge, P. J. H. Bloemen, F. J. A. den Broeder in "Ultrathin magnetic structures I", edited by J. A. C. Bland, B. Heinrich, Springer-Verlag (1994), p. 65.

5.2. Néel, J. Phys. Rad. **15**,225 (1954).

5.3. M. T. Johnson, P. J. H. Bloemen, F. J. A den Broeder, J. J. de Vries, Rep. Prog. Phys. **59,** 1409 (1996).

5.4. F. J. A. den Broeder, W. Hoving, P. J. H. Bloemen, J. Magn. Magn. Mater. **93.** 562 (1991).

5.5. Z. Q. Qiu, J. Pearson, S. D. Bader, Phys. Rev. Lett. **70**, 1006 (1993).

5.6. D. P. Pappas, K. -P. Kämper, H. Hopster. Phys. Rev. Lett. **64**, 3179 (1990).

5.7. R. Allenspach, M. Stampanoni, A. Bischof, Phys. Rev. Lett. **65**, 3344 (1990).

5.8. F. Huang, M. T. Kief, G. J. Mankey, R. F. Wills, Phys. Rev. B **49**, 3962 (1994).

5.9. W. L. O'Brien, B. P. Tonner, Phys. Rev. B **49**, 15370 (1994).

5.10. B. Schulz, K. Baberschke, Phys. Rev. B **49**, 13476 (1994).

5.11. J. Shen, J. Giergiel, J. Kirshner, Phys. Rev. B **52**, 8454 (1995).

5.12. S. Ueda, S. Imada, Y. Saitoh, T. Muro, M. Kasashima, A. Kimura, A. Kakizaki, S. Suga, J. Electron Spectrosc. Relat. Phenom. **88-89**, 191 (1998).

5.13. S. Muller, B. Schulz, G. Kostaka, M. Farle, K. Heinz, K. Baberschke, Surface Science, **364**, 235 (1966).

5.14. C. M. Schneider, U. Pracht, W. Kuch, C. Chassé, and J. Kirschner, Phys. Rev. **B54**, R15618 (1996).

5.15. J. R. Cerdá, P. L. de Andres, A Cebollada, R. Miranda, E. Navas, P. Schuster, C. M. Schneider, J. Kirschner , J. Phys. Condens. Matter **5**, 2055 (1993).

5.16. W. Clemens, T. Kachel, E. Vescovo, S. Blügel, C. Carbone, W. Eberhardt, Solid State Commun. **81**, 739 (1992).

5.17. A. Kotani, Y. Toyozawa, J. Phys. Soc. Jpn. **35**, 1073 and 1082 (1973).

5.18. S. Hüfner, G. K. Wertheim,Phys. Lett. **51**, 299 (1975).

5.19. C. Guillot, Y. Ballu, J. Paigné, J. Lecante, K. Jain, P. Thiry, R. Pinchaux, Y. Pétroff, L. M. Falocov, Phys. Rev. Lett. **39**, 1632 (1977).

5.20. A. Kakizaki, J. Electron Spectrosc. Relat. Phenom. **88-89**, 163 (1998).

5.21. W. Kuch, R. Frömter, J. Gills, D. Hartmann, Ch. Zeithen, C. M. Schneider, G. Schonhense, W. Swiech, J. Kirschner, Surf. Rev. Lett. to be published (private communication).

5.22. H. B. Rose, T. Kinoshita, Ch. Roth, F. U. Hillebrecht, E. Kisker, Surf. Rev. Lett. **4**, 915 (1997).

5.23. G. van der Laan, M. A. Hoyland, M. Surman, C. F. J. Flipse, B. T. Thole, Phys. Rev. Lett. **69**, 3827 (1992).

5.24. Y. Saitoh, S. Ueda, T. Muro, S. Imada, S. Suga, A. Kimura, A. Kakizaki, Physica **B 237-238**, 397(1997).

5.25. L. A. Feldkamp, L. C. Davis, Phys. Rev. Lett. **43**, 151 (1979).

5.26. T. Kinoshita, T. Ikoma, A. Kakizaki, T. Ishii, J. Fuji, H. Fukutani, K. Shimada, A. Fujimori, T. Okane, S. Sato, Phys. Rev. B **47**, 6787 (1993).

5.27. G. Van der Laan, C. Westra, C. Haas, G. A. Sawatzky, Phys. Rev. **B 23,** 4369 (1981).

5.28. J. Zaanen, G. A. Sawatzky, J. W. Allen, Phys. Rev. Lett. **55,** 418 (1985).

5.29. K. S. Kim, Phys. Rev. **B 11,** 2177 (1975).

5.30. K. Wertheim, S. Hüfner Phys. Rev. Lett. **28**, 1028 (1972).

5.31. G. Lee, S.-J. Oh, Phys. Rev. **B 43,** 14674 (1991).

5.32. N. F. Mott, Proc. Phys. Soc. London Sect. A **62**, 416 (1949).

5.33. Hubbard, Proc. R. Soc. London Ser. A **276**, 238 (1963).

5.34. A. Fujimori, F, Minami, Phys. Rev. Lett. **53**, 2339 (1985).

5.35. Z. X. Shen, J. W. Allen, P. A. P. Lindberg, D. S. Dessau, B. O.Wells, A. Borg, W. Wills, J. S. Kang, S. –J. Oh, I. Lindau, W. E. Spicer, Phys. Rev. B **42**, 1817 (1990).

5.36. K. Okada, A. Kotani, J. Phys. Soc. Jpn. **61**, 449 (1992).

5.37. B. Klingenberg, F. Grellner, D. Borgmann, G. Wedler, Surf. Sci. **383**, 13 (1997), Surf. Sci. **296**, 374 (1993).

5.38. L. Gonzalez, R. Miranda, M. Salmerón, J. A. Vergés, F. Ynduráin, Phys. Rev. B **24**, 3245 (1981).

5.39. W. Clemens, E. Vescovo, T. Kachel, C. Carbone, W. Eberhardt, Phys. Rev. B **46**, 4198 (1992).

5.40. C. R. Castro, J. Küppers, Surf. Sci. **123**, 456 (1982).

5.41. T. Matsuyama, A. Ignatiev, Surf. Sci. **102**, 18 (1981).

5.42. H. Li, B. P. Tonner, Surf. Sci., **237**, 141 (1990).

5.43. A. K. Schimd, J. Kirschner, Ultramicroscopy, **42**, 483 (1992).

5.44. P. H. Citrin, G. K. Wertheim, Y. Baer, Phys. Rev. Lett. **41**, 1427 (1978).

5.45. R. Miranda, D. Chandesris, J. Lecante, Surf. Sci., **130**, 269 (1983).

5.46. J. Noffke, L. Fritsche, J. Phys., C14, **89** (1981).

5.47. D. S. Wang, A. J. Freeman, H. Krakauer, Phys. Rev. B **26**, 1340 (1982).

5.48. A. Rosencwaig, G. K. Wertheim, J. Electron. Spectrosc. **1**, 493 (1973).

5.49. A. Fanelsa, R. Schellenberg, F.U. Hillebrecht, E. Kisker, Surf. Rev. Lett. 4, 919 (1997).

5.50. W. L. O'Brien, B. P. Tonner, Surf. Sci., **334**, 10(1995).

5.51. M. Getzallf, J. Bansmann, G. Schönhense, J. Electron Spectrosc. Relat. Phenom. **77**, 197 (1996).

Chapter 6

General summary

In this thesis, the results of the photoemission experiment for rare earth compounds TmX (X=S, Se and Te) and thin film systems of the 3*d*-transition metal (Ni films on Co/Cu and oxidized Co films) were described. In both cases (4*f*- and 3*d*-systems), the evidence of the effect of electron-correlation was found to be very prominent. In order to explain various photoemission results for rare earth compounds and transition metal systems, the influence of electron-correlation was introduced.

The most interesting observation in the chapter 4 (for RE core levels photoemission) in this thesis is the variety of the spectral features for different photoemission spectra. This was occurred due to the different kind of interaction between the core hole and the localized 4*f* electrons. For example, in the 5*p* photoemission for the both on-resonant and off-resonant conditions, the spectra show two sets of spin-orbit peaks. Though the spin-orbit splitting is not so large for Tm5*p*, the spin-orbits peaks were nearly identified. The 5*p* (hole)-4*f* interaction is not so strong enough to change the spectral features into a complex one. On the other hand, several multiplet structures appear in each spin-orbit peaks due to the core hole-4*f* interactions. In the resonant photoemission, the features of the peaks are changed due to the presence of multiplet structures and their individual resonance effect.

In case of Tm4*d* and Tm4*p* photoemission results, the situation has been changed for having the similar principle quantum number to 4*f* electrons. But the nature of the 4*d*(hole)-4*f* interaction and 4*p*(hole)-4*f* interaction are quite different. It was found that the 4*d*(hole)-4*f* interaction is the most strong, and, therefore, the Tm4*d* photoemission spectra do not show actually any spin-orbit peaks. Instead, large number of multiplet structures are present in a wide range of energy region (~40eV). These multiplet structures show lifetime broadening effect. The lifetime broadening effect was also explained by the electron-correlation effect, in other words, by the 4*d*-4*f*4*f* super Coster-Kronig decay process. In case of Tm4*p* photoemission, the spin-orbit splitting is larger than that of Tm4*d* levels. This large spin-orbit splitting primarily dominates the Tm4*p* spectral feature, which is not so complex as Tm4*d* is. But, soon after the effect of the configuration interaction (CI) is introduced, the peak shape in the higher binding energy is changed and smeared out. Here, the CI was described through the 4*p*-4*d*4*d* Auger type decay process and this process has different impact on "$4p_{1/2}$" and "$4p_{3/2}$"peak regions. The lifetime broadening effect in the 4*p* XPS was also discussed by introducing configuration interaction (CI). It was shown that the broadening effect is not

constant over the whole $4p$ binding energy range. The "$4p_{1/2}$" region was found to be more smeared out than the "$4p_{3/2}$".

Finally for Tm$3d$, the strength of the $3d$(hole)-$4f$ interaction is again decreased. Therefore, the spin-orbit peaks are well distinguished. The lifetime broadening effect related to the $4f$ electrons very weak. But, several multiplet peaks are still present in the each spin-orbit peaks and the peaks are therefore locally broadened.

Thus, a rich information of the final state effects, such as multiplet splitting, lifetime broadening, configuration interaction, valence fluctuation were derived from these core level photoemission.

In case of transition metal Ni, the formation of satellite structures in the valence band photoemission and its resonance behavior are the well-known effect of the electron-correlation. Ferromagnetism is also a direct consequence of the spin-dependent electron-correlation. The magnetic dichroism study is thus directly related to the spin-dependent electron correlation. Though the calculated results were not shown for the Ni$3d$-MLD results, it can be assumed that the spin-dependent electron-correlation has strong influence on MLD signal for the correlation induced satellite structure.

The core level photoemission for CoO also shows the satellite structures. But in this case, the origin of the satellite is considered to be the charge transfer mechanism. The mechanism is also similar to that of metal and thus the satellite in CoO reflects the effect of strong electron-correlation. The spectral weights of the main peak (Co$2p$) and the correlation-induced satellite peak were found to be different in the oxidized Co-film depending on the oxygen-exposure or Co-thickness. The presence of the correlation-induced multiplet structures is also verified by comparing with the previous calculated results.

During the present study, a preparation chamber for epitaxial growth of thin films and sample preparation was installed as an improvement of the photoelectron system. The manipulator was also improved by constructing a He-cryostat for performing temperature dependent photoemission experiments. Several experiments were thus successfully carried out after all these improvements.

The results in the chapter 4 are summarized in the following:

1. In case of $5p$ level, the evidence of mixed valence was found in XPS and resonant photoemission spectra. In the TmX, two $5p$ spin-orbit peaks ($5p_{3/2}$ and $5p_{1/2}$) show the

chemical shifts depending on the Tm-valence. The values of the spin-orbit splitting are also different for two Tm valences and were estimated by the help of resonant effect and calculation. The values obtained from the present experiment are considered more reasonable than those of the previous reports. Especially by the resonant photoemission study, the evidence of the presence of the multiplet structures is very clear for each 5*p* peak.

2. Tm4*d* shows multiplet structures and the different multiplets show different resonance enhancement depending on the excitation conditions around the Tm 3*d*-4*f* absorption edges (hv=1450-1550eV). The lifetime broadening effect depending on the binding energy is present in both the on- and off-resonant photoemission. Through this experiment, the divalent and trivalent components in Tm4*d* were successfully separated and identified. It was found that one of the decay channels after Tm3*d*-4*f* absorption was a preferential one towards the Tm4*d* levels. This means that the among the several decay channels, the contribution of one decay channel is significant for Tm4*d* resonant behavior.
3. In case of 4*p* level, the evidence of effect of the configuration interaction (CI) phenomenon was found in the photoemission spectra. Between two spin-orbit peaks, the "$4p_{1/2}$" peak region shows strong influence of the CI effect and this region is more broadened and smeared out with short core hole lifetime. In order to clarify the CI effect, the comparison with calculation was also shown.
4. Tm3*d* core level was also measured for the mostly trivalent TmS. Because of the weak 3*d*-4*f* interaction, the spectrum is not so complex as Tm4*d* or 4*p* levels. It is found that the spin-orbit peaks are separated and locally broadened due to the existence of multiplet structures.
5. The probable origin of the deviation of mean valences in different measurement was also discussed by considering the surface and bulk sensitivity of particular measurement. The result shows the surface of TmS is not exactly the divalent as predicted earlier. On the other hand, result indicates that surface of TmTe has trivalent characteristics and TmSe is homogeneously intermediate valent.

In the relevant chapter (ch.5) of the magnetic thin films, the results for Ni/Co systems were described at first. Magnetic linear dichroism (MLD) in valence band and core level photoemission was used to study the magnetic properties of Ni film on Co/Cu(001). The results can be summarized as the following way:

1. The resonance effect is present on magnetic linear dichroism (MLD) for "6eV-satellite" in valence band at Ni 3*p*-3*d* excitation edge. The present result is similar to the previous MCDAD (Magnetic circular dichroism in angular distribution) results for bulk Ni (110) sample, but not to MLDAD (L, linear) result.
2. The MLD result of Ni3*p* and Co3*p* core levels shows that the Ni and Co are ferromagnetically coupled.
3. The present result also indicates that magnetization of the Ni films of 2.3, 8 and 11ML within the surface plane (in-plane magnetization)is possible.
4. Comparing with the MCDAD and MLDAD techniques, the MLD was also found to be suitable for studying of the magnetic properties of thin films.

In the second part of the ch.5, the Co2*p* core level photoemission spectra were discussed in order to show the modification of electronic and magnetic structures of oxidized Co film. The results are as follows:

1. It was found that the behavior of the early oxidization followed by saturated CoO formation was different depending on the Co-thickness. Thinner films are more reactive and show an earlier formation of CoO than that of thicker films. The present result is different from the previous one where thickness independent oxidization in the early stage was reported.
2. In the present study, it was estimated that two types of CoO phase depending on the thickness were formed on Co surface upon exposing oxygen. The CoO phases are two-dimensional (2D) and three-dimensional (3D). It is predicted that the generally accepted CoO_6 model for 3D CoO phase might not be suitable for describing the core level spectra in case of 2D CoO phase.
3. In the section of magnetism studies of oxidized Co film, MUDAD (U, unpolarized) measurement in Co2*p* level photoemission was used. MUDAD signal was found from the oxidized film even with higher exposure (40L). The result is different from the previous spin-resolved photoemission result. The present result concludes that

the MD signal for O(40L)/Co(5ML) system probably is coming from the deeper and unaffected Co-site.

There are some future plans for thin film magnetism. Among them, the temperature dependent magnetic dichroism study and oxidization of transition metal are of interest. In order to measure the magnetic properties, the MCD and MLDAD techniques will be used because the dichroism signal form these techniques is more intense than that of the MLD. The use of the spectromicroscopy with higher lateral resolution and STM (scanning tunneling microscopy) techniques is also planned in order to study the microstructures, especially for oxidized transition metal thin films. The results for Ni MLD of the valence band including satellite and Co MLD of core level will be compared with the calculation.

Appendix A

Spectromicroscopy: Magnetic domain imaging of Fe(110)

The current appendix describes some spectromicroscopy results of magnetic domain that were measured as the demonstrations of the VGESCALAB 220i-XL photoelectron system [A.1]. Usual size of the magnetic domains on the ferromagnetic materials is rather large (several hundreds μm), which is suitable to observe by the photoelectron spectromicroscope. Magnetic contrast [2] in photoemission was used to perform this experiment. The origin of the magnetic contrast is the same as the magnetic dichroism phenomenon that was described in chapter 5. In this experiment, both the linearly polarized light (synchrotron radiation) and unpolarized light (conventional laboratory x-ray gun) were used to excite the photoelectron from the Fe$2p_{3/2}$ level. Namely, applied techniques are the MLDAD and MUDAD.

Before taking the domain image, the surface of the Fe(110) was scanned spatially by photoelectron spectroscopy. The result is shown in Fig. A.1. In this case, the unpolarized x-

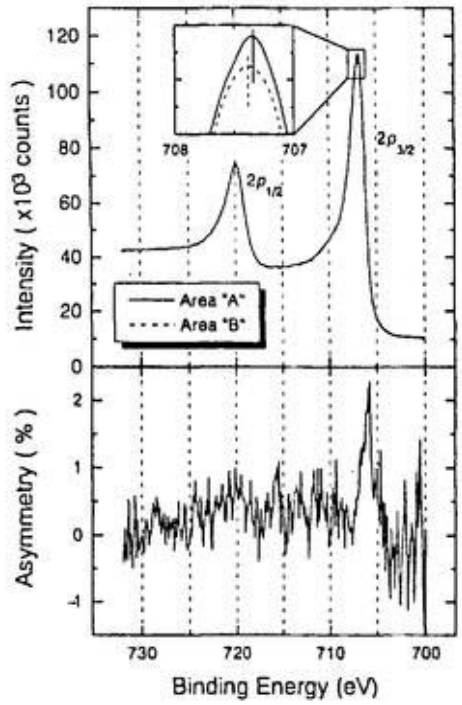

Figure A.1. Small area (50μm x 50μm) photoemission spectra (upper) from two different regions ("A" and "B") of the Fe(110) surface excited by Al$K\alpha$ radiation. The MUDAD signal (asymmetry) is shown in bottom part. Maximum asymmetry is obtained at the binding energy of 706eV.

ray source Al$K\alpha$ (hν=1486.6eV) was used for excitation of the photoelectrons. Because of the unpolarized light, the dichroism signal is small, but distinguished. The maximum asymmetry was found at binding energy of 706.0eV near Fe$2p_{3/2}$ peak. On the basis of occurrence of dichroism signal upon reversing the direction of magnetic field for ferromagnetic material, it can be said that the dichroism signal from two regions is obtained due to the antiparallel directions of local magnetization of two regions. In other words, domains with different direction of magnetic moments may exists in those two regions, "A" and "B". The existence of domain is shown in Fig. A.2 (using Al$K\alpha$ line) and in Fig. A.3 (using synchrotron radiation from the BL7A at UVSOR facility).

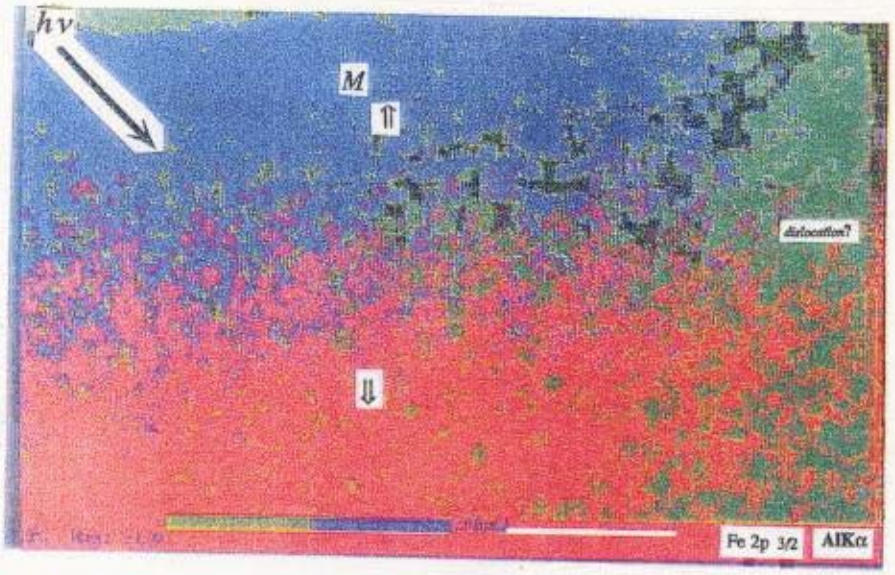

Figure A.2. Magnetic domain image of Fe(110) surface by using MUDAD effect. Al$K\alpha$ x-ray line was used for electron excitation. The Fe$2p_{3/2}$ photoelectrons at E_B=706eV and E_B=704eV are corrected. The direction of the magnetic moment of each magnetic domain ("A" bright) or ("B" dark) is indicated.

In Fig. A.2, the magnetic domain image of Fe(110) is shown. The magnetic contrast by using unpolarized light was used for this purpose. After taking two images at E_B=706eV and

E_B=704eV, the subtraction and normalization process was done to get the final domain image. The direction of the incident photon is shown by arrow in one corner of the figure. The expected direction of local magnetic moment for the domains "A" bright area and "B" dark area are indicated when the easy direction of magnetization is considered to show along Fe(100). Thus, MUDAD signal in photoelectron spectroscopy in Fig. A.1 can be observed reflecting the magnetic domain imaging or vice versa. The MUDAD effect is not so large as shown in Fig. A.1, the contrast of the image is therefore not so clear. That's why the zone boundary of two magnetic domains is not clearly visible. Instead, the image taken by linearly polarized light shows more clear contrast as discussed below.

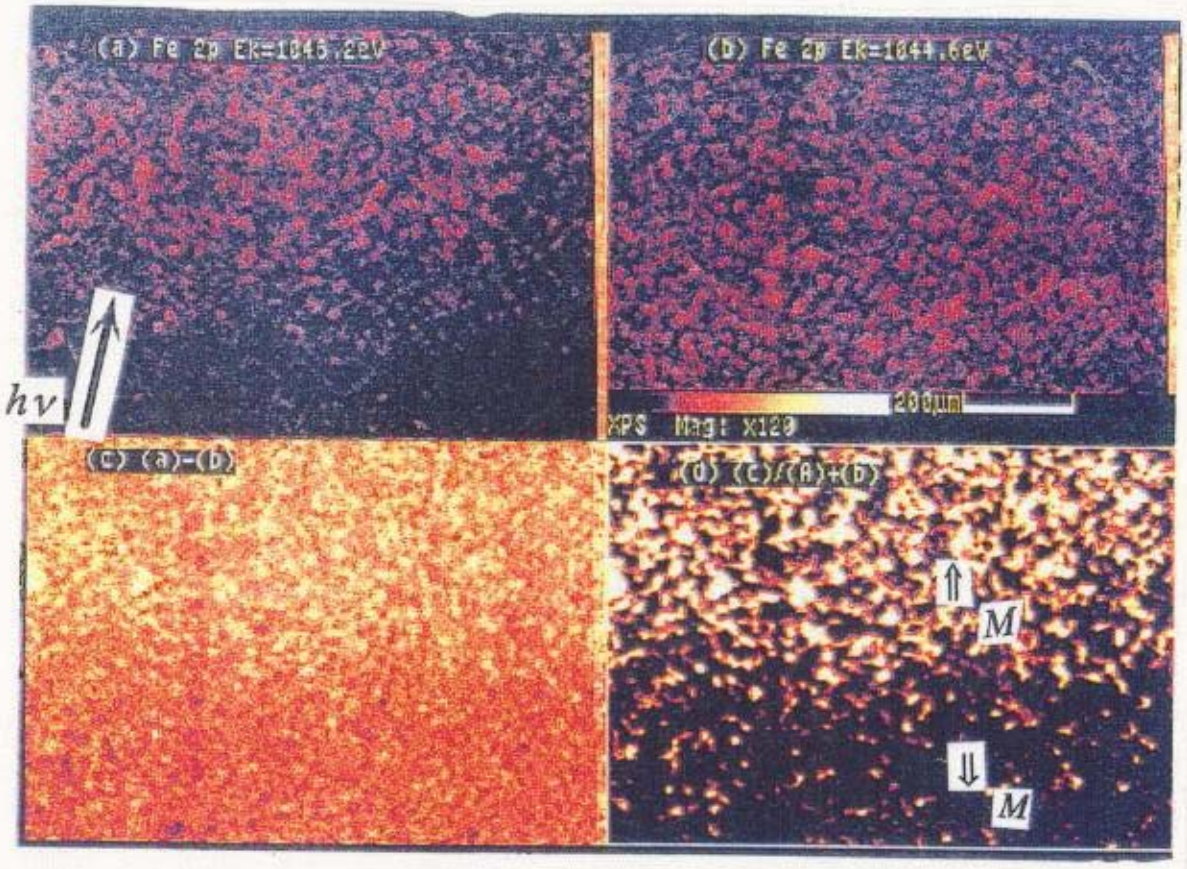

Figure A.3. Magnetic domain of Fe(110) surface. Magnetic dichroism effect of the Fe$2p_{3/2}$ photoelectron by linearly polarized light (hν=1758eV) was used. (a) and (b) represent images for photoelectron at kinetic energy, E_k=1046.2eV and at E_k=1044.6eV, respectively. After subtraction (in c) and normalization, the magnetic domain with opposite direction is obtained (in d).

In Fig.A.3, magnetic domain image was taken with MLDAD effect of Fe$2p_{3/2}$ photoelectron. The photon energy was 1758eV. The linearly polarized light was impinged from the bottom as shown in (a). Initially two images were taken simultaneously for photoelectron at E_k=1046.2eV (a) and at E_k=1044.6eV (b). The magnification of each image is 120 times, where the detection area was 1mm x 1mm. After subtraction (c = a-b) and normalization (d = c/(a+b)) of two images, the domain structure (d) is obtained. Arrows indicate the probable directions of the local magnetization. The contrast between the up magnetized region and the down one is apparent.

References

A.1. T. Kinoshita, K. G. Nath, Y. Haruyama, M. Watanabe, S. Yagi, S. Kimura, A. Fanelsa, J. Electron Spectrosc. Relat. Phenom., **92**, 165 (1998).

A.2. C. M. Schneider, J. Mag. Mag. Mat. **175**, 160 (1997).

Appendix B

Test experiment by using He-cryostat

The following core level photoemission experiment in Eu-compound was carried out as a test experiment of the newly constructed He-cryostat. The sample is the temperature-induced valence transition material $EuNi_2(Si_{0.25}Ge_{0.75})_2$ [1]. This is an intermediate valent type compound. The valence transition is occurred at T=110K. Figure B.1 shows the Eu3*d* core level photoemission spectra measured by using Al*K*α radiation for oxidized sample and clean sample.

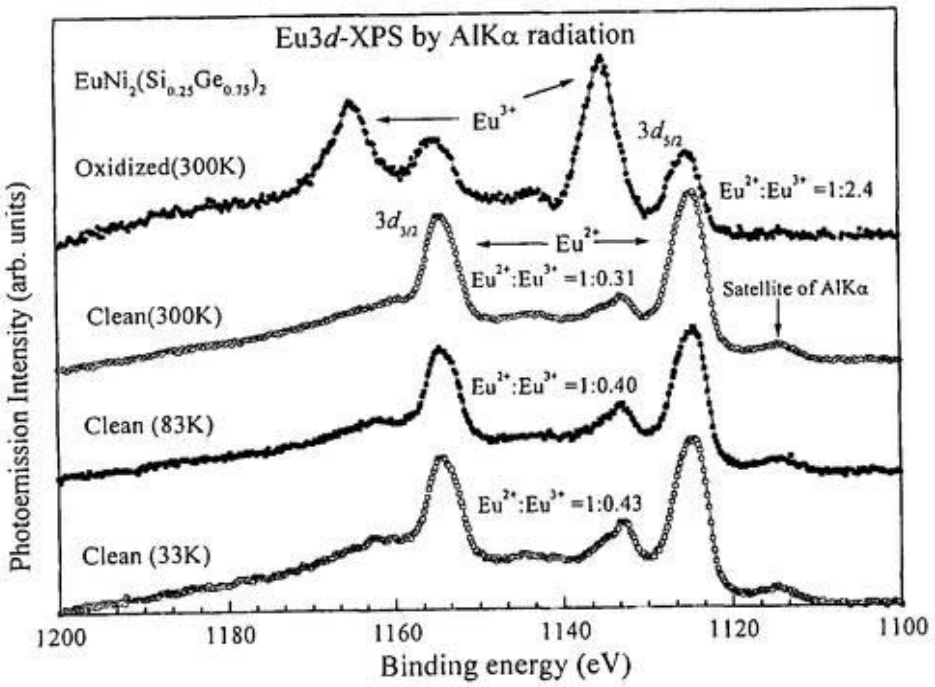

Figure B.1. Eu3*d* core level photoemission spectroscopy measured by Al*K*α radiation. The top most spectrum (solid circle) is for oxidized sample taken at 300K. The ratio Eu^{2+}: Eu^{3+} = 1:2.4. The other three spectra are for clean sample but at different temperatures. The valence transition occurs towards trivalent with decreasing the sample temperature as seen in the three clean sample spectra where the ratio is 1:0.31 at 300K (open circle), 1:0.40 at 83K (solid square) and 1:0.43 at 33K (open square).

In the resonant photoemission experiment of Eu-valence band at Eu 3*d*-4*f* absorption edges [B.2], it was found that the photoemission signals belong to the trivalent Eu show the enhancement at low temperature. The same kind of valence transition is occurred here in core level photoemission. In order to get very low temperature, liquid He (constant flow) was inserted inside of the cryostat. The minimum temperature 33K was achieved, which was checked by Al-Cr thermocouple. By using liquid nitrogen in the same cryostat, the temperature went down to about 83K. The clean sample was achieved by scraping the sample surface with diamond filler in UHV condition.

In the figure, each spectrum shows two sets of spin-orbit peaks corresponding to two valences. For spectrum (solid circle) of oxidized sample as shown in top of the figure, the ratio, Eu^{2+}: Eu^{3+} is 1:2.4. This value was estimated from the total photoemission cross-sectional area under the "Eu3$d_{5/2}$" peak region. The ratio means that the oxidized sample shows more trivalent nature than the clean sample, because of the existence of Eu_2O_3. But for clean sample at 300K, the amount of trivalent component is reduced. The ratio was found to be 1:0.31 for the clean sample (open circle) at room temperature. The estimated mean valence is 2.24. On the other hand, the trivalent component was increased with decreasing the temperature. In the figure, the ratio (Eu^{2+}: Eu^{3+}) is 1:0.40 at 83K (solid square) and 1:0.43 at 33K (open square). The corresponding mean valences are 2.29 and 2.30, respectively. It is clear from this measurement that the valence transition is occurred for the Eu compound depending on the temperature.

Reference

B.1. H. Wada, A. Nakamura, A. Mitsuda, M. Shiga, T. Tanaka, H. Mitamura, T. Goto, J. Phys. Condens. Matter. **9**, 7913 (1993).

B.2. H. P. N. J. Gunasekara, Y. Takata, S. Kimura, T. Kinoshita, N. Kosugi, K. G. Nath, H. Wada, A. Mitsuda, M. Shiga, UVSOR Activity report 1997, p. 144.

Appendix C

Electrochemical polishing

The electrochemical polishing was carried out in order to get mirror surface for Cu substrate. After the mechanical polishing, usually some damages or some polishing materials and lubricant are left on the sample surface. At this stage, even the ultrasonic cleaning is not enough to remove them. As a result, the usual ultra high vacuum cleaning (sputtering and annealing) is not sometimes enough to get the clean surface. The electrochemical polishing is thus very essential to perform. Though the process itself has some risk to destroy the surface partially and to produce some pits on the surface, it is very much effective to get cleaner surface. In the present thin film measurement where the electrochemical etched Cu substrate was used, the sample surface had some damages. But these damages did not affect the experiment because the detection area of the photoemission measurement was less than 1 mm. The procedure of electrochemical polishing is described below.

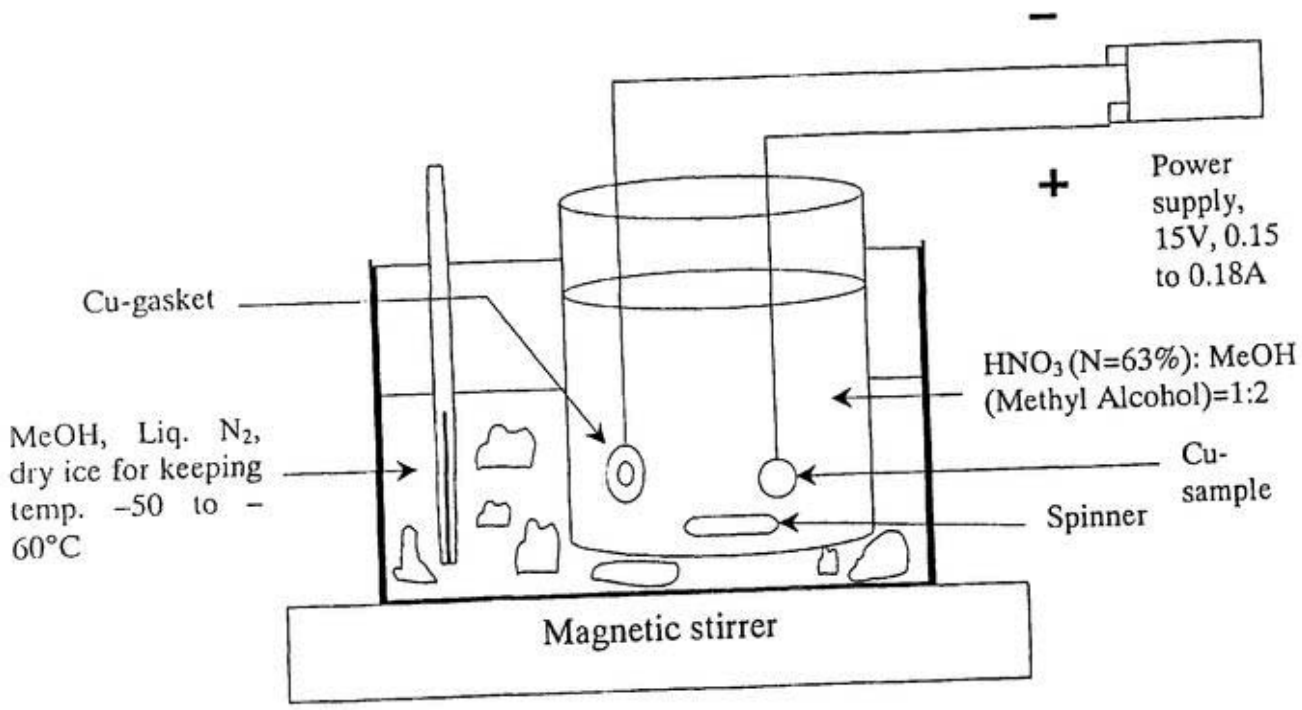

Figure C.1. Arrangement of electrochemical polishing.

The arrangement of the chemical polishing is shown in Fig. C.1. An acid solution [HNO_3 (concentration, N=63%): MeOH = 1 : 2] was used for this purpose. The acid solution was kept inside of a cool reservoir whose temperature was maintained at –50 to –60°C. Two electrodes, the Cu-sample as cathode and a small Cu-gasket as anode, were used to supply the current. At –50 to –60°C, the power supply was turned on with 0.15A and 15V for nearly 7 minutes. During this time, a fresh Cu-surface was appeared due to the chemical reaction. Later, the sample was washed by methanol and dried.

Appendix D

Calculation details (done by Dr. H. Ogasawara in Prof. Kotani group, ISSP, Tokyo University)

The calculations are done for Tm^{2+} and Tm^{3+} ions using an atomic model in the spherical symmetric space. The initial state is taken to the Hund's rule lowest state, which is ${}^2F_{7/2}$ for Tm^{2+} ($4f^{13}$) and ${}^3H_6$ for Tm^{3+} ($4f^{12}$), respectively.

The total Hamiltonian consists of three parts,

$$H=H_{so}+H_{e\text{-}e}+V_o, \tag{D.1}$$

where H_{so} represents the spin-orbit interaction, $H_{e\text{-}e}$ the electron-electron interaction, and V_o the optical transition, respectively.

The spectrum is calculated by the formula

$$F(\varepsilon,\nu) = \sum_{k,\beta} \left|\langle k\beta|T|g\rangle\right|^2 \delta(h\nu + E_g - E_{k\beta})\delta(\varepsilon - \varepsilon_k), \tag{D.2}$$

where $h\nu$ represents the incident photon energy, ε the kinetic energy of the photoelectron, $|g\rangle$ the ground state of H_0, E_g its energy, $|k\beta\rangle$ the final states, and $E_{k\beta}$ their energies. Here the interaction between the photoelectron and the Tm system is ignored, so that the final states $|k\beta\rangle$ and their energies can be decoupled as $|k\beta\rangle=|k\rangle|\beta\rangle$ and $E_{k\beta} = \varepsilon_k + E_\beta$, where $|k\rangle$ and ε_k represents the photoelectron state and its energy, and $|\beta\rangle$ and E_β the final state of the Tm ion and its energy, respectively. The operator T is the t-matrix, which is the optical transition in off-resonance case or the electron-electron interaction plus optical transition in on-resonance.

The Cowan's program suits [D1] was used to obtain parameter values and reduced matrix elements.

1. Tm *4p* photoemission

As mentioned above, the *4p* photoemission spectra of the rare-earth elements show strong configuration interaction (CI) effect. In this calculation, the configuration interaction between two configurations $4p^5 4d^{10} 4f^n$ and $4p^6 4d^8 4f^{n+1}$ is considered. It is assumed that the CI counterpart is below the continuum threshold, because it is found from atomic Hartree-Fock calculations that the energy position of configuration $4p^6 4d^8 4f^{\nu}\varepsilon f$ is several rydbergs higher than the $4p^6 4d^8 4f^{n+1}$.

The system Hamiltonian consists of spin-orbit and Coulomb-exchange interactions within each two configurations and the electron-electron interaction between them (CI).

The t-matrix is the optical transition. The parameter values required in this calculation are given in the Table I. These values are obtained by Cowan's Hatree-Fock program with relativistic corrections. The values of $F^k(4d,4d)$, $F^k(4f,4f)$ are reduced to 80%, $F^k(4p,4f)$, $F^k(4d,4f)$ to 75%, $G^k(4p,4f)$, $G^k(4d,4f)$ to 66% and $R^k(4p4f,4d^2)$ to 90%, respectively.

The energy distance between the two configurations defined as

$$\Delta E = E_{AV}(4p^6 4d^8 4f^{n+1}) - E_{AV}(4p^5 4d^{10} 4f^n) \qquad (D.3)$$

is also required in the calculation. The calculated values are 16.3eV for Tm^{3+} and 16.4eV for Tm^{2+}, respectively. The ΔE is treated as a free parameter, because ΔE might be different from the atomic value in solid.

2. Tm *5p* resonant photoemission

The *5p* resonant-photoemission spectra in the *4d* resonance region was calculated. In this case the system Hamiltonian consists of the spin-orbit and Coulomb-exchange interactions within a single configuration, while the t-matrix consists of the Auger and the optical transitions. It is expressed as

$$T = V_O + V_A [1/(z-H_0)]T \qquad (D.4)$$

with

$$z = h\nu + E_g + i\eta \qquad (\eta \rightarrow +0), \qquad (D.5)$$

where optical transition V_O up to the first order and the Auger transition V_A up to the infinite order are taken into account. The detail of the calculation method was given in reference [D2].

Three major decay channels, which are $4d$-$4f4f\varepsilon g$, $4d$-$4f5s\varepsilon p$, and $3d$-$4d5p\varepsilon(s, d, g)$ Auger decay processes are considered. The kinetic energy of the photoelectron is determined so as to keep the total energy of the system conserves. Although results are not shown in this paper, *5s* and *4f* resonant photoemission are obtained. The result for *4f* resonant photoemission was already published [D2].

The parameter values used in the calculation are given in Table II.

The values of $F^k(4f,4f)$ are reduced to 80%, $F^k(4d,4f)$, $F^k(5p,4f)$ to 75%, $G^k(4d,4f)$, $G^k(5s,4f)$, $G^k(5p,4f)$ to 66% , respectively. The other values are used in raw values.

3. Tm *3d* photoemission

The *3d* photoemission spectrum is also calculated for Tm^{3+} ion. In this case, the system Hamiltonian consists of the spin-orbit and Coulomb-exchange interactions within a single configuration, and the t-matrix is simply the optical transition. This is the most basic model

without CI and resonance effect.

The parameter values used in the calculation are given in Table III. All the Slater integrals are reduced to 80%.

4. Tm 4*d* resonant photoemission

The on- and off-resonant photoemission spectra of 4*d* core level for Tm^{2+} and Tm^{3+} ions were calculated using an atomic model with spherical symmetry. The initial states are taken to the Hund's rule lowest states, which are $^2F_{7/2}$ for Tm^{2+} ion ($4f^{13}$) and $^3H_6$ for Tm^{3+} ion ($4f^{12}$), respectively. The method is the same as that used in Tm5*p* resonant photoemission. The final states of $3d \rightarrow 4f$ XAS (X-ray absorption spectra) are identified by several intermediate states of resonant photoemission with $3d^9 4f^{n+1}$ configuration (n= 12 or 13). There are one and four intermediate states for Tm^{2+} and Tm^{3+} ion, respectively.

There are a lot of decay channels from the intermediate states. The most important channels are 3*d*-4*f*4*f*, 3*d*-4*d*4*f* and 3*d*-4*d*4*d* Auger decay. Three channels in the calculation are included for simplicity. This is a fair approximation, because the decay process other than 3d-4*d*4*f* affects indirectly the resonant 4*d* photoemission spectra through the lifetime broadening in the intermediate state. The parameter values used in the calculation are given in table IV. A linearly energy dependent function $\Gamma = 0.1(E_B - E_0)$ eV, (where E_0 is the lowest binding energy in the 4*d* XPS) is used to approximate the lifetime broadening effect of 4*d* photoemission final states, taking into account that the lifetime of 4*d* XPS strongly depends on the multiplet term.

References

D1. R. D. Cowan, The theory of Atomic Structure and Spectra, University of California Press, Berkeley, 1981.

D2. Y. Ufuktepe, S. Kimura, T. Kinoshita, K. G. Nath, H. Kumigashira, T. Takahashi, T. Matsumura, T. Suzuki, H. Ogasawara and A. Kotani, J. Phys. Soc. Jpn., 67, 2018(1998).

Table I. Parameter values used for $4p$ XPS. All values are given in the unit of eV.

	Tm^{3+}		Tm^{2+}	
ground state				
$F^2(4f,4f)$	13.18		---	
$F^4(4f,4f)$	8.26		---	
$F^6(4f,4f)$	5.94		---	
ζ_{4f}	0.33		0.31	
final state				
	$4p^54d^{10}4f^{12}$	$4p^64d^84f13$	$4p^54d^{10}4f^{13}$	$4p^64d^84f^{14}$
$F^2(4f,4f)$	14.01	---	---	---
$F^4(4f,4f)$	8.83	---	---	---
$F^6(4f,4f)$	6.37	---	---	---
$F^2(4d,4d)$	---	17.64	---	17.54
$F^4(4d,4d)$	---	11.82	---	11.75
ζ_{4f}	0.36	0.36	0.34	---
ζ_{3p}	31.63	---	31.47	---
$\zeta_{\square d}$	---	3.34	---	3.31
$F^2(4p,4f)$	14.89	---	14.44	---
$G^2(4p,4f)$	11.36	---	10.98	---
$G^4(4p,4f)$	7.87	---	7.60	---
$F^2(4d,4f)$	---	14.33	---	---
$F^4(4d,4f)$	---	9.19	---	---
$G^2(4d,4f)$	---	14.78	---	---
$G^4(4d,4f)$	---	9.35	---	---
$G^6(4d,4f)$	---	6.63	---	---
$R^1(4p4f,4d^2)$	22.55		22.17	
$R^3(4p4f,4d^2)$	14.08		13.81	

Table II. Parameter values used for 5*p* resonant XPS. F, G, ζ are
given in eV, R in $(eV)^{1/2}$, (4d|r|4f) in Bohr radius a_B, (nl|r|εl') in a_B / $(eV)^{1/2}$.

	Tm^{3+}	Tm^{2+}
Intermediate states		
	$4d^9 4f^{13}$	$4d^9 4f^{14}$
ζ_{4f}	0.34	---
ζ_{4d}	3.29	3.27
$F^2(4d,4f)$	13.85	---
$F^4(4d,4f)$	8.85	---
$G^2(4d,4f)$	14.30	---
$G^4(4d,4f)$	9.01	---
$G^6(4d,4f)$	6.38	---
(4d|r|4f)	-0.575	-0.576
final state		
	$4f^{11}\varepsilon l$ (ε_{kin}=10.2Ry)	$4f^{12}\varepsilon l$ (ε_{kin}=11.7Ry)
$F^2(4f,4f)$	13.86	13.18
$F^4(4f,4f)$	8.73	8.26
$F^6(4f,4f)$	6.29	5.94
ζ_{4f}	0.35	0.33
$R^1(4f^2,4d\varepsilon g)$	-0.80	-0.82
$R^3(4f^2,4d\varepsilon g)$	-0.43	-0.44
$R^5(4f^2,4d\varepsilon g)$	-0.29	-0.29
(4f|r|εg)	0.044	0.043
	$5s^{14}f^{12}\varepsilon l$ (ε_{kin}=6.4Ry)	$5s^{14}f^{13}\varepsilon l$ (ε_{kin}=7.6Ry)
$F^2(4f,4f)$	13.44	---
$F^4(4f,4f)$	8.44	---
$F^6(4f,4f)$	6.08	---
ζ_{4f}	0.34	0.34
$G^3(5s,4f)$	2.72	2.75

$R_d^1(4f5s,4d\varepsilon p)$	0.42	0.41
$R_e^2(4f5s,4d\varepsilon p)$	0.15	0.15

$(5s\|r\|\varepsilon p)$	0.0090	0.0085

	$5p^54f^{12}\varepsilon l(\varepsilon_{kin}=8.7Ry)$	$5p^54f^{13}\varepsilon l(\varepsilon_{kin}=9.8Ry)$
$F^2(4f,4f)$	13.37	---
$F^4(4f,4f)$	8.40	---
$F^6(4f,4f)$	6.04	---
ζ_{4f}	0.34	0.32
ζ_{5p}	4.12	3.78
$F^2(5p,4f)$	5.34	5.15
$G^2(5p,4f)$	2.29	2.34
$G^4(5p,4f)$	1.80	1.79

$R_d^1(4f5p,4d\varepsilon s)$	0.13	0.12
$R_e^3(4f5p,4d\varepsilon s)$	0.077	0.072

$R_d^1(4f5p,4d\varepsilon d)$	0.43	0.41
$R_d^3(4f5p,4d\varepsilon d)$	0.26	0.14
$R_e^1(4f5p,4d\varepsilon d)$	0.13	0.13
$R_e^3(4f5p,4d\varepsilon d)$	0.14	0.14

$R_d^3(4f5p,4d\varepsilon g)$	0.25	0.24
$R_d^5(4f5p,4d\varepsilon g)$	0.14	0.14
$R_e^1(4f5p,4d\varepsilon g)$	0.13	0.13
$R_e^3(4f5p,4d\varepsilon g)$	0.11	0.11

$(5p\|r\|\varepsilon s)$	0.012	0.011
$(5p\|r\|\varepsilon d)$	0.0033	0.0029
$(5s\|r\|\varepsilon g)$	---	---

Table III. Parameter values used for 3*d* XPS. All values are given in the unit of eV.

	Tm^{3+}	Tm^{2+}
final state		
$F^2(4f,4f)$	14.33	---
$F^4(4f,4f)$	9.03	---
$F^6(4f,4f)$	6.51	---
ζ_{4f}	0.39	0.37
ζ_{3d}	18.0	18.0
$F^2(3d,4f)$	9.52	9.09
$F^4(3d,4f)$	4.54	4.31
$G^1(3d,4f)$	7.05	6.68
$G^3(3d,4f)$	4.14	3.92
$G^5(3d,4f)$	2.86	2.71

Table IV. Parameter values used for 4*d* resonant XPS.

	Tm^{3+}	Tm^{2+}
4f numbers	12	13
$F^2(4f, 4f)$	13.9	13.2
$F^4(4f, 4f)$	8.7	8.3
$F^6(4f, 4f)$	6.3	5.6
ζ_{4f}	0.35	0.33
ζ_{4d}	3.3	3.3
ζ_{3d}	18.1	18.1
$F^2(4d, 4f)$	14.3	13.9
$F^4(4d, 4f)$	9.2	8.9
$G^1(4d, 4f)$	14.8	14.3
$G^3(4d, 4f)$	9.4	9.0
$G^5(4d, 4f)$	6.6	6.4
$F^2(4d, 4d)$	17.6	17.6
$F^4(4d, 4d)$	11.8	11.8
$F^2(3d, 4f)$	9.1	--
$F^4(3d, 4f)$	4.3	--
$G^1(3d, 4f)$	6.7	--
$G^3(3d, 4f)$	3.9	--
$G^5(3d, 4f)$	2.7	--

$R^1(3d\varepsilon g, 4f^2)$	0.19	0.18
$R^3(3d\varepsilon g, 4f^2)$	0.12	0.12
$R^5(3d\varepsilon g, 4f^2)$	0.09	0.08
$R^0(3d\varepsilon d, 4d^2)$	0.11	0.11
$R^2(3d\varepsilon d, 4d^2)$	0.09	0.09
$R^4(3d\varepsilon d, 4d^2)$	0.05	0.05
$R_d^1(3d\varepsilon f, 4f4d)$	0.12	0.12
$R_d^3(3d\varepsilon f, 4f4d)$	0.05	0.05
$R_d^5(3d\varepsilon f, 4f4d)$	0.03	0.03
$R_e^0(3d\varepsilon f, 4f4d)$	0.04	0.04
$R_e^2(3d\varepsilon f, 4f4d)$	0.05	0.05
$R_e^4(3d\varepsilon f, 4f4d)$	0.03	0.03
$(4f\|r\|3d)$	0.12	0.12
$(\varepsilon g\|r\|4f)$	0.0015	0.0014
$(\varepsilon f\|r\|4d)$	0.0028	0.0028

Acknowledgements

It is a great pleasure for me to express my sincere gratitude to my supervisor Professor Toyohiko Kinoshita, who kindly received me as a Monbusho student and encouraged me for doing the present photoemission experiment. I am indebted to Prof. Kinoshita for his continuous support, suggestion, and letting me to be familiar with the frontier of photoemission and synchrotron radiation during my study in Japan.

I wish to express my gratitude to Prof. Masao Kamada (UVSOR) and Prof. Tsuneo Urisu (IMS) for their advice, encouragement and for many valuable discussions and suggestion.

I would like to express my sincere acknowledgment to Prof. Akio Kotani and Dr. Haruhiko Ogasawara (ISSP, Tokyo Univ.) for providing me their theoretical calculation to analysis the experimental data of core level photoemission for TmX. Especially, I deeply thank Dr. H. Ogasawara for his continuous help, discussion through electronic mail, and sincere encouragement.

I acknowledge Dr. Takeshi Matsumura (Tohoku Univ.) for providing the thulium monochalcogenides samples.

I deeply thank Prof. Shin-ichi Kimura (Kobe Univ.) for his kind help, discussion, and advice during my study. I acknowledge that I have learned many things about the photoemission and ultrahigh vacuum techniques from Dr. Yuichi Haruyama (UVSOR-IMS). Special thanks to Dr. Masamitsu Watanabe (KEK-PF) and Dr. Shinya Yagi (HISOR), from whom I received many suggestion and help at the early days of my stay in Japan. I also thank Prof. Kozo Okada (Okayama Univ.) with whom I met in several conferences and discussed about the core level photoemission of transition metal oxides.

During my study, I have had a lot of opportunity to collaborate with some researchers from inside and outside of Japan. It is my pleasure to express my sincere acknowledgements to Prof. Yüksel Ufuketepe (Univ. of Cukurova, Turkey), Mr. Hiroshi Kumigashira (Tohoku Univ.), Mr. H. P. N. J. Gunasekara (CISIR, Sri Lanka) and Dr. Andreas Fanelsa (Heinrich-Heine Univ. Germany).

I sincerely acknowledge Drs. Kazuhiko Mase (IMS) and Shin-ichiro Tanaka (UVSOR) for their valuable suggestion about the low temperature system. I deeply thank Mr. Nobuo Mizutani (Equipment Development Center, IMS) for manufacturing the He-cryostat.

It is pleasure to express my gratitude to Prof. Ajoy K. Roy (Dhaka Univ. Bangladesh) for his continuous support and encouragement about my research in Japan.

As a graduate student in the UVSOR, I spent an excellent and fruitful time and enjoyed a wonderful working atmosphere. I would like to thank all staff members of the UVSOR facility for their every kind of help and nice accompany. I thank Ms. Hisayo Hagiwara and Ms. N. Onitake for their friendly cooperation.

I thank my family for their endless support and encouragement for doing research in Japan.

Publications:

1. **Krishna G. Nath, Y. Ufuktepe, S. Kimura, T. Kinoshita, H. Kumigashira, T. Takahashi, T. Matsumura, T. Suzuki, H. Ogasawara, A. Kotani; "*4d Core- level resonant photoemission spectroscopy of thulium monochalcogenides around the Tm 3d threshold.*" J. Electron Spectrosc. Relat. Phenom., 88-91,** 369-375 **(1998).**

2. **Krishna G. Nath, Y. Haruyama, S. Kimura, Y. Ufuktepe, T. Kinoshita; "*Study of Magnetic Linear Dichroism (MLD) for different thickness of Ni-film grown on ferromagnetic Co(001) in element specific photoemission*", J. Electron Spectrosc. Relat. Phenom. (in print).**

3. **T. Kinoshita, Krishna G. Nath, Y. Haruyama, M. Watanabe, S. Yagi, S. Kimura, A. Fanelsa; "*Photoelectron spectromicroscopy experiments at the UVSOR facility*" J. Electron Spectrosc. Relat. Phenom., 92,** 165-169 **(1998).**

4. **T. Kinoshita, Y. Ufuktepe, Krishna G. Nath, S. Kimura, H. Kumigashira, T. Takahashi, T. Matsumura, T. Suzuki, H. Ogasawara and A. Kotani; "*Resonant photoemission studies of thulium monochalcogenides around the Tm 3d threshold*" J. Electron Spectrosc. Relat. Phenom., 88-91,** 377-384 **(1998).**

5. **Y. Ufuktepe, S. Kimura, T. Kinoshita, Krishna G. Nath, H. Kumigashira, T. Takahashi, T. Matsumura, T. Suzuki, H. Ogasawara and A. Kotani; "*Resonant Photoemission Studies of Thulium Monochalcogenides around the Tm 4d Threshold*" J. Phys. Soc. Jpn., 67,** 2018-2026 **(1998).**

6. **S. Kimura, Y. Ufuktepe, Krishna G. Nath, T. Kinoshita, H. Kumigashira, T. Takahashi, T. Matsumura, T. Suzuki, H. Ogasawara, A. Kotani; "*4d-4f and 3d-4f resonant photoemission of TmX (X= S, Se and Te)*", J. Mag. Mag. Mat., 177-181,** 349-350 **(1998).**

7. **T. Kinoshita, Y. Takata, T. Matsukawa, H. Aritani, S. Matsuo, T. Yamamoto, T. Takahashi, H. Yoshida, T. Yoshida, Krishna G. Nath, Y. Ufuktepe, S. Kimura and Y. Kitajima; "*Performance of the YB_{66} soft X-ray monochromator crystal at the wiggler beamline of the UVSOR facility*" J. Synchrotron Rad., 5,** 726-728 **(1998).**

***8. S. Kimura, Krishna G. Nath, Y. Haruyama, T. Kinoshita, S. Yoshii. M. Kasaya; "*Anisotropic optical conductivity of RPtAs (R= La, Ce)*", Physica B (in print).**

***9. Y. Haruyama, Krishna G. Nath, S. Kimura, Y. Ufuktepe, T. Kinoshita, K. Hiraki, K. Kanoda; "*Electronic structures of organic salts $(DI\text{-}DCNQI)_2M$ (M= Ag and Cu) using photoelectron spectromicroscopy*", Solid State Commun. (in print).**

*** not included in thesis**

Presentations:

1. Krishna G. Nath et al.; *"4d-4f resonant photoemission study of TmX (X=S, Se and Te)"* **Japanese Physical Society meeting, March 97, Nagoya (oral presentation).**
2. Krishna G. Nath et al.; *"Core level photoemission spectroscopy and resonant behavior of mixed-valence Tm monochalogenides"*, **Seventh International Conference on Electron Spectroscopy (ICES-7), September 97, Chiba (poster presentation).**
3. Krishna G. Nath et al.; *"Core level photoemission spectroscopy and resonant behavior of mixed-valence Tm monochalogenides"*, **Japanese Physical Society meeting, October 97, Kobe (oral presentation).**
4. Krishna G. Nath et al.; *"Resonant photoemission study of Tm core levels in Tm-monochalcogenides"*, **Japanese Synchrotron Radiation Society meeting, January 98, Himeji (oral presentation).**
5. Krishna G. Nath et al.; *"Study of magnetic thin film by photoelectron spectromicroscopy"* **Joint international conference on MMM /Intermag., January 98, Sendai (poster presentation).**
6. Krishna G. Nath et al.; *"Study of magnetic thin film by photoelectron microscopy: Magnetic behaviors of Ni/Co/Cu(001) by MLD and Ni3p resonant effect on MLD of Ni 6eV satellite"*, **Japanese Physical Society meeting, march 98, Chiba (oral presentation).**
7. Krishna G. Nath et al.; *"Magnetic dichroism study by unpolarized light: a convenient option to study magnetic thin film in element specific photoemission"* **Meeting on nano-scale magnetism and transport, July 98, Nagoya (oral presentation).**
8. Krishna G. Nath et al.; *"Study of Magnetic Linear Dichroism (MLD) for different thickness of Ni thin film grown on ferromagnetic Co (001) in element specific photoemission"*, **12th International Conference on Ultraviolet Radiation physics (VUV-XII), August 98, San Francisco (poster presentation).**
9. Krishna G. Nath et al.; *"Variation of electronic and magnetic structure of oxidized C-thin film as a function of oxygen-coverage by core level photoemission spectroscopy"*, **Japanese Physical Society meeting, September 98, Okinawa (poster presentation).**
10. Krishna G. Nath et al.; *"Study of electronic structure and magnetic phase of Co film on oxygen-rich Cu(001)(√2x2√2)R45°-O surface"* **Meeting on nano-scale magnetism and transport, January 99, Kyoto (oral presentation).**

ELSEVIER

Journal of Electron Spectroscopy and Related Phenomena 88–91 (1998) 369–375

JOURNAL OF ELECTRON SPECTROSCOPY and Related Phenomena

4*d* Core-level resonant photoemission spectroscopy of thulium monochalcogenides around the Tm 3*d* threshold

K.G. Nath[a], Y. Ufuktepe[1 b], S. Kimura[b], T. Kinoshita[b], H. Kumigashira[c], T. Takahashi[c], T. Matsumura[c], T. Suzuki[c], H. Ogasawara[d], A. Kotani[d]

[a]*Department of Structural Molecular Science, The Graduate University for Advanced Studies, Okazaki 444, Japan*
[b]*UVSOR Facility, Institute for Molecular Science, Okazaki 444, Japan*
[c]*Department of Physics, Tohoku University, Sendai 980-77, Japan*
[d]*Institute for Solid State Physics, University of Tokyo, Tokyo 106, Japan*

Abstract

We report the results of 4*d* core-level photoemission spectra for thulium monochalcogenides, TmX (X = S, Se, Te) around the 3*d*–4*f* absorption edge. The resonance effect for Tm 4*d* emission occurs through partial decay channels of the 3*d*–4*f* excited states. The lifetime-broadening phenomenon, which depends strongly on the binding energy, is also employed here for elucidation of 4*d* photoelectron spectral features. The behavior of a particular decay channel, referred to as 3*d*–4*d*4*f*, followed by preferential excited states was studied extensively. © 1998 Elsevier Science B.V.

Keywords: Resonant photoemission; Rare earth compounds; Lifetime broadening; Core level

1. Introduction

Photoemission spectroscopy has been widely utilized to characterize the final-state multiplet structures of the inner electronic shells of atoms with fundamental interest [1,2]. Its importance is enhanced especially for rare earth systems, where the multiplet structures are complex owing to the existence of the unfilled and localized 4*f* shell [1–3]. Considerable attention has been paid to observing the inner-shell line width in photoemission by introducing the relaxation and decay of core holes [4,5]. The dynamics of a core hole collapsing to its ground state can be observed directly through lifetime-broadened features in the core-level photoemission spectra. Recently, Ogasawara and co-workers studied the lifetime effect on the multiplet structure of 4*d* X-ray photoemission (XPS) spectra for heavy rare earth systems [6]. They showed that the lifetime-broadening effect on the multiplet structure of the 4*d* XPS spectra varies strongly with binding energy. It would be very interesting to know the effect on the final state through lifetime broadening in core-level photoemission depending on the excitation conditions. In order to investigate these complex features of core-level photoemission spectra in more detail, the resonant photoemission technique may be useful.

Resonant enhancement is generally caused by the coherent superposition of a direct electron emission and an Auger-like emission followed by Coster–Kronig or super Coster–Kronig decay. This spectroscopic process has already been established as an essential technique for investigating the behavior of

[1] Visiting scientist on leave from Physics Department, University of Cukurova, 01330 Adana, Turkey.

PII S0368-2048(97)00183-7

strongly correlated electrons; for example, 4*f* electrons in rare earth metals and their compounds [7–9].

The thulium ion in thulium compounds is known to take two forms: Tm^{2+} and Tm^{3+}. Because of the different ionic states of thulium, these compounds show different physical and electrical properties. Recently some resonant photoemission studies were reported for thulium compounds. It was found in these experiments that a large resonant enhancement occurs in Tm 4*f* emission around the Tm 4*d* absorption edge [8,9] and also around the Tm 3*d* absorption edge [10,11]. The valence structures of these compounds were investigated precisely by those experiments. The results are consistent with those obtained from other experiments such as magnetic susceptibility measurements. It was found that metallic TmS can be considered as almost trivalent, TmTe is divalent and shows semiconductor nature, and TmSe is treated as homogeneously mixed valence [12]. In the resonant photoemission, it is supposed that the core hole may decay via several routes following the absorption process. In the case of 3*d*–4*f* absorption, every possible decay channel to 3*d* core holes causes excitation of the $3d_{5/2}$ (only at the $3d_{3/2}$ edge), 4*f*, 4*d*, 4*s*, 4*p*, 5*s*, 5*p* or some satellite electrons to a continuum state [7,10].

So far, most of the resonant photoemission experiments on thulium compounds and others based on heavy rare earth elements were mainly confined to studying the 4*f* and 5*p* levels around the 4*d* absorption edge. The resonance behavior of deeper core levels, such as the 4*d*, has not been studied so extensively. The results by Laubschat et al. represent a preliminary report related to the resonance effect in the 4*d* photoemission at the 3*d* absorption edge for some heavy rare earth compounds [10]. Although they explained the resonance effect in Tm 4*d* photoemission by means of the energy distribution curve (EDC) and constant initial state (CIS) results for the trivalent compound $TmAl_2$, they did not discuss the existence of 4*d* multiplet structures and the corresponding resonance behavior. There are also some results discussing the 4*d* core-level resonant effect for europium [13,14]. For example in [13], the authors discussed the resonance effect of the Eu 4*d* core level at the excitation energies of the 3*d*–4*f* absorption edge. The 4*d* multiplet structure in the final state was not observed in their results. But we must consider the final-state multiplet structure in the 4*d* core-level photoemission of any heavy rare earth system to discuss its resonance behavior. Furthermore, in the case of thulium compounds, the contribution of divalent and trivalent components should be included to describe resonant photoemission completely. This requires a detailed study for Tm 4*d* resonant photoemission by considering the multiplet structure and different valence components.

In this paper, we present the results of a 3*d*–4*f* resonant photoemission study of the 4*d* level for TmS and TmSe. We discuss the lifetime-broadening effect in the 4*d* emission depending on the multiplete structure. At the same time, we give an explanation of the different decay channels connected to the peaks of the 4*d* multiplet and thulium valences followed by the 3*d* resonance absorption. The results of theoretical calculations are compared with the experimental ones at every stage.

2. Experiment

The experiments were performed in the same way as described in our previous report for the 3*d*–4*f* resonant photoemission of TmX [11]. The 4*d* photoemission experiments around the 3*d* absorption edge of TmX were performed at the beam line, BL7A, of the UVSOR facility, which employs a YB_{66} double crystal monochromator. A VG ESCALAB-220i-XL photoelectron analyser system, with a base pressure of less than 2×10^{-10} torr, was connected to the beam line for these experiments. The overall energy resolution of the core-level photoemission spectra was less than 1 eV both for on- and off-resonant conditions. The surfaces of the single-crystal samples were cleaned by Ar-ion bombardment or by scraping. Oxygen contamination was checked by monitoring the O (1*s*) XPS peak and found to be negligible.

3. Calculation

We have calculated the on- and off-resonant photoemission spectra of the 4*d* core level for Tm^{2+} and Tm^{3+} ions by using an atomic model with spherical symmetry. The initial states are taken to the lowest states given by Hund's rule, which are $^2F_{7/2}$ for Tm^{2+} ions ($4f^{13}$) and $^3H_6$ for Tm^{3+} ions ($4f^{12}$). The method is

the same as that used in another report [9,11]. The final states of $3d \rightarrow 4f$ X-ray absorption spectra (XAS) are identified by several intermediate states of resonant photoemission with $3d^9 4f^{n+1}$ configuration (n = 12 or 13). There are one and four intermediate states for the Tm^{2+} and Tm^{3+} ion, respectively.

There are many decay channels from the intermediate states. The most important channels are $3d$–$4f4f$, $3d$–$4d4f$ and $3d$–$4d4d$ Auger decay. We include only these three channels in the calculation for simplicity. This is a fair approximation, because decay processes other than the $3d$–$4d4f$ affect the resonant $4d$ photoemission spectra indirectly through the lifetime broadening in the intermediate state. The parameter values used in the calculation are the same as those in [11]. A linear energy-dependent function $\Gamma = 0.1(E_B - E_0)$ eV, where E_0 is the lowest binding energy in the $4d$ XPS, is used to approximate the lifetime-broadening effect of $4d$ photoemission final states, taking into account that the lifetime of $4d$ XPS depends strongly on the multiplet term [6].

4. Results and discussion

4.1. XPS spectra of the trivalent Tm 4d core level

As mentioned in Section 1, TmS is known to be an

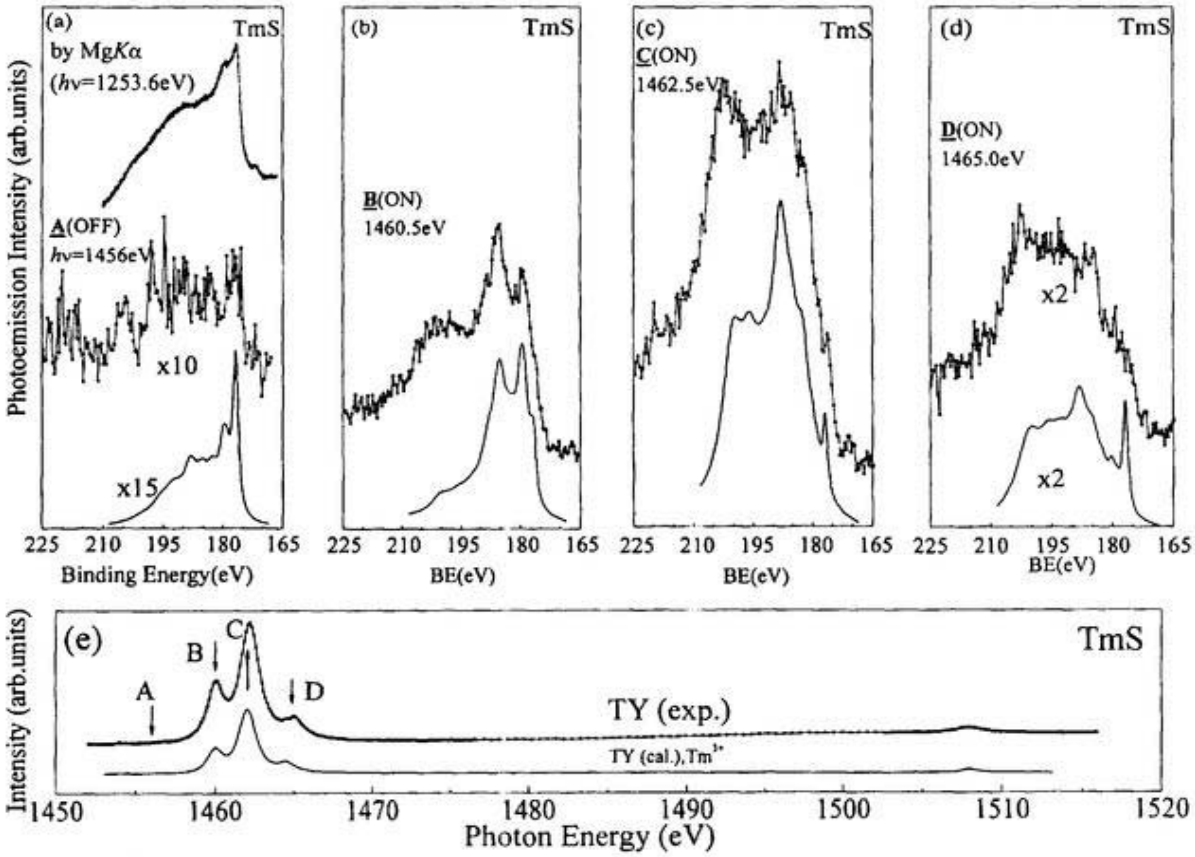

Fig. 1. (a)–(d) Tm $4d$ resonant photoemission spectra of TmS. (a) shows the off-resonant spectrum along with the XPS spectrum excited by Mg K_α radiation; (b)–(d) show the on-resonant spectra. All solid curves represent the calculated spectrum for each resonance condition of the trivalent thulium ion. (e) $3d$–$4f$ total photoelectron yield spectrum for the mostly trivalent compound, TmS. B, C and D indicate the resonance peak maxima, corresponding to the three resonant conditions of the trivalent thulium ion, and A shows the off-resonant condition. The calculated absorption spectrum for a trivalent thulium ion is also shown for comparison.

almost trivalent compound. In order to study the 4*d* core-level photoemission spectra for a trivalent ion, we show the results of TmS in this section. Fig. 1(a)–(d) show the on- and off-resonant 4*d* core-level photoemission results for TmS at various photon energies along with the XPS spectrum excited by Mg K_α radiation. The spectra show almost trivalent nature, but with a small amount of the divalent component. The backgrounds are subtracted by Shirley's method for all photoemission spectra [15]. The excitation energies indicated by letters (A to D) are selected from the TY (total photoelectron yield corresponding to absorption) spectrum shown in Fig. 1(e). Three of these excitation energies (B to D) represent the resonant conditions of the trivalent thulium ion, i.e., corresponding to $^3H_6$, $^3G_5$ and $^1H_5$ intermediate states. It is noticed that the 4*d* spectra are greatly enhanced (about 10 times the off-resonant one) under the 3*d*–4*f* resonant condition. The resonance effect of the spectra in Fig. 1(b)–(d) is explained by considering the interference between the direct 4*d* photoemission and the 4*d* excitation to continuum state due to the decay channel, $3d^{10}4d^{10}4f^{12} + h\nu \rightarrow 3d^9 4d^{10}4f^{13} \rightarrow 3d^{10}4d^9 4f^{12} + \varepsilon l$. This is one of the autoionization channels taking place in the 3*d* core-hole decay process as described in Section 3. A similar phenomenon (but with a different number of 4*f* electrons) has been reported for europium [13]. Instead of a single 4*d* peak in [13], we observed several multiplet peaks in both off- and on-resonant spectra as in Fig. 1(b)–(d). Each 4*d* multiplet spectrum is extended over the binding energy width of 40 eV [6]. Every possible final state in the 4*d* multiplet for the Tm^{3+} ion was calculated from line spectra in [6]. The measured 4*d* spectrum was considered as the convoluted form of these line spectra by lifetime broadening and the experimental resolution. The off-resonant spectrum excited by Mg $K\alpha$ radiation in Fig. 1(a) also shows the complex multiplet structures.

In order to describe the resonance effect of the 4*d* multiplet peaks we have to consider the preferential decay channels of individual excited states, i.e., the decay process of an intermediate state. Some of the final states are considered to take part strongly in the decay excitation process and show relatively stronger resonant enhancement. For example, in Fig. 1(b), the spectrum at $h\nu$ = 1460.5 eV shows two dominant enhanced peaks with binding energies of ~180.5 eV and ~185.5 eV. Calculation also shows almost the same feature. In the second and third resonance conditions (at $h\nu$ = 1462.5 and 1465 eV, respectively), the higher-binding-energy parts are more enhanced than lower-binding-energy parts. This distinction of the resonant effect in 4*d* multiplet peaks depends on the strength of the relevant Auger decay of the individual excited state. At the same time, the shape of both on- and off-resonant spectra is affected by the lifetime of the 4*d* core hole as described below. Accordance between the experiment and the calculation seems to be fairly good, but some differences between the observed results and calculations still exist for the on-resonant condition. For example, in Fig. 1(b) and (c), the peak at the binding energy of ~200 eV in the calculated spectra is not as intense as it is in the experimental ones. The possible reasons for this are discussed later.

We have already mentioned in Section 1 that the lifetime broadening of the several core states in the multiplet structure varies strongly with their binding energy. Because of the strong coupling between the core hole and the localized 4*f* shell [1], the constant lifetime concept [5] can be rejected for the complex multiplet structure. Therefore the lifetime of the core hole depends on the super Coster–Kronig (sCK) transition rate involving 4*f* electrons [4]. It has already been noted that the 4*d* photoemission depends on the preferential decay channels in the 3*d*–4*f* resonance. So we can assume that the sCK transition rate depends on the resonance-induced 4*d* final state.

The broadening effect according to selective Auger transition can be easily understood by the spin selection rule and the electron correlation effect [4–6]. The lower states are described with spin-parallel electrons (holes) separated by the Pauli exclusion principle. The states with spin-antiparallel electrons stay at the higher-binding-energy side and these electrons interact strongly. This higher-order interaction, which is denoted as the "configuration interaction" between continuum states by sCK decay, causes more a broadened feature in the higher-binding-energy side. The general tendency of the 4*d* spectrum is to be more broadened at higher binding energy than at lower one, so that the lower-binding-energy peaks are sharp with a long lifetime as shown for the spectrum excited by Mg $K\alpha$ in Fig. 1(a). However, the linearity between the spectral broadening and the binding energy does

not hold exactly in the higher-binding-energy region [6]. This is considered to be the reason why some of the multiplet peaks in the calculation do not show similar features to the experimental ones. To get better agreement between the calculated and experimental results, some kinds of modification considering the influence of preferential decay channels is needed.

Further, it is noticed that the 4*d* photoemission channel is a preferential one in the 3*d*–4*f* excitation, which is understood from the CIS results for 4*d* photoemission spectra (not shown here). The CIS spectra for the $^3H_6$ intermediate state show a large enhancement for each 4*d* multiplet peak, whereas the CIS spectrum for the 4*f* emission shows a smaller resonance for the $^3H_6$ intermediate state.

4.2. XPS spectra of the divalent Tm 4d core level

In order to study the resonant effect for divalent components, we have measured the 4*d* spectra for TmSe, a typical mixed-valence compound. Unfortunately we could not get a clean TmTe (typical divalent sample) surface during the beam time, and therefore we show here only an off-resonant XPS for TmTe by

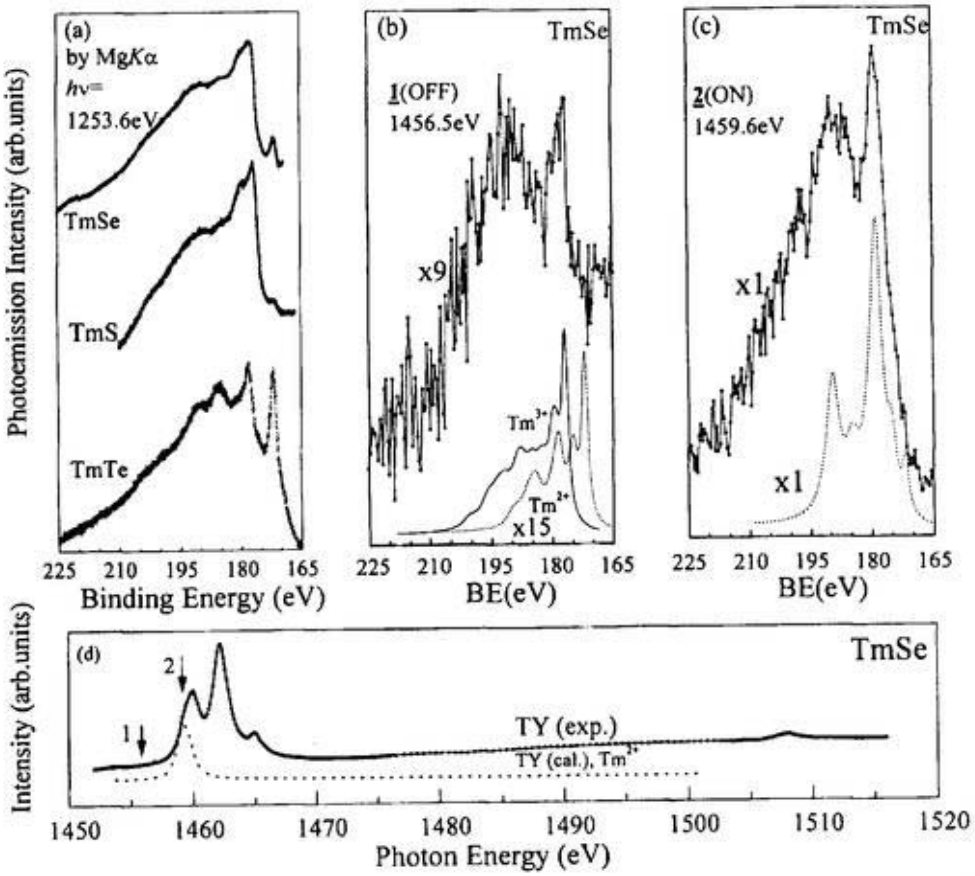

Fig. 2. (a) The XPS spectra of TmS, TmSe and TmTe excited by the Mg K_α line. The spectra are shown for reference to the off-resonant spectrum (b) and for clarifying the divalent and trivalent nature of the 4*d* core-level spectra. (b), (c) Tm 4*d* core-level photoemission spectra near the 3*d*–4*f* excitation conditions for TmSe. The excitation condition of spectrum (c) corresponds to the on-resonant condition of Tm^{2+} ions. The dotted curves represent the calculation for Tm^{2+} ions in each excitation condition. Because TmSe is mixed valence, the calculated spectrum of the Tm^{3+} ion (solid line) is also shown in the off-resonant spectrum. (d) 3*d*–4*f* total photoelectron yield spectra of TmSe. The energy positions 1 and 2 indicated by arrows show the off- and on-resonance conditions for divalent thulium ions. The calculated result for the divalent thulium ion is shown.

using the Mg K_α line. Fig. 2(b) and (c) show some of the 4*d* resonant XPS results for TmSe around the 3*d* excitation region. In order to clarify the divalent component of the 4*d* core level, the off-resonant XPS spectra for TmSe, TmS and TmTe are shown together in Fig. 2(a). The TY spectrum for TmSe in Fig. 2(d) has to be considered as a superposition of trivalent and divalent peaks. The dominant features of the TY spectra are similar to those of TmS in Fig. 1(e): i.e., trivalent peaks at the photon energy of 1460.5, 1462.5, 1465 and 1508 eV. In addition, there obviously exits a shoulder at the photon energy of 1459.6 eV which belongs to the divalent component [11], as shown in the calculated curve. This is the condition for obtaining the on-resonant photoemission spectrum of the divalent 4*d* core level in Fig. 2(c). Since the resonance condition of the trivalent peak is very close to that of the divalent one, it is rather difficult to separate completely the divalent parts from the trivalent ones. The photoemission spectra of TmSe at the trivalent resonant condition are not shown here because their spectral features are almost the same as those of TmS in Fig. 1. From the comparison with the calculated spectrum, it can be said that the spectrum in Fig. 2(c) shows almost divalent nature with a small amount of trivalent nature. The spectral shape of the buried trivalent part in this condition may be similar to that in Fig. 1(b). It is concluded that the 4*d* core level originating from the divalent thulium ion is also enhanced. It is clear from the comparison of experimental and calculated results that the lifetime broadening depending on the multiplet structure is also affected by the resonant condition as in the case of trivalent 4*d* spectra.

Since the off-resonant spectrum in Fig. 2(b) shows mixed-valence nature, we could not separate the divalent components. The calculated results for both divalent and trivalent parts are shown for reference. From the comparison of the off-resonant XPS spectra for the three samples in Fig. 2(a), we can estimate that the divalent part of 4*d* peaks stays at the lower-binding-energy side of the trivalent one. The peak at the binding energy of ~172.5 eV can be considered as the first peak of the divalent part. However, it is difficult to clarify other peaks because the multiplet peaks from the divalent component are superposed on the trivalent one at the higher-binding-energy side.

5. Summary

We have presented results concerning resonant photoemission of the 4*d* core level for thulium monochalcogenides around the 3*d*–4*f* excitation photon energy. It was found that the final-state multiplet of the 4*d* core level belonging to both the trivalent and divalent components resonates strongly at the 3*d*–4*f* absorption edge. The resonance behavior of 4*d* multiplet peaks is attributed to the involvement of the preferential decay channels of individual excited states after 3*d*–4*f* resonant absorption. The spectral features of the 4*d* multiplet in the final state vary according to the excitation conditions and different thulium valences. At the same time, the lifetime-broadening phenomenon is also introduced to describe this variation of spectral shape. This means that the lifetime-broadening effect, which is explained by considering the spin selection rule and the electron correlation effect between core holes and valence electrons, can be employed for both off- and on-resonant conditions. It does specify that the lifetime broadening of the multiplet states changes strongly with binding energy by the help of the resonant effect. Calculations in which such decay processes are considered contain the same arguments as our experiments.

Acknowledgements

This work was supported by the Joint Studies Program (1996–1997) of the Institute for Molecular Science. The authors would like to thank the staff members of the UVSOR facility for their kind help during experiments. Y.U. received financial support from the Scientific and Technical Research Council of Turkey (TUBITAK).

References

[1] A. Kotani, Inner shell photoelectron process in solids, in: G.V. Marr (Ed.), Handbook on Synchrotron Radiation, vol. 2, North-Holland Physics Publishing, Amsterdam, 1987.
[2] A. Kotani, H. Ogasawara, J. Electron Spectrosc. Relat. Phenom. 60 (1992) 257.
[3] P. Kowalczyk, N. Edelstein, F.R. McFeely, L. Ley, D. Shirley, Chem. Phys. Lett. 29 (1974) 491.

[4] E.G. McGuire, Phys. Rev. A9 (1974) 1840.
[5] M. Ohno, G. Wendin, Phys. Rev. A31 (1985) 2318.
[6] H. Ogasawara, A. Kotani, B.T. Thole, Phys. Rev. B50 (1994) 12332.
[7] J.P. Connerade, J.M. Esteva, R.C. Kartanak (Eds.), Giant Resonances in Atoms, Molecules and Solids, Plenum Press, New York, 1987.
[8] S.-J. Oh, J.W. Allen, I. Lindau, Phys. Rev. B30 (1984) 1937.
[9] Y. Ufuktepe, S. Kimura, T. Kinoshita, K.G. Nath, H. Kumigashira, T. Takahashi, T. Matsumura, T. Suzuki H. Ogasawara, A. Kotani, submitted to J. Phys. Soc. Jpn.
[10] C. Laubschat, E. Weschke, G. Kalkowski, G. Kaindl, Physica Scripta 41 (1990) 124.
[11] T. Kinoshita, Y. Ufuktepe, K.G. Nath, S. Kimura, H. Kumigashira, T. Takahashi, T. Matsumura, T. Suzuki H. Ogasawara, A. Kotani, J. Electron Spectrosc. Relat. Phenom., in press.
[12] E. Bucher, K. Andres, F.J. di Salvo, J.P. Maita, A.C. Gossard, A.S. Cooper, G.W. Hull Jr., Phys. Rev. B11 (1975) 500.
[13] U. Becker, H.G. Kerhoff, D.W. Lindle, P.H. Kobrin, T.A. Ferret, P.A. Heimann, C.M. Truesdale, D.A. Shirley, Phys. Rev. A34 (1986) 2858.
[14] S. Cramm, U. Grabowski, C. Kunz, J. Schimdt-May, F. Senf, L. Incoccia, J. Electron Spectrosc. Relat. Phenom. 42 (1987) 89.
[15] D.A. Shirley, Phys. Rev. B5 (1972) 4709.

ELSEVIER

Journal of Electron Spectroscopy and Related Phenomena 1 (1999) 000–000

JOURNAL OF ELECTRON SPECTROSCOPY and Related Phenomena

Study of magnetic linear dichroism (MLD) for different thickness of Ni thin film grown on ferromagnetic Co (001) in element specific photoemission

Krishna G. Nath[a,*], Yuichi Haruyama[b], Shin-ichi Kimura[b,c], Yüksel Ufuktepe[b,1], Toyohiko Kinoshita[b]

[a]Department of Structural Molecular Science, The Graduate University for Advanced Studies, Okazaki 444-8585, Japan
[b]UVSOR Facility, Institute for Molecular Science, Okazaki 444-8585, Japan
[c]Graduate School of Science and Technology, Kobe University, Kobe 657-8501, Japan

Abstract

The magnetic linear dichroism (MLD) was used to study the magnetic properties of Ni-ultrathin film grown on ferromagnetic substrate Co(001). The MLD in photoemission has been measured for either the valence Ni3*d* states around the Ni3*p* threshold or 3*p* core level. Our dichroism measurements of the valence Ni3*d* states conclude that the resonance effect is present on MLD for '6eV-satellite' in the valence band photoemission whereas the main valence band peak shows nearly same MLD signal for the both on and off resonance. It is shown for the thinner film that the dichroism from Ni and Co3*p* core levels shows same sign with each other. This means that the Ni and Co are ferromagnetically coupled.

Keywords: Thin film; Ferromagnetic substrate; Linear dichroism; 6eV-satellite

1. Introduction

It is now well known and firmly established that the ultrathin film in nanometer range of 3*d*-materials often shows very interesting and striking magnetic properties different from its bulk. Because of rich variety of unusual magnetic properties, the thin film magnetism is getting much more interest to both experimentalists and theoreticians [1–4]. By varying the preparation conditions, i.e. different substrates (non-magnetic, magnetic or semiconductor), substrate temperatures or film thickness, one can modify the electronic structures as well as the magnetic properties of the film.

Magnetic dichroism (MD) measurement in both the photoemission and photoabsorption is considered to be one of the most powerful methods to study such kind of magnetism [2,3]. It provides information of both the surface and interface magnetism. The absolute value of MD intensity can be used to identify the degree of magnetic ordering, since it is proportional to the net magnetization of the system [4]. The study of element specific magnetism selecting different electronic levels is very useful when the thin film system consists of more than one element. MD experiment in the photoelectron spectroscopy can be performed by using circularly, linearly, or

[1]Visiting scientist on leave from Physics Department, University of Cukurova, 01330 Adana, Turkey.
*Corresponding author. Tel.: +81-564-557403; fax: +81-564-547079; e-mail: nath@ims.ac.jp

0368-2048/99/$ – see front matter
PII: S0368-2048(98)00455-1

unpolarized light [2–7]. A variety of experimental geometry has been introduced so far to carry out several dichroism experiments. According to the experimental condition, the available techniques are known as MLD (magnetic linear dichroism), MCD (magnetic circular dichroism), MLDAD or MCDAD (AD: angular distribution) in photoemission and absorption. When we use linearly polarized (s- and p-polarized) or unpolarized (mixed state of s- and p-polarized) light, the experiments are performed only by changing the directions of magnetization keeping the entire geometry fixed. In a pioneering work, Roth et al. [6] studied the MLD and MLDAD effect for Fe(001) using linearly s- and p-polarized light. In the case of MLD, the plane of two orthogonal magnetization directions is nearly parallel to the plane of electric vector (E) of s-polarized light. But in MLDAD, the plane of electric vector (E) of p-polarized light is perpendicular to the magnetization plane. In this case, the magnetization directions are opposite to each other and the dichroism signal is affected by photoelectron diffraction effect. To perform the MD in photoemission experiment by our apparatus [7], the geometry of MLD is more suitable. In the present study, we report the results of the MLD in valence band and 3p core level photoemission spectra for Ni/Co(001) system.

The reasons why we choose the Ni/Co system are as the followings. At first, it concerns the element specific photoemission for Ni3d states. It is now experimentally established that the Ni on Cu(001) substrate shows a transition of magnetization from in-plane to out-of plane. This transition starts at 6.7 ML (monolayer is derived from the interlayer distance, d=1.70 Å and nearest neighbor distance a_p≈2.51 Å) and continues up to 11 ML [8]. In our experiment, we wanted to concentrate on only in-plane magnetization region by avoiding any in-plane to perpendicular transition for Ni-film. So Ni on Cu confines our option into a limited thickness range below 6.7 ML. In the case of Ni film of less than 6.7 ML on Cu(001), the Ni3d emission is overlapped with Cu3d emission. Especially, the Ni 6-eV satellite structures are overlapped with the tail of the broad 3eV–Cu3d emission. As a result, the element specific emission is not possible for Ni 6eV-satellite peak from Ni/Cu system. Instead, if we use different substrate, for example Co, then we can get satellite peak as a pure element specific emission because there is no Co emission around the satellite region.

Secondly, although Ueda et al. [9] reported the MLDAD and the MCDAD effect for the bulk Ni(110) sample around the 3p excitation threshold, it is interesting to know whether the resonant effect on the MLD signal for the valence band of Ni-thin film system occurs or not.

Finally, it is very curious to study the capability of epitaxial growth and corresponding magnetic phases of Ni on ferromagnetic Co. Comparing the magnetism of any uncoupled film (ferromagnetic film on non-magnetic substrate, Ni/Cu) with coupled film (ferromagnetic film on magnetic substrate, Ni/Co) is also technologically influential. The Ni/Co system has not been extensively studied like Ni/Cu system. The MUDAD result for Ni2p level for 12 ML Ni on Co was reported by Schneider et al. [10]. This can be considered as a primary result of this system. So it is important to study the magnetism of Ni/Co for different Ni-thickness.

2. Experiments

The experiments were performed on the plane grating monochromator beamline BL5B at the UVSOR facility, Institute of Molecular Science, Okazaki. The VG ESCALAB 220i-XL [7], a commercial electron analyzing system with base pressure of 2×10^{-10} mbar, was connected to the beam line. The total energy resolution of the photoelectron spectra at photon energy of 67.2 eV was about 300 meV, which was estimated from the width of the Fermi level in the Ni valence band spectra. The photoemission experiments and film evaporation were carried out at room temperature. The Cu (001) substrate was prepared by several cycles of Ar ion sputtering and subsequent careful annealing until sharp LEED pattern was observed. The magnetic substrate Co was grown on Cu to thickness of approximately 10 ML. The Co film is known to exhibit a tetragonally distorted FCC structure having layer spacing of ~1.73 Å along Co [001] direction [11]. The Ni film evaporated on the FCT Co(001) also shows same LEED pattern as Co on Cu(001). We use some considerations to estimate the film growth structure of Ni on Co. The Co-film on Cu

grows in a nearly perfect layer by later mode. On the other hand, Ni on Cu shows also tetragonally distorted FCC structure with vertical layer spacing ≈1.70 Å (for 5–11 ML) [12]. Because the close lateral lattice match between Co and Cu, we expect that Ni/Co(001) exhibits similar structures to those of Ni/Cu(001). Here we do not consider the effect of interface energies and surface free energies of Ni/Co and Ni/Cu that may modify the details of growth mode. High purity (4 N) Ni and Co rods were used for the evaporation. The deposition rate, ~0.8 ML/min, was calibrated by a quartz thickness monitor placing the same position of sample before and after the deposition.

The geometry of the MLD experiment is shown in Fig. 1. The sample surface is determined to be parallel to the *XY* plane. Cu[100] direction is along *Y*-axis. The s-polarized light with electric vector (*E*) impinges on the sample surface at an angle $\alpha=15°$ along *Y*-axis out of *XY*-plane. Photoelectrons are collected at an angle $\theta=8°$ out of the sample *Z*-axis (see inset). The film was magnetized along *X*- and *Y*-axis. It is not confirmed about the easy magnetization direction for Ni/Co(001) system because sufficient information has not been reported about this system. But in the present study, we successfully magnetize the sample along [100] direction and observe the MLD. Two spectra, $I(M_x)$ and $I(M_y)$, were recorded individually after the magnetization of the film along the *X* and *Y*-directions in the *XY*-plane. The dichroism signal is obtained by calculating the asymmetry, i.e. the difference between those two spectra divided by sum of them, $[I(M_x)-I(M_y)]/[I(M_x)+I(M_y)]$.

3. Results and discussion

3.1. Ni-3d MLD

In Fig. 2(a), we show the photoemission spectra of valence band region for different thickness (n=ML) of Ni on Co(001) at $3p$–$3d$ resonant condition; $h\nu=67.2$ eV. The photoemission spectra except for $n=0$ show the two dominant peaks. One is located near the Fermi level known to be as main band peak

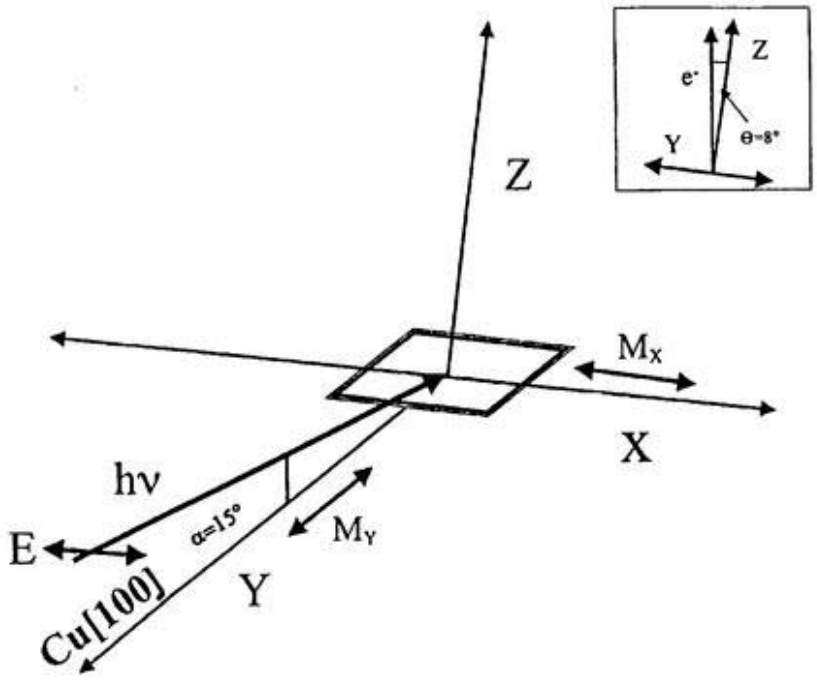

Fig. 1. Schematic geometry of MLD experiment (See the text).

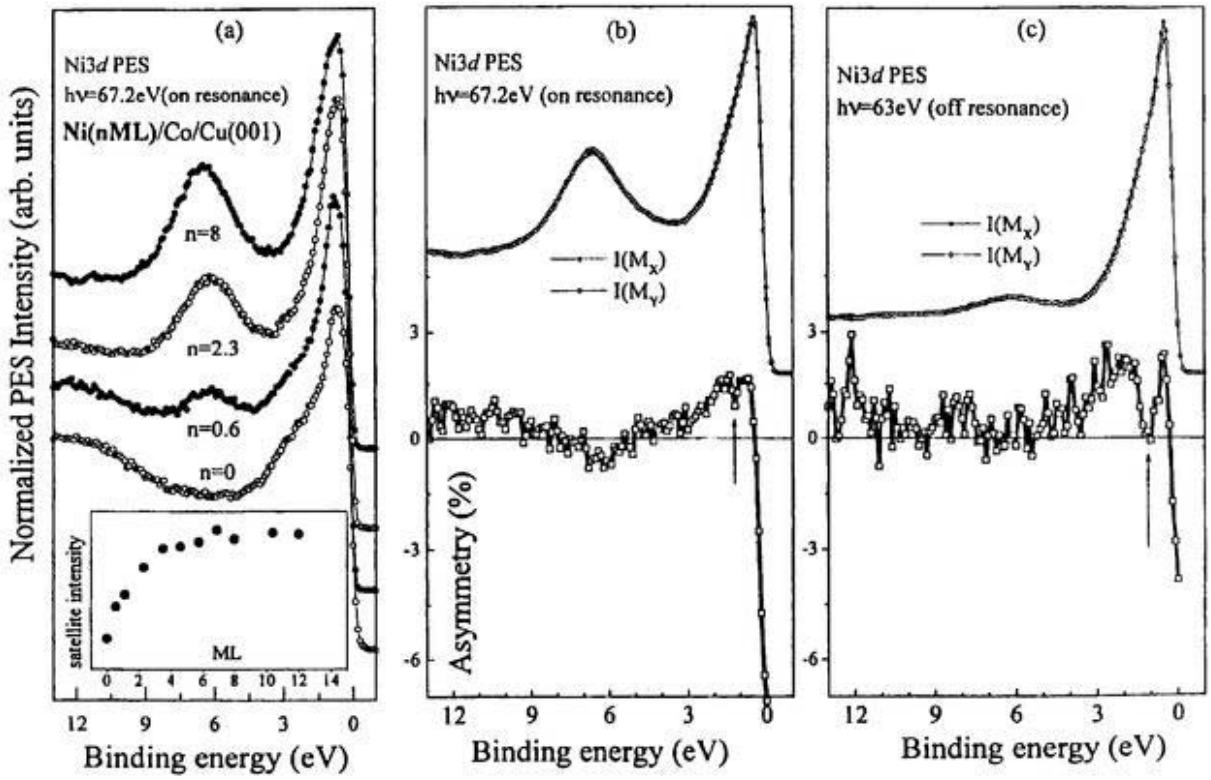

Fig. 2. : (a) Photoelectron intensities of Ni3*d* states for different thickness (n=ML) of Ni grown on Co(10 ML)/Cu(001) at Ni3*p*–3*d* on resonant condition. The variation of 6 eV-satellite peak intensity as a function of Ni thickness is shown in inset. The satellite intensity is normalized by the intensity of maximum thickness (n=12). (b, c) Photoemission spectra (upper part) and corresponding asymmetry (lower part) at on and off resonant conditions, respectively. The thickness of Ni-film was ~8 ML. In these photoelectron spectra, the full circle represents the $I(M_x)$ for $M\|X$, i.e. $(M\|E)$ and open circle does $I(M_y)$ for $M\|Y$, i.e. $(M\perp E)$. The photon energies were 67.2 eV (on resonance) and 63 eV (off resonance). The intensity is normalized so as to obtain the same background count rates of the two spectra for the higher binding energy side.

with Ni3d^9 configuration. Other peak stays at 6 eV below the main peak. This is the '6 eV-satellite' peak assigning as Ni3d^8 final state configuration. This satellite peak shows a strong resonant enhancement at the 3*p*-excitation energy that was explained via super-Coster–Kronig (sCK) decay process [13]. From these spectra, it is clear that the 6 eV-satellite emission is not overlapped with any signal from Co-site. Thus the satellite peak can be considered as a pure element specific emission. The satellite peak intensity in these spectra is increased with increasing the film thickness. But at nearly 4.5 ML (8 Å), the intensity shows almost saturated value [see inset]. In the case of Ni3d^9 main peak, we could not generalize the variation of peak intensity because the Ni-main peak is overlapped with Co3*d* band emission. If we correlate the changing nature of satellite peak to the main peak, same behavior can be estimated for main peak. Besides, the electron mean free path with kinetic energy around 60 eV is not more than 8 Å. So, above 4.5 ML of Ni, the Ni3d^9 main peak is considered to be Co-free emission.

In Fig.2(b) and (c), the MLD results for Ni(8 ML)/Co(10 ML)/Cu(001) taken at the photon energies of 67.2 eV (on resonance) and 63 eV (off resonance) are shown, respectively. It is assumed here that no Co-emission is present in the whole energy range of photoemission as explained above.

In the upper panels [Fig. 2(b) and (c)], the two spectra represent the intensities for two different magnetized states, one is along to X-axis (full circle) and another is parallel to Y-axis (open circle). The lower panels in Fig. 2(b) and (c) show the asymmetry between those two spectra. The observed MLD signal is the direct evidence of the magnetism (in-plane magnetization) of the Ni/Co(001) system.

In the lower panel of Fig. 2(b), both the main peak ($3d^9$) and the satellite peak ($3d^8$) show asymmetry (i.e. MLD) but in opposite direction to each other. In the previous study, Ueda et al. [9] reported the results for MLDAD and MCDAD measurements for the bulk Ni(110) sample. In MLDAD, the 6 eV-satellite does not show any prominent dichroism signal whereas the main peak shows signal at $3p$ excitation threshold. On the other hand, the MCDAD is rather strong for both the 6 eV-satellite and the main peak with opposite sign. Our result is similar to that reported for the MCDAD result. The shape of asymmetry for the main peak is almost same for the off resonant condition in Fig. 2(b) and on resonant condition in Fig. 2(a). But the dip structure (marked by arrow) at the binding energy of ~1.2 eV of off resonant condition is stronger than that of on resonant condition. Probably this variation may arise from the photon energy dependence from different Ni3d states and its polarization effect on the MD signal. The asymmetry for satellite peak at off resonance is not so strong as the on resonance one, although it shows the opposite trend from the main peak. It can be interpreted that the $3d$–$3p$ resonant process mainly guides intensity of the asymmetry for 6 eV-satellite. We could not estimate the contribution of dichroism signal from different multiplet peaks around the satellite region. A detailed theoretical interpretation needs for clear understanding of dichroism behavior in the satellite region.

We also measured Ni3d MLD for 11 ML Ni film on the same Co(001) substrate at Ni3p resonance (not shown here). This thicker film also shows dichroism with positive direction for main peak and negative direction for satellite peak. So, 11 ML Ni film on Co(001) also indicates the presence of in-plane magnetization. But in the case of Ni film of 12 ML on Cu(001), we did not observe any dichroism for the both main peak and satellite peak under the same experimental geometry. This indicates that 12 ML Ni film on Cu does not show any in-plane magnetization that agrees with the results reported previously [8].

3.2. Ni–Co core level (3p) MLD

In the case of thinner film, for example, 2.3 ML (4 Å) on Co(001), the photoemission intensity of Ni3d states does not have saturated value. At the same time, the Ni3d main peak emission is not totally free from Co-valence band emission as shown in Fig. 2(a). As a result, some ambiguities are appeared to find out the true MLD signal for Ni of the both main peak and satellite peak. The magnetic properties from this kind of multilayer system can be easily studied by the core level spectroscopy, which is considered as an element specific measurement [4,14]. In Fig. 3, we show the MLD results for Ni3p and Co3p core levels that are measured simultaneously for 2.3 ML Ni-film. The experimental geome-

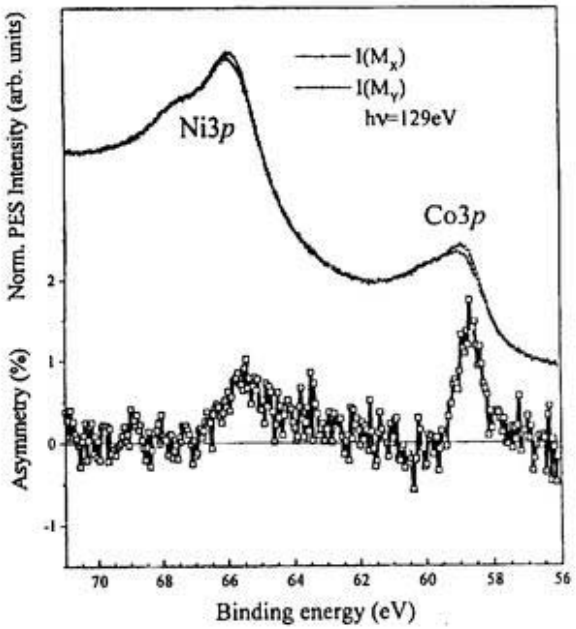

Fig. 3. : In the upper part, Ni3p and Co3p photoelectron spectra for two magnetized states measured simultaneously at the same experimental geometry are shown. The Ni-film was ~2.3 ML (4 Å) on 10 ML Co(001) substrate. The photon energy was 129 eV. The lower part shows the asymmetry where the MLD sign for two elements is in the same direction.

try was the same as Ni3*d* MLD measurement. The excitation photon energy was 129.0 eV. The lower panel in this figure shows the dichroism signal (asymmetry) for the both Co and Ni. The features of dichroism signal for the both Co3*p* and Ni3*p* levels consist of a sharp positive peak at lower binding energy and a broadened negative structure at the higher binding energy. The shape of Co3*p* MLD signal can be compared with the previous MLDAD results measured for Co-film on Cu(100) [15]. In the case of Ni3*p* MLD, our result is nearly similar to the experimental and calculated MCD results for bulk Ni(110) sample reported by van der Laan et al. [16]. Besides MCD [16], our Ni3*p* result is also comparable with the previous MLDAD result for the same bulk sample [17]. The same MLD signs (positive peak at lower binding energy) for these two elements indicate that the Ni–Co interface has ferromagnetic coupling. But from this result, we could not separate the individual contribution of MLD signal from Ni–surface and Ni–Co interface.

4. Conclusion

The magnetic properties of Ni ultrathin film of different thickness grown on ferromagnetic Co-substrate are studied by magnetic linear dichroism in element specific photoemission. We tried to identify the nature of MLD signal for different Ni3*d* states around the Ni3*p*–3*d* resonance. The measurement shows the dichroism signal for the both Ni main peak and satellite peak at on resonance condition of 8 ML Ni on Co. The sign of MLD for main peak is opposite to that of satellite peak. The dichroism signal for satellite region at off resonance condition is not so strong as that of the main peak. Thus it is predicted that the 3*p* resonant effect is present on the MLD of the 6 eV-satellite. We also studied 11 ML Ni in the same way. The result shows the same MLD feature as that of 8 ML Ni. In the case of 2.3 ML Ni, we select the 3*p* core level photoemission instead of valence band emission to ensure the element specific emission. It was found from the MLD signal that Ni and Co are ferromagnetically coupled at the interface. All Ni-films studied here show in-plane magnetization. In future, the magnetic and electronic states of the Ni on Co will be compared with the calculation.

Acknowledgements

The authors would like to thank the staff members of the UVSOR facility for their help during the experiments. This work is partly supported by the Grant-in-Aid for Scientific Research from the Ministry of Education, Science, Sports and Culture in Japan. YU received financial support from the Scientific and Technical Research Council of Turkey (TUBITAK).

References

[1] M.T. Johnson, P.J.H. Bloemen, F.J. A den Broeder, J.J. de Vries, Rep. Prog. Phys. 59 (1996) 1409.
[2] C.M. Schneider, J. Mag. Mag. Mater. 175 (1997) 160.
[3] H. Ebert, G. Schütz (Eds.), Magnetic Dichroism and Spin Polarization in Valence Band Photoemission, in Spin-orbit-influenced Spectroscopies of Magnetic Solids, Springer, Berlin, 1995.
[4] W.L. O'Brien, B.P. Tonner, Surf. Sci. 334 (1995) 10.
[5] D. Venus, Phys. Rev. B 49 (1994) 8821.
[6] Ch. Roth, H.B. Rose, F.U. Hillebrecht, E. Kisker, Solid State Commun. 86 (1993) 647.
[7] T. Kinoshita, K.G. Nath, Y. Haruyama, M. Watanabe, S. Yagi, S. Kimura, A. Fanelsa, J. Electron Spectrosc. Relat. Phenom. 92 (1998) 165.
[8] B. Schulz, K. Baberschke, Phys. Rev. B 50 (1994) 13467.
[9] S. Ueda, S. Imada, Y. Saitoh, T. Muro, M. Kasashima, A. Kimura, A. Kakizaki, S. Shuga, J. Electron Spectrosc. Relat. Phenom. 88–89 (1998) 191.
[10] C.M. Schneider, U. Pracht, W. Kuch, C. Chassé, J. Kirschner, Phys. Rev. B54 (1996) R15618.
[11] J.R. Cerdá, P.L. de Andres, A. Cebollada, R. Miranda, E. Navas, P. Schuster, C.M. Schneider, J. Kirschner, J. Phys. Condens. Mat. 5 (1993) 2055.
[12] K. Baberschke, Appl. Phys. A62 (1996) 417.
[13] C. Guillot, Y. Ballu, J. Paigné, J. Lecante, K. Jain, P. Thiry, R. Pinchaux, Y. Pétroff, L.M. Falocov, Phys. Rev. Lett. 39 (1977) 1632.
[14] C.T. Chen, Y.U. Idzerda, H.-J. Lin, G. Meigs, A. Chaiken, G.A. Prinz, G.H. Ho, Phys. Rev. B48 (1993) 642.
[15] H.B. Rose, T. Kinoshita, Ch. Roth, F.U. Hillebrecht, E. Kisker, Surf. Rev. Lett. 4 (1997) 915.
[16] G. van der Laan, M.A. Hoyland, M. Surman, C.F.J. Flipse, B.T. Thole, Phys. Rev. Lett. 69 (1992) 3827.
[17] Y. Saitoh, S. Ueda, T. Muro, S. Imada, S. Suga, A. Kimura, A. Kakizaki, Physica B 237–238 (1997) 397.

ELSEVIER

Journal of Electron Spectroscopy and Related Phenomena 92 (1999) 165–169

JOURNAL OF ELECTRON SPECTROSCOPY and Related Phenomena

Photoelectron spectromicroscopy experiments at the UVSOR facility[1]

T. Kinoshita[a,*], K.G. Nath[b], Y. Haruyama[a], M. Watanabe[a2], S. Yagi[a3], S.-i. Kimura[a], A. Fanelsa[c]

[a]*UVSOR Facility, Institute for Molecular Science, Okazaki 444-8585, Japan*
[b]*Department of Structural Molecular Science, Graduate University for Advanced Studies, Okazaki 444-8585, Japan*
[c]*Institut für Angewandte Physik, Heinrich-Heine-Universität Düsseldorf, Düsseldorf D-40225, Germany*

Abstract

Photoelectron spectromicroscopy experiments have been started at the UVSOR facility of the Institute for Molecular Science. The commercial system (FISONS instruments, ESCALAB 220i-XL) has been connected to two beamlines which cover the photon energy range of 10 eV–5 keV. It is expected that spatial resolution of 2 μm for the imaging mode and 20 μm for the spectroscopic mode can be achieved. In conjunction with monochromatized (and polarized) synchrotron radiation light from the UVSOR storage ring, it is planned to undertake some experiments using this apparatus, not only for surface science but also for spectroscopy of small samples.

As a demonstration of the apparatus, the magnetic domain image of Fe(110) surface with magnetic dichroism effect is shown. The photoemission spectra from small organic materials $(DI\text{-}DCNQI)_2$-M (M = Ag, Cu) are also presented.

Keywords: Microscopy; Photoelectron spectroscopy; Imaging; Magnetic domain; Organic materials

1. Introduction

Recent advances of photoelectron microscopy are very productive. Especially in the third generation synchrotron radiation (SR) light sources, the development of the photoelectron microscope with high spatial resolution becomes one of the most important plans in the community of the researchers of SR. Combining spectroscopy technique with microscope technique may give us a lot of advantages such as element-specific imaging of sample surfaces, possibility of studying very small samples, getting precise information from inhomogeneous surfaces and so on. For these kinds of studies, not only spatial resolution but also energy resolution (of photons and/or electrons) is the important factor. That is why we are using the term spectromicroscopy according to the review by Tonner et al. [1] and references therein.

So far, two types of photoelectron spectromicroscopies have been developed to achieve micro-analysis. One combines a micro-beam of photons obtained by a zone plate system or a mirror system with a conventional photoelectron analyzer. To get an element-specific image of the sample, the photoelectron

* Corresponding author: e-mail: toyohiko@ims.ac.jp; fax:+81-564-54-7079.

[1] Presented at the Todai Symposium 1997 and the 6th ISSP International Symposium on Frontiers in Synchrotron Radiation Spectroscopy, Tokyo, Japan, 27–30 October 1997.

[2] Present address: Institute of Materials Structure Science, High Energy Accelerator Research Organization (KEK) Oho 1-1, Tsukuba 305, Japan.

[3] Present address: Department of Material Science, Faculty of Science, Hiroshima University, Kagamiyama 1-3, Higashi-Hiroshima 724, Japan.

0368-2048/98/$19.00
PII S0368-2048(98)00118-2

signal is recorded from every position of the sample surface which is moved in very small steps. This is called a scanning photoelectron microscope. The other uses a special electron energy analyzer and an electrostatic lens elements and/or a magnetic lens elements to obtain a magnified image of the photoelectrons, in which light with normal beam size (several mm) can be used. There are also two possibilities of getting an element-specific image. One takes photoelectron signals as a function of photon energy without electron energy analysis, which has been established as photoelectron emission microscope (PEEM). Another analyzes the energy of photoelectrons, but spatial resolution is poorer than that of PEEM. Now the spatial resolution of these microscopes is almost coming to the region of several or several tenths of a nanometre [1].

Although it is rather difficult to construct photoelectron spectromicroscope equipment with high performance at the UVSOR facility, a second generation SR light source, there still exist many interesting subjects for photoelectron spectromicroscopy. In this paper, we introduce our photoelectron spectromicroscope equipment (with an electron energy analyzer) and show two examples of our results. One is magnetic domain imaging with linearly polarized or unpolarized light, and another is photoemission spectroscopy of small samples (DI-DCNQI)$_2$-M (M = Ag, Cu).

2. Photoelectron spectromicroscopy equipment at the UVSOR facility

Since it is rather difficult to obtain a micro-beam of photons with enough intensity at the UVSOR for bending magnet beamlines, we have chosen a way of magnifying the photoelectron image by an electrostatic and magnetic lens system. As reviewed by Holldack and Grunze [2], a commercial system of photoelectron spectromicroscopy is now available. They used the ESCASCOPE (FISONS Instruments) for X-ray photoelectron spectromicroscopy and performed some successful experiments at the BESSY. In their system, lateral imaging for defined kinetic energy electrons by multi-channel plate with a florescence screen is possible (imaging mode). Photoemission spectroscopy for the defined area is also possible (spectroscopic mode). Recently, FISONS Instruments modified the system and developed a new system called the ESCALAB 220i-XL. We connected this modified equipment to the UVSOR beamlines. The concept of the equipment is almost similar to the ESCASCOPE, but the performance is very much advanced. Especially, by using the additional magnetic lens (XL lens), the count rate of photoelectron signals and the spatial resolutions became better. In addition to the commercial system, we attached some components.

The schematic view of the system is shown in Fig. 1. It consists of a hemispherical electron analyzer with a radius of 150 mm, an electrostatic lens system, a magnetic lens system, an X-ray tube (MgK_α, AlK_α) for photoexcitation, a sputtering gun, and so on. In order to prepare well-ordered surfaces, the sample preparation chamber with low energy electron diffraction (LEED) optics, the evaporators, the quartz thickness monitor and the sample transfer system are attached to the main chamber. It is expected from the commercial argument that spatial resolution of 2 μm for the imaging mode and 20 μm for the spectroscopic mode can be achieved. The experiments are performed at the two beamlines BL5B [3] and BL7A[4] at the UVSOR. By using these two beamlines, we can perform photoelectron

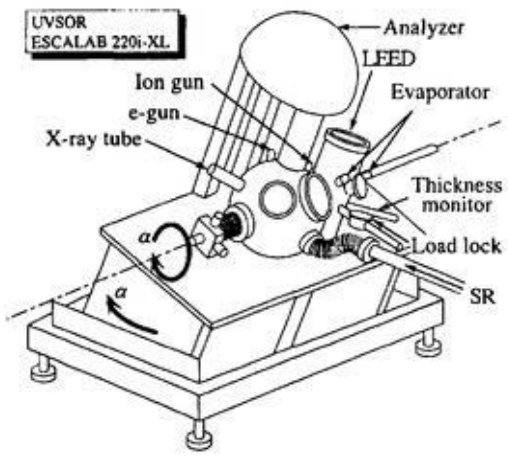

Fig. 1. Schematic view of the photoelectron spectromicroscopy equipment at the UVSOR (FISONS ESCALAB 220i-XL). To impinge SR light from oblique angle, the whole system is rotated by tilting the platform of the system. For preparation and characterization of samples, such as a LEED optics, evaporators, an ion gun, a quartz thickness monitor etc. are attached.

spectromicroscopy experiments with a very wide range photon energy region (from 10 eV to 5 keV). To impinge the SR light at an oblique incidence angle, we set-up the whole system on a rotary stand and connect the port to the end port of the beamline via a bellow tube. The maximum rotation angle is α = 7.5°, which is limited by the inner bore radius of the port for SR incidence in the analyzer chamber.

3. Application to magnetic domain imaging with linearly polarized or unpolarized light

In this section, we show the magnetic domain image with magnetic dichroism. The usual size of magnetic domains of ferromagnetic materials is known to be several hundred μm, which is suitable for the observation by the photoelectron spectromicroscope. There were several experimental examples in which the magnetic domains of the ferromagnetic films and surfaces were observed by photoelectron microscope. Most of the experiments were to observe the magnetic circular dichroism (MCD) effect in the spectra around absorption edges or in the photoemission spectra or in the Auger signals [1,2,5]. Recently, the possibility of observing the magnetic domain using linearly polarized light has also been suggested. Actually, the new type of magnetic linear dichroism (MLD) was observed [6] in total electron yield (absorption) spectroscopy. The magnetic domain image of the Fe(001) surface based on this effect is shown in [7], where the commercial PEEM system was used for imaging of secondary electrons. It has been shown that the combination of the MLD with the MCD gives us the overall information about the local magnetic moment of each magnetic domain.

Not only the MLD effect of absorption edges but also the MLD effect at photoemission peaks can be used for the magnetic domain imaging. Namely, the MLD [8] or magnetic linear dichroism in angular distribution (MLDAD) [9] effect of photoemission spectra may be useful for the magnetic domain imaging. We have succeeded in observing the magnetic domains of the Fe(110) surface using the MLD effect around the Fe $2p_{3/2}$ photoemission peak at BL7A [10]. The observed image is similar to that shown below (in Fig. 2a), but the contrast is clearer.

Since the unpolarized light can be considered as the incoherent superposition of s- and p-polarized lights, it is also possible to observe the magnetic dichroism effect in angle-resolved photoemission by using a conventional X-ray tube or a discharge lamp [11,12]. The effect is called as MDAD. In [12], the MDAD signal caused by Fe 3p photoemission spectra from the different sample positions was observed. We have taken the magnetic domain image of the Fe(110) surface by recording Fe 2p photoelectrons at E_B = 706 eV and at E_B = 704 eV binding energies as shown in Fig. 2(a). As discussed below (Fig. 2b), the maximum asymmetry difference of the MDAD was observed at this condition. The acceptance angle of photoelectrons was less than 6°. The emission angle of the photoelectrons was about 5° from the surface normal along the (100) direction, in which the maximum of the MDAD effect has been reported [11,12]. By considering the direction of easy axis of magnetization (100), the expected directions of the magnetic moment for the domains "A" (the bright area) and "B" (the dark area) are indicated. The imaging process accords to the way discussed in [2]. Fig. 2(b) shows the Fe 2p photoemission spectra (the detection area being 50 μm) from two different positions of the sample surface. The MDAD effect is observed reflecting the direction of the magnetic moment of each magnetic domain ("A" or "B").

Because the MDAD effect is not so large as shown in Fig. 2, the contrast of the image is not clear. This is one of the reasons why the zone boundary of two magnetic domains is not clearly observed. The MLD effect is also not as large as the MCD. Therefore, we plan to measure the MCD using a new beamline for circularly polarized undulator light at the UVSOR facility (BL5A) [13]. The experiment would be valuable for further studies of magnetic thin films.

4. Photoemission spectroscopy of very small samples

As an example of the photoelectron spectroscopy experiments of very small samples, we show here the valence band photoemission spectra of (DI-DCNQI)$_2$-M (M = Ag, Cu). Although some photoemission results for similar organic materials, (DMe-DCNQI)-M salts, have been reported [14], no

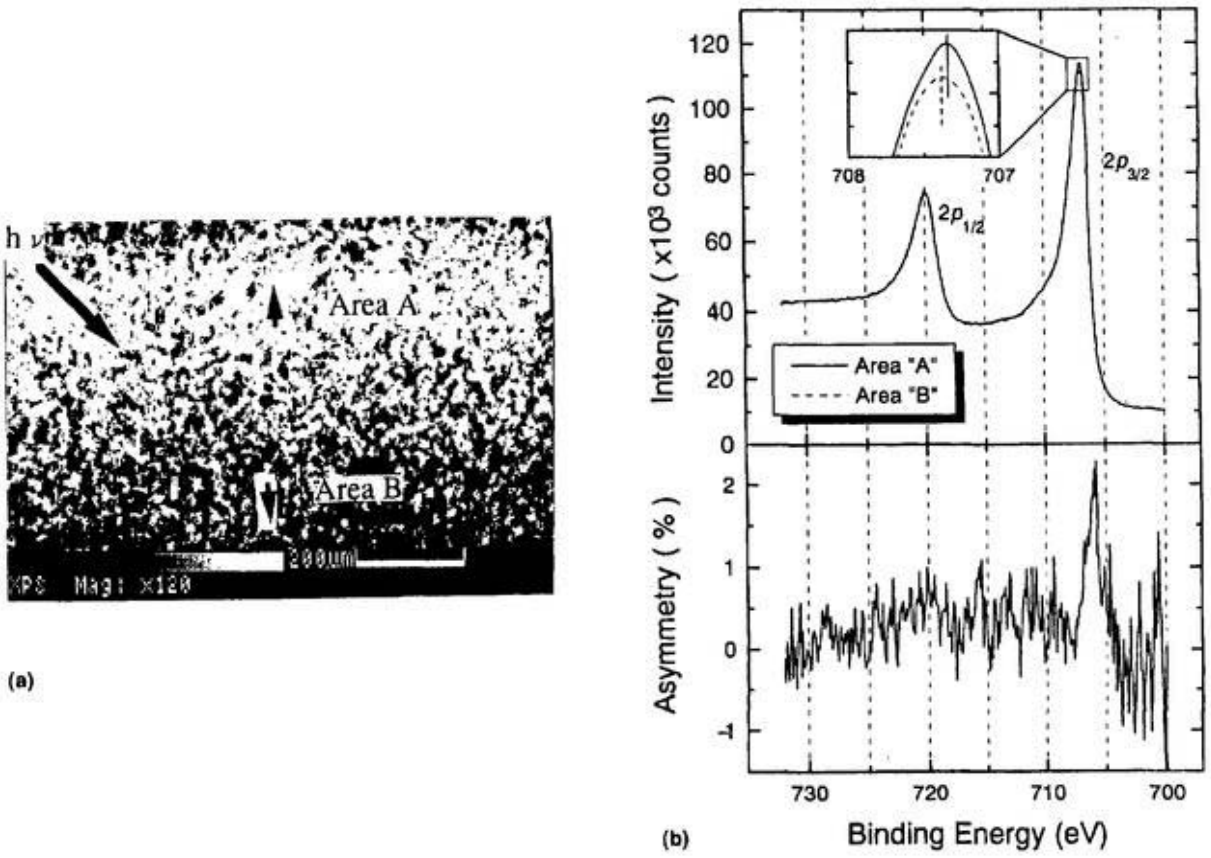

Fig. 2. (a) Magnetic domain image of Fe(110) surface by using MDAD effect. Al K_α X-ray line was used for photoelectron excitation. The unpolarized light was impinged from the upper left. The Fe 2p electrons at $E_B = 706$ eV and at $E_B = 704$ eV were corrected. After subtraction and normalization of the two sets of data, we got the magnetic domain image. The direction of the magnetic moment for each magnetic domain ("A" (bright) or "B" (dark)) is indicated (see text). (b) Small area (50 μm) photoemission spectra from two different regions ("A" and "B") of the Fe (110) surface excited by AlK_α X-ray line. The intensity is normalized so as to obtain the same background count rates of the two spectra for both the higher binding energy side and the lower binding energy side. The MDAD signal can be observed reflecting the magnetic domain information.

photoemission studies have been performed for (DI-DCNQI)$_2$-M. It is rather difficult to synthesize big samples for these kinds of materials. The size of samples used here was smaller than 1000 × 100 μm^2. It is expected from the NMR, conductivity and magnetic susceptibility measurements [15] that the (DI-DCNQI)$_2$-Ag should show the localized nature of Ag 4d electrons, whereas that of Cu should show the itinerant nature of Cu 3d electrons.

Fig. 3 shows the comparative photoemission spectra of (DI-DCNQI)$_2$-Ag and -Cu taken at $h\nu = 70$ eV. The detection area of the photoemission spectra was 50 μm, which is smaller than the sample size. The needle-shaped samples are mounted like bridges on the 1 mmϕ diameter holes of the sample holder. The photoelectrons were counted only when the detection area was fixed just on the sample, whereas no electrons were detected when the detection area was not on the sample. It is noticed from the figure that the Ag 4d bands are located around a 5 eV binding energy and localized within a 2.5 eV width. On the other hand, the Cu 3d bands seem to be situated around 3.5 eV and show a broader band width. The result is a direct evidence of the localized nature of Ag 4d electrons and the itinerant nature of Cu 3d electrons. We have also measured the photon energy

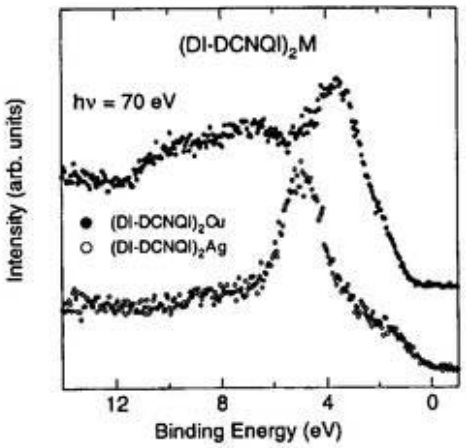

Fig. 3. Valence band photoemission spectra for (DI-DCNQI)$_2$-Ag and (DI-DCNQI)$_2$-Cu samples taken at $h\nu$ = 70 eV. The detection area was 50 μm.

dependence and the polarization dependence of the spectra, which will be described elsewhere [16].

It is known that these kinds of organic materials are easily damaged by radiation. If we use a micro-beam with high intensity, the spectral features may be immediately changed. In this sense, there still exists an advantage in performing the photoemission measurements for such kinds of small organic materials at the UVSOR facility using our spectro-microscopy system.

5. Summary

We have started photoelectron spectromicroscopy experiments at the UVSOR facility. The image of the magnetic domain of the Fe(110) surface with magnetic dichroism effect at the Fe $2p_{3/2}$ core level photoemission was presented. The valence band photoemission spectra for the small samples (DI-DCNQI)$_2$-M (M = Ag, Cu) were also shown.

Acknowledgements

This work is partially supported by a Grant-in-Aid for Scientific Research from Ministry of Education, Science, Sports and Culture. We thank Professor Kronmller for lending us a Fe(110) single crystal. We also would like to express gratitude to Professor Kisker and Dr Hillebrecht for their encouragement and discussion. Professor Kanoda and Dr Hiraki are acknowledged for providing the DCNQI samples. The staff members of the UVSOR facility are acknowledged for their experimental support.

References

[1] B.P. Tonner, D. Dunhum, T. Droubay, J. Kikuma, J. Denlinger, E. Rotenberg, A. Warwick, J. Electron Spectrosc. Relat. Phenom. 75 (1995) 309.
[2] K. Holldack, M. Grunze, Analytica Chimica Acta 297 (1994) 125.
[3] M. Sakurai, S. Morita, J. Fujita, H. Yonezu, K. Fukui, K. Sakai, E. Nakamura, M. Watanabe, K. Yamashita, Rev. Sci. Instrum. 60 (1989) 2089.
[4] T. Murata, T. Matsukawa, S. Naoé, T. Horigome, O. Matsudo, M. Watanabe, Rev. Sci. Instrum. 63 (1992) 1309.
[5] C. M. Schneider, in: H. Ebert, G. Schütz (Eds), Spin-Orbit-Influenced Spectroscopies of Magnetic Solids, Springer, Berlin, 1995, p.179.
[6] T. Kinoshita, H.B. Rose, Ch. Roth, D. Spanke, F.U. Hillebrecht, E. Kisker, J. Electron Spectrosc. Relat. Phenom. 78 (1996) 237.
[7] F.U. Hillebrecht, T. Kinoshita, D. Spanke, J. Dresselhaus, Ch. Roth, H.B. Rose, E. Kisker, Phys. Rev. Lett. 75 (1995) 2224; D. Spanke, J. Dresselhaus, T. Kinoshita, Ch. Roth, H.B. Rose, F.U. Hillebrecht, E. Kisker, J. Electron Spectrosc. Relat. Phenom. 78 (1996) 299.
[8] Ch. Roth, H.B. Rose, F.U. Hillebrecht, E. Kisker, Solid State Commun. 86 (1993) 647.
[9] Ch. Roth, F.U. Hillebrecht, H.B. Rose, E. Kisker, Phys. Rev. Lett. 70 (1993) 3479.
[10] T. Kinoshita, K. G. Nath, M. Watanabe, S. Yagi, S. Kimura, A. Fanelsa, UVSOR Activity Report 1996, 1997, p. 154.
[11] A. Fanelsa, PhD. Thesis, Düsseldorf University, 1996; A. Fanelsa, E. Kisker, J. Henk, R. Feder, Phys. Rev. B54 (1996) 2922.
[12] F.U. Hillebrecht, W.D. Herberg, Z. Phys. B93 (1994) 299.
[13] M. Kamada, K. Sakai, S. Tanaka, S. Ohara, S. Kimura, A. Hiraya, M. Hasumoto, K. Nakagawa, K. Ichikawa, K. Soda, K. Fukui, Y. Fujii, E. Ishiguro, Rev. Sci. Instrum. 66 (1995) 1537.
[14] I.H. Inoue, M. Watanabe, T. Kinoshita, A. Kakizaki, R. Kato, A. Kobayashi, A. Fujimori, Phys. Rev. B47 (1993) 12917; A. Tanaka, A. Chainani, T. Yokoya, T. Takahashi, T. Miyazaki, S. Hasegawa, T. Mori, Phys. Rev. B52 (1995) 7951.
[15] K. Hiraki, K. Kanoda, Synthetic Metals 86 (1997) 2103.
[16] Y. Haruyama, K. G. Nath, Y. Ufkutepe, S. Kimura, T. Kinoshita, K. Hiraki, K. Kanoda, in preparation.

ELSEVIER

Journal of Electron Spectroscopy and Related Phenomena 88–91 (1998) 377–384

JOURNAL OF ELECTRON SPECTROSCOPY and Related Phenomena

Resonant photoemission studies of thulium monochalcogenides around the Tm 3*d* threshold

T. Kinoshita[a], Y. Ufuktepe[1a], K.G. Nath[b], S. Kimura[a], H. Kumigashira[c], T. Takahashi[c], T. Matsumura[c], T. Suzuki[c], H. Ogasawara[d], A. Kotani[d]

[a]*UVSOR Facility, Institute for Molecular Science, Okazaki 444, Japan*
[b]*Department of Structural Molecular Science, The Graduate University for Advanced Studies, Okazaki 444, Japan*
[c]*Department of Physics, Tohoku University, Sendai 980-77, Japan*
[d]*Institute for Solid State Physics, University of Tokyo, Tokyo 106, Japan*

Abstract

We have studied 4*f* photoemission spectra of thulium monochalcogenides at excitation photon energies of the 3*d*–4*f* resonance region ($h\nu$ = 1450–1520 eV). The experimental results are compared with theoretical calculations. The contributions from the 4*f* divalent part and the trivalent part in the 3*d*–4*f* resonance are more clearly distinguished and resolved than for the 4*d*–4*f* resonant photoemission. The calculated results are in good agreement with the experimental ones both for divalent and trivalent features of thulium ions. We have estimated the mean valence of TmS, TmSe and TmTe samples from 3*d* absorption spectra and from off-resonant photoemission spectra. The latter should reflect more bulk-sensitive information than that reported for the 4*d*–4*f* resonance region. It is concluded that the 3*d*–4*f* resonant photoemission is a more useful technique to investigate 4*f* electronic structures than the 4*d*–4*f* photoemission, when we perform the experiments with relatively higher energy resolution. © 1998 Elsevier Science B.V.

Keywords: Thulium compounds; 3*d*–4*f* resonance; Photoemission

1. Introduction

Rare earth metals and those compounds characterized by an electronic structure of incompletely filled and localized 4*f* states have been studied by photoemission spectroscopy for the last two decades. The resonant photoemission technique, in particular, has been used to study 4*f* electronic structure since it is suitable for showing the enhancement of weak emissions and easily separates the emissions from different valence states (as well as core levels) [1]. The enhancement of the 4*f* emission may be interpreted as an interference effect between the direct photoemission from 4*f* states and an *nd*–4*f* excitation (n = 3 or 4) followed by Coster–Kronig (CK) or super Coster–Kronig (sCK) decay. Depending on the excitation energy of the respective absorption peak, the resonance behavior can be used to separate that particular valence emission.

It is known that thulium has two ionic configurations: i.e., Tm^{2+} [$4f^{13}(5d6s)^0$] and Tm^{3+} [$4f^{12}(5d\,6s)^0$]. Some resonant photoemission work has been reported to date for the thulium compounds. Most of these studies are concerned with the 4*d*–4*f* resonant excitation [2]. Recently, we also performed a systematic study of resonant photoemission of TmX (X = S, Se and Te) compounds, both experimentally

[1] Visiting scientist on leave from Physics Department, University of Cukurova, 01330 Adana, Turkey.

PII S0368-2048(97)00184-9

and theoretically, around the Tm 4*d* absorption edge [3]. In that report, we discussed the resonance of 4*f* emissions and separated the states for both divalent and trivalent parts. We estimated the mean valences from the off-resonant spectra and the absorption (total electron yield (TY)) spectra. We also compared the experimental spectra with the theoretical calculations. It was concluded that the experimental and calculated results agreed quite well.

In the present paper we report the results of a similar study but around the Tm 3*d* absorption edge, as a complementary study. The advantages of performing a 3*d*–4*f* resonant photoemission study in addition to the 4*d*–4*f* study are as follows. First, the kinetic energy of the photoelectrons is higher and the results should reflect bulk-sensitive information. Second, the absorption peaks of Tm 3*d* are much sharper than the 4*d* edge peaks and show well-separated multiplet structures [4–7]. Since the intrinsic cross-section of 4*f* photoemission is very small in this photon energy range, the resonant photoemission spectra might show very obvious enhancement for each peak. (The cross-section of other valence electrons should be much smaller than that of the 4*f* electrons.) These advantages are of great importance for the study of mixed valence materials.

However, resonant photoemission work around the 3*d* excitation threshold of heavy rare earth compounds is not so easy. So far, only a limited number of 3*d*–4*f* resonant photoemission studies have been done for heavy rare earth compounds [8–12]. This is due to the difficulty in obtaining a photon flux with high intensity and high resolution in these photon energy ranges ($h\nu$ = 1.25–1.6 keV). The range is just situated in the area between those covered by a crystal monochromator and by a grazing-incidence grating monochromator. Recently, the YB_{66} monochromator crystal became available for use in spectroscopic studies over the 1.2–2 keV range at the UVSOR facility [13]. We used the YB_{66} double crystal monochromator to excite the Tm 3*d* edge and obtained resonant photoemission spectra with relatively higher energy resolution. In this report, we show the results of 4*f* electronic structures of divalent and trivalent ions of TmSe. We have also obtained the 4*d* core-level photoemission data for TmS and TmSe in these resonance energies, which are described elsewhere [14]. The experimental results are compared with theoretical calculations to explain the resonant behavior of each multiplet structure for both the divalent and trivalent components. The mean valence values estimated from the TY and off-resonant energy distribution curves (EDC) for TmX are also presented.

2. Experiment

The spectroscopy experiments were performed with the double crystal monochromator (DXM) beam line BL7A of the UVSOR facility. At the BL7A, wiggler radiation with 4 T magnetic field is provided to obtain a higher photon flux around the soft X-ray region [15]. We used a pair of YB_{66} crystals [13] as the monochromator crystal to cover the photon energy range around the Tm 3*d* excitation threshold, i.e., 1450–1520 eV. A photon flux of about 10^8 photons/s was obtained. The photoelectron spectroscopy system is a commercial one (Fisons, ESCALAB-220i-XL), which is suitable for a photoelectron microscope with higher performance. By using this higher performance hemispherical analyser with the large area detection mode, photoemission experiments became possible in spite of such a lower photon flux. X-ray absorption spectra (XAS) were measured by the total photoelectron yield (TY) method, by recording the sample drain current as a function of photon energy. The energy resolution of the light was estimated to be less than 0.7 eV around $h\nu$ = 1.5 keV. The overall energy resolution was about 0.8–0.9 eV for both the on- and off-resonant condition. This energy resolution is almost comparable with that obtained by conventional X-ray photoelectron spectroscopy (XPS). In order to check the cleaniness and stoichiometry of the sample surfaces and to measure the off-resonant spectra with higher statistics, we also used the Mg K_α ($h\nu$ = 1253.6 eV) line. The base pressure of the system was less than 2×10^{-10} mbar. The excitation spectra for EDC peaks, namely constant initial state (CIS) spectra, were obtained by plotting the corresponding peak intensity normalized by photon flux as a function of photon energy.

The samples were the same ones as used for the previous 4*d*–4*f* resonant photoemission measurements [3]. TmX (X = S, Se, Te) single crystals were grown by the Bridgman method. These samples were

characterized by the Debye–Scherrer method and by magnetic susceptibility measurements. The mean valence values obtained from the susceptibility experiments were 2.799, 2.530 and 2.017 for TmS, TmSe and TmTe, respectively. These values are almost the same as those reported before [16,17]. Clean sample surfaces were obtained by Ar-ion sputtering or by scraping with a file at room temperature. The cleaning process was repeated frequently to keep the sample surface clean.

3. Calculation

We have calculated the resonant photoemission spectra for Tm^{2+} and Tm^{3+} ions by using an atomic model with spherical symmetry. The initial state is taken to be the lowest state given by Hund's rule, which is $^2F_{7/2}$ for Tm^{2+} ($4f^{13}$) and $^3H_6$ for Tm^{3+} ($4f^{12}$). The method of calculation is almost the same as that used before [3]. The Hamiltonian is written as

$$H = H_0 + V_r + V_a \tag{1}$$

where H_0 describes the thulium ion system, V_r the radiative dipole transitions and V_a the Auger decay transition.

The spectrum of the resonant photoemission is written as

$$F(\varepsilon,\nu) = \sum_{k,\beta} |\langle k\beta|T|g\rangle|^2 \delta(h\nu + E_g - E_{k,\beta})\delta(\varepsilon - \varepsilon_k) \tag{2}$$

where $h\nu$ represents the incident photon energy, ε the kinetic energy of the continuum electron, $|g\rangle$ the ground state of H_0, E_g its energy, $|k\beta\rangle$ the final states, and $E_{k\beta}$ their energies. Here we ignore the interaction between the continuum electron and the thulium system, so that the final states, $|k\beta\rangle$, and their energies can be decoupled as $|k\beta\rangle = |k\rangle|\beta\rangle$ and $E_{k\beta} = \varepsilon_k + E_\beta$, where $|k\rangle$ and ε_k represent the εl continuum electron state and its energy, and $|\beta\rangle$ and E_β the final states of the thulium ions and their energies, respectively. The operator T is the t-matrix, which is defined as

$$T = V_r + V_a[1/(z - H_0)]T \tag{3}$$

with

$$z = h\nu + E_g + i\eta \quad (\eta \to +0) \tag{4}$$

where we take into account V_r up to the first order and V_a up to the infinite order.

After some algebra, we obtain, from eqns (2) and (3), the expression

$$F(\varepsilon,\nu) = \sum_{k,\beta} \left| \langle k\beta|V_r|g\rangle + \sum_{\alpha,\alpha'} \langle k\beta|V_\alpha|\alpha\rangle\langle\alpha|G|\alpha'\rangle \times \left(\left\langle \alpha \middle| V_r \middle| g \right\rangle + \sum_{k',\beta'} \frac{\left\langle \alpha' \middle| V_a \middle| k'\beta' \right\rangle \left\langle k'\beta' \middle| V_r \middle| g \right\rangle}{z - E_{k'\beta'}} \right) \right|^2 \times \delta(h\nu + E_g - E_{k\beta})\delta(\varepsilon - \varepsilon_k) \tag{5}$$

where $|\alpha\rangle$ represent the intermediate states with $3d^9 4f^{n+1}$ configuration (n = 12 or 13) and E_α their energies. $|\alpha\rangle$ correspond to the final states of the $3d \to 4f$ XAS. There are one and four intermediate states for the Tm^{2+} and Tm^{3+} ion, respectively. The Green's function, $\langle\alpha|G|\alpha'\rangle$, is obtained by matrix inversion from

$$\left\langle \alpha \middle| G^{-1} \middle| \alpha' \right\rangle = (z - E_\alpha)\delta_{\alpha\alpha'} - \sum_{k,\beta} \frac{\left\langle \alpha \middle| V_\alpha \middle| k\beta \right\rangle \left\langle k\beta \middle| V_\alpha \middle| \alpha' \right\rangle}{z - E_{k,\beta}} \tag{6}$$

There are many decay channels from the intermediate state. The most important channels are $3d$–$4f4f$, $3d$–$4d4f$ and $3d$–$4d4d$ Auger decay. We include only these three channels in the calculation for simplicity. This is fair approximation, because decay process other than the $3d$–$4f4f$ affect the resonant $4f$ photoemission spectra indirectly through lifetime broadening in the intermediate state.

The parameter values are given in Table 1. These parameters and the reduced matrix elements required are obtained by Cowan's program suits [18].

4. Results and discussion

4.1. 3d–4f resonant photoemission of TmSe

In this section, we report the results of $3d$–$4f$ resonant photoemission of TmSe. Since TmSe is

Table 1
Parameter values used in the calculation. F, G and ζ are given in eV, R in $\sqrt{\text{eV}}$, $\langle 4f|r|3d\rangle$ in a_0 (Bohr radius), and $\langle \varepsilon l|r|nl\rangle$ in $a_0\sqrt{}$(eV)

	Tm^{3+}	Tm^{2+}
$4f$ numbers	12	13
$F^2(4f, 4f)$	13.9	13.2
$F^4(4f, 4f)$	8.7	8.3
$F^6(4f, 4f)$	6.3	5.6
ζ_{4f}	0.35	0.33
ζ_{4d}	3.3	3.3
ζ_{3d}	18.1	18.1
$F^2(4d, 4f)$	14.3	13.9
$F^4(4d, 4f)$	9.2	8.9
$G^1(4d, 4f)$	14.8	14.3
$G^3(4d, 4f)$	9.4	9.0
$G^5(4d, 4f)$	6.6	6.4
$F^2(4d, 4d)$	17.6	17.6
$F^4(4d, 4d)$	11.8	11.8
$F^2(3d, 4f)$	9.1	—
$F^4(3d, 4f)$	4.3	—
$G^1(3d, 4f)$	6.7	—
$G^3(3d, 4f)$	3.9	—
$G^5(3d, 4f)$	2.7	—
$R^1(3d\varepsilon g, 4f^2)$	0.19	0.18
$R^3(3d\varepsilon g, 4f^2)$	0.12	0.12
$R^5(3d\varepsilon g, 4f^2)$	0.09	0.08
$R^0(3d\varepsilon d, 4d^2)$	0.11	0.11
$R^2(3d\varepsilon d, 4d^2)$	0.09	0.09
$R^4(3d\varepsilon d, 4d^2)$	0.05	0.05
$R^1_d(3d\varepsilon f, 4f4d)$	0.12	0.12
$R^3_d(3d\varepsilon f, 4f4d)$	0.05	0.05
$R^5_d(3d\varepsilon f, 4f4d)$	0.03	0.03
$R^0_e(3d\varepsilon f, 4f4d)$	0.04	0.04
$R^2_e(3d\varepsilon f, 4f4d)$	0.05	0.05
$R^4_e(3d\varepsilon f, 4f4d)$	0.03	0.03
$\langle 4f\|r\|3d\rangle$	0.12	0.12
$\langle \varepsilon g\|r\|4f\rangle$	0.0015	0.0014
$\langle \varepsilon f\|r\|4d\rangle$	0.0028	0.0028

known to be a material with mixed valence, i.e., including Tm^{2+} and Tm^{3+} ions, this material can be a typical example to explain the resonant behavior of both divalent and trivalent peaks. Fig. 1(a) shows the valence-band photoemission EDC spectra of TmSe in some representative conditions with different photon energies both on- and off-resonance around the Tm $3d$ excitation threshold. Excitation photon energies were selected from the TY spectrum shown in Fig. 1(b), which are indicated by numerical labels. The intensities of the spectra were normalized by the incident photon flux. The calculated spectra for divalent and trivalent thulium ions are shown for comparison both in EDC and TY spectra. The calculated line spectra are convoluted with a Gaussian width of 0.9 eV (FWHM) to mimic instrumental resolution. In Fig. 1(c), the $3d$–$4f$ CIS spectra of each EDC peak (A–E in Fig. 1(a)) are also shown together with the theoretical calculations for divalent and trivalent thulium ions for comparison. The CIS spectra are obtained by plotting the normalized peak intensity in Fig. 1(a).

First, we discuss the TY spectrum in Fig. 1(b). It is noticed from the figure that the measured TY spectra of TmSe are understood as a superposition of the divalent and trivalent absorption peaks of theoretical calculation. This is consistent with the mixed valence nature of TmSe. The trivalent spectrum is composed of four peaks at photon energies of 1460.5, 1462.5, 1465 and 1508 eV, which are identified with the transition to the final states $^3H_6$, $^3G_5$, $^1H_5$ and $^3H_5$, respectively. Meanwhile, the divalent single peak ($^2D_{5/2}$) is observed as a shoulder at 1459.2 eV overlapped with the trivalent $^3H_6$ peak. We performed curve fitting to estimate the mean valence by changing the relative intensity of the theoretical absorption spectra for each divalent and trivalent component. The results of the mean valences will be presented later, together with those obtained from the XPS spectra.

The photoemission spectrum obtained at position 1 corresponds to the almost off-resonant spectrum. The spectral features are composed of both divalent and trivalent components. Spectrum 2 is the on-resonant one for almost only the divalent component. It is obvious that very sharp peaks belonging to the divalent component (0–5.6 eV binding energy) are enhanced whereas the trivalent peaks are very weak. The spectra at conditions 3–6 are the on-resonant ones for the trivalent component (5.6–14 eV binding energy). Spectrum 3 still shows the divalent nature, because this is also within the divalent resonant condition. Spectra 4, 5 and 6 seem to show almost only trivalent nature and almost no divalent

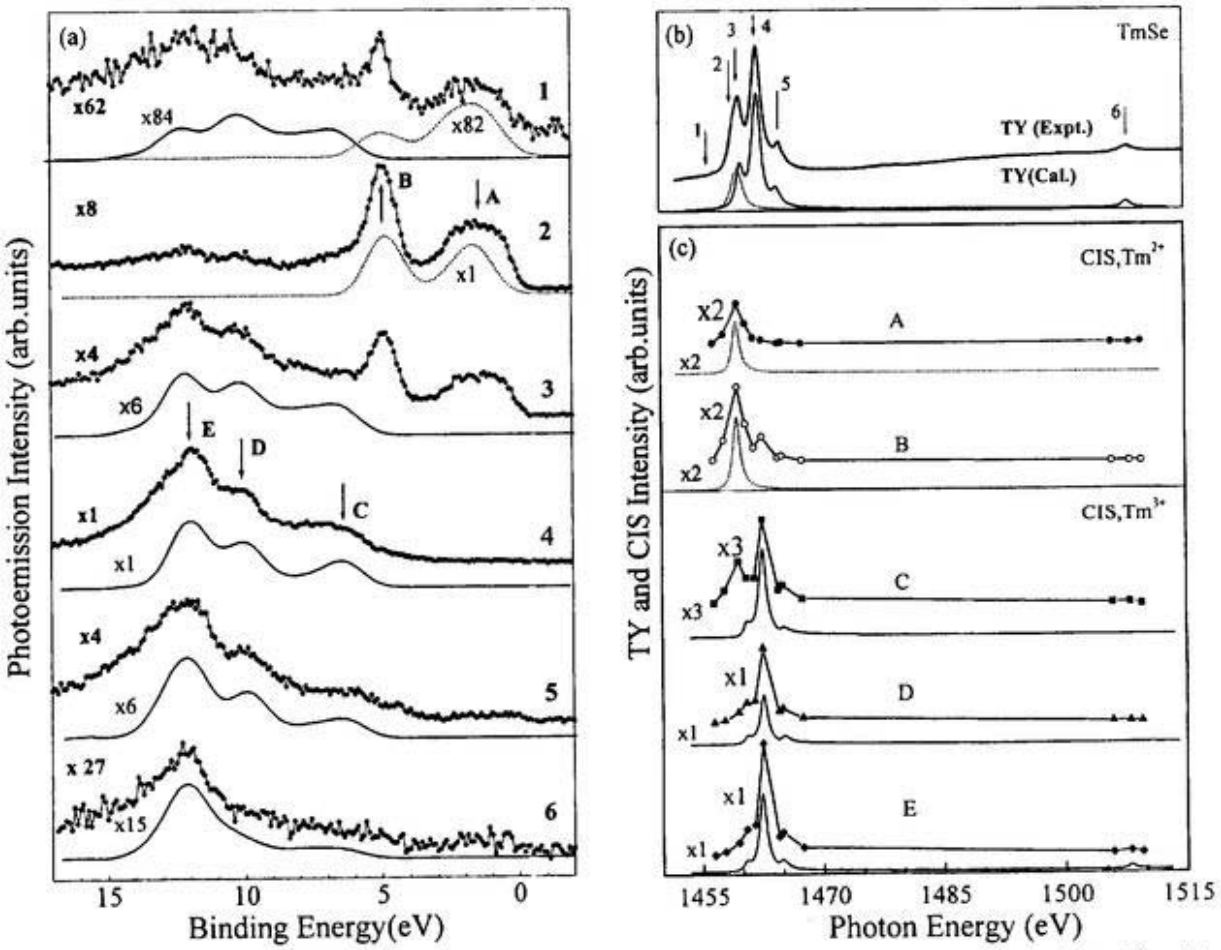

Fig. 1. (a) $3d$–$4f$ resonant photoemission spectra of TmSe. The spectra are taken at the representative photon energy positions indicated by numbers in the absorption (TY) spectrum in Fig. 1(b). The results of theoretical calculation for divalent (dot) and trivalent (solid) Tm ions are also shown for comparison. Since the resonant enhancement is so large, the factors multiplying to the arbitrary intensity are given for easier comparison of the spectra between on- and off-resonance. The excitation condition 1 is not completely off-resonance one but the corresponding calculation was performed for off-resonant spectra. The intensities of the calculated spectra are normalized as those of the on-resonant conditions, being unity both for divalent and trivalent components. The mean valence value is not considered for the intensity normalization process. (b) $3d$–$4f$ TY spectrum for TmSe. The calculated XAS spectra for divalent and trivalent contributions are also shown. The intensity ratio of the calculated spectra for divalent and trivalent components reflects the mean valence value in Table 2. (c) $3d$–$4f$ CIS spectra for TmSe. Each CIS curve is obtained by plotting the normalized intensity of the peak positions labeled in the photoemission spectra in Fig. 1(a) as a function of excitation photon energy. The calculated CIS spectra for divalent and trivalent contributions are also shown. The factors multiplying to the CIS intensities derived from both the measured and the calculated EDC results in Fig. 1(a) are common for divalent and trivalent components.

peaks are observed. We noted both from the experimental and calculated spectra for the trivalent component that the spectral features depend on the excitation conditions. It is concluded from the figure that the calculated results are in good agreement with the experimental ones.

We also notice in Fig. 1(a) that a very strong resonant enhancement of the trivalent component occurs (about 62 times the off-resonant spectrum). Since the condition 1 is located on the tail of peaks 2 and 3, in a slightly on-resonant condition, the enhancement ratio of on-resonance to completely

off-resonance should be much larger. As expected from a comparison of calculations carried out at completely off-resonant condition and the on-resonant one, the factor should be 84 for the trivalent component. This value is much larger than that for the $4d$–$4f$ resonant photoemission. We can conclude from these results that the contributions from the $4f$ divalent part and the trivalent part are more clearly distinguished and resolved than for the previous $4d$–$4f$ resonant photoemission [3].

In Fig. 1(c) we did not take many data points for the CIS spectra but the agreement between the calculated and experimental results seems to be qualitatively good. The shape of the CIS spectra is almost in accordance with the TY spectrum. Every trivalent CIS spectrum shows four peaks (the fourth peak at 1508 eV is very weak but exists) and the divalent ones show a single peak, although the divalent CIS spectrum for B shows additional structure owing to a strong background effect from the trivalent part. Peak E for the trivalent component and peak B for the divalent component show the strongest enhancement both in calculated and observed spectra. Although the CIS spectral features for each multiplet component show almost the same shape as those for TY spectra, the trivalent first CIS peak at 1460.5 eV, corresponding to the $^3H_6$ final state in the absorption spectrum, is weaker than that of the TY spectrum both in the calculation and experiment. (In the CIS spectra for C, the first peak is larger. This is due to the background effect from the divalent peak B.) Instead, the CIS spectrum for the trivalent $4d$ photoemission peak shows a strong peak at 1460.5 eV [14]. This means that the $3d$–$4f$ excitation states at 1460.5 eV decay preferentially to the $4d$ photoemission channel as reported for $TmAl_2$ [11], whereas the $4d$–$4f$ excitation states decay mostly to the $4f$ channel [3].

4.2. Off-resonant XPS spectra of TmS, TmSe and TmTe

Fig. 2 shows the off-resonant $4f$ XPS spectra for TmS, TmSe and TmTe taken at $h\nu = 1253.6$ eV. As discussed in the previous study [3], the metallic nature of TmS and TmSe and the semiconducting nature of TmTe are confirmed from the emission around the Fermi level. The calculated EDC curves of $4f$ electrons for Tm^{3+} and Tm^{2+} ions are compared with the

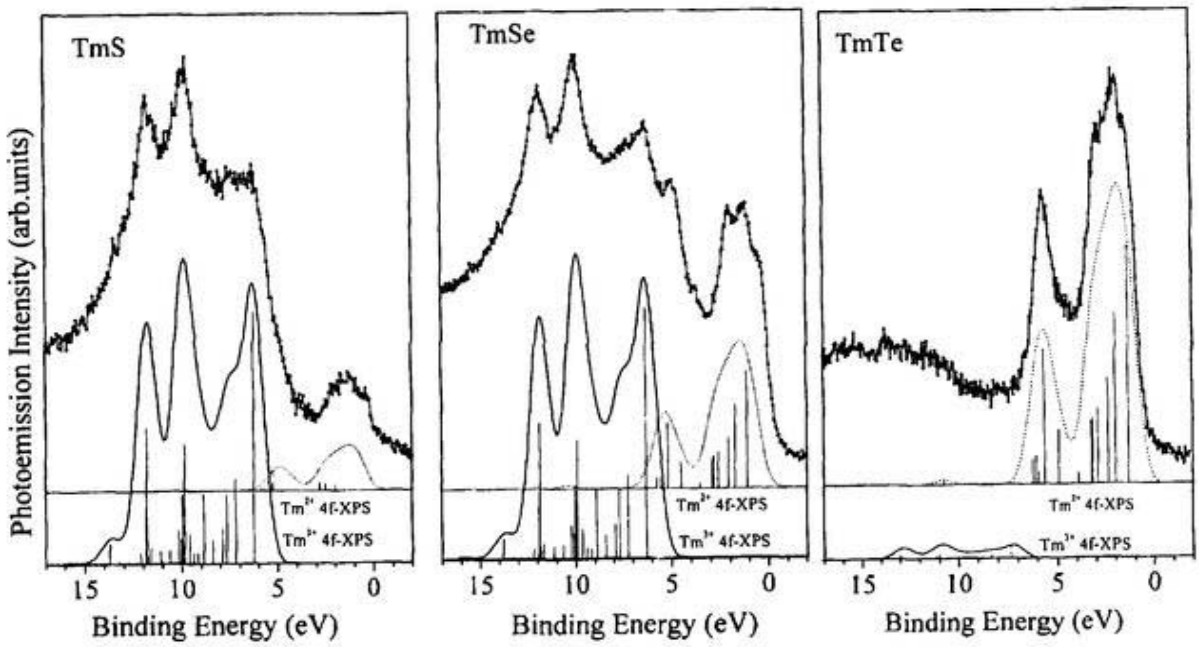

Fig. 2. XPS spectra of TmS, TmSe and TmTe. The theoretical calculations for divalent and trivalent $4f$ components at the off-resonant condition are shown for comparison.

Table 2
Mean valence values of TmS, TmSe and TmTe estimated by 4*d* TY spectra, 3*d* TY spectra, EDC at the excitation energy of $h\nu$ = 140 eV and EDC at $h\nu$ = 1253.6 eV. The mean valence values determined from the inverse of the magnetic susceptibilities (χ) are shown as a reference. We did not measure the 3*d* TY spectrum for TmTe

	4*d* TY	3*d* TY	EDC $h\nu$ = 140 eV	EDC $h\nu$ = 1253.6 eV	χ
TmS	2.91	2.82	2.93	2.88	2.799
TmSe	2.79	2.63	2.68	2.69	2.530
TmTe	2.15	—	2.35	2.05	2.017

measured spectra, where the Gaussian width of 0.6 eV (FWHM) is used. The absolute energy position of divalent and trivalent peaks cannot be determined from the theoretical calculation. We set the energy positions of the calculated peaks to fit the experimental peak positions. As confirmed in the previous section and previous reports [4,5], we set the divalent peaks in the 0–5.6 eV binding energy region and the trivalent peaks in the 6–15 eV region. The agreement between the calculated and the measured results seems to be satisfactory on relative peak positions and intensities.

In our experimental condition of ~0.9 eV energy resolution, the surface shift reported previously [19] could not be observed. This means that the spectral features in Fig. 2 include components of both surface and bulk. However, the results should reflect bulk information rather than the previous results of 4*d*–4*f* resonant photoemission because of the deeper penetration depth of electrons with higher kinetic energy.

We tried to estimate the mean valence of each material from the intensity ratio between divalent and trivalent components in the off-resonant XPS spectra. The curve-fitting procedure is the same as used previously [3]. The values are shown in Table 2, together with the values obtained by other methods [20]. The EDC of 140 eV is the most surface-sensitive of the four kinds of estimation method, whereas the EDC of 1253.6 eV is rather bulk-sensitive as are the TY methods.

5. Conclusion

We have systematically studied the resonant photoemission spectra of TmX (X = S, Se, Te) compounds around the Tm 3*d* threshold. The resonant behavior of the photoelectron spectral features of 4*f* levels is in good agreement with those calculated for divalent and trivalent components. The contributions from the 4*f* divalent part and the trivalent part are more clearly distinguished and resolved than for previous results of 4*d*–4*f* resonant photoemission. The CIS spectral features for each multiplet component show almost the same shape as those for TY spectra, but show a difference in the lowest photon energy peak. This means that the decay channel of the 3*d*–4*f* excited state is not only to the 4*f* photoemission channel, but also preferentially to other core-level emission channels. In addition, we have estimated the mean valence of TmS, TmSe and TmTe samples from 3*d* absorption spectra and from off-resonant photoemission spectra. The latter should reflect more bulk-sensitive information than that reported for the 4*d*–4*f* resonance region.

Acknowledgements

This work was supported by the Joint Studies Program (1996–1997) of the Institute for Molecular Science. The authors would like to thank staff members of the UVSOR facility for their help during the experimental work. The participation of Y.U. was supported financially by the Scientific and Technical Research Council of Turkey (TUBITAK).

References

[1] J.P. Connerade, J.M. Esteva, R.C. Karnatak (Eds.), Giant Resonances in Atoms, Molecules and Solids, Plenum Press, New York, 1987.
[2] S.-J. Oh, J.W. Allen, I. Lindau, Phys. Rev. B30 (1984) 1937.
[3] Y. Ufuktepe, S. Kimura, T. Kinoshita, K.G. Nath, H.

Kumigashira, T. Takahashi, T. Matsumura, T. Suzuki, H. Ogasawara, A. Kotani, submitted to J. Phys. Soc. Jpn.
[4] A. Belrhmi-Belhassan, R.C. Karnatak, N. Spector, C. Bonnelle, Phys. Lett. 82A (1981) 174.
[5] G. Kaindl, W.D. Brewer, G. Kalkowski, F. Holtzberg, Phys. Rev. Lett. 51 (1983) 2056.
[6] G. Kaindl, G. Kalkowski, W.D. Brewer, B. Perscheid, F. Holtzberg, J. Appl. Phys. 55 (1984) 1910.
[7] B.T. Thole, G. van der Laan, J.C. Fuggle, G.A. Sawatzky, R.C. Karnatak, J.-M. Esteva, Phys. Rev. B32 (1985) 5107.
[8] J.W. Allen, S.-J. Oh, I. Lindau, L.I. Johansson, Phys. Rev. B29 (1984) 5927.
[9] U. Becker, H.G. Kerkhoff, D.W. Lindle, P.H. Kobrin, T.A. Ferrett, P.A. Heimann, C.M. Truesdale, D.A. Shirley, Phys. Rev. A34 (1986) 2858.
[10] S. Cramm, U. Grabowski, C. Kunz, J. Schmidt-May, F. Senf, L. Incoccia, J. Electron Spectrosc. Relat. Phenom. 42 (1987) 89.
[11] C. Laubschat, E. Weschke, G. Kalkowski, G. Kaindl, Physica Scripta 41 (1990) 124.
[12] T. Hanyu, H. Ishii, S. Hashimoto, T. Yokoyama, K. Jokura, H. Sato, T. Miyahara, J. Electron Spectrosc. Relat. Phenom. 78 (1996) 67.
[13] T. Kinoshita, Y. Takata, T. Matsukawa, H. Aritani, S. Matsuo, T. Yamamoto, M. Takahashi, H. Yoshida, T. Yoshida, Y. Ufuktepe, K.G. Nath, S. Kimura, Y. Kitajima, J. Synchrotron Radiation, in press.
[14] K.G. Nath, Y. Ufuktepe, S. Kimura, T. Kinoshita, H. Kumihashira, T. Takahashi, T. Matsumura, S. Suzuki, H. Ogasawara, J. Electron Spectrosc. Relat. Phenom., in this volume.
[15] E. Nakamura, H. Hama, J. Yamazaki, T. Kinoshita, O. Matsudo, H. Yonehara, T. Kasuga, G. Isoyama, M. Watanabe, J. Electron Spectrosc. Relat. Phenom. 80 (1996) 421.
[16] B. Batlogg, H.R. Ott, E. Kaldis, W. Thoni, P. Wachter, Phys. Rev. B19 (1979) 247.
[17] F. Holtzberg, J. Flouquet, P. Haen, F. Lapierre, Y. Lassailly, C. Vettier, J. Appl. Phys. 57 (1985) 3152.
[18] R.D. Cowan, The Theory of Atomic Structure and Spectra, University of California Press, Berkeley, 1981.
[19] G. Kaindl, C. Laubschat, B. Reihl, R.A. Pollak, N. Mrtensson, F. Holtzberg, D.E. Eastman, Phys. Rev. B26 (1982) 1713.
[20] S. Kimura, Y. Ufuktepe, K.G. Nath, T. Kinoshita, H. Kumigashira, T. Takahashi, T. Matsumura, T. Suzuki, H. Ogasawara, A. Kotani, to be published in Proc. ICM'97, 1997, Australia, in press.

Journal of the Physical Society of Japan
Vol. 67, No. 6, June, 1998, pp. 2018-2026

Resonant Photoemission Studies of Thulium Monochalcogenides around the Tm 4*d* Threshold

Yüksel UFUKTEPE*, Shin-ichi KIMURA, Toyohiko KINOSHITA, Krishna G. NATH[1], Hiroshi KUMIGASHIRA[2], Takashi TAKAHASHI[2], Takeshi MATSUMURA[2], Takashi SUZUKI[2], Haruhiko OGASAWARA[3] and Akio KOTANI[3]

UVSOR Facility, Institute for Molecular Science, Okazaki 444-8585
[1]*Department of Structural Molecular Science, The Graduate University for Advanced Studies, Okazaki 444-8585*
[2]*Department of Physics, Tohoku University, Sendai 980-8578*
[3]*Institute for Solid State Physics, University of Tokyo, Tokyo 106-8666*

(Received July 15, 1997)

Electronic structures of thulium monochalcogenides (TmS, TmSe, TmTe) were studied both experimentally and theoretically using a resonant photoemission technique in the photon energy range around Tm 4*d* edge (100–190 eV). The experimental results show a large resonant enhancement of 4*f* photoelectron emission around the 4*d* threshold with sharper multiplet structures than those reported before. The calculated results are in good agreement with the experimental ones both for divalent and trivalent features of Tm ions. We observed different types of valence structures for TmS, TmSe and TmTe compounds, due to change in mean valence. We have estimated the mean valence of each sample from absorption spectra and from off-resonant photoemission spectra. The meaning of these values is discussed as compared with those for the values obtained from the measurements of magnetic susceptibilities.

KEYWORDS: resonant photoemission, TmS, TmSe, TmTe, mixed valence

§1. Introduction

Rare earth (RE) metals, characterized by electronic structure of incompletely filled and localized 4*f* states which overlap the extended 5*d*6*s* valence orbits, have been studied by photoemission spectroscopy for more than two decades. At the same time resonant photoemission has been efficiently utilized to study this interesting electronic structures of rare earth metals and their compounds.[1-12] Enhancement of weak emissions and separation of emissions from different valence states (as well as core levels) are the common implements of resonant photoemission.[1] The enhancement of 4*f* emission occurs as one of the consequences of *d*-shell resonant absorption[4,8,11,13] into the localized 4*f* shells. A core electron from 4*d* or 3*d* shell is excited into an empty 4*f* orbital with the photon energy near the absorption edge. In the 4*d* case, this process can be written as $4d^{10}4f^n+h\nu \rightarrow 4d^9 4f^{n+1}$, in which the final state is treated as the intermediate state of resonant photoemission. Following absorption, the created 4*d* hole state may decay via several ways, for example, by creating a 4*f* photoelectron (i.e. $4d^9 4f^{n+1} \rightarrow 4d^{10}4f^{n-1}+e^-$). The process after absorption is termed super- Coster-Kronig (sCK) decay which combines with direct 4*f* photoemission. The interference between the direct process and sCK process is the origin of the resonance of 4*f* photoemission. Because of electrostatic interactions of 4*f* electrons and 4*d* core holes, the resonant absorption is spread over a particular energy range showing multiplet structures.[11,13] The existence of multiplet structure at absorption features relates to the excitation of particular valence state.[3] As a result, the resonance behavior of any particular valence state depends on the excitation energy of respective absorption peak. This can be used to separate that particular valence emission.

In this paper, we report the results of the resonant photoemission study of thulium monochalcogenides, TmX (X=S, Se and Te). It is known that Tm, a member of heavy RE series, has two ionic ground state configurations; Tm^{2+} ($4f^{13}$) and Tm^{3+} ($4f^{12}$). The intermediate states of resonant photoemission for these two ionic states lead to simpler photoabsorption spectra. Therefore thulium is considered as a simple system to study the resonant photoemission where the number of decay channels is relatively less. Previous photoemission results clearly showed two final state valence multiplets, $4f^{11}$ and $4f^{12}$ excited from $4f^{12}$ and $4f^{13}$ initial states, respectively, where the $4f^{12}$ final states stay near the Fermi edge.[14-17] This unique series of isostructural compounds (NaCl type) showing antiferromagnetic orderings at low temperatures[18-20] was selected because of their extremely varied physical and electron transport properties. It is determined by specific heat measurements[21] that the ground state of TmS has a metallic character. The measurements of transport properties and the photoemission results[15] indicate that TmS is mostly a trivalent compound. TmSe is a mixed-valent compound which was determined by photoemission experiments[15,16,18] and also by measurements related to magnetic properties, resistivity and specific heat.[22-26]

* Permanent address: Physics Department, University of Cukurova, 01330 Adana, Turkey. E-mail: ufuk@pamuk.cc.cu.edu.tr

TmTe, mostly a divalent compound, has semiconductor property which is confirmed by photoemission studies.[14-16]

Most of the photoemission experiments for Tm metal and its compounds were related to the study of Tm valence structures,[13,16,17,19,27] valence fluctuation,[14,16,17] coordination dependent valency[28] and surface effect of $4f$ emission.[15] Whereas experiments related to $4d$-$4f$ resonant photoemission are few. Johanson, Allen and Lindau[13] have done limited photoemission measurements for Tm-metal in the photon energy range of 100–200 eV without providing resonance information, though they observed the resonant absorption features. Nicklin and co-workers[29] have observed the $4d$-$4f$ resonant photoemission spectra for Tm thin film. But in their report, the relative positions of photon energies for tri- and divalent maxima at $4d$-$4f$ absorption spectra are different from those of other results.[3,11,13] Among these three TmX compounds, only one resonant photoemission study has been reported which related results for TmSe.[3] They noted the behavior of each multiplet photoemission peak as a function of photon energy. But in ref. 3, each component of $4f$ final state multiplets is not so clear like off-resonant previous results.[15,16] So it can not be considered as providing a complete information about the resonant behaviors of every $4f$ state. That means we do not have full information concerning the resonance effect of these Tm compounds. We have done this systematic experiment with relatively higher energy resolution for the first time, which aimed to accumulate all different resonance behaviors for different Tm systems. We have also performed theoretical calculations to explain resonant behavior of each multiplet structure both for divalent and trivalent components. The absorption spectra will also be discussed.

§2. Experiment

The spectroscopy experiments were performed at the Grasshopper beam line (BL2B1) of the synchrotron radiation facility UVSOR, a 750 MeV electron storage ring at the Institute for Molecular Science, Okazaki, Japan. X-ray absorption spectra (XAS) were measured by total photoelectron yield (TY) method by recording the sample drain current as a function of photon energy. Photoelectron spectra were measured with a double-pass cylindrical mirror analyzer (DCMA). The overall energy resolution was less than 0.5 eV. Experiments were conducted inside an ultrahigh vacuum chamber with the base pressure of less than 2×10^{-10} torr. We have also measured the excitation spectra for energy distribution curve (EDC) peaks, namely, constant initial state (CIS) spectra.

TmX (X=S, Se, Te) single crystals were grown by Bridgman method with a sealed tungsten crucible and a high frequency induction furnace. High purity Tm (99.9% Ames Lab. USA) and S, Se and Te (99.999%) metals with the respective composition ratio were used as starting materials. Those samples were characterized by Debye-Scherrer method and magnetic susceptibilities measurement. The lattice constants were 5.41 Å, 5.69 Å, and 6.35 Å for TmS, TmSe and TmTe, respectively. Effective Bohr magneton (μ_B) estimated from the susceptibility from 100 K to 300 K were 7.066, 6.328, and 4.609 for TmS, TmSe and TmTe, respectively. The mean valence values obtained from those experiments were 2.799, 2.530 and 2.017 for TmS, TmSe and TmTe, respectively. These values are almost the same as those reported before.[3,19,22,30]

The samples were mounted on sample holders which can be transferred between main chamber and preparation chamber. It is known that crystals with NaCl structure are easily cleaved. We tried to cleave the samples to obtain clean surfaces. Unfortunately, the cleaved surfaces were not clean enough, because the sample probably has had crack already at the cleaved position. Therefore, a clean surface was prepared by scraping the sample with a diamond file at room temperature. This process was repeated every 2 hours to keep the sample surface clean. Possible oxygen contamination was checked by monitoring the O (1s) photoemission peak (at $h\nu = 800$ eV). After the measurement period of up to 2 hours the peak intensity of oxygen was within the noise level. The Fermi level was determined by measuring an Au film which was evaporated on the sample at the end of the beam run.

§3. Calculational Details

We have calculated the photoelectron spectra and their excitation spectra for Tm^{2+} and Tm^{3+} ions using an atomic model with spherical symmetry. The method of calculation is almost the same as that used for the La compounds.[31] The ground state is the Hund's rule lowest state, which is $^2F_{7/2}$ for Tm^{2+} ion ($4f^{13}$) and $^3H_6$ for Tm^{3+} ion ($4f^{12}$), respectively. The corresponding Hamiltonian can be written as

$$H = H_0 + V_r + V_a, \tag{1}$$

where H_0 describes the $4f$ and $4d$ electronic state of the Tm ion which includes the Coulomb, exchange and spin-orbit interactions, V_r the radiative dipole transitions of $4d \rightarrow 4f$ and $4f \rightarrow \varepsilon l$ (εl being the continuum electron of l-symmetry), and V_a the Auger transition of $\langle 4d^9 4f^{n+1}|1/r|4d^{10}4f^{n-1}\varepsilon l\rangle$ ($n = 12$ or 13).

The spectrum of the resonant photoemission is written as

$$F(\varepsilon, \nu) = \sum_{k,\beta} |\langle k\beta|T|g\rangle|^2 \delta(h\nu + E_g - E_{k\beta}) \times \delta(\varepsilon - \varepsilon_k), \tag{2}$$

where $h\nu$ represents the incident photon energy, ε the kinetic energy of the continuum electron, $|g\rangle$ the ground state of H_0, E_g its energy, $|k\beta\rangle$ the final states with $4f^{n-1}\varepsilon l$ configuration, and $E_{k\beta}$ their energies. Here we ignore the interaction between the continuum electron and the Tm system, so that the final states $|k\beta\rangle$ and their energies can be decoupled as $|k\beta\rangle = |k\rangle|\beta\rangle$ and $E_{k\beta} = \varepsilon_k + E_\beta$, where $|k\rangle$ and ε_k represents the εl continuum electron state and its energy, $|\beta\rangle$ and E_β the states with $4f^{n-1}$ configuration and their energies, respectively. The operator T is called the t-matrix, which

is defined as

$$T = V_r + V_a[1/(z - H_0)]T \tag{3}$$

where

$$z = h\nu + E_g + i\eta \quad (\eta \to +0), \tag{4}$$

we can take into account V_r up to the first order and V_a up to infinite order.

After some algebra, we obtain the expression from eqs. (2) and (3),

$$F(\varepsilon, \nu) = \sum_{k,\beta} \left| \langle k\beta|V_r|g\rangle + \sum_{\alpha,\alpha'} \langle k\beta|V_a|\alpha\rangle\langle\alpha|G|\alpha'\rangle \times \left(\langle\alpha'|V_r|g\rangle + \sum_{k',\beta'} \frac{\langle\alpha'|V_a|k'\beta'\rangle\langle k'\beta'|V_r|g\rangle}{z - E_{k'\beta'}} \right) \right|^2 \delta(h\nu + E_g - E_{k\beta})\delta(\varepsilon - \varepsilon_k), \tag{5}$$

where $|\alpha\rangle$ represent the intermediate states with $4d^9 4f^{n+1}$ configuration, and E_α their energies. $|\alpha\rangle$ correspond to the final states of the $4d \to 4f$ XAS. There are one and four intermediate states for the Tm^{2+} and Tm^{3+} ion, respectively, according to dipole selection rule $\Delta J = 0, \pm 1$. The Green's function $\langle\alpha|G|\alpha'\rangle$ is obtained by matrix inversion from

$$\langle\alpha|G|\alpha'\rangle = \frac{1}{z - E_\alpha}\delta_{\alpha\alpha'} + \frac{1}{z - E_\alpha} \times \sum_{k,\beta,\alpha''} \frac{\langle\alpha|V_a|k\beta\rangle\langle k\beta|V_a|\alpha''\rangle}{z - E_{k\beta}} \langle\alpha''|G|\alpha'\rangle. \tag{6}$$

The required parameters are the Slater integrals $F^k(4f, 4f)$ for the $4f$ Coulomb interaction, $F^k(4d, 4f)$ and $G^k(4d, 4f)$ for $4d$-$4f$ Coulomb and exchange interactions, $R^k(4d\varepsilon l, 4f^2)$ for the Auger process, the spin-orbit coupling constants ζ_{4f} for $4f$ and ζ_{4d} for $4d$ orbital, the radial integral $\langle 4d|r|4f\rangle$ for transition to intermediate states, and $\langle 4f|r|\varepsilon l\rangle$ for $4f$ photoelectron emission.

These parameter values are estimated by the Hartree-Fock method with relativistic corrections.[32] Values of $F^k(4f, 4f)$, $F^k(4d, 4f)$ and $G^k(4d, 4f)$ are reduced to 80%, 75% and 66%, respectively. These reduction ratios are typical values to reproduce the experimental multiplet structure of rare earth $4d \to 4f$ XAS.[11] The density of states of the continuum is assumed to be constant over the whole incident photon energy. Kinetic energy of the continuum electron is decided so that the total average energies of $4d^9 4f^{n+1}$ and $4d^{10} 4f^{n-1}\varepsilon l$ configurations are identical. There are two symmetries which are allowed by dipole transition ($l = d, g$) and five by Auger transition ($l = s, d, g, i, l$) for the continuum electron. We only consider the g-symmetry in this calculation, because it is the most dominant path.

The parameter values are given in Table I. The reduced matrix elements in eqs. (5) and (6) are obtained by one of the Cowan's program suit.[32] Those matrix elements are passed to the resonant photoemission program which calculates the value $F(\varepsilon, n)$. EDC spectrum is derived from $F(\varepsilon, n)$ as a function of the binding energy ($E_B = h\nu - \varepsilon$) for a fixed value of ν and CIS as a function of ν for fixed E_B. The TY spectrum is obtained by integrating $F(\varepsilon, \nu)$ over emitted electron energy ε,

$$I_{TY}(\nu) = \int d\varepsilon F(\varepsilon, \nu). \tag{7}$$

§4. Results and Discussion

4.1 Absorption spectra of TmS, TmSe and TmTe

Figure 1 shows the absorption (TY) spectra of TmS, TmSe and TmTe, respectively. We compare the experimental results with the theoretical calculation. In the upper panel, we show the theoretical spectrum of Tm^{3+} with the experimental spectrum of TmS for comparison. In the middle, the calculated spectrum for Tm^{2+} is shown with experimental TmTe spectrum. The shape of the theoretical spectra is similar to the experimental ones. But it is noticed from the figure that the measured TY spectra of TmX have features of the both divalent and trivalent absorption peaks. The spectrum for TmS originates mostly from trivalent features. We observed three peaks at photon energies of 171.2, 174.3 and 178.2 eV. The spectrum of TmTe shows mostly divalent single peak at $h\nu \cong 173$ eV with weak trivalent 3 peaks. We note that the position of the absorption peaks is dif-

Table I. Parameter values used in the calculation for the ground, intermediate and final states. F, G, ζ are given in eV, R in $\sqrt{\text{eV}}$, $\langle 4f|r|4d\rangle$ in a_0 (Bohr radius), and $\langle \varepsilon g|r|4f\rangle$ in $a_0/\sqrt{\text{eV}}$.

	Tm^{3+}	Tm^{2+}
$4f$ numbers	12	13
$F^2(4f, 4f)$	13.2	—
$F^4(4f, 4f)$	8.3	—
$F^6(4f, 4f)$	5.9	—
ζ_{4f}	0.33	0.31
$F^2(4f, 4f)$	13.2	—
$F^4(4f, 4f)$	8.3	—
$F^6(4f, 4f)$	5.9	—
ζ_{4f}	0.33	—
ζ_{4d}	3.3	3.2
$F^2(4d, 4f)$	13.8	—
$F^4(4d, 4f)$	8.9	—
$G^1(4d, 4f)$	14.3	—
$G^3(4d, 4f)$	9.0	—
$G^5(4d, 4f)$	6.4	—
$F^2(4f, 4f)$	13.9	13.2
$F^4(4f, 4f)$	8.7	8.3
$F^6(4f, 4f)$	6.3	5.9
ζ_{4f}	0.35	0.33
$R^1(4d\varepsilon g, 4f^2)$	−0.82	−0.80
$R^3(4d\varepsilon g, 4f^2)$	−0.44	−0.43
$R^5(4d\varepsilon g, 4f^2)$	−0.29	−0.29
$\langle 4f|r|4d\rangle$	−0.58	−0.58
$\langle \varepsilon g|r|4f\rangle$	0.043	0.043

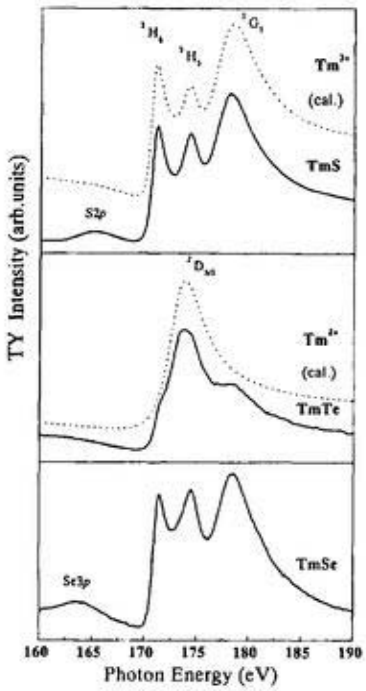

Fig. 1. Total yield (TY) spectra (solid curves) for TmS (top), TmTe (middle) and TmSe (bottom) around the Tm 4d edge. It is shown that the S 2p peak for TmS and the Se 3p peak for TmSe overlap in the pre-threshold region of the spectra. Calculated X-ray absorption spectra of Tm^{3+} and Tm^{2+} ions are indicated by the dotted lines in the top panel and the middle, respectively. Transitions to the final states $^3H_6$, $^3H_5$, $^3G_5$ for the trivalent ion and $^2D_{5/2}$ for divalent ion are labeled, respectively.

ferent from that reported by Nicklin *et al.*[29] but almost the same as other reports.[3, 11, 13] The absorption spectrum of TmSe shows both divalent and trivalent features.

We performed curve fitting to estimate the mean valence by changing the relative intensity of theoretical absorption spectra for each divalent and trivalent components. The procedure is as follow. First, the intensities of two experimental peaks of $^3H_6$ and $^3G_5$ were fitted from the theoretical trivalent curve because the divalent component is not dominant in these peaks. Secondly, the experimental spectra were subtracted by the fitted theoretical curve. Finally, the subtracted spectra were fitted by the theoretical divalent curve. The ratio between multiple factors to theoretical trivalent and divalent curves gives the mean valence. The results are 2.91 for TmS, 2.79 for TmSe and 2.15 for TmTe, respectively. These values are almost consistent with those obtained in the previous studies[3, 15, 19] and our measurements of susceptibilities. The small differences of the values might originate from the difference in surface sensitivity of each method, which will be discussed later. In particular, the deviation of the value for TmTe from the obtained value by susceptibility measurements seems to be due to surface component of Tm trivalent ions.

In the above fitting procedure, we have assumed that the TY spectrum of mixed-valent Tm compounds is given by a simple superposition of the spectra in Tm^{2+} and Tm^{3+} ions. If the hybridization strength is large as

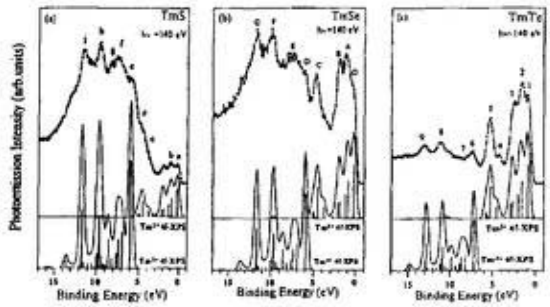

Fig. 2. Valence band photoemission spectra of TmX measured at off-resonant condition at $h\nu = 140$ eV. Calculated results of divalent and trivalent Tm ions are shown for comparison.

the case of mixed-valent Ce compounds, the configuration interaction between the different $4f$ configurations would modify the spectral shape from the simple superposition. In the case of Tm compounds, however, the hybridization strength is small enough to localize the $4f$ states owing to the contraction of the $4f$ wave function, so that our assumption is considered to be reasonable.

4.2 Off-resonant photoemission spectra

Figure 2 shows the valence band photoemission spectra for TmS, TmSe and TmTe respectively taken at $h\nu = 140$ eV. The measurement at $h\nu = 140$ eV corresponds to off-resonant condition, which is easily confirmed from the absorption spectra. The valence band spectra of TmS and TmSe show density of state at the Fermi level due to the metallic character of both samples. In the spectrum of TmTe, the onset of the EDC is located 0.43 eV below the Fermi level, which shows that TmTe is a semiconductor and is consistent with previous results.[15, 17] The calculated EDC curves of $4f$ electrons for Tm^{3+} and Tm^{2+} ions are compared with the measured spectra. It is known from the calculation that the EDC for the Tm^{2+} comprises 69 final states allowed for the $4f^{13}\ (^2F_{7/2}) \rightarrow 4f^{12}\varepsilon g$ dipole transition. The EDC of Tm^{3+} consists of 211 final state components. The calculated line spectra are convoluted with Gaussian width of 0.5 eV (FWHM) to mimic instrumental resolution. The absolute energy position of divalent and trivalent peaks cannot be determined from the theoretical calculation. We set the energy positions of the calculated peaks to fit the experimental peak positions. The evidence that the divalent peaks are situated in 0–5.6 eV binding energy region and the trivalent peaks in 6–15 eV is confirmed by resonant behavior of each peak described in the following sections and by previous results.[3, 14, 16, 29]

As in the case of TY spectra discussed in the previous section, the overall spectral features of TmX is understood as the superposition of divalent and trivalent components. For TmS, the trivalent parts are dominant in the spectrum, whereas the divalent ones are dominant for TmTe. The spectrum of TmSe shows almost equal contribution of both divalent and trivalent components. In our experimental condition of about 0.5 eV energy resolution, the surface shift reported previously[15] could not be observed. This means that the spectral fea-

tures in Fig. 2 include both components of surface and bulk. However, we can resolve each multiplet component rather well as compared with the spectra in ref. 3. The agreement between the theoretical and the experimental results is satisfactory on relative peak positions and intensities.

It is noted that the peak positions of trivalent multiplet for TmTe is very different from those of TmS and TmSe. This might be due to surface shift as will be discussed in subsection 4.5.

We tried to estimate the mean valence of each material from the intensity ratio between divalent component and trivalent one of the off-resonant spectra. The evaluation method is described as the followings. First, the background due to the secondary electrons is subtracted from the experimental spectrum. Secondly, the components of divalent and trivalent are separated, and integrated respectively. Finally, the mean valence is calculated according to the formula of $2+I(Tm^{3+})\times13/[I(Tm^{2+})\times12+I(Tm^{3+})\times13]$. Here, $I(Tm^{2+})$ and $I(Tm^{3+})$ are the integrated intensities of the Tm^{2+} and Tm^{3+} components, respectively. The estimated values are 2.93 for TmS, 2.68 for TmSe and 2.35 for TmTe. As discussed above, we could not separate the surface contribution from the bulk one. Therefore, the obtained mean valence includes information both from the surface and bulk. It is known that the TY spectra reflect more bulk information than photoemission spectra. (Of course, the values obtained from transport properties or magnetic susceptibilities are mostly bulk sensitive.) This means that the values obtained by photoemission may deviate from intrinsic ones due to surface effects. In addition to the surface effect, the existence of other valence electrons such as ligand valence electrons and $5d6s$ electrons may be an origin to deform the curve fitting results, since the cross section of other valence electrons may not be negligible in this energy range of off-resonant condition. In this sense, we have to perform the curve fitting for photoemission spectra excited by higher photon energies. These experiments for the same samples have been already carried out around the Tm $3d$-$4f$ excitation region.[33] The cross section ratio between the $4f$ electrons and other valence electrons around 1–2 keV photon energy range is expected to be very large. We observed decrease of the trivalent $4f$ peak while the divalent peak increases in intensity of the TmTe spectrum in ref. 33. The obtained values are close to those obtained by the $4d$ absorption spectra. For TmS and TmSe, the obtained values are not so different from those obtained by the $4d$ XAS and the present photoemission spectra, i.e., within small error of the estimation procedure.

In order to discuss the resonant behavior of each multiplet peak easily in the following sections, we name the representative peaks by alphabet (a-i) for TmS, (A-G) for TmSe and by numerical number (1–9) for TmTe as shown in the figure. For peak O of TmSe, we did not measure the CIS spectrum but calculated it. TmSe includes both Tm^{2+} and Tm^{3+} components and is a typical example to explain the resonant behavior of both divalent and trivalent peaks.

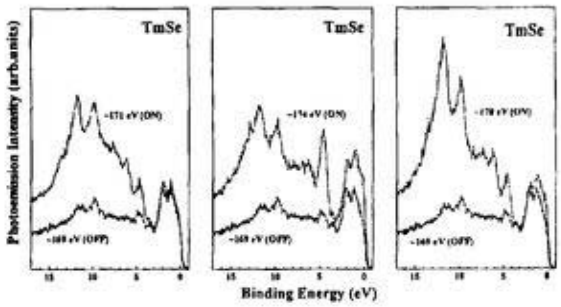

Fig. 3. Representative valence band photoemission spectra of TmSe at on ($h\nu \cong 171$, 174 and 178 eV) and off ($h\nu \cong 169$ eV) resonant conditions.

4.3 Resonant photoemission results of TmSe

Figure 3 shows the valence band photoemission EDC's of TmSe in some representative conditions with different photon energies both on- and off-resonance around the Tm $4d$ threshold. Excitation photon energies were selected from the TY spectrum in Fig. 1, namely $h\nu \cong 169$ eV for off resonant condition and three resonant conditions of $h\nu \cong 171$, 174 and 178 eV, respectively. The intensity of the spectra is normalized by incident photon flux. For the help to discuss the spectra easily, the off-resonant spectrum at 169 eV is shown in every panel. It is noticed that our spectra show much multiplet $4f$ structures than those reported in ref. 3 even in the resonant conditions because of higher resolution. As discussed in above section, the divalent part ($4f^{12}$ final state) of the TmSe spectrum was estimated to be situated from 0 to 5.6 eV binding energy (B.E.) and Tm $4f^{11}$ trivalent state in 5.6–14 eV B.E. range. We observed large resonant photoemission intensity enhancement from both divalent and trivalent parts of Tm $4f$ final state multiplets at 174 eV. At 171 and 178 eV, mostly trivalent parts are enhanced. Further, comparing the off-resonant spectra at $h\nu = 169$ eV with the spectrum at 140 eV in Fig. 2(b), we notice that the intensity ratio between the trivalent and divalent components is rather different in spite of the fact that both condition should be off resonance. At 169 eV, the divalent peaks are stronger than that at 140 eV. These phenomena can be explained as follows. Namely, the $4d$ absorption spectrum for divalent is relatively wider. Therefore, the position at 169 eV is still in the tail of resonant condition of divalent component. The single broad $^2D_{5/2}$ peak seems to overlap with the relatively sharper $^3H_6$ peak of trivalent ion, which can be seen in the calculated TY spectra in Fig. 1. Because of the broadness of the $4d$ TY spectra for both Tm^{2+} and Tm^{3+}, it is rather difficult to separate the trivalent components and the divalent ones by a subtracting procedure. The $3d$-$4f$ resonant photoemission study may be more useful to separate the divalent and trivalent contributions because of very sharp and well separated absorption peak structures of Tm $3d$ edge. The detail will be described elsewhere.[33]

In order to discuss the resonant behavior in more detail and in order to justify the valency of each EDC peak, we show the experimental results of the CIS spectra in

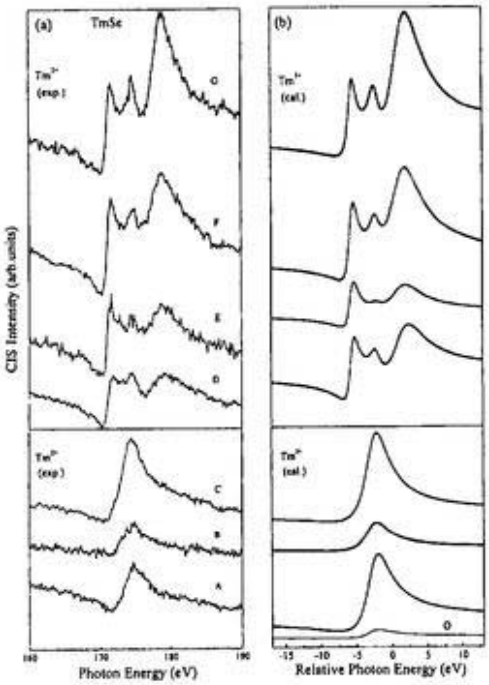

Fig. 4. (a) Upper: CIS spectra for D-G EDC peaks of TmSe in Fig. 2(b). Lower: CIS spectra for A-C EDC peaks of TmSe in Fig. 2(b). (b) Upper: Calculated CIS spectra for Tm^{3+} corresponding D-G EDC peaks. Lower: Calculated CIS spectra for Tm^{2+} corresponding A-C EDC peaks. Spectrum for O peak is also calculated but not measured.

Fig. 4(a). The CIS spectra of TmSe were obtained for representative peaks A-G labeled in Fig. 2(b). It is obvious in Fig. 4(a) that three resonance peaks exist in the CIS spectra for trivalent part (D-G) and only one peak for the divalent part (A-C) similar to the Fano line shape.[9] This can be again a proof of the justification for the valence.

The calculated CIS spectra are shown in Fig. 4(b). The lower panel of the figure shows CIS curves for the Tm^{2+} ion. They are calculated at peaks A to C shown in Fig. 2(b), which correspond to experimental result of lower panel of Fig. 4(a). In addition, we showed the CIS spectrum for the peak O. Peak O is at just below the Fermi level, which is observed in the experimental EDC. But we did not measure the CIS spectrum for peak O. These CIS have one resonance peak, because there is only one intermediate state ($4d^9 4f^{14}$; $^2D_{5/2}$) by dipole selection rule. The final states with J=7/2, and 9/2 give uniform background. The enhancement ratio is different, depending on the multiplet terms in the final states. It is especially found that the peak C shows the largest enhancement, which is observed both from the calculation and the experiment. These results are consistent with the previous analysis for Yb^{3+} ion, which has the iso-electronic configuration as Tm^{2+} ion.[6]

The upper panel of Fig. 4(b) shows the calculated CIS curves for the Tm^{3+} corresponding to the peaks D to G of the EDC. It is seen that there are three resonance peaks in the CIS curves as well as the TY spectrum. In fact, there are four intermediate states, but one of them is too weak to be observed. These four states are $^3H_5$, $^3G_5$, $^1H_5$, and $^3H_6$. The three states with J=5 are not pure LS terms but slightly mixed with each other by spin-orbit interaction. The $^3H_6$, $^3H_5$ and $^3G_5$ terms correspond to the first, second and the third intermediate states. The highest energy intermediate state $^1H_5$ is the weakest one, because this is the singlet level and only dipole-allowed through the spin-orbit coupling. There are no J=7 intermediate states so that the J=7 final states do not have resonance. The difference in the shape of each CIS curve for Tm^{3+} is due to the multiplet structure and the multiplet dependence of the Auger matrices. It is also noticed that the agreement between the calculation and experimental results is quite well. For example, the CIS for E indicates that the middle peak is smallest both in calculation and experiment. The CIS for D shows that the dip between the $^3H_6$ and $^3H_5$ intermediate state peaks is remarkable.

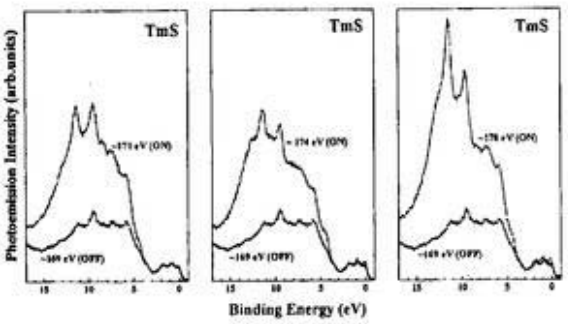

Fig. 5. Same as in Fig. 3, but for TmS.

When we compare our results with the corresponding ones in ref. 3, we noticed that our EDC spectra have rich structures and detailed information about the resonant behavior because of better resolution. The stoichiometry of their sample in ref. 3 seemed to be different from ours, namely more divalent character. These might be reasons why they did not get a clear result of CIS spectrum for trivalent EDC peak especially at 6.2 eV B.E. which corresponds to peak D in our spectra.

4.4 Resonant photoemission results of TmS

Figure 5 shows the valence band photoemission EDC of TmS with different photon energies both at on- and off-resonance around the Tm 4d threshold, which were obtained in the same way as Fig. 3. It is noted that the trivalent parts of the spectra show big resonance at three peak positions of trivalent TY spectrum. On the other hand, the enhancement of the divalent part is not so clearly visible even in its resonant condition at $h\nu \cong$ 174 eV ($^2D_{5/2}$ intermediate state).

In order to see the modulation of the valence band emission more clearly, the CIS spectra of divalent and trivalent part peaks are shown in Fig. 6. The corresponding EDC peak binding energies (at $h\nu$ = 140 eV) are indicated in Fig. 2(a) by alphabet (a-i). The CIS spectra show three main peaks for the trivalent part, and single maximum for divalent part, which is similar to the result of TmSe. One may expect that the CIS spectra for c (3.5 eV B.E.) and d (4.5 eV B.E.) should behave as divalent component. But in Fig. 6, we observe

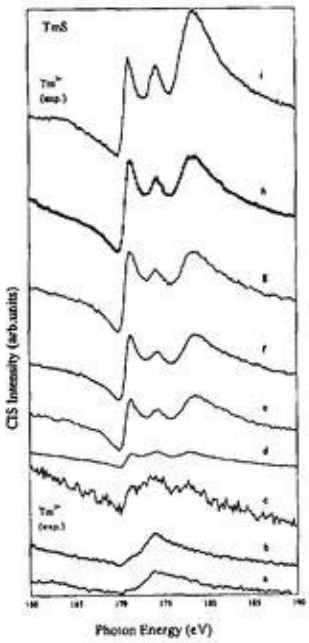

Fig. 6. CIS spectra for TmS around Tm 4*d* edge. The labels a-i refer to the peak positions of the EDC in Fig. 2(a).

that the two CIS spectra show three peaks, i.e., behave as trivalent emission. This might be due to weak emission of divalent parts. Namely, the emitted electrons at 3.5 eV and 4.5 eV B.E. mostly seem to come from the tail of trivalent peaks situated at higher B.E. side.

From the comparison with the results of TmSe, we note that the trivalent parts of TmS behave as almost the same way as those for TmSe. We notice the differences in the divalent part between the results of TmS and TmSe as described follows.

First, the peak "a" just below the Fermi level which corresponds to the peak (shoulder) "O" in TmSe is more clearly observed in spite of the weak intensity. This can be explained by the effect of surface shifted peak. Since the TmS and the TmSe are metallic, the part of the lowest B.E. peak is situated above the Fermi level. It can be supposed that the position of the maximum of the bulk component may be situated in the unoccupied region. This may be a reason why the peak "O" of TmSe is weaker than peak "A" whereas the intensity of the lowest B.E. peak is strongest in the calculation (Fig. 2). It has been reported by Kaindl *et al.*[15] that the surface component of the divalent peak is shifted to higher B.E. about 0.3 eV as compared with the bulk component. If the contribution of the peak "a" mostly comes from surface component, the position of the maximum of the peak can be shifted below the Fermi level. As a result, the density of states just below the Fermi level should become stronger and be clearly observed.

Second difference from the result of TmSe is that the resonance for divalent part seems to be weaker. As discussed above, the cross section of the other valence electrons such as 5*d*6*s* of Tm and ligand's (S) valence electrons is not negligible in this photon energy. Hence the part of the intensity between 0–5.6 eV B.E. emission may

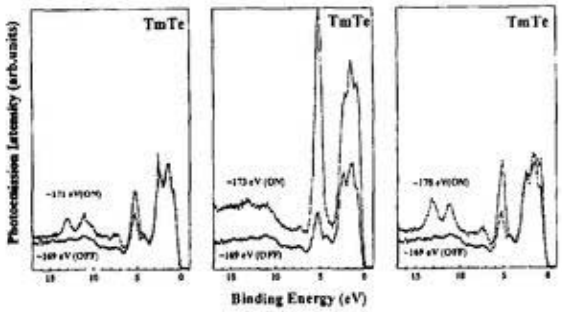

Fig. 7. Same as in Fig. 5, but for TmTe. The resonant condition of divalent component is $h\nu \cong 173$ eV.

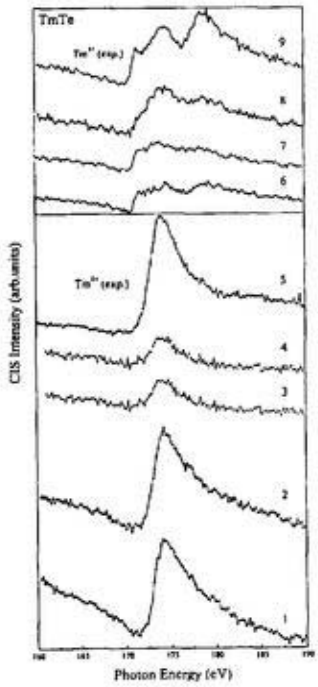

Fig. 8. Same as in Fig. 6, but for TmTe. The numerical labels refer to the peak positions of the EDC in Fig. 2(c).

not come only from divalent 4*f* component but also from others, as being due to 4*f*-5*d* hybridization. Similar hybridization effects have been observed from other rare earth metals.[12] This may be a reason why the clear resonance is not observed in divalent features region in TmS.

4.5 Resonant photoemission results of TmTe

We have measured resonant photoemission spectra for TmTe under the same experimental conditions as for TmS and TmSe. Figure 7 shows the valence band photoemission EDC of TmTe with different photon energies both at on- and off-resonance around the Tm 4*d* threshold. The CIS spectra obtained in the same way as those for TmS and TmSe are shown in Fig. 8.

In general, the strong resonant photoemission enhancement of divalent part is observed whereas the trivalent part shows less resonance. The CIS spectra for divalent components (0.9–5.2 eV B.E.; numbered 1–5) show a strong single peak. Especially, the No. 5 peak shows the

biggest resonance, which is consistent with the calculation as shown in the subsection of TmSe but more clearly observed. The shape of the CIS spectra for trivalent peaks (7.3–8.9 eV B.E.; numbered 6–9) is not completely consistent with those expected for Tm^{3+}. Probably, the most of the intensity of the electron between 7.3–8.9 eV B.E. is due to strong background electrons originating from the divalent part. This may deform the shape of the CIS spectra. From these results, we can conclude that Tm ion in TmTe has mostly divalent character but with small amount of trivalent ion. This result is consistent with some of the previous reports[19,34,35] but is contrary to an earlier report[15] of off-resonant photoemission. They argued that the valence structure of TmTe is completely divalent. They observed small peaks around the trivalent B.E. region. But their explanation was that the origin of those peaks is not from trivalent but from surface oxidized component or shake up (two hole) satellite.

The valence structure of such kind of samples strongly depends on the stoichiometry. The mean valence of our sample obtained from the result of magnetic susceptibility measurement is 2.017. This value means that there should be almost no characters of trivalent for TmTe. The mean valence values obtained in this study by TY (2.15) and off-resonant photoemission spectra (2.35) as well as the CIS measurements suggest the existence of trivalent component. This means that the trivalent component observed in our spectra mainly comes from surface. The peak positions of the trivalent multiplet of the spectra in Figs. 2(c) and 7 shift to higher B.E. than those for TmS and TmSe. The shift is more than 1 eV. This is not only due to the semiconducting nature of TmTe but also the surface shift of the trivalent component. The trivalent surface component of TmTe is not discussed in the earlier report.[15] But the trivalent surface component of Tm films was observed.[27-29] In the refs. 27–29, the shift for Tm film is also in the same direction as in our results, i.e., higher B.E. with 0.7 eV.

§5. Conclusion

We have systematically studied resonant photoemission spectra of the TmX (X=S, Se, Te) compounds around the Tm 4d threshold. The experimental results showed a large resonant enhancement of 4f photoelectron emission around the 4d threshold with sharper multiplet structures than those reported before. The calculated results are in good agreement with the experimental ones both for divalent and trivalent features of Tm ions. The resonant behavior of the photoelectron spectral features of 4f levels is in good agreement with those calculated for divalent and trivalent 4f components. The CIS spectral features for each multiplet component show almost similar shape to that for TY spectra.

It was confirmed that the photoelectron spectra of TmS originate mostly from trivalent Tm 4f electrons with small surface component of Tm^{2+} ion. TmSe showed mixed valent character of both divalent and trivalent 4f features as reported before. TmTe shows mostly divalent character but there are some evidences for that trivalent Tm 4f electrons exist in TmTe owing to surface effect.

We have estimated the mean valence of each sample from absorption spectra and from off-resonant photoemission spectra. The meaning of these values is discussed as compared with that for the value obtained from the measurements of magnetic susceptibilities. The estimated mean valence includes some ambiguities due to the surface effect and the contribution of other valence electrons. Further detailed resonant photoemission experiments with higher energy resolution are needed to understand the electronic structure of these samples to separate the surface effect more precisely. The subtraction procedure of the contribution of other valence electrons may also be necessary.

Acknowledgments

This work was supported by the Joint Studies Program (1996–1997) of the Institute for Molecular Science. The authors would like to thank the staff members of the UVSOR facility for their help during the experimental work. One of the authors (Y.U.) received financial support during this work from the Scientific and Technical Research Council of Turkey (TUBITAK).

1) "*Giant Resonances in Atoms, Molecules and Solids*", ed. J. P. Connerade, J. M. Esteva and R. C. Kartanak: (Plenum Press, New York, 1987).
2) "*Synchrotron Radiation Research: Advances in Surface and Interface Science, Volume 1: Techniques*", ed. Robert Z. Bacharach: (Plenum Press, New York, 1992).
3) S.-J. Oh, J. W. Allen and I. Lindau: Phys. Rev. B **30** (1984) 1937.
4) C. Laubschat, E. Weschke, G. Kalkowski and G. Kaindl: Physica Scripta **41** (1990) 124.
5) D. J. Friedman, C. Carbone, K. A. Bertness and I. Lindau: J. Electron Spectrosc. Relat. Phenom. **41** (1986) 59.
6) J. Schmidt-May, F. Gerken, R. Nyholm and L. C. Davis: Phys. Rev. B **30** (1984) 5560.
7) J. W. Allen , L. I. Johansson, I. Lindau and S. B. Hagström: Phys. Rev. B **21** (1980) 1335.
8) J. W. Allen, L. I. Johansson, R. S. Bauer, I. Lindau and S. B. M. Hagström: Phys. Rev. Lett. **41** (1978) 1499.
9) U. Fano: Phys. Rev. **124** (1961) 1866.
10) O. P. Sairanen and S. Aksela: J. Phys. Cond. Matter. **4** (1992) 3337.
11) J. Sugar: Phys. Rev. B **5** (1972) 1785.
12) P. A. Dowben, D. Lagraffe, D. Li, L. Dottl, C. Hwang, Y. Ufuktepe and M. Onellion: J. Phys. Condens. Matter **2** (1990) 8801.
13) L. I. Johansson, J. W. Allen and I. Lindau: Phys. Lett. **86A** (1981) 442.
14) M. Campagna, E. Bucher, G. K. Wertheim, D. N. E. Buchanan and L. D. Longinotti: Phys. Rev. Lett. **32** (1974) 885.
15) G. Kaindl, C. Laubschat, B. Reihl, R. A. Pollak, N. Mårtensson, F. Holtzberg and D. E. Eastman: Phys. Rev. B **26** (1982) 1713.
16) G. K. Wertheim, W. Eib, E. Kaldis and M. Campagna: Phys. Rev. B **22** (1980) 6240.
17) R. Suryanaryanan G. Güntherodt, J. L. Freeouf and F. Holtzberg: Phys. Rev. B **12** (1975) 4215.
18) E. Bucher, K. Andres, F. J. di Salvo, J. P. Maita, A. C. Gossard, A. S. Cooper and G. W. Hull Jr.: Phys. Rev. B **11** (1975) 500.
19) H. R. Ott and F. Hulliger: Z. Phys. B **49** (1983) 323.
20) Y. Lassailly, C. Vettier, F. Holtzberg, J. Flouquet, C. M. E. Zeyen and F. Lapierre: Phys. Rev. B **28** (1983) 2880.

21) A. Berton, J. Chaussy, J. Flouquet, J. Odin, J. Peyrard and F. Holtzberg: Phys. Rev. B **31** (1985) 4313.
22) B. Batlogg, H. R. Ott, E. Kaldis, W. Thoni and P. Wachter: Phys. Rev. B **19** (1979) 247.
23) K. Andres, W. M. Walsh, Jr., S. Darack, L. W. Rupp Jr. and L. D. Longinotti: Solid State Commun. **27** (1978) 825.
24) P. Haen, F. Lapierre, J. M. Mignot, R. Tournier and F. Holtzberg: Phys. Rev. Lett. **43** (1979) 304.
25) M. Ribault, J. Flouquet, P. Haen, F. Lapierre, J. M. Mignot and F. Holtzberg: Phys. Rev. Lett. **45** (1980) 1295.
26) A. Berton, J. Chaussy, B. Cornut, J. Flouquet, J. Odin, J. Peyrard and F. Holtzberg: Phys. Rev. B **23** (1981) 3504.
27) M. Bodenbach, A. Höhr, C. Laubschat, G. Kaindl and M. Methfessel: Phys. Rev. B **50** (1994) 14446.
28) M. Domke, C. Laubscaht, M. Prietsch, T. Mandel, G. Kaindl and W. D. Schneider: Phys. Rev. Lett. **56** (1986) 1287.
29) C. L. Nicklin, C. Binnis, S. Mozley, C. Norris, E. Alleno, M. G. Barthes-Labrousse and G. van der Laan: Phys. Rev. B **52** (1995) 4815.
30) F. Holtzberg, J. Flouquet, P. Haen, F. Lapierre, Y. Lassailly and C. Vettier: J. Appl. Phys. **57** (1985) 3152.
31) H. Ogasawara, A. Kotani, B. T. Thole, K. Ichikawa, O. Aita and M. Kamada: Solid State Commun. **81**, (1992) 645.
32) R. D. Cowan: *The Theory of Atomic Structure and Spectra* (University of California Press, Berkeley, 1981).
33) T. Kinoshita, Y. Ufuktepe, K. G. Nath, S. Kunura, H. Kumigashira, T. Takahashi, T. Matsumura, T. Suzuki, H. Ogasawara and A. Kotani: J. Electron Spectrosc. Relat. Phenom. **88–91** (1998) 377.
34) G. Kaindl, G. Kalkowski, W. D. Brewer, B. Perscheid and F. Holtzberg: J. Appl. Phys. **55** (1984) 1910.
35) G. Kaindl, W. D. Brewer, G. Kalkowski and F. Holtzberg: Phys. Rev. Lett. **51** (1983) 2056.

J. Synchrotron Rad. (1998). 5, 726–728

Performance of the YB_{66} soft X-ray monochromator crystal at the wiggler beamline of the UVSOR facility

Toyohiko Kinoshita,[a]* Yasutaka Takata,[a] Tokuo Matsukawa,[b] Hirofumi Aritani,[c]† Shigehiro Matsuo,[c] Takashi Yamamoto,[c] Masao Takahashi,[d] Hisao Yoshida,[e] Tomoko Yoshida,[f] Yüksel Ufuktepe,[a]‡ Krishna G. Nath,[g] Shin-ichi Kimura[a] and Yoshinori Kitajima[h]

[a]Institute for Molecular Science, Okazaki 444-8585, Japan, [b]Department of Physics, Naruto University of Education, Naruto 772-8502, Japan, [c]Department of Molecular Engineering, Kyoto University, Kyoto 606-8501, Japan, [d]The Institute of Scientific and Industrial Research, Osaka University, Ibaraki, Osaka 567-0047, Japan, [e]Department of Applied Chemistry, School of Engineering, Nagoya University, Nagoya 464-8603, Japan, [f]Division of Energy Science, Center for Integrated Research in Science and Engineering, Nagoya University, Nagoya 464-8602, Japan, [g]Department of Structural Molecular Science, Graduate University for Advanced Studies, Okazaki 444-8585, Japan, and [h]Institute of Materials Structure Science, High Energy Accelerator Research Organization (KEK), Oho 1-1, Tsukuba 305-0801, Japan. E-mail: toyohiko@ims.ac.jp

(Received 4 August 1997; accepted 18 November 1997)

Soft X-ray spectra have been measured using a pair of $YB_{66}(400)$ monochromator crystals at the double-crystal monochromator beamline BL7A of the UVSOR facility, where the wiggler radiation has a magnetic field of 4 T. Deformation of the YB_{66} crystal due to heat load from the synchrotron radiation is almost negligible. The photon flux is about 10^8 photons s^{-1} $(100\ mA)^{-1}$ in the energy region 1.2–2 keV and the energy resolution is 0.7 ± 0.1 eV around $h\nu = 1.5$ keV. These results show that the YB_{66} crystal is suitable for use as a monochromator crystal. Its application to soft X-ray spectroscopy is discussed.

Keywords: soft X-ray beamlines; YB_{66} crystals; double-crystal monochromators; wigglers.

1. Introduction

YB_{66} [$2d = 11.76$ Å for (400) reflection] is known to be one of the best monochromator crystals covering the soft X-ray region from 1.1 to 2 keV, with high performance (Wong *et al.*, 1990) such as high-energy resolution, no absorption structures originating from the elements of the crystal in the photon energy range, resistance to radiation damage *etc.* So far, only the SSRL (Stanford Synchrotron Radiation Laboratory) group has used a YB_{66} crystal (Rowen *et al.*, 1993), since there are several difficulties associated with the use of YB_{66} crystals in synchrotron radiation facilities. One of the difficulties is that a single crystal of sufficient size has not, until very recently, been available. The other difficulty is that such a crystal has a very low thermal conductivity and is easily deformed by the high heat load from synchrotron radiation from a high-energy machine. Even in the SSRL facility, there seems to be some difficulty in using the crystal for spectroscopy experiments because of the heat load.

The storage ring of the UVSOR facility is operated at a rather low energy (750 MeV) and is expected to produce a lower heat load than a high-energy machine. For example, at the double-crystal monochromator beamline BL11B of the Photon Factory (2.5 GeV), the power density was estimated as 3.3 W mm^{-2} on the first crystal (Funabashi *et al.*, 1989). However, the density in the present case is less than 0.03 W mm^{-2}. A wavelength-shifter-type wiggler with a 4 T magnetic field (Nakamura *et al.*, 1996) is installed at the UVSOR beamline BL7A (Murata *et al.*, 1992) to provide a high photon flux in the soft X-ray region. This prompted us to examine the performance of a YB_{66} monochromator crystal at the UVSOR facility. The crystal ($10 \times 20 \times 1$ mm size) is a commercial product, synthesized by Crystal Systems Inc., Yamanashi, Japan.

2. Overview of the wiggler beamline at UVSOR

Fig. 1 shows a schematic view of the double-crystal monochromator (DXM) beamline BL7A. The superconducting magnet wiggler is installed in the straight section upstream of the bending-magnet section B7. When the higher-energy light from the wiggler is used with crystals such as InSb(111) and Ge(111), the beamline is fixed just downstream of the straight section (0° line). In the case of synchrotron radiation from the bending section, the DXM accepts synchrotron radiation emitted at a point on the electron orbit that is 2° downstream of the edge of the bending section. In order to avoid radiation damage to the insulator crystals of, *e.g.* beryl and quartz (energy being covered 0.8–2 keV), we use bending-magnet radiation. Between the use of wiggler radiation and bending-magnet radiation, the beamline set-up is changed from the 0° line to the 2° line. YB_{66} is a semiconductor and may be better at withstanding radiation damage than insulator crystals. If we succeed in using a YB_{66} crystal in the lower photon energy region, it will not be necessary to change the beamline between the wiggler and bending lines. This will enable us to provide high-performance beamtime to users.

3. Performance of the YB_{66} monochromator crystal

Fig. 2 shows the throughput of the monochromator with the use of $YB_{66}(400)$. The absolute value of the photon flux was obtained by measuring the photocurrent from a Si photodiode (Interna-

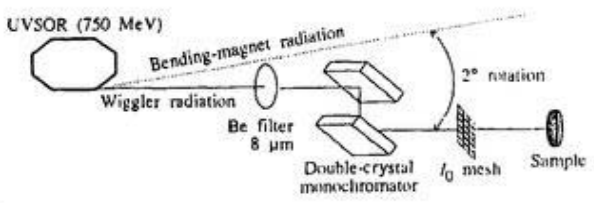

Figure 1
A schematic view of the soft X-ray beamline BL7A at UVSOR.

† Present address: Department of Chemistry and Material Technology, Faculty of Engineering and Design, Kyoto Institute of Technology, Kyoto 606-8585, Japan.
‡ Visiting scientist on leave from Physics Department, University of Cukurova, 01330 Adana, Turkey.

tional Radiation Detectors Inc., USA) whose quantum efficiency has been calibrated absolutely. When radiation from the wiggler is used, the photon flux is approximately 10^8 photons s^{-1} (100 mA)$^{-1}$. The decrease in the flux at lower photon energy is due to the cut-off of the Be foil. A flux of 10^4–10^7 photons s^{-1} (100 mA)$^{-1}$ is obtained with bending-magnet radiation.

The X-ray absorption fine-structure (XAFS) spectra for Mg and Al oxides in Fig. 3 were measured by the total photoelectron yield method as described previously (Murata *et al.*, 1992). The step width of the monochromator scanning was 0.01°, which corresponds to about 0.15 eV at $h\nu$ = 1310 eV. The reproducibility of energies was within the step width. The spectra obtained using the YB_{66} crystal show almost the same features as those obtained using beryl and quartz crystals. During the spectroscopy measurements, we also checked the effects of the heat load. We monitored the beam intensity at the sample position and tuned the angle of the second monochromator crystal to maximize the intensity. The angle deviation originating from the change of the lattice spacing in the first crystal was estimated by measuring the deviation of the tuning angle of the second crystal. The angle correction due to the heat-load effects was estimated to be less than 0.01°, which corresponds to energy shifts of less than 0.15 eV around $h\nu$ = 1.3 keV. The value of the energy shift is much less than that in the SSRL, where an approximately 3 eV shift is reported (Wong, private communication). It is concluded from the above result that the effect of heat load at BL7A is almost negligible for spectroscopy measurements.

We have tried to measure the rocking curves of the YB_{66} crystal by rotating the second crystal in order to estimate energy resolution (not shown here). The rocking curves showed some multi-structures and were wider than those reported before (Rowen *et al.*, 1993). This may result from the multi-domain structures of the crystal, as will be discussed below. If we assume the multi-structures are a convolution of single peaks, the width of each single peak is estimated to be about 0.7 ± 0.1 eV around $h\nu$ = 1.5 keV. This value is equal to the deconvoluted value of the photoemission resolution discussed in §4 and almost comparable with that in the SSRL beamline under standard conditions. We have also observed the image of output light with the fluorescence screen. The image was not homogeneous. These results mean that the crystal is not an ideal single crystal, but instead consists of multi-domains. The effect of the multi-domains is not a serious problem. For example, we have obtained reasonable spectra [except for the problem of the (600) reflection as described below] with higher-energy resolution than that of beryl crystal, as shown in Fig. 3. If we could obtain a crystal with single domain, the intensity and resolution may be improved.

These results show that the YB_{66} crystal is suitable for use as monochromator crystal. However, there remains anothe problem which needs to be solved in order to use the YB_{66} crysta for spectroscopy. The problem is that two positive glitches a 1385.6 and 1438 eV are observed in Figs. 2 and 3(*a*). These gli ches are known to be due to the sharp reflectivity increas associated with anomalous scattering of the (600) reflection at th Y $L_{2,3}$-edges (Tanaka *et al.*, 1997). The original [(400) reflectio light] peaks are also observed in Fig. 2 at 2080 and 2156 e respectively. In order to record more precise extended XAF spectra, the high-energy component of the light must be reduce for the next step of the beamline improvement. We plan to insta a pair of pre-focusing mirrors coated by Si between the B window and the front end. The Si-coated mirror system i expected to be useful not only as a focusing system but also as high-cut filter.

4. Application to spectroscopy

We have applied the light monochromated with the YB_{66} crysta not only to measurements of absorption spectroscopy but also t photoemission measurements. We present here, as an example the resonant photoemission study of heavy rare-earth compound (Kinoshita *et al.*, 1998). Although the photon intensity is not grea enough, the photoemission study becomes possible by using high-performance electron analyser (Fisons, ESCALAB220i XL).

Fig. 4 shows the 3*d*–4*f* resonant photoemission result for TmSe which is typically known to be a material of mixed valency Despite the advantages of studying 3*d*–4*f* resonant photoemissio for heavy rare-earth compounds, in addition to 4*d*–4*f* resonance only a few investigations have so far been performed. The reason why such experiments are difficult is that grating mono chromators cannot cover such high-energy light with high-energ resolution and high intensity. As shown in Fig. 4, the spectra hav

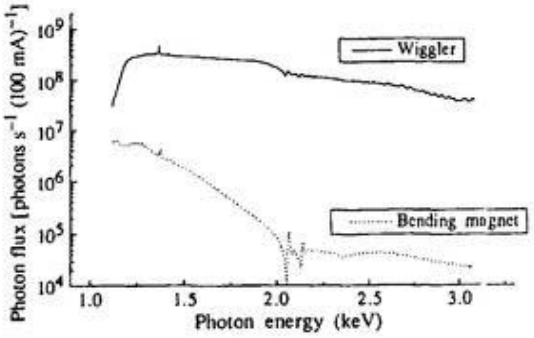

Figure 2
The throughput of the double-crystal monochromator with YB_{66}(400). Radiation from the wiggler and the bending-magnet section is used.

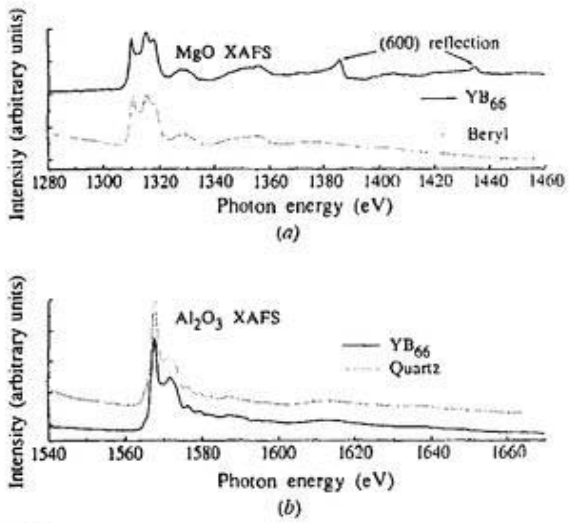

Figure 3
(*a*) Comparative X-ray absorption spectra of MgO around the Mg *K*-ed taken by YB_{66} and beryl crystals. (*b*) Comparative X-ray absorpti spectra of Al_2O_3 around the Al *K*-edge taken by YB_{66} and quartz cryst

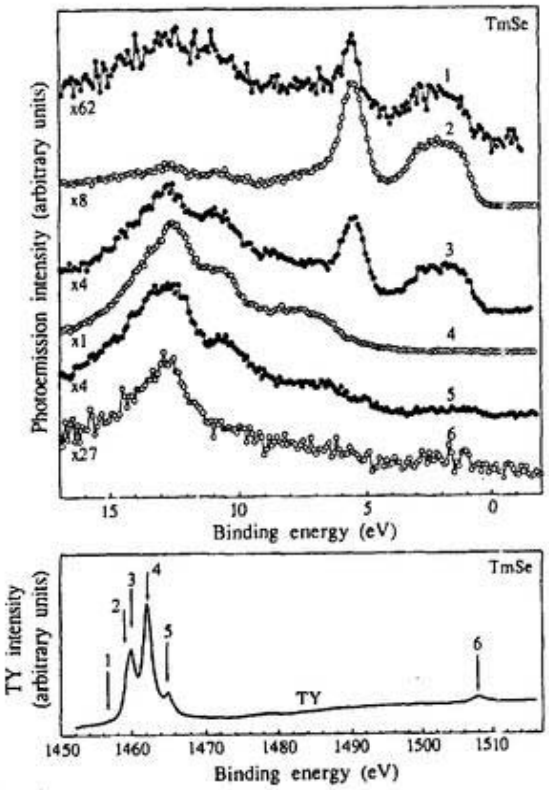

Figure 4
The photoemission spectra of TmSe at an excitation photon energy of the $3d$–$4f$ resonance region. The photoemission spectra were measured at the photon energies of the points indicated by arrows in the absorption (total photoelectron yield; TY) spectrum (bottom).

been obtained with a resolution of 0.9 ± 0.1 eV and a reasonable S/N ratio in the photon energy region 1.45–1.52 keV. The resolution of the data seems to be better than that obtained for a $TmAl_2$ sample with a beryl monochromator crystal (Laubschat *et al.*, 1990), especially in off-resonant conditions. It is clearly observed that the divalent peaks (located at a binding energy less than 5.6 eV) and the trivalent peaks (located at a binding ene greater than 5.6 eV) show resonance at different excitat energies.

5. Conclusions

We have succeeded in measuring soft X-ray spectra using YB_{66} monochromator crystal at the DXM beamline BL7A of UVSOR facility. The combination of the YB_{66} crystal and wiggler at such a low-energy storage ring performs well in soft ray measurements. The YB_{66} crystal may be very valuable for in future studies of soft X-ray spectroscopy at UVSOR. The Y crystal has already been used by some users. Photoabsorpt and photoelectron spectroscopy experiments in such a pho energy region are now possible.

The authors would like to thank the staff of the UVS facility for their support. TK and YT thank Dr T. Tanaka and J. Wong for invaluable discussions.

References

Funabashi, M., Nomura, M., Kitajima, Y., Yokoyama, T., Ohta, T Kuroda, H. (1989). *Rev. Sci. Instrum.* **60**, 1983–1986.
Kinoshita, T., Ufkutepe, Y., Kimura, S., Nath, K. G., Kumigashira, Takahashi, T., Matumura, T., Suzuki, T., Ogasawara, H. & Kotani (1998). *J. Electron Spectrosc. Relat. Phenom.* In the press.
Laubschat, C., Weschke, E., Kalkowski, G. & Kaindl, G. (1990). *Phys.* **41**, 124–129.
Murata, T., Matsukawa, T., Naoé, S., Horigome, T., Matsudo, O Watanabe, M. (1992). *Rev. Sci. Instrum.* **63**, 1309–1312.
Nakamura, E., Hama, H., Yamazaki, J., Kinoshita, T., Matsudo, Yonehara, H., Kasuga, T., Isoyama, G. & Watanabe, M. (1996 *Electron Spectrosc. Relat. Phenom.* **80**, 421–424.
Rowen, M., Rek, Z. U., Wong, J., Tanaka, T., George, G. N., Pickering, Via, G. H. & Brown, G. E. Jr (1993). *Synchrotron Radiat. News*, **6**, 27.
Tanaka, T., Aizawa, T., Rowen, M., Rek, Z. U., Kitajima, Y., Higash Wong, J. & Ishizawa, Y. (1997). *J. Appl. Cryst.* **30**, 87–91.
Wong, J., Shimkaveg, G., Goldstein, W., Eckart, M., Tanaka, T., Rek, Z & Tompkins, H. (1990). *Nucl. Instrum. Methods A*, **291**, 243–249.

Journal of Magnetism and Magnetic Materials 177–181 (1998) 349–350

ELSEVIER

Journal of magnetism and magnetic materials

4d–4f and 3d–4f resonant photoemission of TmX (X = S, Se, Te)

S. Kimura[a,*], Y. Ufuktepe[b], K.G. Nath[c], T. Kinoshita[a], H. Kumigashira[d], T. Takahashi[d], T. Matsumura[d], T. Suzuki[d], H. Ogasawara[e], A. Kotani[e]

[a] *UVSOR Facility, Institute for Molecular Science, Myodaiji, Okazaki 444, Japan*
[b] *Physics Department, University of Cukurova, 01330 Adana, Turkey*
[c] *Department of Structural Molecular Science, The Graduate University for Advanced Studies, Okazaki 444, Japan*
[d] *Department of Physics, Tohoku University, Sendai 980-77, Japan*
[e] *Institute for Solid State Physics, The University of Tokyo, Tokyo 106, Japan*

Abstract

The electronic structures of thulium monochalcogenides (TmX; X = S, Se, Te) were studied both experimentally and theoretically using resonant photoemission around the Tm 4d and 3d absorption edges. The fundamental electronic structures and the mean valences are analyzed.

Keywords: Rare earth chalcogenides; Photoemission

Rare-earth compounds have been studied very well because they show characteristic properties. Ce^{3+} compounds are studied more than other rare-earth compounds. Yb^{3+} and Tm^{2+} compounds are also studied because occupied and unoccupied electronic states of Ce^{3+} compounds are interchanged in Yb^{3+} and Tm^{2+} compounds.

Tm monochalcogenides (TmX; X = S, Se, Te) have been studied from 1970s and many papers were published. As for the results, TmS shows a Kondo lattice-like behaviour [1], TmSe shows a valence fluctuation [1] and TmTe is a semiconductor with an energy gap of 0.4 eV [2]. From a recent study, it is seen that TmTe becomes metallic in the pressure of about 2 GPa and a Kondo effect appears above the pressure [3].

Many photoemission studies of TmX have also been done until now [4–8]. However, most of the studies were limited to the experiments at fixed photon energy, except for that done by using 4d–4f resonance of TmSe [4]. In this study, we measured resonant photoemission spectra around the energies of the Tm 4d and 3d absorption edges. We divide the spectral components between Tm^{2+} and Tm^{3+} states and determine the mean valence of TmX.

TmX single crystals were grown by the Bridgman method using a sealed tungsten crucible and a high-frequency induction furnace [9]. The photoemission measurements were performed at the synchrotron radiation facility, UVSOR, of the Institute for Molecular Science. 4d–4f resonant photoemission was measured at BL2B1 with a grasshopper monochromator and a double-pass cylindrical mirror electron analyzer. 3d–4f resonant photoemission measurement was done at BL7A with a double YB_{66} crystal monochromator and a hemispherical electron analyzer. The total energy resolutions of these spectroscopic systems were less than 0.5 eV for 4d–4f and less than 1 eV for 3d–4f measurements. The clean surfaces of the samples were obtained by scraping using a diamond file or by Ar sputtering.

Obtained total-yield spectra of TmX around 4d and 3d absorption edges are shown in Fig. 1a and Fig. 1b, respectively. In the figures, calculated absorption spectra of Tm^{3+} and Tm^{2+} ions are also given. According to the line-shape fitting analysis, the mean valences are determined. The obtained mean valences are shown in Table 1.

From the energy distribution curve (EDC) of off-resonance photoemission at the excitation energy of 140 and 1253.6 eV (Mg Kα line), the mean valence can also be derived. First, the divalent and trivalent 4f states should be divided. The peak character can be determined by the valence band EDC of TmSe. For instance, a series of EDC at the excitation energy of the 3d absorption edge is shown in Fig. 2. It is noticed from the figure that the peaks in the binding energy range of 0–5.6 eV were enhanced at the resonant condition of Tm^{2+} ion whereas

* Corresponding author. Fax: +81 564 54 7079; e-mail: kimura@ims.ac.jp.

0304-8853/98/$19.00
PII S0304-8853(97)00558-1

Table 1
Mean valences of TmS, TmSe and TmTe determined by 4d absorption (4d XAS), 3d absorption (3d XAS), EDC at the excitation energy of 140 eV and EDC at 1253.6 eV. The mean valences determined from the magnetic susceptibilities (χ) are shown as the reference

	4d XAS	3d XAS	EDC $h\nu$ = 140 eV	EDC $h\nu$ = 1253.6 eV	χ
TmS	2.91	2.81	2.93	2.88	2.799
TmSe	2.79	2.63	2.68	2.69	2.530
TmTe	2.15	—	2.35	2.05	2.017

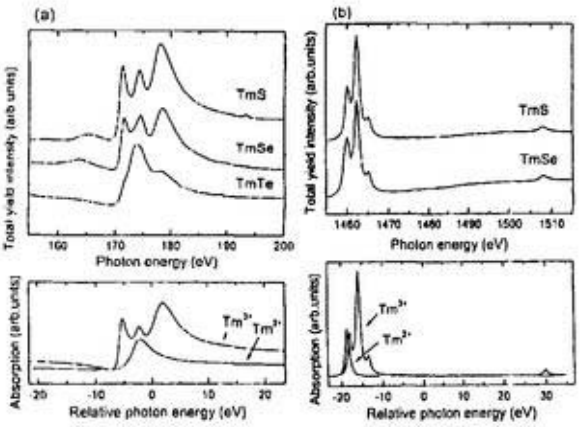

Fig. 1. (a) Total yield spectra of TmS, TmSe and TmTe at the 4d absorption edge and (b) those of TmS and TmSe at the 3d absorption edge in comparison with theoretical one.

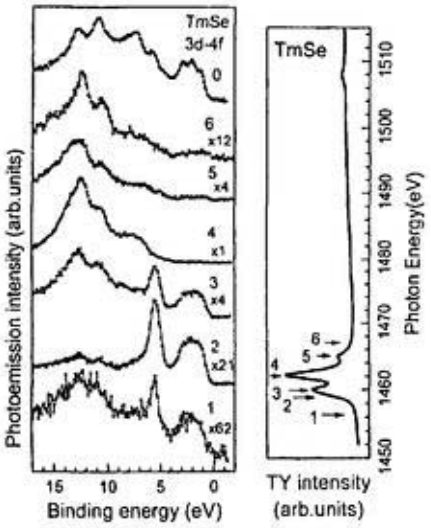

Fig. 2. Resonant photoemission spectra of TmSe at the 3d absorption edge. The spectrum marked by 0 is the XPS using Mg Kα line (1253.6 eV).

the peaks of 7–13 eV at the condition of Tm^{3+}. This is an evidence that the peaks at 0–5.6 eV originate from Tm^{2+} $4f^{12}$ states and those at 7–13 eV from $Tm^{3+}4f^{11}$. Then we derive the mean valence from off-resonance EDCs at the excitation energy of 140 and 1253.6 eV. The mean valence is derived from the function, (mean valence) $= 2 + I(Tm^{3+}) \times 13/[I(Tm^{2+}) \times 12 + I(Tm^{3+}) \times 13]$, where $I(Tm^{3+})$ means the intensity of $Tm^{3+}4f^{12}$ peaks. The estimated mean valences are also shown in Table 1.

The estimated mean valences of TmS and TmSe are in good agreement with those of magnetic susceptibility data. However, TmTe has a weak trivalent component, which is different from the magnetic susceptibility data. The EDC of 140 eV excitation is mostly surface sensitive in the four kinds of estimation methods. Therefore, the trivalency of Tm might be attributed to the surface properties or to be due to the contamination on the surface. The result is in the same situation of YbB_6 [10, 11].

References

[1] E. Bucher, K. Andres, F.J. di Salvo, J.P. Maita, A.C. Gossard, A.S. Cooper, G.W. Hull Jr., Phys. Rev. B 11 (1975) 500.
[2] B. Batlogg, E. Kaldis, A. Schlegel, P. Wachter, Phys. Rev. B 14 (1976) 5503.
[3] T. Matsumura, T. Kosaka, J. Tang, T. Matsumoto, H. Takahashi, N. Môri, T. Suzuki, Phys. Rev. Lett. 78 (1997) 1138.
[4] S.-J. Oh, J.W. Allen, I. Lindau, Phys. Rev. B 30 (1984) 937.
[5] G. Kaindl, C. Laubschat, B. Reihl, R.A. Pollak, N. Mårtensson, F. Holtzberg, D.E. Eastman, Phys. Rev. B 26 (1982) 1713.
[6] R. Suyanarayanan, G. Günterodt, J.L. Freeouf, F. Holtzberg, Phys. Rev. B 12 (1975) 4215.
[7] G. Kaindl, W.D. Brewer, G. Kalkowski, F. Holtzberg, Phys. Rev. Lett. 51 (1983) 2036.
[8] M. Campagna, E. Bucher, G.K. Wertheim, D.N.E. Buchanan, L.D. Longinotti, Phys. Rev. Lett. 32 (1974) 885.
[9] T. Suzuki, Jpn. J. Appl. Phys. Ser. 8 (1993) 44.
[10] A. Kakizaki, A. Harasawa, T. Kinoshita, T. Ishii, T. Nanba, S. Kunii, Physica B 186–188 (1993) 80.
[11] T. Nanba, M. Tomikawa, Y. Mori, N. Shino, S. Imada, S. Suga, S. Kimura, S. Kunii, Physica B 186–188 (1993) 557.